Universiteit Gent
Faculteit Toegepaste Wetenschappen
Vakgroep Informatietechnologie

De eindige-differenties-in-het-tijdsdomein-methode voor de simulatie van geluidspropagatie in een bewegend medium

The finite-difference time-domain method for simulation of sound propagation in a moving medium

---

Timothy Van Renterghem

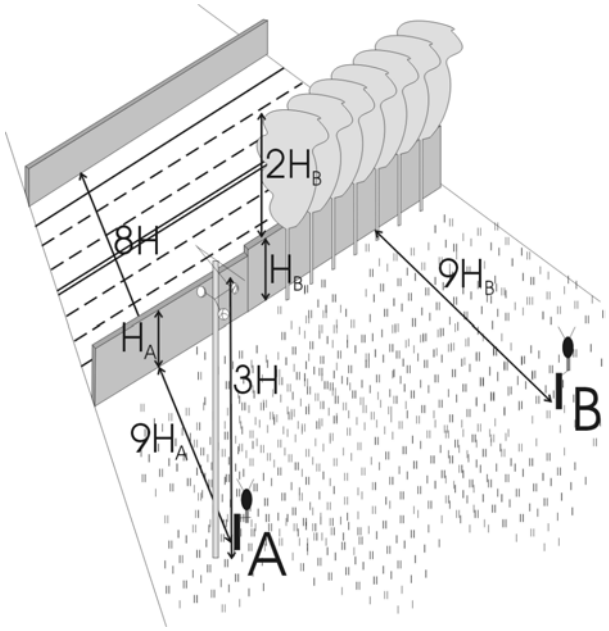

Proefschrift tot het behalen van de graad van
Doctor in de Toegepaste Wetenschappen
Academiejaar 2003-2004

PROMOTOR: [1]PROF. DR. IR. DICK BOTTELDOOREN

CO-PROMOTOR: [2]PROF. DR. IR. DONALD GABRIELS

[1] UNIVERSITEIT GENT

FACULTEIT TOEGEPASTE WETENSCHAPPEN

VAKGROEP INFORMATIETECHNOLOGIE

SINT-PIETERSNIEUWSTRAAT 41

B-9000 GENT, BELGIË

[2] UNIVERSITEIT GENT

FACULTEIT LANDBOUWKUNDIGE EN TOEGEPASTE BIOLOGISCHE WETENSCHAPPEN

VAKGROEP BODEMBEHEER EN BODEMHYGIËNE

COUPURE LINKS 653

B-9000 GENT, BELGIË

THESISINFO

Dankwoord

Dat bij akoestische studies heel wat komt kijken, heb ik de afgelopen 4 jaar wel degelijk ondervonden. Toen ik in 1999 aan dit doctoraat begon, kon ik me wel voorstellen dat ik heel wat uren door zou brengen achter de computer. Op een bepaald moment drong experimentele validatie zich op. Op basis van interessante bevinding in een windtunnelstudie, werd ook besloten om een veldexperiment uit te voeren. Dit resulteerde o.a. in het afzoeken van de grote autosnelwegen in Vlaanderen naar geschikte locaties, tot uiteindelijk een meetwagen uit een drassige weide proberen te krijgen. Dus heel wat meer afwisseling dan eerst verwacht !

Dick Botteldooren dient in de eerste plaats bedankt te worden. Zijn ruime ervaring en kennis in heel wat subdomeinen van de akoestiek waren meer dan nuttig. Zijn vele interessante ideeën zorgden ervoor dat ik me geen moment hoefde te vervelen. Ondanks drukke bezigheden stond hij de afgelopen jaren steeds klaar om kleine en grote problemen uit de weg te helpen. De talrijke "leesbeurten" de laatste maanden, waarbij resultaten steeds kritisch werden bekeken, zorgden zeker voor een meerwaarde in dit werk. Ook dient Donald Gabriels bedankt om de windtunnel enkele weken vrij te houden om de nodige experimenten uit te voeren.

De vakgroep Informatietechnologie (INTEC) werd ervaren als een goed uitgebouwde onderzoeksomgeving, waarbij jonge onderzoekers voldoende kansen krijgen. Deze verdiensten zijn in eerste plaats toe te schrijven aan de vakgroepvoorzitter Paul Lagasse.

De mensen van de onderzoeksgroep akoestiek op INTEC mogen zeker ook niet vergeten worden. De hulp van Andy (Verkeyn) en Tom (De Muer) bij de talrijke "problemen" bij het schrijven en compileren van C++ code werden zeer gewaardeerd. Marc (Declercq) dient bedankt voor de hulp bij het experimenteel werk, alsook voor assistentie bij het opzetten van de meetopstelling in de veldstudie. Luc (Dekoninck) maakte me wegwijs in het gebruik van de verschillende meettoestellen en de verwerking van meetresultaten.

De laatste 4 jaar is ook op persoonlijk vlak veel veranderd. Maaiken is mijn vrouw geworden. Tulien en onlangs nog Timon kwamen ons gezin vervoegen. Tezelfdertijd trokken we in ons nieuwe huis. Op zijn minst gezegd een zeer drukke periode. Vooral de laatste maanden heeft Maaiken enkele "huisvaderlijke taken" overgenomen, om mij toe te laten op een rustige manier het schrijven van deze doctoraatsthesis te beëindigen. Hiervoor zeer veel dank. Verder dient mijn mama bedankt om mij "wetenschappelijk asiel" te verlenen in het ouderlijke huis, op de momenten dat het bij ons thuis net iets te druk was om te werken.

Augustus 2003

Timothy Van Renterghem

Inhoudsopgave - Table of Contents

Publicaties

TIJDSCHRIFTEN

- T. Van Renterghem, D. Botteldooren, W. Cornelis, D. Gabriels : Reducing screen-induced refraction of noise barriers in wind with vegetative screens. Acustica - Acta Acustica **88** (2002) 231-238.

- T. Van Renterghem, D. Botteldooren : Effect of a row of trees behind noise barriers in wind. Acustica - Acta Acustica **88** (2002) 869-878.

- T. Van Renterghem, D. Botteldooren : Addition to: "Reducing screen-induced refraction of noise barriers in wind with vegetative screens". Acustica - Acta Acustica **89** (2003) 381.

- T. Van Renterghem, D. Botteldooren : Numerical simulation of the effect of trees on downwind noise barrier performance". Acustica - Acta Acustica **89** (2003) 764-778.

- T. Van Renterghem, D. Botteldooren : Bomenrijen ter verbetering van de efficiëntie van geluidsschermen in wind. Geluid **26** (2003) 50-52.

CONFERENTIE PROCEEDINGS

- T. Van Renterghem, D. Botteldooren : Effect of flow on performance of reactive acoustic structures using finite-difference time-domain simulations. Proceedings of Euronoise 2001, Patras, Griekenland.

- T. Van Renterghem, D. Botteldooren, W. Cornelis, D. Gabriels : Modifying wind profiles to improve the efficiency of noise barriers in wind. Proceedings of Internoise 2001, Den Haag, Nederland.

- T. Van Renterghem, D. Botteldooren : Improving noise barrier performance in wind using a row of trees : a field experiment. Proceedings of 9th International Congress on Sound and Vibration (2002), Orlando, VSA.

- T. Van Renterghem, D. Botteldooren : Using windscreens to improve the efficiency of noise barriers in wind : finite-difference time-domain simulations. Proceedings of Forum Acusticum 2002, Sevilla, Spanje.

- T. Van Renterghem, D. Botteldooren : Numerical simulation of sound propagation over rows of houses in the presence of wind. Proceedings of 10th International Congress on Sound and Vibration (2003), Stockholm, Zweden.

NEDERLANDSTALIGE SAMENVATTING

A. Inleiding

Het doel van dit werk is het effect van complexe stromingen op geluidspropagatie gedetailleerd in rekening brengen. Vooral de interactie tussen geluid en wind in de buitenomgeving zal bestudeerd worden.

Een belangrijke toepassing is een geluidsscherm in een windsituatie. Een sterke daling van de schermefficiëntie treedt immers op voor windafwaartse waarnemers. Dit negatief effect wordt toegeschreven aan de soms grote gradiënten in de windsnelheid, die geluid neerwaarts afbuigen in de akoestische schaduwzone. Het verwaarlozen van het effect van wind leidt tot een sterke overschatting van de windafwaartse schermwerking. Dit is een belangrijk probleem, daar het plaatsen van geluidsschermen een vaak gebruikte, geluidsreducerende maatregel is in verkeerssituaties. Naast een adequate modellering van de schermefficiëntie bij wind, wordt in dit werk ook een mogelijke oplossing voorgesteld voor dit probleem. Dit laatste onderzoek gebeurt door middel van experimenten en met numerieke simulaties.

Geluidshinder vormt steeds meer een bedreiging voor de kwaliteit van het leefmilieu. In Vlaanderen, net als in de meeste geïndustrialiseerde regio's, is wegverkeer de belangrijkste oorzaak van geluidshinder [1], naast hinder door luchtverkeer, burengeluid en dergelijke. Aangezien de belangrijkste bronnen zich in de buitenomgeving bevinden, plant geluid zich voort doorheen de atmosfeer alvorens het kan waargenomen worden (met uitzondering van direct burengeluid). De toestand waarin de atmosfeer zich bevindt heeft een belangrijke invloed op de geluidsvoortplanting. De lucht is immers geen stilstaand propagatiemedium. Windsnelheid en temperatuur variëren sterk met de hoogte boven het aardoppervlak. De wind in de atmosferische grenslaag is meestal turbulent : de windsnelheid varieert sterk op een welbepaalde plaats, zelfs op zeer beperkte tijdschalen. Aangezien de typische afstanden die geluidsgolven afleggen in de buitenomgeving groot zijn, dient men rekening te houden met atmosferische effecten voor het maken van accurate berekeningen. Adequate buitenpropagatiemodellen zijn o.a. nodig voor het uitvoeren van geluidsimpactstudies, alsook wanneer het effect van geluidsreducerende maatregelen onderzocht wordt. Gestandaardiseerde modellen als ISO 9613-2 [2], die rekening houden met meteorologische condities door middel van correctiefactoren, kunnen in dit opzicht een algemeen beeld geven, maar zijn echter niet bruikbaar wanneer specifieke en lokale effecten onderzocht worden.

De koppeling tussen de stroming en de akoestische beweging is in de meeste gevallen van geluidspropagatie in de buitenomgeving beperkt. De typische

windsnelheden zijn klein. Dit betekent dat geluidsgeneratie door de stroming onbelangrijk wordt. Verder wordt geacht dat de geluidsfrequenties van belang voor omgevingslawaai de (gemiddelde) stroming niet zullen verstoren. In dit werk wordt getracht de belangrijkste invloeden van wind op geluidspropagatie te simuleren namelijk convectie, afbuiging (refractie) en verstrooiing.

Een aantal simulatietechnieken, besproken in volgende paragrafen, worden vaak gebruikt om geluidspropagatie in de buitenomgeving te simuleren. Deze werden ontwikkeld met als doel geluidsniveaus op grote afstanden van een bron te berekenen, in de aanwezigheid van wind en een bodem met een eindige impedantie. Benaderingen van de golfvergelijkingen en windprofielen werden gemaakt. Deze simulatietechnieken beschrijven geluidspropagatie in het frequentiedomein.

Met de "Fast Field Program"-methode (*FFP*) (bijvoorbeeld [3]) kan geluidpropagatie gesimuleerd worden in een horizontaal gelaagde atmosfeer, waarbij de impedantie van de grond en de windsnelheidsprofielen constant zijn tussen bron en waarnemer.

Met de parabolische-vergelijkingsmethode ("Parabolic Equation", *PE*) (bijvoorbeeld [5]) kunnen variaties in windsnelheidsprofielen en grondimpedantie wel in rekening gebracht worden. Geluidspropagatie wordt in één richting, namelijk van de bron naar de waarnemer, gesimuleerd. Verder kunnen er enkel in een beperkte hoek vanuit de bron geluidsniveaus berekend worden. Het *PE*-model kan aangepast worden om geluidspropagatie in aanwezigheid van een geluidsscherm te simuleren [6].

De randelementenmethode ("Boundary Elements Method", *BEM*) werd onlangs uitgebreid op basis van de "normal mode solution" [11]. Op deze manier kan geluidspropagatie gesimuleerd worden in het specifieke geval van een lineair windsnelheidsprofiel [10]. De "normal mode solution" veronderstelt verder dat de directe geluidsgolf van bron naar ontvanger verwaarloosbaar is ten opzichte van de gereflecteerde golven op de bodem. Deze voorwaarde is meestal vervuld op voldoende afstand van de bron.

Deze simulatietechnieken hebben hun verdiensten, vooral in het simuleren van geluidspropagatie over grote afstanden. Hun toepasbaarheid wanneer geluidsschermen in een windsituatie voorkomen is eerder beperkt. Deze technieken houden enkel rekening met de windsnelheidscomponent in de propagatierichting. De verticale stromingen rond de geluidsschermen worden verwaarloosd. In de buurt van geluidsschermen komen windsnelheidsprofielen voor met opwaarts en neerwaarts afbuigende gedeeltes, afhankelijk van de hoogte. Een dergelijk profiel kan gesimuleerd met de *FFP*- of de *PE*-methode,

echter niet met de randelementenmethode. Aangezien de windsnelheidsprofielen sterk variëren met de afstand ten opzichte van een geluidsscherm, blijft enkel de *PE*-methode een mogelijk bruikbare techniek.

Een belangrijke toepassing in een verkeerssituatie, namelijk een geluidsbron tussen twee geluidsschermen in de aanwezigheid van wind, kan niet gesimuleerd worden met voorvermelde technieken. De randelementenmethode is zeer geschikt voor de simulatie van complexe en meervoudige schermen in een stilstaand medium. Met de *PE*-methode kan men geluidspropagatie over een eenvoudig, enkel geluidsscherm simuleren in wind, op voorwaarde dat bron en ontvanger zich op voldoende afstand bevinden van het scherm. Meervoudige reflecties tussen schermen kunnen niet in rekening gebracht worden.

Er is dus een gebrek aan gedetailleerde simulatietechnieken om geluidspropagatie te berekenen in specifieke situaties waar complexe stromingen aanwezig zijn. In dit opzicht werd de eindige-differenties-in-het-tijdsdomeinmethode uitgebreid om rekening te houden met een niet-uniforme, rotationele stroming. De eindige-differenties-in-het-tijdsdomeintechniek wordt gebruikt in een groot aantal subdomeinen van de akoestiek [15, 16, 17, 18, 19, 20, 21].

Belangrijke voordelen van deze methode zijn het eenvoudig concept, maar ook de accuraatheid. De golfvergelijkingen worden niet vereenvoudigd. Dit betekent dat alle (complexe) golfverschijnselen zoals verstrooiing op onregelmatige structuren, meervoudige reflecties en meervoudige diffracties kunnen in rekening gebracht worden. De akoestische differentiaalvergelijkingen worden gediscretiseerd in het tijdsdomein. Realistische bronnen, transiënte fenomenen en niet-lineaire effecten kunnen gemodelleerd worden. Een andere voordeel is dat met een enkele simulatie transferfuncties voor een uitgebreid frequentiebereik kunnen opgesteld worden.

Het belangrijkste nadeel echter is dat de eindige-differenties-in-het-tijdsdomeintechniek een grote behoefte heeft aan rekenkracht. Dit zorgt ervoor dat deze techniek beperkt is tot het simuleren van laag- of midden-frequent geluid, zeker wanneer typische buitensituaties worden beschouwd.

Zoals reeds eerder gesteld, wordt enkel de invloed van de stroming op de golfvoortplanting beschouwd. Dit betekent dat de akoestische simulaties en stromingsberekeningen onafhankelijk van elkaar kunnen gebeuren. De golfvergelijkingen gebruiken de “achtergrondstroming” als input. Dit is een vaak toegepaste, praktische rekenmethode [22, 23], temeer beide types van numerieke simulatie verschillende eisen hebben voor wat betreft de ruimtelijke discretisatie en de tijdsdiscretisatie.

B. Theoretisch gedeelte

B.1. Mathematisch model

De vergelijkingen van Euler, die de stroming in een niet-visceus medium beschrijven, waarbij de zwaartekracht wordt verwaarloosd, worden gebruikt om de akoestische vergelijkingen af te leiden:

$$\rho_t\left[\frac{\partial \mathbf{v_t}}{\partial t} + (\mathbf{v_t}\cdot\nabla)\mathbf{v_t}\right] + \nabla p_t = 0\,, \tag{1}$$

$$\frac{\partial \rho_t}{\partial t} + \nabla\cdot(\rho_t \mathbf{v_t}) = 0\,. \tag{2}$$

In deze vergelijkingen stelt p_t de druk voor, $\boldsymbol{v_t}$ de snelheidsvector en ρ_t de massadichtheid.

B.1.1. Snelheidsvergelijking

Een alternatieve vorm van de impulsvergelijking (1) wordt gebruikt om behoud van kinetische energie te verzekeren. De vergelijking zoals voorgesteld in (1) kan resulteren in onstabiele simulaties in complex stromingen [25]. Volgende vorm is nodig om een numeriek schema te ontwikkelen, bruikbaar in een brede waaier van toepassingen:

$$\rho_t\left[\frac{\partial \mathbf{v_t}}{\partial t} - \mathbf{v_t}\times(\nabla\times\mathbf{v_t})\right] + \nabla p_t + 0.5\rho_t\nabla(\mathbf{v_t}\cdot\mathbf{v_t}) = 0\,. \tag{3}$$

In deze vorm verschijnt de kinetische-energieterm expliciet. Op deze manier is het ook mogelijk om veronderstellingen te maken in verband met de rotor van de akoestische snelheid, zoals verder besproken in dit hoofdstuk.

De akoestische vergelijkingen worden beschouwd als een perturbatie van de Euler-vergelijkingen. De druk, de dichtheid van het propagatiemedium en de snelheid worden opgesplitst in een deel toegekend aan de (achtergrond)stroming (met onderschrift *0*), en een akoestisch gedeelte:

$$\rho_t = \rho_0 + \rho\,, \tag{5}$$

$$\mathbf{v_t} = \mathbf{v_0} + \mathbf{v}\,, \tag{6}$$

$$p_t = p_0 + p\,. \tag{7}$$

De achtergrondstroming wordt onsamendrukbaar verondersteld:

$$\nabla \rho_0 = 0\,, \tag{9}$$

Op grotere schaal drukt bovenstaande voorwaarde de homogeniteit uit van het propagatiemedium. Variaties in de omgevingsdruk en omgevingsdichtheid worden niet beschouwd in dit werk.

Verder wordt de achtergrondstroming tijdsinvariant verondersteld:

$$\frac{\partial \mathbf{v_0}}{\partial t} = 0\,, \tag{10}$$

$$\frac{\partial \rho_0}{\partial t} = 0\,. \tag{11}$$

Gebruik van vergelijking (5)-(11) in vergelijking (3) resulteert in

$$\rho_0 \left[\frac{\partial \mathbf{v}}{\partial t} - \mathbf{v} \times \left(\nabla \times \mathbf{v_0} \right) - \mathbf{v_0} \times \left(\nabla \times \mathbf{v} \right) \right] + \nabla p + \rho_0 \nabla \left[\mathbf{v} \cdot \mathbf{v_0} \right] = 0\,. \tag{12}$$

Deze vergelijking is gelineariseerd in de akoestische grootheden. Dit betekent dat gemengde akoestische termen verwaarloosd werden. Brontermen, die geen akoestische grootheden bevatten, werden weggelaten aangezien geluidsgeneratie niet wordt beschouwd. Kwadratische termen in Mach getal (dit is de verhouding van de stroomsnelheid en de geluidssnelheid) werden verwaarloosd.

Het akoestisch snelheidsveld ***v*** kan, zoals elke vectoriële grootheid, geschreven worden als

$$\mathbf{v} = \nabla \phi \; + \nabla \times \mathbf{A} = \mathbf{v_g} + \mathbf{v_r}\,, \tag{13}$$

waarbij ϕ de snelheidspotentiaal is, en $\nabla \times \mathbf{A} = \mathbf{v_r}$ het rotationeel gedeelte voorstelt. In een isotroop, stilstaand medium is het rotationeel deel van de akoestische perturbutie gelijk aan 0.

De veronderstelling (6) dat ***v*** het akoestisch gedeelte is van het snelheidsveld vertaalt zich in:

$$\mathbf{v_g} \gg \mathbf{v_r}\,. \tag{14}$$

Vergelijking (13) wordt gebruikt om de grootte-orde van de eerste termen in (12) te vergelijken in het frequentiedomein:

$$\frac{\partial \mathbf{v}}{\partial t} \to O\left[\omega \left| v_g \right|\right], \tag{15}$$

$$\mathbf{v_0} \times \left(\nabla \times \mathbf{v}\right) \to O\left[M\omega \left| v_r \right|\right]. \tag{16}$$

Aangezien $\nabla \times \nabla \phi = 0$, bevat term (16) enkel het rotationeel gedeelte van het snelheidsveld. De Mach getallen in de toepassingen die beoogd worden in dit werk zijn veel kleiner dan 1 (denk bijvoorbeeld maar aan typische windsnelheden). Er kan dus besloten worden op basis van ongelijkheid (14) dat

$$\mathbf{v_0} \times \left(\nabla \times \mathbf{v}\right) \ll \frac{\partial \mathbf{v}}{\partial t}. \tag{17}$$

De akoestische snelheidsvergelijking reduceert zich uiteindelijk tot

$$\frac{\partial \mathbf{v}}{\partial t} - \mathbf{v} \times \left(\nabla \times \mathbf{v_0}\right) + \frac{1}{\rho_0} \nabla p + \nabla\left[\mathbf{v} \cdot \mathbf{v_0}\right] = 0. \tag{18}$$

B.1.2. Drukvergelijking

Ook in de massavergelijking (2) worden de stromingsgrootheden opgesplitst volgens (5)-(7). De veronderstelling van een tijdsinvariante stroming en linearisatie van het akoestisch veld resulteert in

$$\frac{\partial \rho}{\partial t} + \nabla \cdot \rho \mathbf{v_0} + \nabla \cdot \rho_0 \mathbf{v} + S_p = 0. \tag{19}$$

Brontermen werden weggelaten in de bovenstaande vergelijking. Onsamendrukbaarheid en tijdsinvariantie van de achtergrondstroming resulteert in een divergentieloze stroming:

$$\nabla \cdot \mathbf{v_0} = 0. \tag{20}$$

Vergelijking (19) herleidt zich verder tot

$$\frac{\partial \rho}{\partial t} + \mathbf{v_0} \cdot \nabla \rho + \rho_0 \nabla \cdot \mathbf{v} = 0. \tag{21}$$

De akoestische compressies en expansies kunnen geïdealiseerd worden als adiabatische processen voor de frequenties van belang in akoestische studies.

Een lineaire druk-dichtheidsrelatie is gebruikt [24]:

$$p = c^2 \rho\,, \tag{22}$$

waarbij c de adiabatische geluidssnelheid is, die verondersteld wordt tijdsinvariant te zijn, net zoals de achtergrondstroming.

Aangezien dit werk zich toespitst op het effect van wind op geluidspropagatie, wordt geen rekening gehouden met temperatuursgradiënten (die zorgen voor lokale verschillen in de geluidssnelheid). Toegepast op vergelijking (21) resulteert dit in de drukvergelijking:

$$\frac{\partial p}{\partial t} + \rho_0 c^2 \nabla \cdot \mathbf{v} + \mathbf{v_0} \cdot \nabla p = 0\,. \tag{23}$$

B.2. Eindige-differenties-in-het-tijdsdomeinmodel

De akoestische snelheden en drukken bevinden zich niet op dezelfde fysische locaties in de gebruikte rekenroosters ("verschoven" of "staggered"). Ook worden de drukvelden en snelheidsvelden niet berekend op dezelfde, discrete tijden. De spatiale organisatie van een driedimensionale rekencel is weergegeven in Figuur 1. Een dergelijke opstelling resulteert in een tweede-orde-accurate benadering wanneer de tijds- en ruimte-afgeleiden centraal worden benaderd [28].

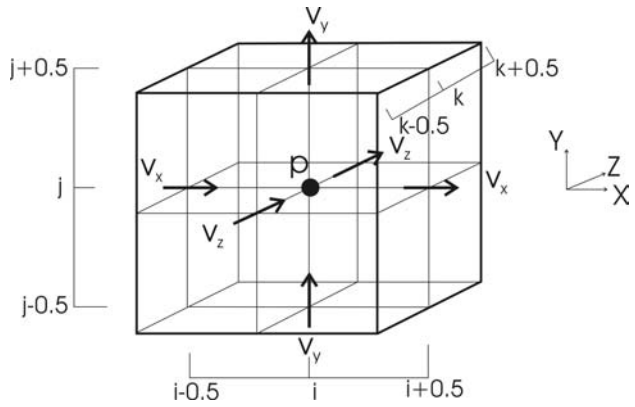

Figuur 1 Ruimtelijke organisatie van een *EDTD*-rekencel in een driedimensionaal, "verschoven" grid.

De componenten van de achtergrondstroomsnelheid worden gediscretiseerd op dezelfde posities als de akoestische snelheidscomponenten.

In afwezigheid van een achtergrondstroming zijn de gediscretiseerde druk- en snelheidsvergelijking eenvoudig af te leiden:

$$v^{l+0.5}_{\alpha(\alpha+0.5)} = v^{l-0.5}_{\alpha(\alpha+0.5)} - \frac{dt}{\rho_0}\left[\frac{p^l_{(\alpha+1)} - p^l}{d\alpha}\right], \tag{24}$$

$$p^{l+1} = p^l - dtc^2\rho_0\sum_\beta\left(\frac{v^{l+0.5}_{\beta(\beta+0.5)} - v^{l+0.5}_{\beta(\beta-0.5)}}{d\beta}\right). \tag{25}$$

In deze vergelijkingen stelt α één van de drie Cartesische indices voor. De sommatie over β loopt over de drie indices. De ruimtelijke indices *(i, j, k)* in de gediscretiseerde grootheden zijn weggelaten voor de eenvoud. De plaats ten opzichte van deze positie wordt aangeduid met *(β+0.5)*, *(β–0.5)* enz. De onderschriften stellen de discrete plaats voor, de bovenschriften de discrete tijden. De drukvelden worden berekend op tijden *l dt*, terwijl de snelheidsvelden op de tussenliggende tijden *(l+0.5) dt* worden bepaald. $d\beta$ is de ruimtelijke discretisatiestap volgens coördinaatas β en *dt* de tijdstap.

Er werd aangetoond in [28] dat volgende voorwaarde nodig is om stabiliteit te verzekeren:

$$c\,dt\sqrt{\sum_\beta \frac{1}{d\beta^2}} \le 1. \tag{26}$$

In de aanwezigheid van een achtergrondstroming, is het bekomen van de gediscretiseerde vergelijkingen minder voor de hand liggend. De tijdsafgeleiden worden benaderd door volgende, bi-lineaire transformatie [29]:

$$\frac{\partial}{\partial t} \to \frac{2}{dt}\frac{\left(1 - z^{-1}\right)}{\left(1 + z^{-1}\right)}, \tag{27}$$

waarbij z^{-1} een vertragingsoperator voorstelt, die verschuift over één enkele tijdstap. Een dergelijke benadering resulteert in onvoorwaardelijk stabiele systemen.

B.2.1. Discrete drukvergelijking

Het gebruik van vergelijking (27) in de drukvergelijking (23), en na het verplaatsen van de gekende variabelen op tijdstip *(l+1) dt* naar het rechterlid geeft:

$$p^{l+1} + 0.5dt\left(\mathbf{v_0} \cdot \nabla p^{l+1}\right) = p^l - dtc^2\rho_0\left(\nabla \cdot \mathbf{v}^{\mathbf{l+0.5}}\right) - 0.5dt\left(\mathbf{v_0} \cdot \nabla p^l\right). \quad (28)$$

Dit resulteert in een vergelijking met 7 onbekende drukken op tijd *(l+1) dt*. De *6* naburige akoestische drukken, nodig voor het berekenen van de gradiënt in het linkerlid, worden benaderd door de druk in afwezigheid van stroming:

$$p_{appr.}^{l+1} \approx p^l - dtc^2\rho_0\left(\nabla \cdot \mathbf{v}^{\mathbf{l+0.5}}\right). \quad (29)$$

Op deze manier wordt beoogd een efficiënt en een expliciet schema te bekomen. Deze benadering is equivalent met het verwaarlozen van tweede-orde termen in Mach getal, en is accuraat voor lage stroomsnelheden. Ook bij grote snelheden kan nog voldoende accuraat gewerkt worden, echter wel met gebruik van een sterk verfijnd rekenrooster (zie hoofdstuk B.5, handelend over numerieke accuraatheid).

Dit resulteert in de gediscretiseerde akoestische drukvergelijking. Centrale, eindige differenties worden gebruikt voor de ruimte-afgeleiden. Lineaire interpollatie wordt toegepast wanneer de plaatsen van de akoestische snelheden dienen gekend te zijn op een druklocatie:

$$\begin{aligned} p^{l+1} = p^l - dtc^2\rho_0 \sum_\beta \left(\frac{v_{\beta(\beta+0.5)}^{l+0.5} - v_{\beta(\beta-0.5)}^{l+0.5}}{d\beta} \right) \\ -dt\left[\sum_\beta \left(\frac{v_{0\beta(\beta+0.5)} + v_{0\beta(\beta-0.5)}}{2} \right) \left(\frac{\xi_{(\beta+1)}^{l+0.5} - \xi_{(\beta-1)}^{l+0.5}}{2d\beta} \right) \right], \end{aligned} \quad (30)$$

waarbij

$$\xi^{l+0.5} = p^l - 0.5dtc^2\rho_0 \sum_\beta \left(\frac{v_{\beta(\beta+0.5)}^{l+0.5} - v_{\beta(\beta-0.5)}^{l+0.5}}{d\beta} \right). \quad (31)$$

Het gebruik van de grootheid ξ kan geïnterpreteerd worden als een eerste schatting van de akoestische druk op tijdstip *l+0.5* in afwezigheid van stroming.

B.2.2. Discrete snelheidsvergelijking

Naar analogie met de drukvergelijking, wordt de snelheidsvergelijking (18) op dezelfde manier gediscretiseerd. De onbekende, naburige snelheden die nodig zijn om de snelheden op het nieuwe tijdstip *(l+0.5) dt* te berekenen, worden benaderd door de akoestische snelheidvergelijking in afwezigheid van een achtergrondstroming:

$$\mathbf{v}_{appr.}^{\mathbf{l+0.5}} \approx \mathbf{v}^{\mathbf{l-0.5}} - \frac{dt}{\rho_0}\nabla p^l . \tag{32}$$

Dit resulteert in de eindige-differenties-in-het-tijdsdomeinvergelijking om de akoestische snelheid te berekenen:

$$\begin{aligned} v_{\alpha(\alpha+0.5)}^{l+0.5} = v_{\alpha(\alpha+0.5)}^{l-0.5} - dt\sum_{\beta\neq\alpha}\frac{\left(\chi^l_{\beta(\alpha+1,\beta+0.5)} + \chi^l_{\beta(\alpha+1,\beta-0.5)} + \chi^l_{\beta(\beta+0.5)} + \chi^l_{\beta(\beta-0.5)}\right)}{4} R_{0\alpha\beta(\alpha+0.5)} \\ -\frac{dt}{\rho_0}\left[\frac{p^l_{(\alpha+1)} - p^l}{d\alpha}\right] - dt\left[\frac{v_{0\alpha(\alpha+1.5)}\chi^l_{\alpha(\alpha+1.5)} - v_{0\alpha(\alpha-0.5)}\chi^l_{\alpha(\alpha-0.5)}}{2d\alpha}\right] \\ -dt\sum_{\beta\neq\alpha}\left(\frac{\left(\frac{\left(\chi^l_{\beta(\alpha+1,\beta+0.5)} + \chi^l_{\beta(\alpha+1,\beta-0.5)}\right)\left(v_{0\beta(\alpha+1,\beta+0.5)} + v_{0\beta(\alpha+1,\beta-0.5)}\right)}{4}\right) - \left(\frac{\left(\frac{\left(\chi^l_{\beta(\beta+0.5)} + \chi^l_{\beta(\beta-0.5)}\right)\left(v_{0\beta(\beta+0.5)} + v_{0\beta(\beta-0.5)}\right)}{4}\right)}{d\alpha}\right), \end{aligned} \tag{33}$$

waarbij

$$R_{0\alpha\beta(\alpha+0.5)} = \frac{\left(v_{0\alpha(\alpha+0.5,\beta+1)} - v_{0\alpha(\alpha+0.5,\beta-1)}\right)}{2d\beta} - \frac{\frac{\left(v_{0\beta(\alpha+1,\beta+0.5)} + v_{0\beta(\alpha+1,\beta-0.5)}\right)}{2} - \frac{\left(v_{0\beta(\beta+0.5)} + v_{0\beta(\beta-0.5)}\right)}{2}}{d\alpha}, \tag{34}$$

$$\chi^{l}_{\alpha(\alpha+0.5)} = v^{l-0.5}_{\alpha(\alpha+0.5)} - 0.5\frac{dt}{\rho_0}\frac{\left(p^{l}_{(\alpha+1)} - p^{l}\right)}{d\alpha}. \tag{35}$$

Naar analogie met ξ in de drukvergelijking, kan χ^l geïnterpreteerd worden als een eerste schatting van de snelheid op een tussenliggend tijdstip. Zoals benadrukt tijdens de afleiding van de continue vergelijkingen, wordt de gemengde (akoestische en achtergrond stroming) kinetische-energieterm $v_0\chi$ samen gehouden tijdens het nemen van de ruimtelijke afgeleiden.

B.2.3. Ruimtelijke uitgestrektheid van het numeriek schema en tijdsalgorithme

In een laag-orde schema is slechts een beperkt aantal naburige cellen nodig voor de berekening van een nieuwe waarde in een druk- of snelheidspunt. In Figuur 2 wordt een tweedimensionale voorstelling gegeven van de waarden van naburige cellen die nodig zijn om een druk of een snelheid op de nieuwe tijd te berekenen.

De drukken en snelheden die nodig zijn bij de berekening van ξ en χ, geassocieerd met de voorspellende stap tussen twee tijdstappen, worden beschouwd als een geheel. Dit resulteert in een efficiënt numeriek schema. Dezelfde waarden worden immers opgevraagd door naburige drukken en snelheden op elke tijdstap. Overbodige berekeningen worden vermeden door de berekende waarden bij te houden in het geheugen van de computer.

Het opslaan van de drukken en snelheden in één enkele parameter, op verder verwijderde punten ten opzichte van de plaats waar de nieuwe waarde wordt berekend, resulteert in een eenvoudigere behandeling in de buurt van de randen van het rekenrooster. De ξ die buiten het grid valt, wordt verplaatst naar het dichtstbijzijnde punt in het grid zelf. Dit is voorgesteld in Figuur 3. Er dient dan rekening gehouden te worden met een gewijzigde afstand waarover de gradiënt berekend wordt. Om de waarde van χ op een rand zelf te bepalen, dienen aparte formules opgesteld, afhankelijk van het randtype.

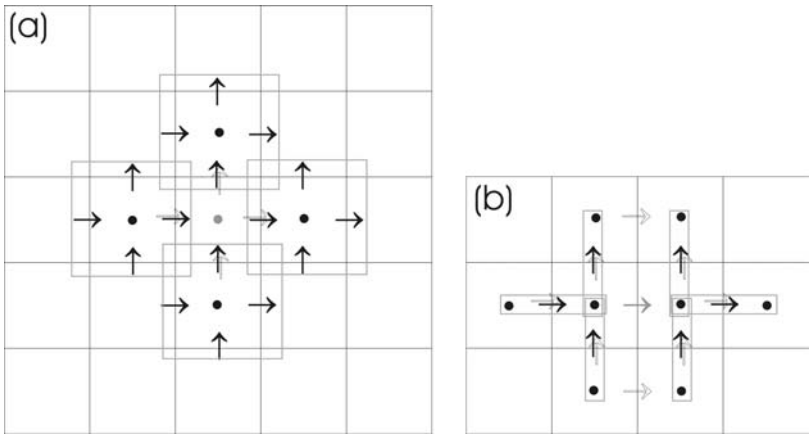

Figuur 2 Overzicht van de locaties van de akoestische drukken (bolletjes), de componenten van de akoestische snelheden (zwarte pijlen) alsook de componenten van de snelheid van de achtergrondstroming (witte pijlen), die gebruikt worden bij de berekening van een bepaalde druk (a) en snelheid (b). De plaatsen waar de golfvergelijkingen geëvalueerd worden zijn aangeduid met de grijze symbolen.

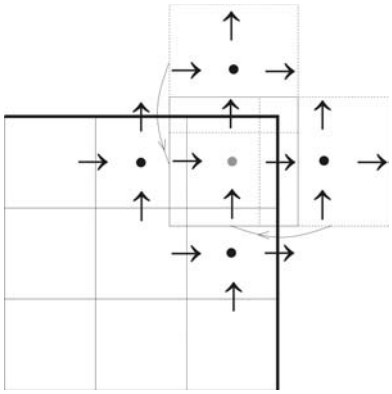

Figuur 3 Het verplaatsen van de locatie waar een berekening van ξ gevraagd wordt, die buiten het rekenrooster valt. De gebieden aangeduid met een stippellijn, die de akoestische snelheden en drukken aanduiden voor de berekening van ξ, worden tijdens de berekening vervangen door het gebied aangeduid met de volle lijnen.

De discrete vergelijkingen werden opgesteld zodat de nieuwe waarden van de akoestische grootheden enkel afhangen van de waarden op de vorige tijd. Het gebruik van een dergelijk compact schema in de tijd resulteert in een belangrijke reductie van gebruik van computergeheugen. De nieuwe waarden vervangen

immers de oude waarden in het geheugen. De verschillende velden, namelijk χ, $\boldsymbol{v}$, ξ en p, worden om beurten vernieuwd in het tijdstap-algorithme.

Het belang van de gebruikte benaderingen voor wat betreft de momentumvergelijking is geïllustreerd door middel van een numeriek voorbeeld. Een structuur die representatief is voor een geluidsdemper op basis van een expantiekamer, met verlengde in- en uitlaten, werd beschouwd. Belangrijke gradiënten in de stroming, alsook circulerende stromingen werden waargenomen. De stroomsnelheid in de inlaat bedroeg 30 m/s. Een breedbandig, akoestisch signaal werd geëxciteerd in de inlaat. Het tijdsantwoord werd geregistreerd in de uitlaat van de demper, en is weergegeven in Figuur 4. Simulaties werden uitgevoerd met verschillende varianten van de momentumvergelijking, waarbij de veronderstelling (17), alsook de energieconservatievorm, al dan niet werden beschouwd. Een voldoende stabiel tijdssignaal werd enkel waargenomen voor de energieconservatievorm in combinatie met veronderstelling (17).

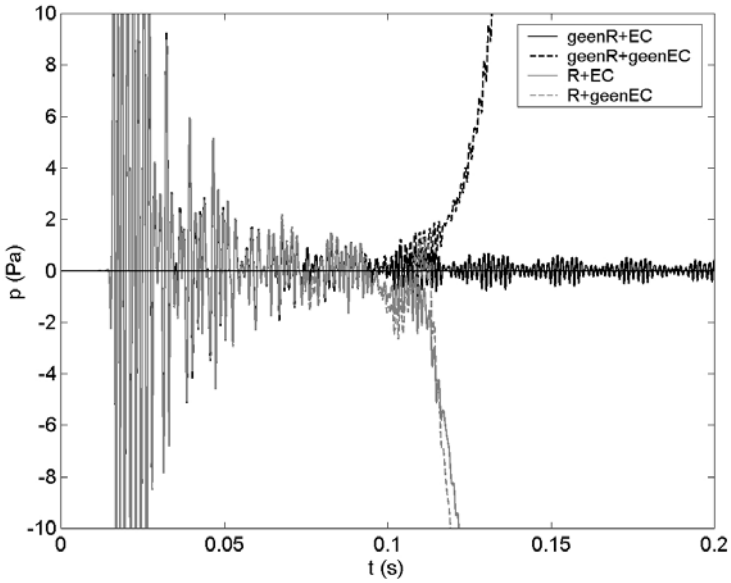

Figuur 4 Tijdsantwoord voor een ontvanger in de uitlaat van een demper. Volgende codes werden gebruikt: *R* betekent dat geen veronderstelling werd gemaakt voor wat betreft de rotor van de akoestische snelheid, *geenR* betekent dat veronderstelling (17) werd gebruikt. *EC* betekent dat de kinetische energiebehoudsvorm werd gebruikt, *geenEC* gebruikt deze vorm niet.

B.3. Randvoorwaarden

B.3.1. Perfect reflecterende randvoorwaarde

Een perfect reflecterend vlak is eenvoudig te simuleren in het gebruikte rekenrooster. De akoestische snelheden die voorkomen op de randen worden op 0 gezet.

B.3.2. Eindige-impedantierandvoorwaarde - Grondmodel

De interactie tussen geluidsgolven en de bodem is belangrijk wanneer geluidspropagatie wordt bestudeerd in een buitenomgeving. Vooral de reflectie op de bodem dient gekend te zijn. Bodems worden dan ook vaak benadered door een vlak met een eindige impedantie. Talrijke grond-impedantiemodellen zijn voorhanden in de akoestische literatuur, gaande van eenvoudige, empirische modellen (bijvoorbeeld [32]) tot meer gedetailleerde modellen (bijvoorbeeld [36]) met een fysische achtergrond. Een impedantiemodel geeft de relatie weer tussen de akoestische oppervlakte-impedantie en de fysische parameters die de structuur van de bodem beschrijven, in functie van de geluidsfrequentie. Deze werden met succes toegepast in allerhande simulatietechnieken in het frequentiedomein.

De simulatie van bodemeffecten in het tijdsdomein is mogelijk via een beschrijving van de geluidspropagatie in de bodem zelf. De bodem kan bijvoorbeeld beschouwd worden als een poreus en elastisch medium ([39, 41]). In een eenvoudiger model wordt enkel toegelaten dat de aanwezige lucht in de grond trilt, terwijl de bodemdeeltjes een vast kader vormen. Een dergelijke model is beschreven door Zwikker and Kosten [42] voor poreuze materialen, maar ook bruikbaar om geluidspropagatie in een bodem te beschrijven. Het model gebruikt drie parameters namelijk de stromingsweerstand (R), porositeit (φ) en de structuur factor (k_s):

$$\nabla \cdot p + \rho' \frac{\partial \boldsymbol{v}}{\partial t} + R\boldsymbol{v} = 0, \tag{36}$$

$$\frac{\partial p}{\partial t} + \rho' c'^2 \nabla \cdot \boldsymbol{v} = 0, \tag{37}$$

$$\rho' = \frac{\rho_0 k_s}{\varphi}, \tag{38}$$

$$c' = \frac{c}{\sqrt{k_s}}. \tag{39}$$

Een dempingsterm is toegevoegd aan de vergelijkingen op basis van de stromingsweerstand. De massadichtheid (ρ') en de geluidssnelheid in de bodem (c') worden aangepast met gebruik van de porositeit en de structuur factor. De impedantie van een dergelijk medium kan begroot worden met volgende uitdrukking:

$$\frac{Z}{Z_0} = \sqrt{\frac{R}{\rho\omega\varphi} j + \frac{k_s}{\varphi^2}}. \tag{40}$$

Een groot aantal natuurlijke bodems kunnen door middel van een dergelijk frequentie-impedantieverloop beschreven worden.

B.3.3. Perfect absorberende randvoorwaarden (*PAR*)

Het gebied waarbinnen berekeningen worden gemaakt, heeft meestal geen fysische randen. Denk bijvoorbeeld maar aan de atmosfeer in de buitenomgeving. Dit betekent dat het onbeperkte gebied waarin geluid propageert, gereduceerd moet worden tot een beperkt simulatiegebied. Dit kan via gebruik van de zogenaamde perfect absorberende randvoorwaarden. Deze beperking mag immers niet leiden tot (niet-fysische) reflecties van geluidsgolven op de grenzen van een simulatiegebied.

In een tijdsdomeinmethode is het mogelijk het gebruik van *PAR*'s te vermijden door te werken met een kort, breedbandig signaal. De opname van het tijdssignaal wordt beëindigd wanneer reflecties, afkomstig van niet-fysische randen, de ontvanger bereiken. Er mag in een dergelijke benadering geen overlapping zijn van het nuttige signaal en ongewenste reflecties. De waarnemer en de randen moeten zich dus op voldoende afstand van elkaar bevinden. Een dergelijke benadering kan met succes toegepast worden voor geluidspropagatie over een vlakke grond [18], of wanneer de invloed van een enkelvoudig geluidsscherm wordt berekend [17].

In situaties met een lang tijdsantwoord, zoals in een typische verkeerssituatie, namelijk een geluidsbron tussen twee geluidsschermen, is een *PAR* noodzakelijk. Het is immers niet mogelijk om het simulatiegebied te blijven uitbreiden om te vermijden dat ongewenste reflecties de ontvangers bereiken alvorens het ontvangen signaal volledig is gedempt.

Eerste-orde randvoorwaarde

Een eerste-orde randvoorwaarde werd uitgewerkt, voor een niet-uniforme stroming, loodrecht op de rand. Een dergelijke situatie treedt bijvoorbeeld op bij stroming doorheen een buis, of bij een logarithmisch windsnelheidsprofiel in de buitenomgeving.

Om de akoestische snelheid op de rand zelf (α+0.5) te berekenen, dient de drukgradiënt over deze rand heen gekend te zijn. Volgende benadering wordt gebruikt:

$$\frac{p^l_{(\alpha+1)} - p^l}{d\alpha} \approx \frac{p^l_{(\alpha+0.5)} - p^l}{0.5 d\alpha}. \tag{41}$$

De drukken zijn echter niet gedefiniëerd op de randen van het rekenrooster. Deze druk wordt gerelateerd aan de snelheid op de rand, met gebruik van de definitie van de akoestische impedantie:

$$p^l_{(\alpha+0.5)} = Z_0 \left(\frac{v^{l+0.5}_{\alpha(\alpha+0.5)} + v^{l-0.5}_{\alpha(\alpha+0.5)}}{2} \right), \tag{42}$$

waarbij Z_0 de impedantie van lucht is. Daar er in een dergelijke benadering geen impedantieverschil is tussen het propagatiemedium en de rand, zal er in theorie geen reflectie van akoestische energie optreden, voor een loodrechte invallende vlakke golf.

Op basis van een vereenvoudigde snelheidsvergelijking, en met gebruik van bovenstaande benaderingen, kan volgende randvergelijking afgeleid worden (voor een rechtse rand, waarbij α loopt van links naar rechts):

$$\begin{aligned} v^{l+0.5}_{\alpha(\alpha+0.5)} \left(1 + \frac{dtZ_0}{d\alpha\rho_0} \right) &= v^{l-0.5}_{\alpha(\alpha+0.5)} \left(1 - \frac{dtZ_0}{d\alpha\rho_0} \right) \\ -dt \sum_{\beta \neq \alpha} \left[\frac{\left(\chi^l_{\beta(\beta+0.5)} + \chi^l_{\beta(\beta-0.5)} \right)}{2} \frac{\left(v_{0\alpha(\alpha+0.5,\beta+1)} - v_{0\alpha(\alpha+0.5,\beta-1)} \right)}{2d\beta} \right] & \\ -dt v_{0\alpha(\alpha+0.5)} \left(\frac{\chi^l_{\alpha(\alpha+0.5)} - \chi^l_{\alpha(\alpha-0.5)}}{d\alpha} \right) + \left[\frac{2dt}{d\alpha\rho_0} \right] p^l. & \end{aligned} \tag{43}$$

Deze benadering van een *PAR* is numeriek goedkoop. De accuraatheid is echter beperkt. Vaak zal een meer geavanceerde techniek nodig zijn, zoals de "Perfect Aangepaste Lagen" (*PAL*)- theorie, voorgesteld in het volgende hoofdstuk.

"Perfect Aangepaste Lagen"-theorie

"Perfect Aangepaste Lagen" werden voor het eerst ontwikkeld voor elektromagnetische toepassingen van de eindige-differenties-in-het-tijdsdomeinmethode [43]. Ook voor akoestische golven werden *PAR*'s met succes gebruikt (bijvoorbeeld in [44, 45, 46, 47]). In een dergelijke benadering wordt het rekengebied uitgebreid met een beperkt aantal cellen, die zorgen voor een sterke, artificiële demping van geluidsgolven. In theorie is er geen reflectie op een dergelijke absorberende randvoorwaarde, voor elke invalshoek en voor elke frequentie van de invallende golf.

Er wordt uitgegaan van de vergelijkingen die geluidsgolven beschrijven in een uniforme achtergrondstroming. Dempingscoëfficiënten κ werden toegevoegd aan de akoestische vergelijkingen. De stromingsrichting α wordt loodrecht verondersteld op de *PAL*:

$$\frac{\partial p_{\perp}}{\partial t} + c^2 \rho_0 \frac{\partial v_{\alpha}}{\partial \alpha} + V_{0\alpha} \frac{\partial p_{\perp}}{\partial \alpha} + \kappa_{1,\perp} p_{\perp} = 0 , \tag{44}$$

$$\frac{\partial p_{//}}{\partial t} + c^2 \rho_0 \sum_{\gamma \neq \alpha} \frac{\partial v_{\gamma}}{\partial \gamma} + V_{0\alpha} \frac{\partial p_{//}}{\partial \alpha} + \kappa_{1,//} p_{//} = 0 , \tag{45}$$

$$p_{\perp} + p_{//} = p , \tag{46}$$

$$\rho_0 \left[\frac{\partial v_{\alpha}}{\partial t} + V_{0\alpha} \frac{\partial v_{\alpha}}{\partial \alpha} \right] + \frac{\partial p}{\partial \alpha} + \kappa_{2,\perp} v_{\alpha} = 0 , \tag{47}$$

$$\rho_0 \left[\frac{\partial v_{\beta}}{\partial t} + V_{0\alpha} \frac{\partial v_{\beta}}{\partial \alpha} \right] + \frac{\partial p}{\partial \beta} + \kappa_{2,//} v_{\beta} = 0 , \beta \neq \alpha . \tag{48}$$

Een belangrijke stap is het opsplitsen van de akoestische druk in twee artificiële componenten : één loodrecht ($p_{\perp}$) op de overgang tussen de Berenger-laag en het rekengebied, de andere component parallel ($p_{//}$) met deze overgang. Deze opsplitsing van het drukveld zorgt voor een extra vrijheidsgraad. Zoniet, kan enkel voor loodrechte inval perfecte absorptie bekomen worden [43]. In de drukvergelijking worden de dempingscoëfficiënten $\kappa_{1,\perp}$ and $\kappa_{1,//}$ toegevoegd,

respectievelijk voor de orthogonale en parallelle component. In de snelheidsvergelijking loodrecht op *PAL* wordt $\kappa_{2,\perp}$ gebruikt, terwijl $\kappa_{2,//}$ wordt geïntroduceerd in de parallelle snelheidsvergelijkingen.

De *PAL* is een anisotroop medium : de demping hangt af van de invalshoek. Dit betekent dat voorwaarde (17) niet werd gebruikt om de snelheidsvergelijkingen af te leiden die de basis vormen voor de Berenger-vergelijkingen. Dit is equivalent met het berekenen van de afgeleide van v_α naar β, in plaats van de afgeleide van v_β naar α in de term van vergelijking (48) die de achtergrondstroming bevat.

Enkele belangrijke tussenstappen in het bekomen van geschikte voorwaarden voor de dempingcoëfficiënten worden hieronder weergegeven.

Een vlakke golf in een uniforme achtergrondstroming V_0, invallend onder een hoek θ (voor een meebewegende waarnemer) ten opzichte van de normaal (richting α) op de overgang tussen het rekengebied en het *PAL*-gebied, is te schrijven als:

$$v_\alpha = v_{0,\alpha} e^{-jk\cos\theta(\alpha - V_{0\alpha}t) - jk\sin\theta\beta} e^{-j\omega t} . \tag{49}$$

$$p = p_0 e^{-jk\cos\theta(\alpha - V_{0\alpha}t) - jk\sin\theta\beta} e^{-j\omega t} . \tag{50}$$

Een analoge golf in de Berenger-laag is gedefinieerd als:

$$v_{\alpha,PML} = T v_{0,\alpha} e^{-jk\cos\theta(\alpha - V_{0\alpha}t) - jk\sin\theta\beta - \gamma_\alpha(\alpha - V_{0\alpha}t) - \gamma_\beta\beta} e^{-j\omega t} . \tag{51}$$

$$p_{PML} = T p_0 e^{-jk\cos\theta(\alpha - V_{0\alpha}t) - jk\sin\theta\beta - \gamma_\alpha(\alpha - V_{0\alpha}t) - \gamma_\beta\beta} e^{-j\omega t} . \tag{52}$$

waarbij T de transmissiecoëfficiënt is, die gelijk gesteld wordt aan 1 wanneer er geen reflecties zijn. Parameters γ_α and γ_β zijn de dempingscoëfficiënten volgens de twee beschouwde coördinaat-assen.

Een eerste voorwaarde die gesteld wordt is de continuïteit op de overgang tussen de *PAL*-cellen het simulatiegebied. Het verband tussen de amplitude van de druk en snelheid in het rekengebied, alsook het relatie tussen beiden in de *PAL* werden opgesteld. De amplitude van de akoestische snelheid die zich op de overgang tussen beide gebieden bevindt, moet via beide benaderingen identiek zijn. Dit levert een eerste voorwaarde op.

In tweede instantie wordt een verband tussen de amplitude van de verschillende drukcomponenten opgesteld, op basis van de loodrechte (44) en parallelle (45) component van de drukvergelijking. Dit resulteert in de volgende set van vergelijkingen:

$$\begin{bmatrix} \left(-j\omega+\kappa_{1,\perp}\right)-c^2\rho_0\dfrac{\left(jk\cos\theta+\gamma_\alpha\right)^2}{\left(-j\omega\rho_0+\kappa_{2,\perp}\right)} & -c^2\rho_0\dfrac{\left(jk\cos\theta+\gamma_\alpha\right)^2}{\left(-j\omega\rho_0+\kappa_{2,\perp}\right)} \\ -c^2\rho_0\dfrac{\left(jk\sin\theta+\gamma_\beta\right)^2}{\left(-j\omega\rho_0+\kappa_{2,//}\right)} & \left(-j\omega+\kappa_{1,//}\right)-c^2\rho_0\dfrac{\left(jk\sin\theta+\gamma_\beta\right)^2}{\left(-j\omega\rho_0+\kappa_{2,//}\right)} \end{bmatrix}\begin{bmatrix} p_{0,\perp} \\ p_{0,//} \end{bmatrix}=0$$

(53)

De determinant van de coëfficiënten-matrix moet gelijk zijn aan 0 opdat een oplossing zou bekomen worden, verschillende van de nuloplossing (p_0=0). Om perfecte absorptie te verkrijgen, moeten γ_α en γ_β naar 0 gaan. Elke impedantie-verandering in de media waartussen geluid propageert resulteert immers in reflectie. De vergelijking kan zich op basis hiervan verder vereenvoudigen en levert, met gebruik van de continuïteitsvoorwaarde:

$$\left(-j\omega+\kappa_{1,\perp}\right)\left(-j\omega+\kappa_{1,//}\right)+\left(-j\omega+\kappa_{1,\perp}\right)\left[c^2\rho_0\frac{k^2\sin^2\theta}{\left(-j\omega\rho_0+\kappa_{2,//}\right)}\right]$$

$$\left[-c^2k^2\frac{\cos^2\theta}{\omega^2\rho_0}\right]\left(-j\omega+\kappa_{1,//}\right)\left(-j\omega\rho_0+\kappa_{2,\perp}\right)=0\,. \quad (55)$$

Voorwaarden voor de dempingscoëfficiënten moeten onafhankelijk zijn van de invalshoek θ. Opdat de invalshoek de oplossing van vergelijking (55) niet mee zou bepalen, wordt de goniometrische eigenschap gebruikt die aanduidt dat de som van de kwadraten van de sinus en cosinus van een hoek gelijk is aan 1. Dit betekent dat de coëfficiënten van de termen die $sin^2\theta$ en $cos^2\theta$ bevatten gelijk moeten zijn:

$$\left(-j\omega+\kappa_{1,\perp}\right)\left[\frac{c^2\rho_0k^2}{\left(-j\omega\rho_0+\kappa_{2,//}\right)}\right]=\left[\frac{-c^2k^2}{\omega^2\rho_0}\right]\left(-j\omega+\kappa_{1,//}\right)\left(-j\omega\rho_0+\kappa_{2,\perp}\right).$$

(56)

Het oplossen van deze vergelijking resulteert in de volgende voorwaarde:

$$\kappa_{2,//}=\kappa_{1,//}=0\,, \quad (57)$$

$$\kappa_{1,\perp}=\frac{\kappa_{2,\perp}}{\rho_0}\,. \quad (58)$$

Wanneer deze condities vervuld zijn, komt er theoretisch geen reflectie voor. In een discreet *EDTD*-rekenrooster zal er echter numerieke reflectie optreden wanneer een geluidsgolf de overgang maakt naar de perfect aangepaste laag door het sterk verschil in dempingseigenschappen. Reflectie zal ook te wijten zijn aan de beperkte afmetingen van de Berenger-laag. Om deze discontinuïteit te beperken, stelde Berenger [49] voor de dempingsparameters gradueel te laten toenemen:

$$\kappa_{1,\perp}\left(x\right) = \kappa_{1,\perp,MAX}\left(\frac{x}{d_{PAL}}\right)^{m}, \tag{59}$$

waarbij x de diepte is in de laag, volgens de normaal op de overgang met het rekengrid, en d_{PAL} de dikte van de *PAL*. Waarden voor de schalingsmacht m variëren tussen 2 en 4 [44, 45, 49].

De performantie van de *PAL* werd onderzocht door middel van enkele numerieke voorbeelden. Een breedbandig signaal werd gebruikt, met een centrale frequentie van 500 Hz en een bandbreedte van 150 Hz. De invloed van de dikte van de *PAL* zonder stroming werd in detail onderzocht voor schuin invallende golven. Dit is een vaak voorkomend geval voor wat betreft simulaties in een buitenomgeving. Aangezien propagatieafstanden groot zijn, dient de hoogte van het rekenrooster zoveel mogelijk beperkt te worden. Het effect van refractie moet echter wel nog voldoende in rekening kunnen gebracht worden. Een lijnbron werd gesimuleerd in een tweedimensionale simulatie, in een stilstaand medium.

Voor elke dikte werd een optimale set van waarden $\kappa_{1,\perp}$ en m gezocht, zodat een minimale, gemiddelde reflectie werd verkregen voor invalshoeken tussen 20 en 80 graden.

Figuur 5 geeft aan dat de eerste-orde *PAR* van weinig praktisch belang is. Voor een loodrechte inval wordt typisch een daling in reflectie bekomen van 40 dB. De reflectie stijgt bij een stijgende invalshoek. Met een geoptimaliseerde *PAL* van slechts 2 cellen kan een (gemiddeld) betere performantie verkregen worden voor de brede waaier van invalshoeken die werden beschouwd.

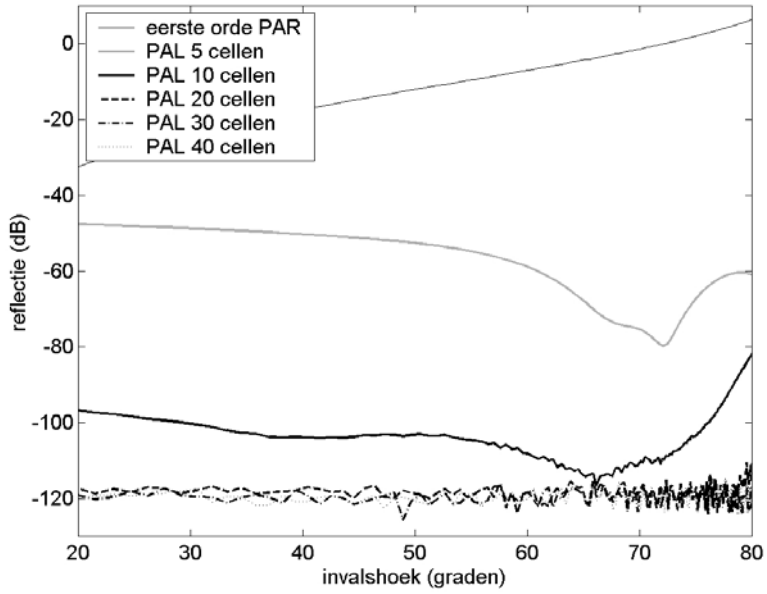

Figuur 5 Reflectie op Perfect Absorberende Randvoorwaarden met stijgende invalshoek. De eerste-orde benadering (zie vergelijking (43)) en Perfect Aangepaste Lagen (*PAL*) met een dikte van 5, 10, 20, 30 en 40 rekencellen werden beschouwd.

Het gebruik van de *PAL* bestaande uit 10 rekencellen zorgt voor een verbetering van de absorptie met enkele grootte-ordes. Vanaf 20 cellen zijn nog slechts beperkte verbeteringen mogelijk. Het gebruik van 30 rekencellen om de *PAL* te vormen geeft een daling in de reflectie van 120 dB, voor elke invalshoek die werd beschouwd. Een reflectie van -100 dB en lager zorgt voor een signaal met ruis, aangezien de amplitudes in dergelijke gevallen bijzonder laag zijn. De geringste numerieke inaccuraatheid resulteert in onregelmatige curves. Voor de *PAL* bestaande uit 5 en 10 cellen, wordt een sterke variatie van het gedrag in functie van de invalshoek waargenomen. Dit is veroorzaakt door het feit dat de doorgelaten golf in de Berenger-laag niet voldoende is uitgedempt als de perfect reflecterende wand, geplaatst na de *PAL*, wordt bereikt. Deze gereflecteerde golf komt opnieuw in het rekenveld, en interfereert met de golven die gereflecteerd worden ter hoogte van de *PAL*.

Het gedrag van de *PAL* in aanwezigheid van een achtergrondstroming werd in tweede instantie onderzocht. Simulaties werden uitgevoerd voor een uniforme

stroming, loodrecht op de overgang tussen gewone rekencellen en de *PAL*, en een niet-uniforme stroming, loodrecht op de overgang, in de aanwezigheid van gradiënten. Een vlakke golf valt loodrecht in op de *PAL*.

De aanwezigheid van een uniforme stroming zorgt met stijgende stroomsnelheid voor een extra daling in performantie ten opzichte van een stilstaand medium. Voor lage stroomsnelheden is deze daling zeer beperkt, en steeds kleiner dan 2 dB voor typische windsnelheden. De oorzaak van deze daling in absorptie dient niet gezocht te worden in de eigenschappen van de *PAL* zelf, maar eerder in het gebruik van de voorspellende stap bij afwezigheid van stroming, tussen twee tijdstappen. Meer informatie over de accuraatheid van deze benadering kan gevonden worden in hoofdstuk B.5.

De *PAL*-condities werden afgeleid voor geluidspropagatie in een uniforme stroming. De aanwezigheid van gradiënten in de achtergrondstroming zorgt dan ook voor een verdere daling van de performantie van de *PAL*. Deze daling werd berekend, relatief tot de reflectie bekomen in een uniforme stroomsnelheid. Een gradiënt van 100/s veroorzaakt een stijging in reflectie van ongeveer 35 dB. Wanneer een *PAL* met een voldoende aantal cellen wordt gebruikt, kan nog steeds een performantie van -80 tot -90 dB worden bereikt. Dergelijke grote gradiënten in de stroming komen slechts lokaal voor, bijvoorbeeld zeer dicht bij de grond in een logarithmisch snelheidsprofiel. In de praktijk hebben de uniforme *PAL*-vergelijkingen dus een brede toepasbaarheid.

B.4. Stabiliteit

De expliciete *EDTD*-methode is niet onvoorwaardelijk stabiel. Bij afwezigheid van stroming, dient het Courant getal kleiner dan of gelijk te zijn aan 1 [28]. Aangezien geen analytische stabiliteitsvoorwaarde bekomen werd voor de discrete vergelijkingen die geluidspropagatie in een algemene stroming beschrijven, werd stabiliteit onderzocht door middel van een numeriek voorbeeld. In een ééndimensionale simulatieruimte propageert een signaal met centrale frequentie 500 Hz een bandbreedte van 250 Hz, tussen bron en ontvanger, in een uniforme achtergrondstroming. De meest stabiele vorm van de momentumvergelijking werd gebruikt, namelijk de energieconservatievorm met in acht name van veronderstelling (17).

Onstabiliteit geeft aanleiding tot een “vals” signaal, wanneer het werkelijk signaal de ontvanger heeft bereikt en voldoende is gedempt. De groeisnelheid van een dergelijke onstabiliteit hangt af het Courant getal, en van de grootte van de achtergrondstroming. De “tijd tot instabiliteit” wordt gedefinieerd (*TTI*). Dit is de simulatietijd tussen het moment dat het werkelijk signaal de ontvanger

bereikt, en het moment dat het onstabiliteitssignaal eenzelfde geluidsdrukniveau bereikt. Het Courant getal (*CN*) in deze ééndimensionale simulatieruimte is gedefinieerd als

$$CN = \frac{(c + v_0)dt}{dx}. \tag{60}$$

De invloed van het Mach getal op stabiliteit is groot (zie Figuur 6). Mach getallen kleiner dan 0.2 resulteren in volledig stabiele simulaties, voor Courant getallen kleiner dan 1.2. Dit betekent dat de introductie van een kleine achtergrondstroming niet zal leiden tot strengere eisen om stabiliteit te bekomen, voor wat betreft simulaties in buitenomgeving. Voor grote Mach getallen is de *TTI* sterk afhankelijk van het Courant getal. Voor elke stroomsnelheid kan een Courant getal gevonden worden waar de helling van de curves in Figuur 6 zeer steil wordt. Zolang het Courant getal kleiner is dan deze waarde, of wanneer de simulatietijd voldoende kleiner is dan de *TTI*, wordt onstabiliteit vermeden.

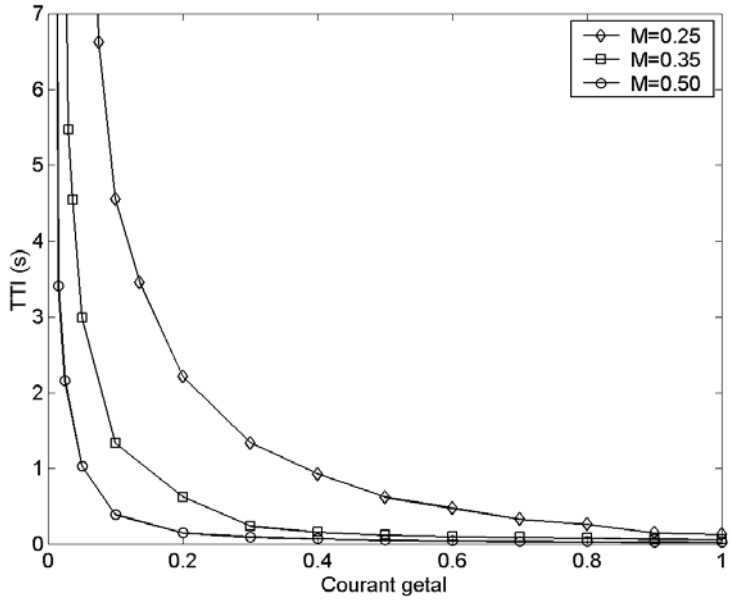

Figuur 6 Tijd tot instabiliteit (*TTI*) in geval van een uniforme achtergrondstroming (Mach getallen gelijk aan *0.25*, *0.35* and *0.50*), in functie van het Courant getal in een ééndimensionale simulatieruimte.

B.5. Numerieke accuraatheid

De numerieke accuraatheid werd onderzocht in een ééndimensionale simulatieruimte. Een pulse propageert tussen 2 punten in een uniforme achtergrondstroming. De theoretische amplitude op beide punten is constant voor elke frequentie, terwijl een lineair faseverschil in functie van de frequentie wordt verwacht. De afstand tussen beide punten bedraagt 40 rekencellen.

Er kan aangetoond worden dat de eindige-differenties-in-het-tijdsdomeinmethode behoud van amplitude kent in afwezigheid van stroming. In Referentie [15] werd een formule afgeleid voor de fasefout in een driedimensionaal, oneindig uitgestrekt gebied. Op basis hiervan kon besloten worden dat er geen fasefout wordt waargenomen in een ééndimensionale simulatieruimte, als het Courant getal gelijk is aan 1. In een twee- of driedimensionale simulatie is de fasefout enkel 0 voor een Courant getal gelijk aan 1 en op voorwaarde dat de propagatie verloopt volgens de diagonaal van de cellen [15].

Enkele resultaten van het onderzoek omtrent de numerieke accuraatheid in stroming worden hieronder weergegeven. Het theoretisch faseverschil tussen beide meetpunten wordt uitgezet ten opzichte van het faseverschil berekend met de *EDTD*-methode in Figuur 7, voor verschillende verhoudingen van de golflengte van het geluid ten opzichte van de ruimtelijke discretisatiestap. Deze simulaties werden uitgevoerd voor verschillende stroomsnelheden. Het Courant getal bij elke stroomsnelheid bedraagt 1. Met een stijgend aantal cellen per golflengte, gaat de fasefout naar 0, voor elke stroomsnelheid. Een stijgend Mach getal zorgt voor een stijging van de fasefout bij een constant aantal cellen per golflengte. Wanneer de verhouding tussen het aantal cellen en de golflengte van het geluid groot is, wordt de invloed van de stroomsnelheid zeer beperkt.

Ook de amplitudefout werd onderzocht, voor een stijgend aantal cellen per golflengte (zie Figuur 8). Met stijgende stroomsnelheid wordt de amplitudefout significant groter, in tegenstelling tot het meer beperkte effect van de stroomsnelheid op de fasefout. Het Courant getal is gelijk aan 1 in alle situaties. In afwezigheid van stroming kunnen afwijkingen ten opzichte van 1 in Figuur 8 niet waargenomen worden.

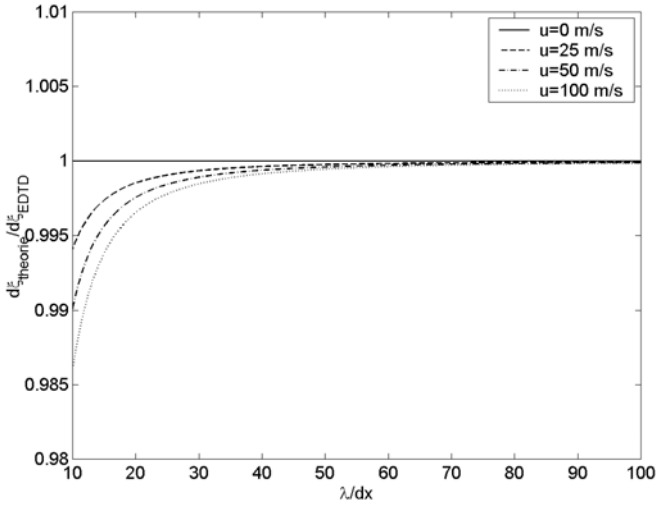

Figuur 7 Accuraatheid voor wat betreft de fase bij een stijgend aantal rekencellen per golflengte, in een ééndimensionale simulatieruimte. Verschillende uniforme achtergrondstroomsnelheden worden beschouwd. Het Courant getal is gelijk aan 1.

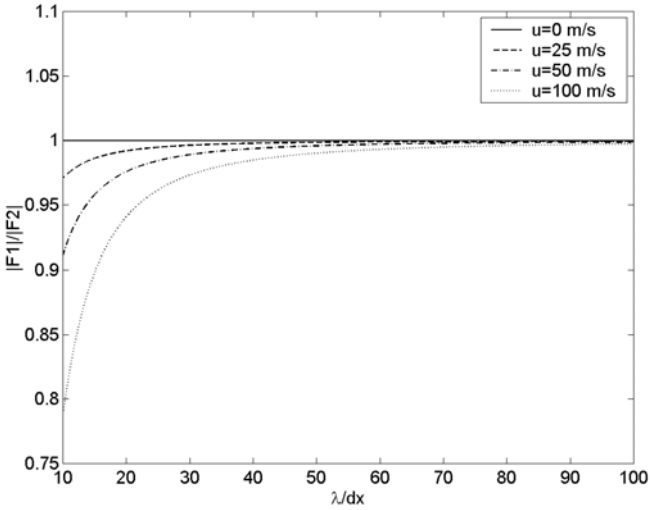

Figuur 8 Accuraatheid voor wat betreft de amplitude, bij een stijgend aantal rekencellen per golflengte, in een ééndimensionale simulatieruimte. Verschillende uniforme achtergrondstroomsnelheden worden beschouwd. Het Courant getal is gelijk aan 1.

De amplitudefout is een illustratie van de benadering toegepast tijdens de discretisatie van de snelheidsvergelijking. De voorspellende stap met verwaarlozing van de stroming tussen twee tijdstappen van zowel de druk- als snelheidsvergelijking zal accurater zijn wanneer de tijdstap klein wordt gehouden. Voor een vaste tijdstap zal deze benadering minder accuraat worden naarmate de stroomsnelheid stijgt.

Er kon verder besloten worden dat een Courant getal gelijk aan 1 zorgt voor een minimale fasefout en een maximale amplitudefout, bij een constante stroomsnelheid. Aan deze tegenstrijdige eisen kan tegemoet gekomen worden door het nemen van een groter aantal cellen per golflengte, hetgeen echter wel leidt tot een grotere simulatiekost. Lage stroomsnelheden zorgen echter niet voor significant grotere fase- en amplitudefouten.

B.6. Turbulente stroming en akoestische verstrooiing

Atmosferische turbulentie

De meeste luchtstromingen in de buitenomgeving zijn sterk turbulent. Een turbulente atmosfeer kan voorgesteld worden door een geheel van ronddraaiende stromingen (of de zogenaamde “eddies”), op verschillende schalen. De gradiënten die aanwezig zijn in de grote, circulerende stromingen zorgen voor wrijving en bijgevolg dissipatie van energie. Op deze manier onstaan eddies op een lager energieniveau. De lengteschalen in de atmosfeer variëren typisch van kilometers tot millimeters [50].

Verschillende modellen kunnen gebruikt worden om de relatie tussen de turbulente energie en de verschillende lengteschalen te beschrijven. Belangrijke voorbeelden zijn het Gaussiaans spectrum, het Kolmogorov spectrum en het von Kármán spectrum. Deze beschrijven een homogeen en isotroop, turbulent veld.

Het spectrum van turbulente bewegingen kan opgesplitst worden in 3 deelgebieden. Met een dalende lengteschaal of met een stijgend ruimtelijk golfgetal kunnen het brongebied of de energiehoudende regio, het inertiegebied en het dissipatiegebied onderscheiden worden.

In het inertiegebied wordt energie op een efficiënte manier doorgegeven tussen opeenvolgende schalen. De dissipatie op elke schaal is beperkt. Dit resulteert in een constante helling in dit gebied van het turbulente energiespectrum. Kolomogorov stelde vast dat voor stromingen met een hoog Reynolds getal, zoals in de atmosfeer, de energie proportioneel is met het ruimtelijk golfgetal tot de macht –5/3 in het inertiegebied [52]. In het dissipatiegebied wordt een

belangrijk gedeelte van de turbulente energie omgezet naar warmte. Dit resulteert in een vlugge afname van de energie met stijgend golfgetal.

Het zijn vooral de bronregio en het inertiegebied die een invloed zullen uitoefenen op de geluidsfrequenties in praktische toepassingen [51]. De bronregio is verantwoordelijk voor fluctuaties van de fase, terwijl variaties in de amplitude veroorzaakt worden door eddies in de inertiezone [53]. Verstrooiing op turbulentie wordt vooral waargenomen wanneer de golflengte van het geluid dezelfde afmetingen heeft van de lengteschalen van de turbulentie, en op plaatsen waar geluidsniveaus klein zijn. Een goede modellering van het inertiegebied is daarom van belang.

Simulatie van turbulente stromingen

De numerieke simulatie van sterk tubulente stromingen vormt nog steeds een uitdaging. Belangrijke technieken zoals de "Direct Numerical Simulation" (*DNS*) en "Large-Eddy Simulation" (*LES*) zijn enkel bruikbaar met zeer sterke computerkracht. In *DNS* worden de Navier-Stokes-vergelijkingen zonder veronderstellingen opgelost, terwijl in *LES* de kleinste schalen van turbulentie worden vervangen door een model.

Statistisch-stabiele turbulente stromingen kunnen berekend worden met de zogenaamde *RANS*-modellen (Reynolds-Averaged Navier-Stokes). Dergelijke simulaties geven geen informatie over het tijdsverloop van de turbulente stroming, en gelden als een praktische simulatiemethode voor het berekenen van turbulente stromingen. Een veel toegepast *RANS*-model is het k-ε-model.

Met een dergelijke benadering worden enkel de grote, ronddraaiende stromingen gemodelleerd. Eddies waarvan de lengteschalen in de buurt liggen van de akoestische golflengtes zijn uitgemiddeld in de berekende stromingsvelden. Het zijn echter deze schalen die van belang zijn voor turbulente verstrooiing.

Generatie van een turbulent verstrooiend veld

In veel gevallen is turbulentie door windsnelheidsfluctuaties dominant ten opzichte van turbulenties veroorzaakt door temperatuurfluctuaties in de atmosfeer [30, 55, 56]. Daarom wordt enkel turbulentie als gevolg van variaties in de ogenblikkelijke windsnelheid gemodelleerd. Een turbulent verstrooiend veld wordt geconstrueerd door middel van de turbule-theorie, beschreven in Referentie [57]. Eddies of turbules met een willekeurige oriëntatie worden op willekeurige plaatsen in het stromingsveld geïntroduceerd. De energie-inhoud

van de verschillende schalen volgt het Kolomogorov spectrum (of von Kármán spectrum) in het inertiegebied. Volgende formule beschrijft een enkele turbule:

$$\boldsymbol{v} = \boldsymbol{\Omega}_{\alpha} \times \left(\boldsymbol{r} - \boldsymbol{b}\right) e^{-\frac{|\boldsymbol{r}-\boldsymbol{b}|^2}{a_{\alpha}^2}}, \tag{61}$$

waarbij $\boldsymbol{b}$ het centrum van de turbule is, $\boldsymbol{r}$ een plaats voorstelt, a_α de lengteschaal is op schaal α, en $\boldsymbol{\Omega_\alpha}$ de hoeksnelheidsvector op schaal α. In Referentie [57] wordt deze laatste parameter gelinkt aan de algemene turbule parameters, de lengteschaal en de snelheids-structuurparameter C_v^2 voor een typisch Kolmogorov spectrum. De snelheids-structuurparameter is een algemene maat voor het uitdrukken van de turbulentiesterkte. De lengteschaal en de grootte van de hoeksnelheid op de verschillende turbulentieschalen zijn met elkaar gelinkt door middel van vaste, eenvoudige relaties.

In de *EDTD*-rekengrids is de grootste turbulentieschaal waarmee rekening kan gehouden worden beperkt door de dimensies van het simulatiegebied. De kleinste schaal moet voldoende groter zijn dan de ruimtelijke discretisatiestap, om een divergentieloze, roterende stroming te kunnen simuleren. Rekening houdende met een algemeen aanvaarde waarde voor wat betreft accuraatheid van 10 cellen per golflengte, zullen de belangrijkste lengteschalen verantwoordelijk voor verstrooiing aanwezig zijn in de stromingsvelden.

Het turbule-model veronderstelt een “gefixeerd”, turbulent veld. Deze benadering is gerechtvaardigd omdat de tijdsvariaties in stroomvelden meestal veel kleiner zijn dan de tijd die een geluidsgolf nodig heeft om te propageren tussen bron en waarnemer (weliswaar wanneer deze zich op beperkte afstanden van elkaar bevinden) [55, 59]. Het is dan wel noodzakelijk om een aantal willekeurige realisaties van het turbulent stroomveld te beschouwen. Een akoestische simulatie doorheen een aantal realisaties is nodig om statistisch-verantwoorde resultaten te verkrijgen.

In Referentie [58] is een methode voorgesteld om een homogeen turbulent veld te construeren, met als doel het Kolmogorov spectrum te benaderen. De voorwaarden voor homogeniteit en isotropie zijn in praktische situaties meestal niet vervuld [56, 60]. Een mogelijke manier om enigszins rekening te houden met bijvoorbeeld de verhoogde turbulentie in de buurt van obstakels is een schaling toe te passen van de grootte van de hoeksnelheidsvector met de wortel van de lokale, turbulente kinetische energie k, zoals berekend met het k-ε-model.

C. Toepassingen

C.1. Bomenrijen ter verbetering van geluidsschermen in wind

C.1.1. Meteorologische effecten op de efficiëntie van geluidsschermen

Een daling van de efficiëntie van een geluidsscherm voor windafwaartse waarnemers werd reeds uitgebreid geanalyseerd (bijvoorbeeld in [63, 64, 65, 66, 68]). Het plaatsen van een niet-gestroomlijnd obstakel (zoals een geluidsscherm) in wind zorgt voor sterke, positieve gradiënten in de windsnelheid vlak boven de akoestische schaduwzone, en bijgevolg voor een neerwaartse afbuiging van geluidsgolven. Dit fenomeen wordt aangeduid met de term scherm-geïnduceerde refractie van geluid.

Turbulente effecten worden in het algemeen ondergeschikt bevonden ten opzichte van de scherm-geïnduceerde refractie [64, 71].

Adequate maatregelen om de schermefficiëntie in een windsituatie te verbeteren werden tot op heden nog niet voorgesteld. Geluidschermen met kleine openingen, schuine gedeeltes en dergelijke werden onderzocht in aanwezigheid van wind in Referentie [72], en vergeleken met een klassiek, rechthoekig en dun geluidsscherm. Sommige schermen resulteerden in een slechtere situatie wanneer er geen wind was. Verder dient de beperkte verbetering (enkele dB's) die mogelijk is met sommige configuraties in een windsituatie afgewogen te worden tegenover de (sterke) stijging in constructiekosten in vergelijking met een klassieke scherm.

In dit werk wordt een mogelijke oplossing voorgesteld, die zich niet toespitst op het scherm zelf. Het plaatsen van een rij bomen, dat dienst doet als een windscherm na een geluidsscherm, wordt voorgesteld. Op deze manier kan ook een daling in de turbulentiesterkte verwacht worden, en een bijhorende beperking van verstrooiing van akoestische energie in de schaduwzone. Het gebruik van bomen om windeffecten te beperken is geen nieuwe maatregel, en wordt reeds sinds eeuwen gebruikt in landbouwkundige toepassingen.

Bomen na een geluidsscherm plaatsen is een relatief goedkope maatregel, en huidige probleemsituaties kunnen eenvoudig aangepast worden. Verder hebben natuurlijk-lijkende geluidsbarrières positieve psycho-akoestische eigenschappen [73, 74].

Het onderzoek naar het gebruik van bomenrijen om de scherm-geïnduceerde refractie van geluid te beperken bestaat uit drie delen.

In een windtunnelstudie werd een verkeerssituatie op schaal gesimuleerd. Een belangrijk frequentie-interval van het verkeersspectrum werd beschouwd (van 500 Hz tot 1000 Hz op volle schaal). Ook werd een veldexperiment langs een autosnelweg uitgevoerd om de bevindingen uit het windtunnelexperiment aan de praktijk te toetsen. In een derde stap werden numerieke simulaties met de *EDTD*-methode uitgevoerd. Op basis van de experimentele data uit het windtunnel experiment werd de *EDTD*-methode gevalideerd voor wat betreft geluidspropagatie over geluidsschermen in de aanwezigheid van windschermen. Er werd verder gezocht welke parameters een belangrijke invloed hebben bij dergelijke opstellingen, wat de effecten zijn in een breed gebied windafwaarts, en welke opstellingen optimaal zijn in een typische verkeerssituatie.

C.1.2. Windtunnelexperiment

opzet

De experimenten werden uitgevoerd in de gesloten windtunnel van het Internationaal Centrum voor Eremologie [75]. De dikte van de gesimuleerde atmosferische grenslaag in de windtunnel werd kunstmatig verhoogd door het plaatsen van ruwheidselementen en kegels in het gebied vlak voor de testsectie.

Een schaalfactor van 20 werd gebruikt voor dit experiment. De akoestische afscherming en afbuiging van geluid zullen zich op dezelfde manier gedragen op volle schaal als in het schaalexperiment. De sterke van de turbulentie (Reynolds getal) is in het schaalmodel 20 maal kleiner, terwijl luchtabsorptie groter zal zijn dan op volle schaal. In het onderzochte gebied wordt de scherm-geïnduceerde refractie van het geluid veel belangrijker geacht dan turbulente effecten [64]. Effecten van luchtabsorptie zijn verwaarloosbaar aangezien propagatie-afstanden beperkt zijn.

Windafwaartse geluidspropagatie over geluidsschermen werd onderzocht, voor een loodrecht invallende windrichting op het scherm. De windsnelheden in het experiment, gemeten boven de grenslaag, waren 6.4 m/s en 11 m/s. Enkelvoudige geluidsschermen en geluidsschermen aan beide zijden van de bron, in combinatie met verschillende locaties en groottes van windschermen, werden uitgetest. Meetpunten werden geplaatst op afstanden tussen 3H en 10H na het (windafwaartse) geluidsscherm (H is de hoogte van het geluidsscherm en bedraagt 0.18 m in het schaalmodel), op een hoogte van ongeveer een halve schermhoogte. Een overzicht van de opstellingen en afmetingen is terug te vinden in Figuur 9.

Een lijnbron op grondniveau zond signaal uit met een (vlak) frequentie-interval tussen 10 kHz en 20 kHz in het schaalmodel, hetgeen overeenkomt met 500 Hz

tot 1 kHz op volle schaal. Dit is een belangrijke component van het spectrum van verkeersgeluid.

Met behulp van metingen en simulaties, in afwezigheid van geluidsschermen, werd de eindige impedantie van de vezelplaten, die de valse vloer vormden in de windtunnel, gekarakteriseerd als een zachte bodem (met een stromingsweerstand van 5 kPa s/m^2).

Synthetische windschermen werden gebruikt om de windreductie van een rij bomen te simuleren. Porositeit is de belangrijkste eigenschap van een windscherm [77]. In dit opzicht kunnen kunstmatige schermen gebruikt worden als model voor de kruinen van een rij bomen met eenzelfde porositeit.

De porositeit van de gebruikte windschermen bedroeg 32%, hetgeen resulteert in een optimale, globale daling van de windsnelheid in een breed gebied na het scherm. De porositeit van een enkele rij bomen voor de meeste soorten ligt evenwel hoger (50% to 70%). Een lagere porositeit is mogelijk door selectie van laag-poreuze soorten (bijvoorbeeld bepaalde soorten sparren), of door het plaatsen van een extra rij bomen [77].

Resultaten

Het effect van wind op de windafwaartse efficiëntie van een geluidsscherm is groot. Terwijl op korte afstand na het scherm de windeffecten beperkt zijn, is er een totaal verlies aan schermwerking op een afstand gelijk aan 10 maal de schermhoogte voor een enkelvoudig scherm, en voor een windsnelheid van 11 m/s. In geval van een geluidsscherm aan beide zijden van de bron zorgt het plaatsen van een scherm zelfs voor een slechtere situatie voor een dergelijke, grote windsnelheid.

De maximale verbetering van de schermwerking door het plaatsen van windschermen bedroeg ongeveer 3 dB op een afstand gelijk aan 10H voor een enkelvoudige scherm (1*ns+1ws(2H)*), en ongeveer 6 dB voor een geluidsscherm aan beide zijden van de lijnbron (*2ns+1ws(2H)*).

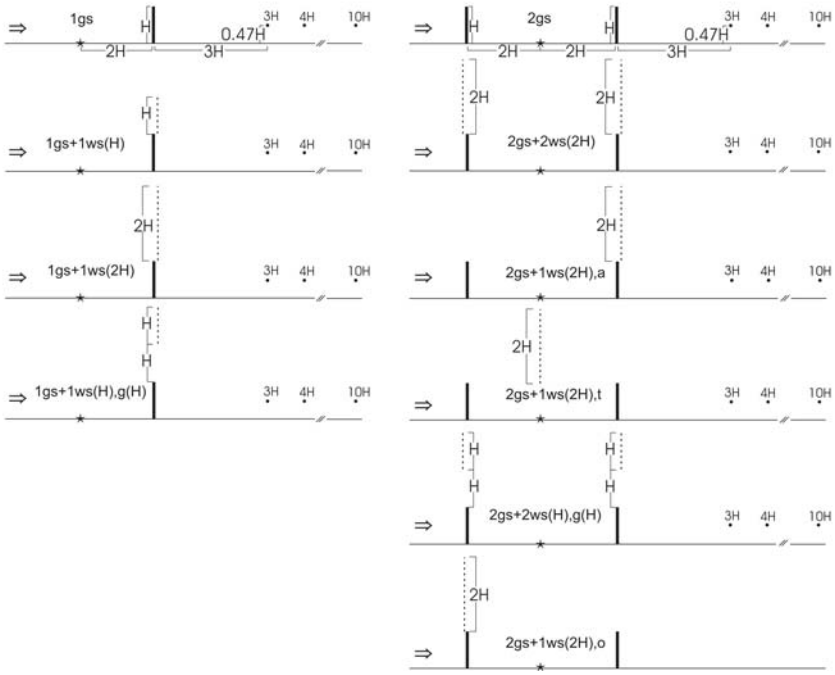

Figuur 9 Overzicht van de beschouwde opstellingen van geluidsschermen (*gs*, volle, dikke lijnen) en windschermen (*ws*, stippellijnen). Afmetingen zijn aangeduid, relatief ten opzichte van de hoogte van het geluidsscherm (*H*).

Numerieke validatie

Via stromingssimulaties werd gedetailleerde informatie verkregen over het windveld in de buurt van de geluidsschermen. De windreductie van de schermen werd benaderd door middel van de drukval over het windscherm. In Referentie [80] werden windschermen met verschillende porositeiten uitgemeten. Met hoge correlatie konden de schermen benaderd worden door middel van volgende kwadratische vergelijking. Geschikte parameters *a* en *b* werden gebruikt.

$$\Delta p_0 = a v_0^2 + b v_0 . \tag{62}$$

Op basis van de experimentale data kon afgeleid worden dat de windschermen nagenoeg akoestisch neutraal zijn. Theoretische beschouwingen hieromtrent voorspellen een beperkte reflectie op de schermen in afwezigheid van wind. De wind zorgt voor een kleine, extra absorptie. Effecten zijn in elk geval lager dan 0.5 dB.

Een vergelijking tussen het gemeten en gesimuleerde netto effect door het plaatsen van windschermen voor verschillende configuraties is weergegeven in Figuur 10. De situaties waarbij geluidsschermen aan beide zijden van de bron voorkomen worden getoond.

Er kon besloten worden dat het ontwikkelde model in staat is om het effect van dergelijke complexe stromingen, als gevolg van de interactie van wind met de geluidsschermen en de windschermen, op de geluidsvoortplanting, op een goede manier te simuleren. Significante verschillen tussen metingen en simulaties worden waargenomen in enkele gevallen waar de scherm-geïnduceerde turbulentie een rol kan spelen. Dit zijn vooral de situaties waarbij de windschermen niet direct aansluiten bij de geluidsschermen, en in geval van een windsnelheid van 11 m/s boven de grenslaag. Toch worden de trends in de metingen ook bij deze situaties teruggevonden in de simulaties (zoals bijvoorbeeld de negatieve schermeffecten).

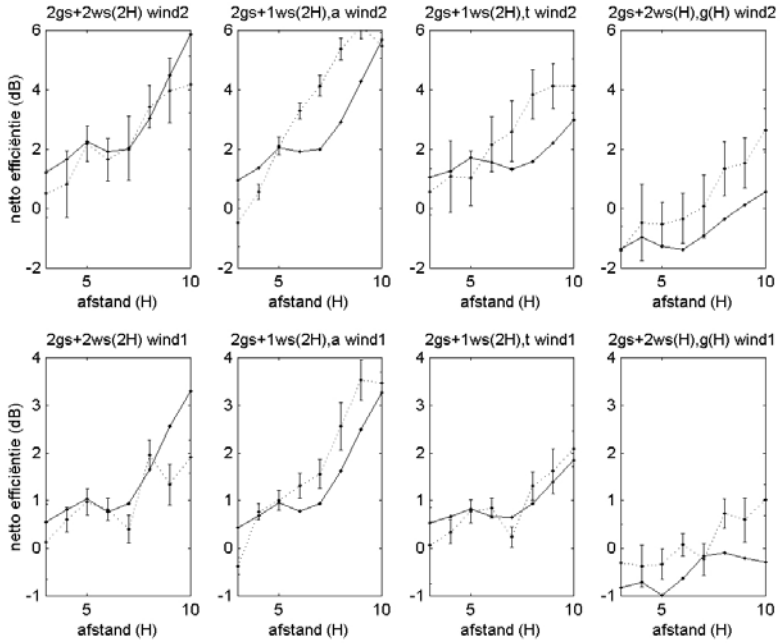

Figuur 10 Vergelijking tussen de gemeten (puntjes lijnen) en gesimuleerde (volle lijnen) netto efficiëntie van de windschermen, voor de opstellingen van geluidsschermen aan beide zijden van de bron (zie Figuur 9). In de bovenste figuren is de invallende windsnelheid, gemeten boven de grenslaag 11 m/s (*wind2*), in de figuren onderaan 6.4 m/s (*wind1*).

C.1.3. Veldexperiment

Opzet

Een veldexperiment werd uitgevoerd langs een drukke autosnelweg namelijk de E40, ter hoogte van Aalst. Een locatie werd gevonden, waarbij op sommige plaatsen na een (lang) geluidsscherm bomenrijen aanwezig waren. Een plaats met en zonder een rij bomen werd gekozen, op korte afstand van elkaar. Een overzicht van de situatie, met aanduiding van de afmetingen (relatief tot de schermhoogte) is weergegeven in Figuur 11. Een continuë meetcampagne werd uitgevoerd tussen eind juli en eind oktober van het jaar 2001. De loofbomen waren in blad gedurende het experiment. A-gewogen equivalente geluidsdrukniveaus over periodes van 1 minuut, alsook gedetailleerde informatie omtrent windsnelheid en windrichting op de locatie zelf, werden gemeten.

Een dergelijke opstelling laat toe het effect van de bomen direct te begroten. De emissie van het wegverkeer wordt gelijk geacht op beide plaatsen, door de beperkte afstand tussen de meetpunten, alsook door het nemen van een voldoende lange integratietijd (1 minuut) voor wat betreft de akoestische metingen. Het geluid van de autosnelweg is dominant ten opzicht van andere bronnen van geluid op de gekozen locaties. Aangezien de bodem op de meetlocaties na het scherm niet gelijk was, werden verschillen in geluidsdrukniveau tussen beide plaatsen in wind vergeleken met het gemiddelde verschil tussen deze plaatsen in afwezigheid van wind.

Een uitgebreide dataset van gecombineerde geluids- en meteogegevens werd bekomen. Doel van het veldexperiment was om het nut van bomenrijen ter verbetering van de schermefficiëntie in wind aan de praktijk te toetsen, alsook het onderzoek van bepaalde parameters dat niet mogelijk was in het windtunnelexperiment.

De metingen in het windtunnelexperiment werden immers uitgevoerd voor twee relatief hoge windsnelheden (6.4 m/s en 11 m/s, gemeten boven de gesimuleerde grenslaag). De dataset verzameld in het veldexperiment bevat alle natuurlijk voorkomende windsnelheden. Ook de efficiëntie van de bomenrijen bij lagere windsnelheden kan nu onderzocht worden. In de windtunnel stond de windrichting steeds haaks op het scherm. Tijdens het veldexperiment kon ook informatie over de efficiëntie van de bomenrijen voor afwijkende windrichtingen afgeleid worden. Een belangrijke reden voor het uitvoeren van een veldexperiment is dat het effect van echte kruinen van bomen kon onderzocht worden. In het windtunnelexperiment werd enkel de windreductie van een rij bomen gemodelleerd.

Het veldexperiment kent ook enkele nadelen: slechts een enkele configuratie van bomenrijen kon getest worden, op slechts één afstand na het scherm. De omstandigheden zijn minder controleerbaar, en bijvoorbeeld de akoestische bron is een stuk moeilijker te karakteriseren dan tijdens het windtunnelexperiment. Bijgevolg is het veldexperiment minder geschikt voor validatie met numerieke modellen.

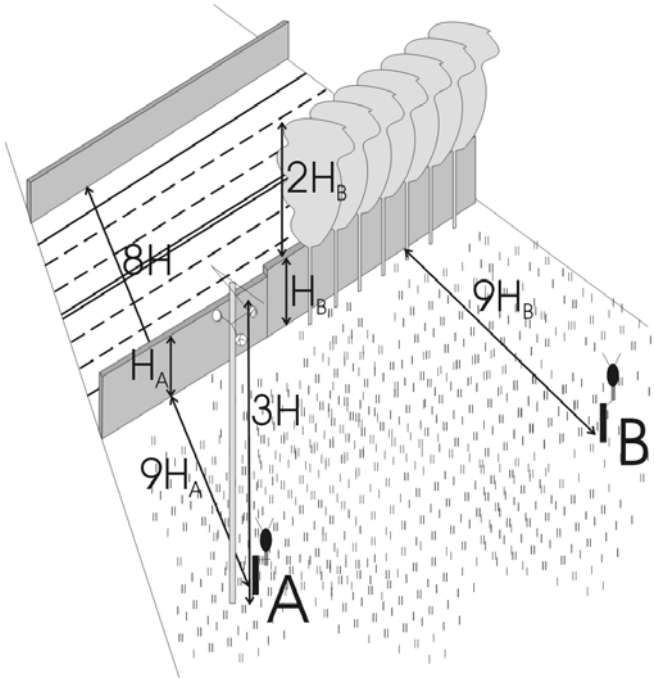

Figuur 11 Overzicht van de situatie in het veldexperiment. De relevante afmetingen, relatief tot de schermhoogtes worden getoond. H_A and H_B zijn de hoogtes van de geluidsschermen op plaats *A* en *B*, terwijl *H* de gemiddelde hoogte is.

Resultaten

De resultaten in geval van een loodrechte windrichting op het scherm, voor windafwaartse en windopwaartse geluidspropagatie, is weergegeven in Figuur 12. Reeds bij lage windsnelheden worden kleine, maar statistisch significante positieve effecten door de aanwezigheid van bomenrijen achter een geluidsscherm waargenomen voor windafwaartse waarnemers. Met stijgende

windsnelheid worden de effecten groter. Een verbetering van de schermwerking met 4 dB werd bekomen voor de beschouwde meetpunten, voor windsnelheden tussen 11 m/s en 12 m/s (gemeten op een hoogte van 12 m). Een bijna lineair verband kon waargenomen worden tussen de verbetering door bomen en de windsnelheid.

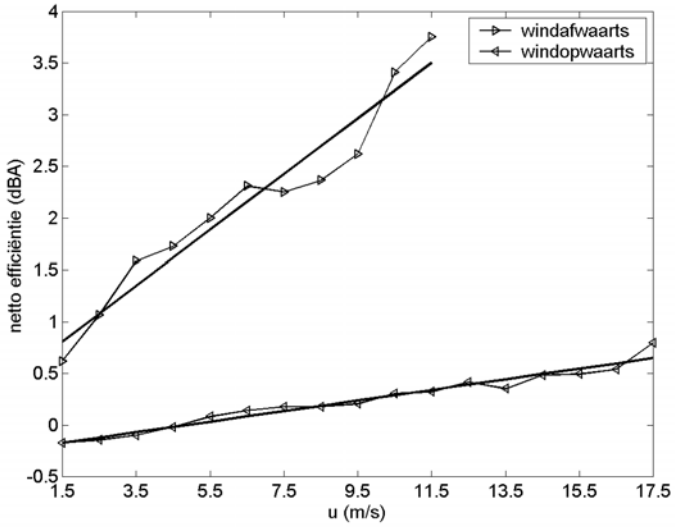

Figuur 12 Gemiddelde, netto efficiëntie van een rij bomen achter een geluidsscherm, bij stijgende windsnelheid. Een windrichting, loodrecht op het geluidsscherm, voor windopwaartse en windafwaartse geluidspropagatie werd beschouwd. De best-aangepaste rechte is weergegeven in beide situaties.

Wanneer afwijkingen tot 45 graden ten opzichte van de normaal op het scherm werden beschouwd, daalde de efficiëntie van de bomenrij met slecht 0.5 dB. Het effect van het plaatsen van een rij bomen is dus niet beperkt tot de (exact) loodrechte richting op het scherm. Bij windopwaartse geluidspropagatie blijft het effect van de rij bomen beperkt.

Metingen hebben uitgewezen dat microfoonruis door wind de metingen niet zal beïnvloeden, aangezien windsnelheden op de microfoonhoogte beperkt zijn, en geluidsniveaus afkomstig van het wegverkeer voldoende hoog waren.

Verder werd op basis van literatuurgegevens geschat dat ongeveer vanaf 10 m/s de geluidsniveaus, veroorzaakt door het ritselen van de bladeren in de bomen

door de wind, in de buurt komen van de verkeersgeluidsniveaus. De bevindingen in dit onderzoek worden dus niet verstoord door het wind-geïnduceerde geluid door de bomen.

Het plaatsen van een rij bomen achter een geluidsscherm resulteert in grotere geluidsniveaus in het hoog-frequent gebied, door verstrooiing op de boomkruinen. Metingen in Referentie [82] bevestigen de eigen bevinding dat laag-frequent geluid niet beïnvloed wordt bij propagatie doorheen een rij bomen na een obstakel, en zelfs beperkt geattenueerd wordt. Typisch verkeersgeluid is voornamelijk laagfrequent. Dit betekent dat de bijdrage van deze hoogfrequente verstrooiing tot totale, A-gewogen, equivalente geluidsdrukniveaus zeer beperkt is. Het plaatsen van een rij bomen achter een geluidsscherm in een verkeerssituatie zal dus niet zorgen voor een slechtere situatie zonder van wind.

Het veldexperiment bevestigt de bevindingen uit het windtunnelexperiment. Ook in een praktijksituatie zorgt het plaatsen van een rij bomen voor een verbeterde windafwaartse schermefficiëntie.

C.1.4. Optimalisaties

In een reeks simulaties werden enkele parameters in verband met het plaatsen van bomenrijen achter een geluidsscherm in wind onderzocht. Het globaal effect werd bekeken in een gebied dat zich uitstrekte tot op een afstand gelijk aan 20H na het (windafwaartse) geluidsscherm, van grondniveau tot op schermhoogte (dit is het “focus” gebied). Alle gridpunten, die zich op een afstand gelijk aan één tiende van de golflengte bevonden in dit gebied, werden beschouwd.

De porositeit van de kruinenlaag, de invloed van de windsnelheid, alsook het effect van de bodembedekking windafwaarts werd onderzocht voor het geval van een enkelvoudig geluidsscherm in combinatie met een hoge rij bomen (configuratie *1gs+1ws(2H)*). Ook de afstand tussen bron en scherm werd gevarieerd, voor een enkelvoudig geluidsscherm en geluidsschermen aan beide zijden van de bron. Volgende parameters werden gebruikt voor de simulaties, tenzij een welbepaalde parameter expliciet werd onderzocht. Een frequentie-interval tussen 250 en 500 Hz werd beschouwd, met een bandbreedte van 250 Hz. Een zeer zachte bodem (zoals in het windtunnelexperiment) werd gekozen opdat reflecties op de bodem de effecten van het wijzigen van de windprofielen niet minder duidelijk zouden maken. De grond windopwaarts of tussen de geluidsschermen was perfect reflecterend. Een windscherm met een porositeit gelijk aan 32% werd gemodelleerd. De windsnelheid op een hoogte van 10 m bedroeg 11 m/s (wrijvingssnelheid was 0.5 m/s, de ruwheidslengte 1 mm).

Porositeit is een belangrijk parameter, en bepaalt in sterke mate de windvangcapaciteit van een kruinenlaag. In geval van loofbomen wordt een sterke daling van de porositeit van de kruinenlaag waargenomen in de wintermaanden. Om een idee te hebben van het globale effect van loofbomen over een gans jaar, werden simulaties uitgevoerd bij verschillende porositeiten. De ruimtelijke verdeling van de netto efficiëntie van de bomenrijen (= verbetering van de schermwerking door het introduceren van een rij bomen) in het focusgebied, voor verschillende porositeiten, wordt getoond in Figuur 13.

Met stijgende porositeit wordt een beperkter positief effect van de bomenrij verkregen. Voor porositeiten gelijk aan 32%, 47%, 59% en 76% wordt de gemiddelde, netto efficiëntie van de bomenrijen in het beschouwde gebied respectievelijk 2.8 dB, 1.6 dB, 1.0 dB en 0.6 dB. Het gemiddelde windeffect (= verschil in schermwerking in aanwezigheid en bij afwezigheid van wind) bedroeg 4.5 dB. De histogrammen in Figuur 13 duiden verder aan dat met stijgende porositeit de fractie van de plaatsen met negatieve effecten groter wordt, alsook dat de maximum waargenomen effecten in het gebied dalen.

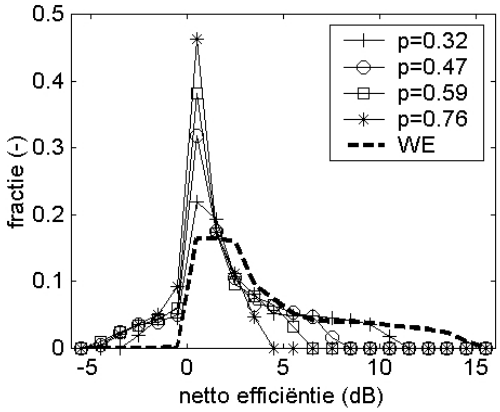

Figuur 13 Ruimtelijke verdeling van de waarden in het focus gebied voor wat betreft het windeffect (*WE*) en de netto efficiëntie door de aanwezigheid van een windscherm. Een frequentie-interval tussen 250 en 500Hz werd beschouwd (met een bandbreedte gelijk aan 250 Hz), voor stijgende porositeit. Configuratie *1gs+1ws(2H)* werd bestudeerd. De invallende windsnelheid op een hoogte van 10 m is 11 m/s.

Met stijgende windsnelheid wordt het plaatsen van een rij bomen belangrijker. Op verschillende afstanden achter het geluidsscherm werden meetpunten geplaatst op halve schermhoogte. Deze resultaten zijn weergegeven in Figuur 14.

Voor afstanden kleiner dan 10*H* wordt een linear verband waargenomen tussen windsnelheid en netto verbetering door het plaatsen van een windscherm, net zoals in het veldexperiment. Op grotere afstanden wordt deze trend niet meer waargenomen. Verder kon besloten worden dat met stijgende windsnelheid het plaatsen van een rij bomen belangrijker wordt.

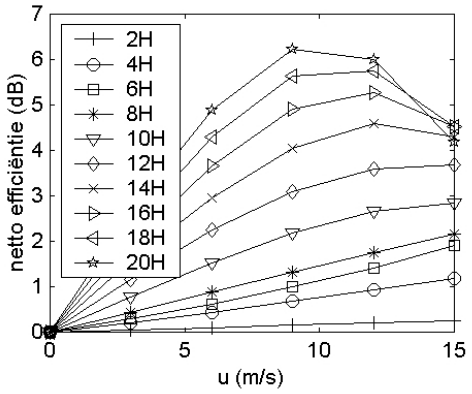

Figuur 14 Netto efficiëntie van een windscherm (met een porositeit gelijk aan 32%) bij stijgende windsnelheid, op verschillende windafwaartse afstanden achter het geluidsscherm (op een vast hoogte, gelijk aan de halve schermhoogte). Configuratie *1gs+1ws(2H)* werd beschouwd, voor een frequentie-interval tussen 250 Hz en 500 Hz (met een bandbreedte gelijk aan 250 Hz).

Wanneer de afstand tussen bron en geluidsscherm vergroot, zorgt de wind voor een verdere daling van de schermwerking. Bij een enkelvoudig scherm volgt de netto verbetering door bomen eenzelfde trend. Bij schermopstellingen aan beide zijden van de bron wordt een ander gedrag waargenomen. Wanneer de bron zich zeer dicht bij het scherm bevindt, wordt de volledige windwerking geneutraliseerd. Met stijgende afstand tussen bron en geluidsscherm daalt het effect van de windschermen echter, terwijl het effect van de wind lichtjes verder stijgt.

De impedantie van de grond windafwaarts speelt slechts een zeer beperkte rol op de netto schermefficiëntie. Simulaties werden verricht voor stromingsweerstanden tussen 10 kPa s/m² en oneindig (perfect reflecterende grond).

In een laatste reeks simulaties werd gezocht naar een optimale opstelling van bomenrijen in een verkeerssituatie. Een typsich verkeersspectrum en een natuurlijke grond (k_s = 3, φ = 0.3 en R=300 kPa s/m²) werden gesimuleerd. In

Figuur 15 worden de (ruimtelijke) distributies in het focusgebied, voor wat betreft de netto efficiëntie van de bomenrijen voor de opstellingen in Figuur 9, weergegeven. De grootte van het windeffect wordt ook getoond. Wanneer de windschermen aansluiten bij de geluidsschermen (*2gs+1ws(2H),o*, *2gs+2ws(2H)* en *2gs+1ws(2H),a*) wordt het windeffect bijna geneutraliseerd. De beste opstelling blijkt het plaatsen van een windscherm achter het windafwaartse geluidsscherm. Eenzelfde conclusie kon ook getrokken worden op basis van het windtunnelexperiment. In deze laatste studie werd slechts op één welbepaalde hoogte gemeten, en werd een gedeelte van het verkeersspectrum beschouwd. Mogelijke verbeteringen voor enkelvoudige geluidsschermen zijn beperkter.

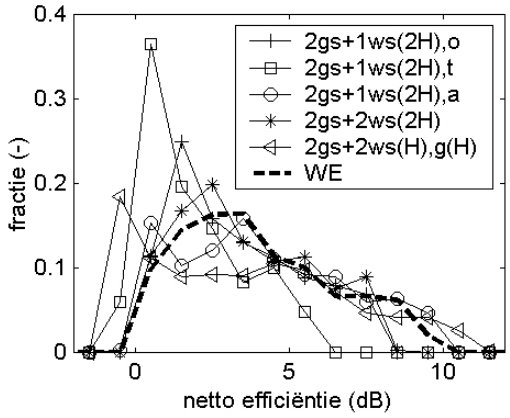

Figuur 15 Ruimtelijke verdeling van de waarden in het focus gebied voor wat betreft het windeffect (*WE*) en de netto efficiëntie door de aanwezigheid van windschermen, voor een typisch verkeersspectrum. Geluidsschermen aan beide zijden van de bron werden beschouwd, voor de locaties van windschermen voorgesteld in Figuur 9. De windsnelheid op een hoogte van 10 m bedroeg 11 m/s, de porositeit van de windschermen was steeds 32%.

Wanneer de windschermen niet aansluiten bij de geluidsschermen, zoals bijvoorbeeld in configuratie *2gs+2ws(H),g(H)*, worden dicht bij het scherm negatieve effecten waargenomen. Op grote afstanden echter is een dergelijke opstelling vergelijkbaar met de andere schermopstellingen qua efficiëntie.

Op basis van deze vaststelling, net als de waarneming dat het plaatsen van windschermen achter beide geluidsschermen een beperkter effect heeft dan enkel een windscherm na het windafwaarts geluidsscherm, kon besloten worden dat de

verbetering van de schermwerking bij wind door het plaatsen van bomenrijen niet eenvoudig is. De netto efficiëntie van een bomenrij is het resultaat van de complexe interactie tussen (meervoudige) diffractie(s) over het scherm, neerwaarts en opwaarts refracterende stromingen, en in sommige gevallen ook turbulente effecten. Gedetailleerde simulaties zijn dus nodig om elke configuratie te evalueren.

C.2. Geluidspropagatie over huizenrijen in wind

In een stedelijk omgeving kan het effect van refractie en turbulente verstrooiing belangrijk worden. Een typische situatie in een (grote) stad is weergegeven in Figuur 16. Geluid propageert vanuit een straat, ingesloten tussen een hoge rij gebouwen ("street canyon"), naar een achtertuintje. Geluidsniveaus in achtertuintjes zijn doorgaans laag. Dit betekent dat voor een accurate berekening van de afscherming van een gebouw, atmosferische effecten in rekening dienen gebracht te worden, alsook bijvoorbeeld het effect van geluidsbronnen op grote afstand.

De aanwezigheid van stille plaatsen in een stad is belangrijk. Onderzoek wees uit dat een makkelijke toegang tot geluidsarme plaatsen het aantal sterk gehinderden doet dalen [100]. Voor het opstellen van bijvoorbeeld geluidskaarten is een accurate berekening op dergelijke plaatsen nodig, om bijvoorbeeld de afscherming van gebouwen niet te overschatten, en hiermee gekoppeld, foute besluiten te maken voor wat betreft de verwachte geluidshinder.

Een overzicht van de randvoorwaarden is terug te vinden in Figuur 16. Als instroomrandvoorwaarde wordt een logarithmisch windsnelheidsprofiel verondersteld, startend op het vlak gedeelte van het windopwaartse dak. Op een hoogte van 5 m boven het dak bedraagt de windsnelheid 10 m/s. De sterkte van de turbulentie werd geschat op basis van metingen in de buurt van een 2.44-m dik en 2.55-m hoog obstakel [107]. Simulaties werden uitgevoerd voor C_v^2 gelijk aan 10 $m^{4/3}/s^2$ en 20 $m^{4/3}/s^2$. Dergelijke waarden duiden een sterk turbulent windveld aan, zoals verwacht kan worden boven een stad.

De turbule theorie wordt gebruikt om de turbulentie, die uitgemiddeld werd in de *RANS*-stromingsberekeningen, opnieuw expliciet te maken. De grootste turbulentieschaal die werd beschouwd bedroeg 1.5 m, terwijl de kleinste schaal die nog voldoende kon beschreven worden op het akoestisch grid 0.047 m was. Elke lengteschaal was steeds de helft van de vorige. Een homogeen en isotroop turbulent veld werd geconstrueerd. Het gemiddelde geluidsdrukniveau op basis van 10 realisaties van het turbulent veld werd berekend.

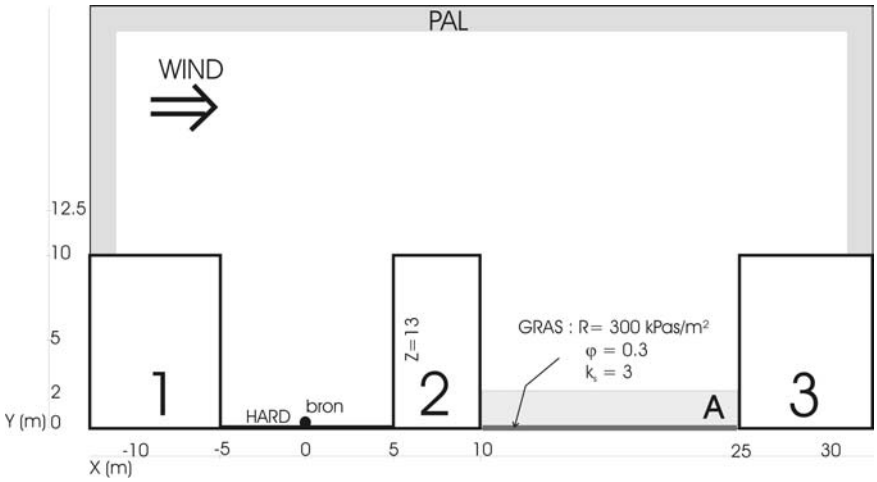

Figuur 16 Overzicht van de configuratie en afmetingen van de gebouwen, met aanduiding van gebied *A*.

Aangezien het turbule-model een driedimensionaal turbulent veld construeert, werd volgende benadering gebruikt. De eddies werden herleid in twee dimensies naar cirkels, met een willekeurige draaizin. Een numeriek experiment wees uit dat het gebruik van het turbule-model in drie dimensies ongeveer voor eenzelfde verstrooiing zorgt in twee dimensies wanneer C_v wordt herleid tot een derde van zijn waarde.

Een geluidsfrequentie van 1000 Hz werd beschouwd, rekening houdende met de beschikbare rekenkracht. Het waargenomen spectrum, afkomstig van verkeersgeluid, zal na een rij huizen trouwens vooral laagfrequent zijn. Met stijgende frequentie worden sterkere effecten verwacht.

Het gebied *A* in het achtertuintje werd beschouwd (van grondniveau tot op een hoogte van 2 m, over de volledige breedte tussen gebouwen 2 en 3, zoals voorgesteld in Figuur 16). In dit gebied komen waarnemers voor. Om een globaal beeld te bekomen, wordt de ruimtelijke verdeling van het windeffect (*WE*) getoond in Figuur 17. Alle gridpunten, die zich op een afstand gelijk aan één tiende van de golflengte bevonden in gebied *A*, werden beschouwd voor het berekenen van deze verdeling. Het windeffect is het verschil in geluidsdrukniveau in aanwezigheid en afwezigheid van wind, op eenzelfde plaats.

Het effect van refractie door de gradiënten in de windsnelheid boven het achtertuintje is groot. Een gemiddelde daling van ongeveer 10 dB wordt

waargenomen voor een windsnelheid van 10 m/s op een hoogte van 15 m. Wanneer ook (klein-schalige) turbulente verstrooiing in de atmosfeer boven de daken wordt beschouwd, stijgt het effect van wind met 1.7 dB en 2.6 dB, respectievelijk voor homogene turbulentie en gebouw-geïnduceerde turbulentie. De turbulentiesterkte wordt gekarakteriseerd door een waarde van C_v^2 (driedimensionaal) gelijk aan 10 $m^{4/3}/s^2$. Wanneer een sterkere turbulentie graad wordt beschouwd (C_v^2 = 20 $m^{4/3}/s^2$), bedragen deze waarden respectievelijk 2.1 dB en 2.7 dB. Wanneer rekening gehouden wordt met de gebouw-geïnduceerde turbulentie wordt de verstrooiing iets sterker.

De gebouw-geïnduceerde refractie blijft echter het belangrijkste effect van de wind. Turbulente verstrooiing zorgt voor een verdere stijging met enkele decibels. Het gebruik van het turbule-model in deze specifieke (en ingewikkelde) situatie werd niet gevalideerd. Resultaten dienen dus met voorzichtigheid gebruikt te worden.

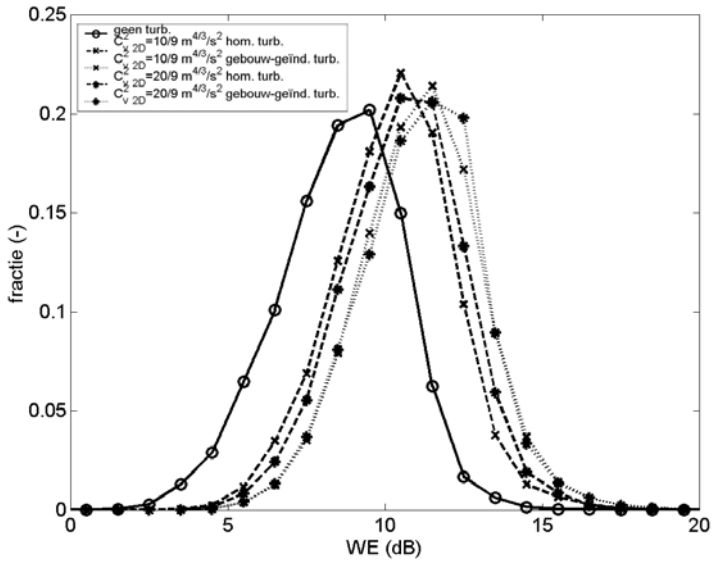

Figuur 17 Ruimtelijke verdeling van de waarden van het windeffect (*WE*) in gebied *A*. Een geluidsfrequentie van 1000 Hz werd beschouwd. De invloed van refractie, alsook van een refracterend, turbulent veld (homogene turbulentie en gebouw-geïnduceerde turbulentie) is weergegeven. Waarden voor wat betreft de sterkte van de turbulentie $C_v^2{}_{2D}$ gelijk aan 10/9 $m^{4/3}/s^2$ en 20/9 $m^{4/3}/s^2$ werden gebruikt.

D. Besluit

Dit werk toont aan hoe de eindige-differenties-in-het-tijdsdomeinmethode kan aangewend worden om geluidspropagatie in een bewegend medium te simuleren. Geluidsvoortplanting wordt in een “achtergrondstroming” beschreven. De koppeling tussen geluid en stroming beperkt zich tot de belangrijkste interacties tussen de wind en geluid in een buitenomgeving namelijk convectie, afbuiging en verstrooiing.

De akoestische grootheden werden beschouwd als een perturbatie van de lineaire Euler-vergelijkingen. Enkele belangrijke stappen en benaderingen tijdens het afleiden van de akoestische vergelijkingen en de discretisatie ervan werden gemaakt. Voor de typische stroomsnelheden in de buitenomgeving daalt de numerieke accuraatheid slechts zeer beperkt (in vergelijking met de *EDTD*-methode in een stilstaand medium), terwijl stabiliteit geen probleem vormt. Een grondmodel werd geïmplementeerd, en de “Perfect Aangepaste Lagen”-techniek werd toegepast om absorptie van geluidsgolven in stroming te bewerkstelligen op niet-fysische randen.

Op basis van windtunnelexperimenten kon het model met succes gevalideerd worden. De voorbeelden in dit werk tonen de kracht van de ontwikkelde rekenmethode. Situaties in een stedelijk omgeving, waar complexe golfverschijnselen optreden, in combinatie met ingewikkelde stromingsvelden, kunnen in detail in rekening gebracht worden. Er werd verder aangetoond door middel van een windtunnelexperiment, een veldexperiment en een reeks simulaties dat het gebruik van bomenrijen achter geluidsschermen een interessante oplossing is in een verkeerssituatie. De (neerwaarts afbuigende) scherm-geïnduceerde refractie voor windafwaartse waarnemers kan in belangrijke mate beperkt worden. Verstrooiing van hoogfrequent geluid op de kruinen van de bomen zorgt niet voor een slechtere situatie in afwezigheid van wind, door het typisch, laagfrequent spectrum van verkeersgeluid.

ENGLISH TEXT

Chapter 1

Introduction and Outline

In this work, a detailed simulation technique to account for the effect of complex flows on sound propagation is developed. In particular, the interaction between sound and wind outdoors is studied. This means that (typical) flow velocities will be small in our applications, which has some consequences for the development of the numerical technique.

An important application is a noise barrier in the presence of wind. A large reduction of noise barrier performance for downwind receivers is observed. This negative effect can be attributed to the presence of large gradients in the wind speed that will refract sound downwardly into the acoustic shadow zone. Neglecting this so-called screen-induced refraction of sound results in a large overestimation of the screening effect in downwind direction. This is an important problem, since the use of noise barriers is a widely applied noise reducing measure for traffic noise. Together with an adequate modelling of the performance of noise barriers in wind, a solution to this problem is proposed in this work, which is investigated both by experiments and simulations.

Noise pollution nowadays becomes an increasingly growing threat for the quality of life. Just like in most industrialized regions, traffic noise is the main source of noise annoyance in Flanders [1], besides annoyance by aviation, neighbours, etc. Most noise sources are present outdoors, so sound propagates through the atmosphere (except for direct neighbour noise) to reach receivers. It is well known that the state of the atmosphere has an important influence on the travelling sound waves. The air outdoors is usually not at rest. Wind speed and temperature vary with height in the atmosphere. The wind encountered outdoors is also turbulent: at a fixed location, wind velocity is not constant in time, even at small time scales. Atmospheric effects become important since typical propagation distances are usually large. Considering the atmosphere outdoors as a medium at rest results in inaccurate calculations. Adequate outdoor sound propagation models are necessary for noise impact analysis and when the effects of noise reducing measures are investigated. Standardized models like the ISO 9613-2 standard [2], that take meteo-conditions into account by means of correction factors, might give a general impression in this context, but are far from accurate when looking at specific, local effects.

The coupling between the fluid flow and the acoustics can be considered limited in most outdoor sound propagation applications. The typical (wind) flow velocities outdoors are small, so generation of sound is considered to be unimportant. The sound frequencies of interest will not couple back to the mean fluid flow and to the vibrating structures. Therefore focus is on the most important fluid-acoustics interaction processes outdoors namely convection, refraction and scattering of sound by wind.

In the next paragraphs, an overview is given of some commonly used outdoor sound propagation models. These models were developed to calculate sound levels at large distances from a source in the presence of wind, over flat finite-impedance grounds. Approximations to the wave equations and to the wind flow were made. The discussed techniques compute sound pressure levels in frequency-domain.

The Fast Field Program (*FFP*) technique (see e.g. [3]) permits the prediction of sound pressure levels in a horizontally stratified atmosphere above a flat ground. Both wind speed profiles and impedance of the ground surface are constant between source and receiver. Turbulence effects can be accounted for [4].

The Parabolic Equation (*PE*) method (e.g. [5]) can handle variations both in wind speed profiles and ground impedance along the propagation path. One-way sound propagation is described: only the sound waves travelling in the direction from the source to the receiver are allowed for. Elevation angles up to about 45° are possible in the wide-angle approximation [6]. Uneven ground surfaces can be simulated by means of the conformal mapping method [7] or by the generalised terrain *PE* [8]. The effect of a turbulent atmosphere may be included in this model [9]. Adaptations to the *PE* method were made to model a (thin, rectangular) single noise barrier [6]. Receiver and source must however be located at sufficient distances from the barrier, due to the limited angle in which sound propagation can be calculated accurately [6].

Recently the boundary element (*BE*) method was extended for the use in a layered atmosphere based on the normal modes solution in a downwardly refracting atmosphere [10]. The normal mode solution assumes a specific sound speed profile, for which an analytical solution can be obtained. When receiver heights are small in comparison to the radius of curvature, this sound speed profile approximates a linear one [11]. The normal mode solution assumes the direct wave to be negligible to the ground reflected waves, which is valid for distant receivers. This *BE* approach however cannot model variations in the sound speed profiles along the propagation path. Uneven ground surfaces do not induce difficulties for this scheme since only the borders of the simulation domain need to be discretised.

These methods have their merits, especially for the calculation of sound pressure levels at large distances. Their applicability when noise barriers in wind are present is rather limited. These methods take in account only the wind velocity in direction of the propagation. The horizontal velocity component is added to the speed of sound at a specific height. This is the effective speed of sound approach. Near noise barriers, also vertical flow is present and this effect will be disregarded with these methods.

The meteo-*BE* method is limited to the use of a linear wind speed profile. This is inappropriate to model the wind velocity profile in the neighbourhood of barriers, where upwardly and downwardly refracting parts are observed, depending on the height. Besides, it is not possible to change wind speed profiles with distance in this model. As a consequence, screen-induced refraction of sound by wind cannot be modelled since wind speed profiles differ considerably at different locations near a barrier. The *PE* method, just like the *FFP* method, can handle wind speed profiles with upwardly and downwardly refracting parts. The *PE* method is able to model the screen-induced refraction for a simple, single noise barrier since wind speed profiles may vary along the propagation path in this model. Restrictions on the locations of the receiver and source relative to the barrier are however present.

None of these techniques can be used to simulate adequately a typical traffic noise situation, namely a source situated in between two (partially) reflecting noise barriers in the presence of wind. In absence of wind, the *BE* method is well suited to model single and multiple noise barriers with complicated forms [e.g. 12, 13, 14]. Although the *PE* method can handle variations in wind speed profiles with distance, this method cannot simulate the multiple reflections between two noise barriers.

So there is a lack of detailed simulation techniques to account for sound propagation in some specific situations where complex flows are observed. In this view, the finite-difference time-domain (*FDTD*) simulation technique is extended to include the effects of a general (non-uniform and rotational) flow field on sound propagation. The acoustic finite-difference time-domain method is a simulation technique with a wide range of applications, going from room acoustics [15], outdoor sound propagation [16, 17, 18] to underwater acoustic problems [19] and ultrasonics [20], as well as to elastic wave propagation [21]. Important advantages are the simple and straightforward concept, but also the effectiveness and accuracy. No simplifications are made to the wave equations. As a result, all important and complex wave phenomena like e.g. scattering from irregular structures, multiple reflections and multiple diffractions will be accounted for. The acoustical partial differential equations are discretised

directly in time-domain, so realistic sound sources (e.g. white noise, wavelets), transient phenomena and non-linear effects can be modelled. A single run makes it possible to calculate transfer functions in frequency-domain efficiently.

The most important disadvantage, as for any full-wave volume-discretisation technique, is the large need for computational resources. As a result, the acoustical *FDTD* method is a low- or mid-frequency simulation technique, certainly as regards sound propagation outdoors.

As stated earlier, the coupling between the acoustics and the flow will be limited to convection, refraction and scattering of sound by the flow. The fluid flow calculations and acoustic calculations can therefore be performed independently. The acoustic equations take the "background flow" as input data. Separating the flow calculations and the acoustic calculations is a common engineering approach [e.g. 22, 23]. Both types of simulations have different demands concerning the computational grids and time-steps. The flows encountered in practical situations are usually complex and highly turbulent. This means that *CFD* grids need to be very dense near obstacles. In wave-based acoustic simulation techniques, the spatial discretisation step needed for accurate calculations is related to the wavelength of sound. For the frequencies of importance in typical outdoor situations, a less dense grid is needed (unless small structures like e.g. resonators need to be modelled). On the other hand, the typical acoustic time scales are small in comparison to the variations of a flow field. Due to these rather contradictory demands, it is more efficient to consider the flow and the acoustics separately.

The approach as stated in previous paragraphs is applied to the Euler equations, where the fluid quantities are split in an acoustic part and a part attributed to the background flow. The acoustics are seen as a perturbation of the flow. Equations are derived to calculate the acoustic velocity and acoustic pressure in the time-domain method in Chapter 2.1. Next, the discrete finite-difference time-domain equations are presented, both in presence and in absence of a background flow. Notes are made concerning some critical approximations during this derivation. Simplified flow equations are presented in order to reduce memory use and computation time. An approach to better model the gradient in the flow in the first cell near a physical boundary is proposed. The object-orientated implementation makes this possible. A one-dimensional grid refinement procedure is implemented to more accurately simulate reflection from finite-impedance boundaries and from mediums with a difference in acoustic impedance.

Boundary conditions are treated in Chapter 2.3. First, physical boundaries are addressed. It will be shown that a perfectly reflecting boundary is easy to

simulate. In a following chapter, it is investigated how reflection from natural grounds (or in general: reflection from frequency-dependent finite-impedance boundaries) can be modelled in the time-domain method. The Zwikker and Kosten porous medium sound propagation model, which has a typical frequency characteristic of outdoor grounds, is implemented. Ground propagation in a few layers in the ground is modelled. Due to the difference in impedance between ground and air, reflection at the interface will be simulated.

The problem of perfectly absorbing boundaries to truncate computational grids is treated in detail. A first-order approximation, as well as the more advanced Perfectly Matched Layer (*PML*) technique in flow is addressed. The derivation of the conditions to obtain zero-reflection at the interface between the interior domain and the *PMLs* is given. The behaviour of these perfectly absorbing boundaries in discrete *FDTD* is illustrated in detail with numerical examples.

In Chapter 2.4 and 2.5, some numerical aspects of the *FDTD* scheme are addressed. The explicit *FDTD* numerical technique is not unconditionally stable. Since a stability condition for the *FDTD* equations in background flow is not easily derived, stability is investigated with a numerical example. Accuracy of the implementation is investigated by quantifying the phase error and amplitude error.

Some notes on the calculation of the flow field are given in Chapter 2.6, more specific concerning turbulent flows and how this is modelled. In practice, an engineering approach to calculate a turbulent flow field namely a *RANS* (Reynolds-Averaged Navier-Stokes) model will be applied. This means however that scattering on turbulent inhomogeneities will not be observed when such a flow field is used during the acoustic calculations, since turbulence is averaged out in time. It is intended to make turbulence explicit again by generating a number of turbulent realisations of the flow field by means of the turbule theory.

In the remainder of this work, the model is applied to investigate some important outdoor sound propagation problems.

General analytical solutions of sound propagating in the presence of flow are not found. Only for a specific wind speed profile, which approximates a linear one when choosing appropriate parameters, a semi-analytical far field approximation is found and a comparison is made with the *FDTD* model (see Chapter 3.1).

In a second example, the effect of wind on the ground dip is simulated, both in upwind and downwind conditions, over unscreened ground (see Chapter 3.2).

The situations encountered outdoors however result in more complex flows, certainly when looking at the specific case of noise barriers in wind. Therefore stress is on the validation of the model based on experimental results. Two wind

tunnel studies are considered, in which the effect of the complex flow around thin noise barriers on sound propagation was investigated. Sound propagation over a single noise barrier in the presence of wind, above a perfectly reflecting ground surface was investigated in Ref. [64]. The experimental data is compared to finite-difference time-domain simulations in Chapter 3.3. Experimental data of a wind tunnel experiment performed by the author is also compared to simulations (Chapter 3.4). Now single noise barriers and noise barriers on either side of the source are considered. Besides the validation of the model in some more complex situations, focus was on how windscreens in the form of a row of trees can be used to improve the downwind noise barrier efficiency. This study also consists in a field experiment and detailed, numerical simulations.

A typical situation in an urban area is considered in Chapter 3.5. Sound propagating from a street canyon to a nearby backyard is simulated. Since sound pressure levels in a backyard are usually low, not only refraction but also scattering of sound waves on vortices in the highly turbulent flow field, as encountered above cities, is investigated.

Chapter 2

Theoretical part

2.1 Mathematical model

The Navier-Stokes equations, describing a general flow, can be obtained by demanding that mass, momentum and energy are conserved. In most practical, unbounded airflows, viscosity can be neglected since Reynolds numbers are high. Only in the boundary layer very close to obstacles and to the ground, viscosity becomes important. In these regions, flow is described by the viscous equations or by special wall functions. These regions will not be considered here. Gravity is only important for extremely low sound frequencies i.e. those in the order or lower than the ratio between the gravitational acceleration and the speed of sound [24]. Assuming non-viscous flow and neglecting gravity leads to the momentum equation of Euler:

$$\rho_t\left[\frac{\partial \mathbf{v_t}}{\partial t}+\left(\mathbf{v_t}\cdot\nabla\right)\mathbf{v_t}\right]+\nabla p_t=0\,, \tag{2.1}$$

where p_t is the fluid pressure, $\boldsymbol{v_t}$ is the fluid velocity vector, and ρ_t is the fluid density. The conservation of mass or the continuity equation for a compressible flow is expressed by equation (2.2):

$$\frac{\partial \rho_t}{\partial t}+\nabla\cdot(\rho_t\mathbf{v_t})=0\,. \tag{2.2}$$

These equations are used as a starting point to derive equations for sound propagation in background flow.

2.1.1 Velocity equation

In a numerical model, the conservation laws need to be obeyed globally and locally. Conservation of momentum and kinetic energy are both governed by the momentum equation. It is known from numerical fluid dynamics that a different form of equation (2.1) is needed to ensure kinetic energy conservation [25]. Lack of guaranteed conservation of kinetic energy results in unstable simulations, especially in complex and unsteady flows [25]. In order to obtain a numerical

scheme that can be used in various applications and for a wide range of flow velocities, a different form of the impulse equation will be derived, according to Ref. [25]. This alternate form of the conservation equation makes the kinetic energy term explicit. Besides, the rotor of the velocity also appears explicitly in the equation. This makes it possible to make some assumptions that will be discussed further in this chapter. The importance of using a kinetic energy conservation form will be illustrated by means of a numerical example in Chapter 2.2.4. From vector calculus, it is known that

$$0.5\nabla(\mathbf{a}\cdot\mathbf{a}) = \mathbf{a}\times(\nabla\times\mathbf{a}) + (\mathbf{a}\cdot\nabla)\mathbf{a}\,. \tag{2.3}$$

Combining equation (2.3), applied to $\boldsymbol{v}_t$, with equation (2.1) results in

$$\rho_t\left[\frac{\partial\mathbf{v_t}}{\partial t} - \mathbf{v_t}\times(\nabla\times\mathbf{v_t})\right] + \nabla p_t + 0.5\rho_t\nabla(\mathbf{v_t}\cdot\mathbf{v_t}) = 0\,. \tag{2.4}$$

This is the extension of the incompressible equation (7.13) on page 156 in Reference [25] to compressible fluid flow. Pressure, fluid density and fluid velocity are split into an ambient (background) part and into an acoustic perturbation:

$$\rho_t = \rho_0 + \rho\,, \tag{2.5}$$

$$\mathbf{v_t} = \mathbf{v_0} + \mathbf{v}\,, \tag{2.6}$$

$$p_t = p_0 + p\,, \tag{2.7}$$

where ρ_0 is the ambient density, ρ is the acoustic part of the density, $\boldsymbol{v_0}$ is the background fluid velocity, $\boldsymbol{v}$ is the acoustic part of the fluid velocity, p_0 is the ambient pressure, and p is the acoustic pressure. When inserting equations (2.5), (2.6) and (2.7) in equation (2.4), one obtains

$$\begin{aligned}(\rho+\rho_0)\left[\frac{\partial(\mathbf{v}+\mathbf{v_0})}{\partial t} - (\mathbf{v}+\mathbf{v_0})\times\left[\nabla\times(\mathbf{v}+\mathbf{v_0})\right]\right] + \nabla\left[p+p_0\right] \\ +0.5(\rho+\rho_0)\nabla\left[(\mathbf{v}+\mathbf{v_0})\cdot(\mathbf{v}+\mathbf{v_0})\right] = 0\,.\end{aligned} \tag{2.8}$$

With respect to the background flow, the following assumptions are made. Compressibility is known to be important for Mach numbers larger than about 0.3 [25]. This is of course far beyond the flow velocities encountered outdoors, so an incompressible background fluid flow is assumed [25]:

$$\nabla\rho_0 = 0\,. \tag{2.9}$$

This statement is allowed because the acoustic perturbations are considered separately. Equation (2.9) expresses a homogeneous (background) atmosphere. In this work, variations of the ambient pressure and ambient density with height are not considered.

It is also assumed that the fluid flow is static:

$$\frac{\partial \mathbf{v_0}}{\partial t} = 0\,, \tag{2.10}$$

$$\frac{\partial \rho_0}{\partial t} = 0\,. \tag{2.11}$$

In this work, only linear acoustics are considered. This means that mixed acoustic terms are neglected. The linearised equation, taking into account assumption (2.10), now reads:

$$\rho_0\left[\frac{\partial \mathbf{v}}{\partial t} - \mathbf{v}\times\left(\nabla\times\mathbf{v_0}\right) - \mathbf{v_0}\times\left(\nabla\times\mathbf{v}\right)\right] + \nabla p + \rho_0\nabla\left[\mathbf{v}\cdot\mathbf{v_0}\right] + S_v = 0\,, \tag{2.12}$$

with

$$S_v = \nabla p_0 - \rho_0\mathbf{v_0}\times\left[\nabla\times\mathbf{v_0}\right] + 0.5\rho_0\nabla\mathbf{v_0}\cdot\mathbf{v_0}\,. \tag{2.13}$$

Terms that are second-order in Mach number like $\rho\left(\mathbf{v_0}\times\left[\nabla\times\mathbf{v_0}\right]\right)$ and $\rho\nabla\mathbf{v_0}\cdot\mathbf{v_0}$ were neglected to obtain equation (2.12). This approach is sufficiently accurate as long as background flow velocities are small.

The parameter S_v contains the source terms that appear in the equations above. Source terms (Lighthill-equivalents) do not contain the acoustic quantities. Sound generation caused by the background flow can be attributed to such terms. In a general outdoor sound propagation situation, generation of sound is supposed to be of minor importance and therefore S_v will be omitted in the remainder of this derivation. The kinetic energy term appears now in the linearised equation (2.12) as a mixed background flow-acoustic term.

Until now the fact that $\boldsymbol{v}$ and p are the acoustic part of the flow field is not explicitly used. Like any vector field the acoustic velocity field $\boldsymbol{v}$ can be written as:

$$\mathbf{v} = \nabla\phi + \nabla\times\mathbf{A} = \mathbf{v_g} + \mathbf{v_r}\,, \tag{2.14}$$

where ϕ is the well-known velocity potential, and $\nabla \times \mathbf{A} = \mathbf{v_r}$ is the rotational part of the field. In an isotropic medium at rest with an acoustic perturbation, $\boldsymbol{v_r}$ equals zero. Also remark that $\boldsymbol{v_r}$ does not influence the acoustic pressure equation directly.

The initial assumption (2.6) that $\boldsymbol{v}$ is the acoustic part of the flow field translates to

$$\mathbf{v_g} \gg \mathbf{v_r}\,. \tag{2.15}$$

Equation (2.14) is inserted in the first terms of equation (2.12) and their order of magnitude is compared in frequency-domain:

$$\frac{\partial \mathbf{v}}{\partial t} \to O\left[\omega \left| v_g \right|\right], \tag{2.16}$$

$$\mathbf{v_0} \times \left(\nabla \times \mathbf{v}\right) \to O\left[M\omega \left| v_r \right|\right]. \tag{2.17}$$

Since $\nabla \times \nabla \phi = 0$, term (2.17) contains only the rotational part of the acoustic velocity field. Noting that Mach numbers are usually much smaller than unity, certainly in outdoor sound propagation applications, following conclusion can be made based on inequality (2.15):

$$\mathbf{v_0} \times \left(\nabla \times \mathbf{v}\right) \ll \frac{\partial \mathbf{v}}{\partial t}\,. \tag{2.18}$$

The term containing the rotor of the acoustic velocity may be omitted from the momentum equation, as long as the time dependence of $\boldsymbol{v_g}$ corresponds to acoustic frequencies. The velocity equation finally reads:

$$\frac{\partial \mathbf{v}}{\partial t} - \mathbf{v} \times \left(\nabla \times \mathbf{v_0}\right) + \frac{1}{\rho_0} \nabla p + \nabla\left[\mathbf{v} \cdot \mathbf{v_0}\right] = 0\,. \tag{2.19}$$

As already mentioned, coupling between acoustics and flow is limited in this equation. Fluid flow influences the acoustic propagation. Generation of sound by the flow is not considered, since source terms in the previous equations are neglected. The acoustic fields do not influence the background flow. So the calculation of the background fluid velocity field can be performed independently of the acoustic calculations. Standard fluid flow software is used e.g. [26, 27]. In Chapter 2.6, the calculation of the (turbulent) background fluid flow is addressed.

2.1.2 Pressure equation

When using equations (2.5), (2.6) and (2.7) in the conservation of mass equation (2.2), one gets

$$\frac{\partial(\rho_0+\rho)}{\partial t}+\nabla\cdot\left[(\rho_0+\rho)(\mathbf{v_0}+\mathbf{v})\right]=0\,. \tag{2.20}$$

Assuming a static background flow (equation (2.11)) gives:

$$\frac{\partial\rho}{\partial t}+\nabla\cdot\left[(\rho_0+\rho)(\mathbf{v_0}+\mathbf{v})\right]=0\,. \tag{2.21}$$

Linearisation in the acoustic field results in

$$\frac{\partial\rho}{\partial t}+\nabla\cdot\rho\mathbf{v_0}+\nabla\cdot\rho_0\mathbf{v}+S_p=0\,, \tag{2.22}$$

where S_p is a source term that equals

$$S_p=\nabla\cdot\rho_0\mathbf{v_0}\,. \tag{2.23}$$

The divergence of the background flow must equal zero due to the assumption of incompressibility (equation (2.9)) and time independency (equation (2.11)) of the background flow:

$$\nabla\cdot\mathbf{v_0}=0\,. \tag{2.24}$$

This is a direct consequence of the conservation of mass equation (2.2) applied to the background flow. Disobeying previous condition would lead to large errors. Indeed: suppose a static fluid flow in combination with non-zero divergence in the background flow. Because the fluid cannot be compressed and the flow pattern is time-independent, on certain places the pressure would go to infinity. Of course, this assumption may be enforced during the calculation of the background velocity field. But due to numerical inaccuracy and interpolations (e.g. when the acoustic grid and background velocity grid do not fit), this is not always guaranteed for the flow field actually inserted in the acoustic equations. For these reasons, this condition is made explicit. Using equation (2.9) and equation (2.24), equation (2.22) reduces to:

$$\frac{\partial\rho}{\partial t}+\mathbf{v_0}\cdot\nabla\rho+\rho_0\nabla\cdot\mathbf{v}=0\,. \tag{2.25}$$

The source term (2.23) in equation (2.22) is omitted. The acoustic compressions and expansions can be idealized as adiabatic processes for the frequencies of interest in acoustical studies [24]. The linear pressure-density relation reads [24]:

$$p = c^2 \rho\,, \tag{2.26}$$

where c is the adiabatic sound speed, which is assumed to be time-invariant just like the background flow. In this work, focus is on the effect of wind on sound propagation in a homogeneous atmosphere. Gradients in temperature, and as a consequence local changes in sound speed, are therefore not considered. Applied to equation (2.25), this finally leads to the pressure equation:

$$\frac{\partial p}{\partial t} + c^2 \rho_0 \nabla \cdot \mathbf{v} + \mathbf{v_0} \cdot \nabla p = 0\,. \tag{2.27}$$

2.2 Finite-difference time-domain model

2.2.1 Staggered in space and time

The use of a staggered grid has particular advantages for acoustic simulations [28]. In a Cartesian grid, the acoustic pressure is determined at the grid positions *(i dx, j dy, k dz)* at sampled times *l dt*:

$$p^{ldt}_{(i\,dx,\,j\,dy,\,k\,dz)}\,, \tag{2.28}$$

where *dx*, *dy*, and *dz* are the spatial discretisation steps and *dt* is the time discretisation step. The indices *i*, *j* and *k* locate the spatial points, the index *l* is the discrete time. The three components of the particle velocity are determined at staggered grid positions

$$v_{x((i\pm0.5)dx,\,j\,dy,\,k\,dz)}^{(l+0.5)dt}\,, \tag{2.29}$$

$$v_{y(i\,dx,\,(j\pm0.5)\,dy,\,k\,dz)}^{(l+0.5)dt}\,, \tag{2.30}$$

$$v_{z(i\,dx,\,j\,dy,\,(k\pm0.5)\,dz)}^{(l+0.5)dt}\,, \tag{2.31}$$

at intermediate times *(l+0.5) dt*. The discrete space is indicated as a subscript, the discrete time is indicated as a superscript. The spatial organisation of the staggered grid for one cell is illustrated in Figure 2.1.

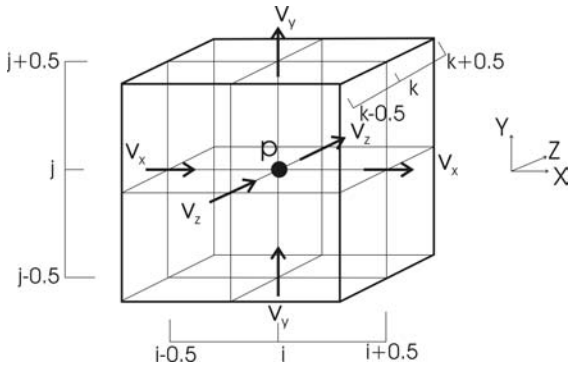

Figure 2.1 Spatial organisation of the staggered grid for one cell in three dimensions.

2.2.2 Absence of background flow

In the absence of background flow, equations (2.19) and (2.27) simplify to

$$\frac{\partial \mathbf{v}}{\partial t} + \frac{1}{\rho_0}\nabla p = 0\,, \tag{2.32}$$

$$\frac{\partial p}{\partial t} + c^2\rho_0 \nabla \cdot \mathbf{v} = 0\,. \tag{2.33}$$

Central-difference approximations are well suited to discretise these equations in a staggered grid. Second-order accuracy for the spatial derivatives is achieved due to symmetry [28]. The discretised velocity respectively pressure can be calculated as follows:

$$v^{l+0.5}_{\alpha(\alpha+0.5)} = v^{l-0.5}_{\alpha(\alpha+0.5)} - \frac{dt}{\rho_0}\left[\frac{p^l_{(\alpha+1)} - p^l}{d\alpha}\right], \tag{2.34}$$

$$p^{l+1} = p^l - dtc^2\rho_0 \sum_\beta \left(\frac{v^{l+0.5}_{\beta(\beta+0.5)} - v^{l+0.5}_{\beta(\beta-0.5)}}{d\beta}\right). \tag{2.35}$$

In the previous equations, α represents one of the three Cartesian indices. A summation over β runs over the three Cartesian indices. For simplicity, the spatial indices *(i, j, k)* of the discretised acoustic quantities are omitted. Offset with respect to this position in direction β is indicated as *(β+0.5)*, *(β–0.5)* etc. v_β indicates the β-component of the acoustic velocity.

In a compact scheme, the velocity at time *(l+0.5) dt* only depends upon the velocity at the previous time *(l-0.5) dt* and on the discretised pressure at the time *l dt* in adjacent positions. The pressure at time *(l+1) dt* on its turn only depends upon the pressure at the previous time *l dt* and on the velocity at time *(l+0.5) dt*. The time derivatives are second-order accurate due to this "leap-frog" time-stepping mechanism.

The explicit finite-difference time-domain method is not unconditionally stable. It can be derived that the Courant number *CN* needs to be smaller than or equal to one to obtain stability [28]:

$$CN = c\,dt\sqrt{\sum_{\beta}\frac{1}{d\beta^2}} \le 1\,. \tag{2.36}$$

To perform accurate calculations, a minimum number of computational cells are needed, relative to the wavelength under investigation. A practical value of 10 is often used. This means however that with increasing frequency, the number of necessary cells increases largely. In a three-dimensional simulation, doubling the frequency of interest results in an increase in the number of cells with a factor 8. At the same time, the temporal discretisation step has to be reduced significantly to ensure stability. The finite-difference time-domain method can be extended to more general grids [28].

2.2.3 Presence of background flow

The components of the background flow velocity are discretised at the same positions where the acoustic velocity components are present:

$$V_{0x((i\pm 0.5)dx,\,j\,dy,k\,dz)}\,, \tag{2.37}$$

$$V_{0y(i\,dx,(j\pm 0.5)\,dy,k\,dz)}\,, \tag{2.38}$$

$$V_{0z(i\,dx,\,j\,dy,(k\pm 0.5)\,dz)}\,. \tag{2.39}$$

When a background flow is present, time and space matching of the staggered grid no longer emerges naturally. To ensure stability and accuracy, more care is needed concerning the discretisation of the equations. To discretise time derivatives, following bilinear transformation [29] is used:

$$\frac{\partial}{\partial t} \to \frac{2}{dt}\frac{\left(1-z^{-1}\right)}{\left(1+z^{-1}\right)}, \tag{2.40}$$

where z^{-1} is the delay operator that shifts over one time-step. From signal processing theory it is known that this results in unconditionally stable systems. The discretisation of respectively the pressure equation and velocity equation is worked out in Chapter 2.2.3.a and 2.2.3.b.

2.2.3.a Pressure equation

Discretising time derivatives in equation (2.27) by using equation (2.40) results in:

$$p^{l+1} - z^{-1}p^{l+1} = -0.5\left(1+z^{-1}\right)dtc^2\rho_0\left(\nabla\cdot\mathbf{v}^{\mathbf{l+1}}\right) - 0.5\left(1+z^{-1}\right)dt\left(\mathbf{v_0}\cdot\nabla p^{l+1}\right), \tag{2.41}$$

The operator $0.5(1+z^{-1})$ causes an interpolation between two consecutive time-steps. Resolving the delay operator and moving known variables just before time $(l+1)\,dt$ to the right hand side results in

$$p^{l+1} + 0.5dt\left(\mathbf{v_0}\cdot\nabla p^{l+1}\right) = p^{l} - dtc^2\rho_0\left(\nabla\cdot\mathbf{v}^{\mathbf{l+0.5}}\right) - 0.5dt\left(\mathbf{v_0}\cdot\nabla p^{l}\right). \tag{2.42}$$

Discrete time-stepping will be used to solve the propagation problem. At time $(l+1)\,dt$, equation (2.42) will be used to calculate the new values of the pressure field. However, when discretising the spatial derivatives of the left-hand side, *6* neighbouring values of p are needed to calculate the gradients. This would ultimately lead to a band matrix to be inverted at each time-step. In this work, it is intended to develop an efficient and explicit calculation scheme, so an alternative approximation is chosen. In the second term of equation (2.42) the unknown pressure at time $(l+1)\,dt$ is replaced in a first approximation by the sound pressure obtained in the absence of background flow:

$$p^{l+1}_{appr.} \approx p^{l} - dtc^2\rho_0\left(\nabla\cdot\mathbf{v}^{\mathbf{l+0.5}}\right). \tag{2.43}$$

This approximation corresponds to neglecting second-order terms in the Mach number ($M = v_0/c$), and is sufficiently accurate as long as the background flow velocity is not too high. It will be shown however in Chapter 2.5 that the problem of accuracy for high Mach number flows can be by-passed using a finer grid than needed in absence of flow.

Including the approximation expressed by equation (2.43) in equation (2.42) results in the pressure equation for discrete time and continuous space:

$$p^{l+1} = p^{l} - dtc^2\rho_0\left(\nabla\cdot\mathbf{v}^{\mathbf{l+0.5}}\right) - dt\left(\mathbf{v_0}\cdot\nabla\left[p^{l} - 0.5dtc^2\rho_0\nabla\cdot\mathbf{v}^{\mathbf{l+0.5}}\right]\right). \tag{2.44}$$

Spatial derivatives are now approximated by central finite-differences in the staggered, Cartesian grid. The background velocity is discretised where acoustic velocities are present. Spatial mismatch is solved by linear interpolation:

$$\begin{aligned} p^{l+1} = p^{l} &- dtc^2\rho_0\sum_{\beta}\left(\frac{v^{l+0.5}_{\beta(\beta+0.5)} - v^{l+0.5}_{\beta(\beta-0.5)}}{d\beta}\right) \\ &-dt\left[\sum_{\beta}\left(\frac{v_{0\beta(\beta+0.5)} + v_{0\beta(\beta-0.5)}}{2}\right)\left(\frac{\xi^{l+0.5}_{(\beta+1)} - \xi^{l+0.5}_{(\beta-1)}}{2d\beta}\right)\right], \end{aligned} \tag{2.45}$$

with

$$\xi^{l+0.5} = p^{l} - 0.5dtc^2\rho_0\sum_{\beta}\left(\frac{v^{l+0.5}_{\beta(\beta+0.5)} - v^{l+0.5}_{\beta(\beta-0.5)}}{d\beta}\right). \tag{2.46}$$

In the previous equations, a summation over β runs over the three Cartesian indices. For simplicity, the spatial indices *(i,j,k)* of the discretised acoustic quantities are omitted. Offset with respect to this position in direction β is indicated as $(\beta+0.5)$, $(\beta-0.5)$ etc. v_β and $v_{0\beta}$ indicate the β-component of the acoustic velocity and the background flow velocity.

The introduction of ξ will result in a more efficient numerical scheme in the object-orientated implementation presented further in this work. Before every calculation of p^{l+1} in the pressure grid, equation (2.46) needs to be evaluated at all grid positions. $\xi^{l+0.5}$ can be interpreted as a first estimate of p at time $l+0.5$, neglecting the effect of the background flow.

2.2.3.b Velocity equation

By analogy with the derivation of the pressure equation, the velocity equation (2.19) is also transformed using equation (2.40):

$$\mathbf{v}^{\mathbf{l+0.5}} = z^{-1}\mathbf{v}^{\mathbf{l+0.5}} + 0.5\left(1+z^{-1}\right)dt\left[\mathbf{v}^{\mathbf{l+0.5}} \times \left(\nabla \times \mathbf{v_0}\right)\right] - 0.5\left(1+z^{-1}\right)dt\frac{1}{\rho_0}\nabla p^{l+0.5}$$
$$- 0.5\left(1+z^{-1}\right)dt\nabla\left[\mathbf{v}^{\mathbf{l+0.5}} \cdot \mathbf{v_0}\right]. \quad (2.47)$$

Resolving the delay operator and moving only known variables just before time *(l+0.5) dt* to the right-hand side gives:

$$\mathbf{v}^{\mathbf{l+0.5}} - 0.5dt\left[\mathbf{v}^{\mathbf{l+0.5}} \times \left(\nabla \times \mathbf{v_0}\right)\right] + 0.5dt\nabla\left[\mathbf{v}^{\mathbf{l+0.5}} \cdot \mathbf{v_0}\right] =$$
$$\mathbf{v}^{\mathbf{l\text{-}0.5}} + 0.5dt\left[\mathbf{v}^{\mathbf{l\text{-}0.5}} \times \left(\nabla \times \mathbf{v_0}\right)\right] - \frac{dt}{\rho_0}\nabla p^l - 0.5dt\nabla\left[\mathbf{v}^{\mathbf{l\text{-}0.5}} \cdot \mathbf{v_0}\right]. \quad (2.48)$$

Instead of solving this equation by using a band matrix that needs to be inverted every time-step, an analogous approximation as for the pressure equation is made. Now, the unknown velocity at time *(l+0.5) dt* is replaced by the velocity obtained in the absence of background flow:

$$\mathbf{v}^{\mathbf{l+0.5}}_{appr.} \approx \mathbf{v}^{\mathbf{l\text{-}0.5}} - \frac{dt}{\rho_0}\nabla p^l. \quad (2.49)$$

Again, this approximation is accurate as long as Mach numbers are not too high. Using equation (2.49) in the second and third term of equation (2.48) gives the following velocity equation, continuous in space and discrete in time:

$$\mathbf{v}^{\mathbf{l+0.5}} = \mathbf{v}^{\mathbf{l\text{-}0.5}} + dt\left[\left(\mathbf{v}^{\mathbf{l\text{-}0.5}} - 0.5\frac{dt}{\rho_0}\nabla p^l\right) \times \left(\nabla \times \mathbf{v_0}\right)\right] - \frac{dt}{\rho_0}\nabla p^l$$
$$- dt\nabla\left[\left(\mathbf{v}^{\mathbf{l\text{-}0.5}} - 0.5\frac{dt}{\rho_0}\nabla p^l\right) \cdot \mathbf{v_0}\right]. \quad (2.50)$$

Devectorising this velocity equation results in

$$v_\alpha^{l+0.5} = v_\alpha^{l-0.5} - dt\sum_{\beta\neq\alpha}\left(v_\beta^{l-0.5} - 0.5\frac{dt}{\rho_0}\frac{\partial p^l}{\partial \beta}\right)\left(\frac{\partial v_{0\alpha}}{\partial \beta} - \frac{\partial v_{0\beta}}{\partial \alpha}\right) - \frac{dt}{\rho_0}\frac{\partial p^l}{\partial \alpha}$$
$$- dt\sum_\beta \frac{\partial\left(v_{0\beta}\left(v_\beta^{l-0.5} - 0.5\frac{dt}{\rho_0}\frac{\partial p^l}{\partial \beta}\right)\right)}{\partial \alpha}. \quad (2.51)$$

Spatial derivatives are approximated by central finite-differences and spatial mismatch is solved by linear interpolation. The *FDTD* equation for the calculation of the velocity not near any boundary then gives:

$$v_{\alpha(\alpha+0.5)}^{l+0.5} = v_{\alpha(\alpha+0.5)}^{l-0.5} - dt\sum_{\beta\neq\alpha}\frac{\left(\chi_{\beta(\alpha+1,\beta+0.5)}^{l}+\chi_{\beta(\alpha+1,\beta-0.5)}^{l}+\chi_{\beta(\beta+0.5)}^{l}+\chi_{\beta(\beta-0.5)}^{l}\right)}{4}R_{0\alpha\beta(\alpha+0.5)}$$

$$-\frac{dt}{\rho_0}\left[\frac{p_{(\alpha+1)}^{l}-p^{l}}{d\alpha}\right]-dt\left[\frac{v_{0\alpha(\alpha+1.5)}\chi_{\alpha(\alpha+1.5)}^{l}-v_{0\alpha(\alpha-0.5)}\chi_{\alpha(\alpha-0.5)}^{l}}{2d\alpha}\right]$$

$$-dt\sum_{\beta\neq\alpha}\left(\frac{\left(\frac{\left(\chi_{\beta(\alpha+1,\beta+0.5)}^{l}+\chi_{\beta(\alpha+1,\beta-0.5)}^{l}\right)\left(v_{0\beta(\alpha+1,\beta+0.5)}+v_{0\beta(\alpha+1,\beta-0.5)}\right)}{4}\right)-}{d\alpha}\right.$$

$$\left.\frac{\left(\frac{\left(\chi_{\beta(\beta+0.5)}^{l}+\chi_{\beta(\beta-0.5)}^{l}\right)\left(v_{0\beta(\beta+0.5)}+v_{0\beta(\beta-0.5)}\right)}{4}\right)}{d\alpha}\right), \quad (2.52)$$

with

$$R_{0\alpha\beta(\alpha+0.5)} = \frac{\left(v_{0\alpha(\alpha+0.5,\beta+1)}-v_{0\alpha(\alpha+0.5,\beta-1)}\right)}{2d\beta} - \frac{\frac{\left(v_{0\beta(\alpha+1,\beta+0.5)}+v_{0\beta(\alpha+1,\beta-0.5)}\right)}{2}-\frac{\left(v_{0\beta(\beta+0.5)}+v_{0\beta(\beta-0.5)}\right)}{2}}{d\alpha}, \quad (2.53)$$

$$\chi_{\alpha(\alpha+0.5)}^{l} = v_{\alpha(\alpha+0.5)}^{l-0.5} - 0.5\frac{dt}{\rho_0}\frac{\left(p_{(\alpha+1)}^{l}-p^{l}\right)}{d\alpha}. \quad (2.54)$$

The same conventions for the notation as for the discrete pressure equation are used. An example might clarify this notation. Suppose the expression above is evaluated at an *x*-velocity, so $v^{l+0.5}_{\alpha(\alpha+0.5)}$ represents $v_{x((i+0.5)dx,j\,dy,k\,dz)}^{(l+0.5)dt}$, and the term $\chi^{l}_{\beta(\alpha+1,\beta+0.5)}$ needs to be calculated. The acoustic quantities involved in evaluating the latter are $v^{ldt}_{y((i+1)dx,(j+0.5)\,dy,k\,dz)}$, $p^{ldt}_{((i+1)\,dx,(j+1)\,dy,k\,dz)}$ and $p^{ldt}_{((i+1)\,dx,j\,dy,k\,dz)}$, when β represents the *y*-direction.

As stressed during the derivation, the mixed acoustic-background flow kinetic energy terms $v_0\chi$ are kept together when taking spatial derivatives. The quantity χ^l can be interpreted as a first estimate of v at time l, neglecting the effect of the background flow.

2.2.4 Other realisations of the momentum equation

When the mixed kinetic-energy term is split, equation (2.51) can be further simplified to:

$$v_\alpha^{l+0.5} = v_\alpha^{l-0.5} - dt\sum_\beta\left[\chi_\beta\frac{\partial v_{0\alpha}}{\partial\beta}\right] - dt\sum_\beta\left[v_{0\beta}\frac{\partial\chi_\beta}{\partial\alpha}\right] - \frac{dt}{\rho_0}\frac{\partial p^l}{\partial\alpha}. \tag{2.55}$$

In this, the gradient of the kinetic energy term is not taken explicitly, in contrast to equation (2.51). Following codes are used to indicate the different realisations of the momentum equation : *R* means that no assumptions are made concerning the rotor of the acoustic velocity, *noR* means that assumption (2.18) is used. *EC* means that the energy conservation form is used as discussed during the derivation of the velocity equation, *noEC* means that the energy conservation form is not used. Equation (2.51) will be indicated with (*noR+EC*), while equation (2.55) will be called (*noR+noEC*).

When no assumptions are made concerning the rotor of the acoustic velocity, the equations stated below are obtained. In the first one, the kinetic energy conservation form is used. Assumption (2.18) is not made, and this leads to an extra term to be discretised namely $\mathbf{v_0}\times\left(\nabla\times\mathbf{v}\right)$.

The equation (*R+EC*) reads:

$$v_\alpha^{l+0.5} = v_\alpha^{l-0.5} - dt\sum_{\beta\neq\alpha}\chi_\beta\left(\frac{\partial v_{0\alpha}}{\partial\beta}-\frac{\partial v_{0\beta}}{\partial\alpha}\right) - dt\sum_{\beta\neq\alpha}v_{0\beta}\left(\frac{\partial\chi_\alpha}{\partial\beta}-\frac{\partial\chi_\beta}{\partial\alpha}\right) - \frac{dt}{\rho_0}\frac{\partial p^l}{\partial\alpha} - dt\sum_\beta\frac{\partial\left(v_{0\beta}\chi_\beta\right)}{\partial\alpha}. \tag{2.56}$$

In case no assumptions are made concerning the rotor of the acoustic velocity and if the kinetic energy conservation form is not used, the derivation of the momentum equation may start directly from equation (2.1). Assuming steady state background flow, linearisation in acoustics and omitting source terms (see Chapter 2.1) leads to (*R+noEC*):

$$v_\alpha^{l+0.5} = v_\alpha^{l-0.5} - dt\sum_\beta\left[\chi_\beta\frac{\partial v_{0\alpha}}{\partial\beta}\right] - dt\sum_\beta\left[v_{0\beta}\frac{\partial\chi_\alpha}{\partial\beta}\right] - \frac{dt}{\rho_0}\frac{\partial p^l}{\partial\alpha}. \tag{2.57}$$

The importance of the assumptions concerning the momentum equation during the derivation in Chapter 2.1.1 is illustrated with a numerical example. A configuration is considered which is representative for an expansion chamber muffler, with an asymmetrical, extended inlet and outlet. A complex flow field is observed in this structure, with large gradients in the background flow and recirculating flows, as shown in Figure 2.2.

A two-dimensional simulation is performed. A broadband acoustic pulse is excited in the inlet duct. A receiver is placed in the outlet duct. In Figure 2.3, the time responses for the different variants of the *FDTD* equations are shown for a flow velocity of 30 m/s in the inlet duct.

A sufficiently stable simulation is obtained, only when the rotor of the acoustic velocity is explicitly removed from the velocity equation, in combination with the use of a kinetic energy conservation form of the momentum equation. When the incident flow velocity is smaller, the simulations stay unstable for the other realisations of the momentum equation, but instability is observed later in time.

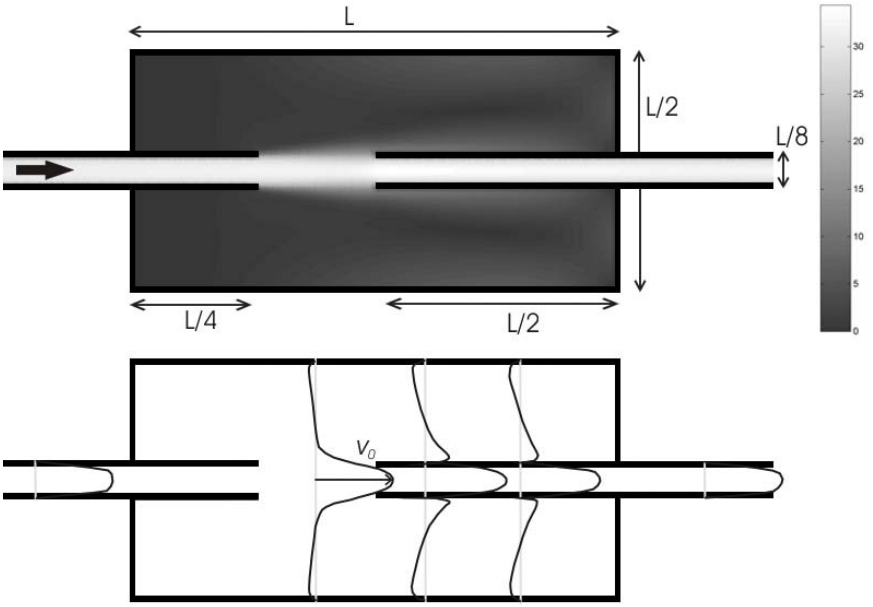

Figure 2.2 Magnitude of the flow (expressed in m/s) in an expansion chamber muffler, with asymmetrical extended inlet and outlet. The length of the expansion chamber *L* equals 1.2 m. In the lower part of this Figure, (horizontal) flow velocity profiles at selected locations are shown. For each profile, the line of zero wind speed is indicated with the grey lines.

The wind velocities encountered outdoors are rather small. The 4 realisations described above are tested in a typical situation namely a noise barrier on either side of a line source, with an incident wind speed of 11 m/s at a height of 10 m. Details concerning this simulation can be found in Chapter 3.4.4. All the realisations described above result in sufficiently stable simulations and yield exactly the same time signals. So assumption (2.18) is experimentally justified since it does not affect the recorded time signals.

In complex flows, in combination with high flow velocities, the assumptions concerning the rotor of the acoustic velocity and kinetic energy conservation become important.

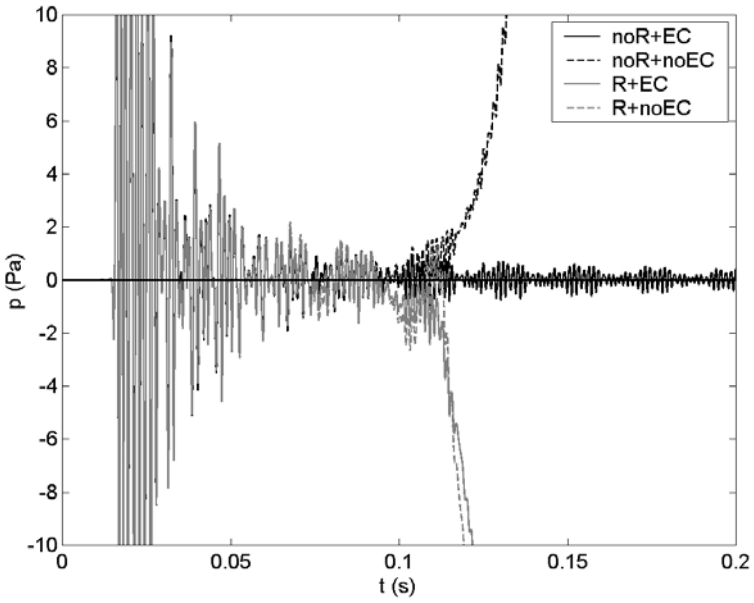

Figure 2.3 Amplitude at the receiver in the outlet duct of the muffler, shown in Figure 2.2, with increasing time. The length of the expansion chamber equals 1.2 m. The flow velocity is 30 m/s. A Gaussian pulse with centre frequency of 500 Hz and a bandwidth of 500 Hz is used. Following codes are used: *R* means that no assumptions are made concerning the rotor of the acoustic velocity, *noR* means that assumption (2.18) is used. *EC* means that the energy conservation form is used as discussed during the derivation of the velocity equation, *noEC* means that the energy conservation form is not used.

2.2.5 Spatial extent of the numerical scheme and time-stepping

An important advantage of using a (spatial) low-order numerical scheme is the limited spatial extent. In the absence of flow, only nearest neighbour pressures and velocity components are needed to perform time-stepping. Introducing various boundaries of the computational domain therefore requires very little numerical overhead. In the staggered grid, acoustic velocities are present at the borders of the grid, normal to that boundary. In this way, a perfectly reflecting boundary e.g. is easily simulated by demanding that the acoustic velocity equals zero.

When a background flow is present, the situation changes slightly. For the calculation of the discretised pressure at a certain place not near any boundary, the time-stepping formula includes *24* discretised velocity values and *6* discretised pressures in a three-dimensional simulation space. For the calculation of velocities not near any boundary, the values of *12* discretised pressures and *10* discretised velocities are used every time-step. A two-dimensional representation of the relevant points for the calculation of a velocity and a pressure is given in Figure 2.4.

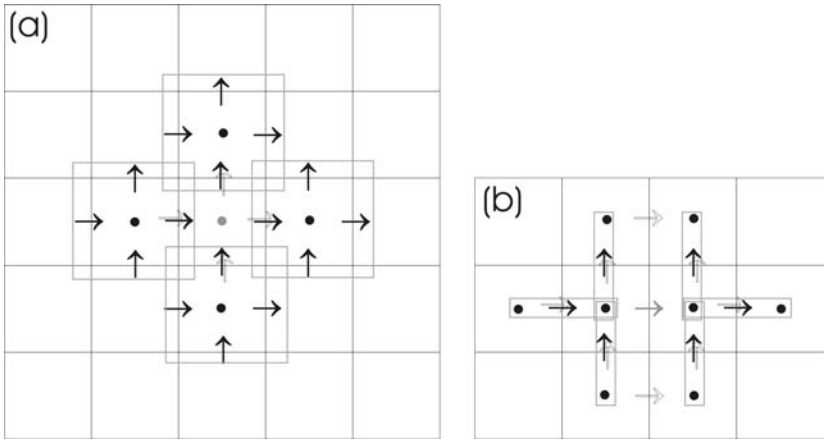

Figure 2.4 Positions of the acoustic pressures, the acoustic velocity components and background flow velocity components, for the calculation of a certain pressure (a) and velocity (b). The points where the time-stepping is performed are indicated in grey. The filled circles represent acoustic pressures, the filled arrows the acoustic velocity components and the open arrows the components of the background flow velocity.

As indicated during the discretisation of the equations, the quantities ξ and χ, associated with the prediction step in between two successive time steps of both the pressure and velocity equation, are considered as a whole (indicated with boxes in Figure 2.4). This results in a more efficient numerical scheme. The value of ξ and χ at a certain place is asked for by different surrounding pressures and velocities every time step. Unnecessary calculations are avoided by keeping these values in memory. Another beneficial effect is that an easy treatment at simulation borders is possible. The ξ that would fall out the grid is shifted to the next relevant point in the grid. This is represented in Figure 2.5. Hence, the distance over which the gradient of this quantity is taken must be halved. To

calculate χ on the border itself, dedicated formulas depending on the type of boundary are needed and some more information on that topic can be found in Chapter 2.3.3.

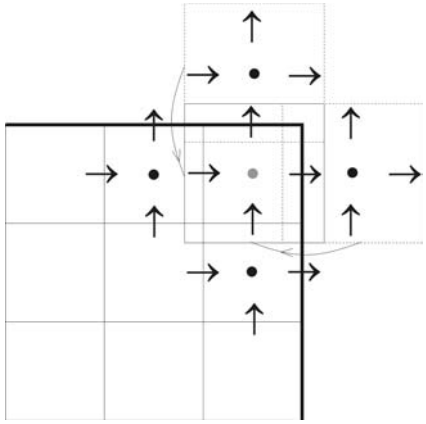

Figure 2.5 Shifting of the location for the calculation of ξ inward the grid. The dotted areas, representing the ξ that does not lie in the simulation space, are replaced during the calculation by the full-bordered areas, situated in the grid.

A compact time-stepping scheme is used. The continuous equations are discretised so that the new values of the acoustic quantities only depend on the quantities of the previous time. As a result, in-place computation is possible: the new values replace the old ones in computer memory. This leads to an important reduction in memory use.

The time-stepping algorithm can be represented as shown in Figure 2.6. Different fields are calculated in turn. In a first step, χ is calculated at every location where a velocity is placed at time *l dt*, based on the velocity at time *(l-0.5) dt* and on the neighbour acoustic pressures at time *l dt*. Next, the acoustic velocity is calculated at time *(l+0.5) dt*, based on the velocity at the previous time *(l-0.5) dt*, based on the pressures of the two neighbour cells at time *l dt* and on χ values at surrounding velocity locations at time *l dt*. Then ξ is computed at time *(l+0.5) dt*, based on the pressure at time *l dt* and on the neighbouring velocities at time *(l+0.5) dt*. Finally, the pressure field at time *(l+1) dt* is obtained based on the pressure at the previous time *l dt*, the velocities at time *(l+0.5) dt* that border the cell where the pressure is calculated, and on ξ values at time *(l+0.5) dt*. In the current model, background flow is assumed to be time-invariant. So the background flow velocity field has to be read in memory once, at the beginning of every simulation.

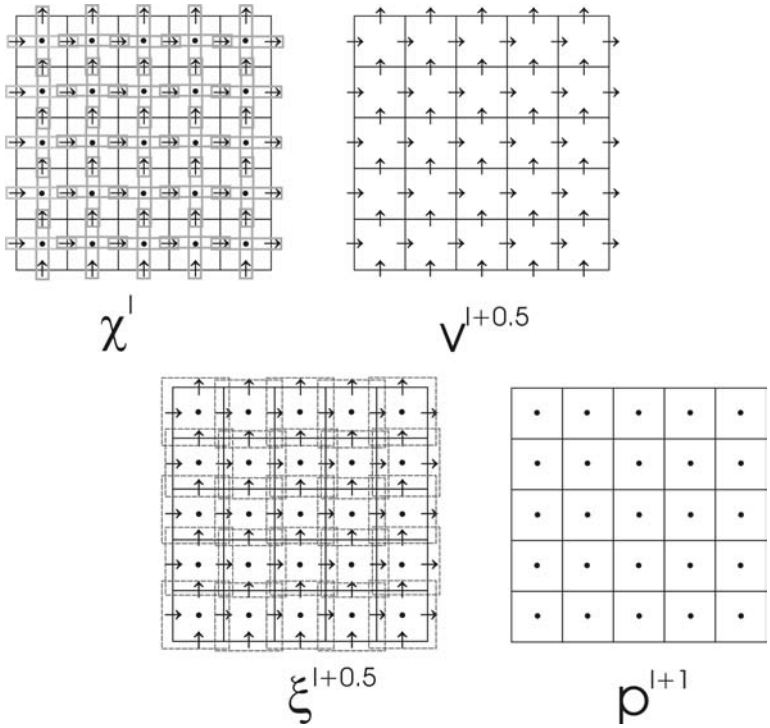

Figure 2.6 Time-stepping algorithm in the presence of background flow not near any boundary, in a two-dimensional grid.

2.2.6 Simplified flow

The equations describing sound propagation in a general flow introduce a strong increase in the use of numerical resources. The flow is often parallel or near parallel in a large part of the simulation region. A straight duct with laminar flow conditions introduces such a parallel flow.

Suppose the direction of flow is α. In the following equations, a summation over β runs over the three Cartesian indices, unless stated otherwise. Simplifying equation (2.51) for this special case gives the following equation, discrete in time and continuous in space:

$$v_\alpha^{l+0.5} = v_\alpha^{l-0.5} - dt\sum_{\beta\neq\alpha}\left[\chi_\beta^l \frac{\partial v_{0\alpha}}{\partial\beta}\right] - dt v_{0\alpha}\frac{\partial\chi_\alpha^l}{\partial\alpha} - \frac{dt}{\rho_0}\frac{\partial p^l}{\partial\alpha}. \tag{2.58}$$

And for the other directions:

$$v_{\beta}^{l+0.5} = v_{\beta}^{l-0.5} + dt\chi_{\alpha}^{l}\frac{\partial v_{0\alpha}}{\partial \beta} - dt\frac{\partial\left[v_{0\alpha}\chi_{\alpha}^{l}\right]}{\partial \beta} - \frac{dt}{\rho_0}\frac{\partial p^{l}}{\partial \beta}. \tag{2.59}$$

The pressure equation simplifies to

$$p^{l+1} = p^{l} - dtc^2\rho_0\sum_{\beta}\frac{\partial v_{\beta}^{l+0.5}}{\partial \beta} - dtv_{0\alpha}\frac{\partial \xi^{l+0.5}}{\partial \alpha}. \tag{2.60}$$

Parallel flow in direction α without gradients perpendicular to that direction results in a complete uniform flow. The velocity equation in the direction of the flow α then simplifies to

$$v_{\alpha}^{l+0.5} = v_{\alpha}^{l-0.5} - dtv_{0\alpha}\frac{\partial \chi_{\alpha}^{l}}{\partial \alpha} - \frac{dt}{\rho_0}\frac{\partial p^{l}}{\partial \alpha}. \tag{2.61}$$

For the directions perpendicular to the direction of the uniform flow, the *FDTD* equation becomes:

$$v_{\beta}^{l+0.5} = v_{\beta}^{l-0.5} - dtv_{0\alpha}\frac{\partial \chi_{\alpha}^{l}}{\partial \beta} - \frac{dt}{\rho_0}\frac{\partial p^{l}}{\partial \beta}. \tag{2.62}$$

The pressure can still be calculated using equation (2.60). When no assumptions concerning the rotor of the acoustic velocity are made, the derivative of χ_α to β in equation (2.62) has to be replaced by a derivative of χ_β to α. This is a more common form of these equations (e.g. see Reference [30]). Since in uniform flow the rotor of the acoustic field is exactly zero, both forms are equivalent. In the object-orientated implementation described in Chapter 2.2.7, it is easy to combine calculations in parallel flow with calculations in more general flow in other parts of the simulation space.

Using the simplified flow equations results in first place in a decrease in CPU time. In absence of flow, about 12.5% of the time necessary to perform an equivalent simulation in a non-uniform, rotational flow is needed. The uniform and parallel flow equations take respectively about 75% and 90% of the simulation time of the general flow equations. Memory use is affected to a smaller degree by the simplifications made in this chapter. In absence of flow and in uniform flow, a reduction of respectively 65% and (only) 5% in memory use is observed. When using the parallel flow equations, no significant changes in memory use relative to the complete flow equations are seen.

The values given in previous paragraph for the simplified flow equations are rather small. Especially memory use, which is often the limiting factor when performing simulations, is only slightly affected by using the simplified flow equations. The main reason is that in the simplified equations orthogonal to the flow direction, the background flow velocity and acoustic velocity in the direction of the flow need to be known. As a result, only a few links to nearby velocities can be omitted when simplifying the equations for sound propagation in a general flow. There is also some overhead in the software, which is kept very general, so part of the allocated computer memory is independent of the equations used.

2.2.7 Object-oriented implementation

The numerical implementation of the *FDTD* equations is based on object-oriented (*OO*) software development. *OO* is known to be in general rather inefficient for solving numerical problems. In the particular case of *FDTD* simulations of sound propagation in background flow, there are some advantages that will be highlighted in this paragraph.

In the implementation, each unknown pressure and particle velocity is implemented as an object. Since low-order *FDTD* schemes only use nearest neighbour values in the time-stepping equations, a few pointers are sufficient to translate the physical geometry to a linked list of objects. This results in flexible research software: each object can implement its own time-stepping equations and the number of different equations used does not introduce any computational overhead. More specific concerning sound propagation in background flow, simulation time (and memory use) can be reduced by using a simplified flow equation, as shown in previous chapter. An interesting and practical application outdoors is assuming uniform flow starting from a certain height when there is a logarithmic background flow profile. In the latter, gradients with height become rapidly negligible with increasing height above a ground surface.

In regions where flow velocities are very low, the sound propagation equations in absence of flow should be considered. Suppose that in a computational grid half of the general flow cells are placed by non-flow cells. This would result in a reduction of about 40% in computational time (see previous chapter). About 5% of the time is needed for overhead operations during the time-stepping mechanism.

The additional variables ξ and χ, introduced in equations (2.46) and (2.54) to simplify notations, are chosen in such a way that they also simplify the *OO* implementation, especially near boundaries, and reduce calculation overhead at

the same time. Because of the physical location where these variables are defined, they are stored in the pressure and particle velocity objects respectively.

2.2.8 Sub-cell modelling of the gradients in a logarithmic wind speed profile near a wall

When the frequencies of interest are small, a large spatial discretisation step may be chosen. As a result, simulations can be performed up to large distances. This means however that the discretisation near a physical boundary will often be too coarse with respect to the flow field. This might lead to inaccurate calculations e.g. when large gradients in the flow are observed near walls or near the ground. In order to avoid a linearisation of the wind profile that would result in an under-prediction of these gradients, a grid refinement may be applied. In such an approach, the first cells near the wall should be very small. It will be shown in Chapter 2.2.9 that a smooth transition between the fine and coarse grid is necessary in order to avoid numerical reflection between layers with different cell sizes. As a consequence, an important increase in the number of cells would be necessary. Besides, this would make it necessary to vary the time-step in order to prevent from (completely) inaccurate calculations (see discussion in Chapter 2.2.9).

In this chapter, a sub-cell model is presented, that does not result in an increase in computational resources, for the case of a logarithmic flow velocity profile. The flow velocity v_0 with increasing height z above a wall or ground in this case can be described by the following function:

$$v_0(z) = a \ln\left(\frac{z}{z_0}\right) \text{ for } z > z_{0,} \tag{2.63}$$

where z_0 is the roughness length, which is defined as the height above a surface where the wind speed is zero. The gradient in the first cell near a wall is computed analytically based on the wind speed profile (2.63), with a priori knowledge of only the roughness length. In the staggered grid, the background flow velocity component parallel to the border V_0 in the first cell is situated at a height that equals half the grid cell size (at $D/2$, where D is the cell height) (thus at the same place as the acoustic velocity component, parallel to that border). Parameter a in equation (2.63) is determined so that the mass flow in the first cells is equal to the one computed with the CFD software (based on the value of the flow at $D/2$), in which the conservation laws are taken into account. The estimated wind speed profile near the ground/wall is shown in Figure 2.7. This approach should be followed since the wind speed profile is often not exactly

known. In a case of interest, namely a noise barrier in wind, at sufficient distances downwind from the barrier, logarithmic wind speed profiles are observed that do not have the same parameters as the inflow boundary condition, and that gradually change with distance. However, when simulating sound propagation over a flat terrain (with a fixed logarithmic wind speed profile), parameter *a* is known and should therefore not be estimated, since it will result in a less accurate calculation of the gradient.

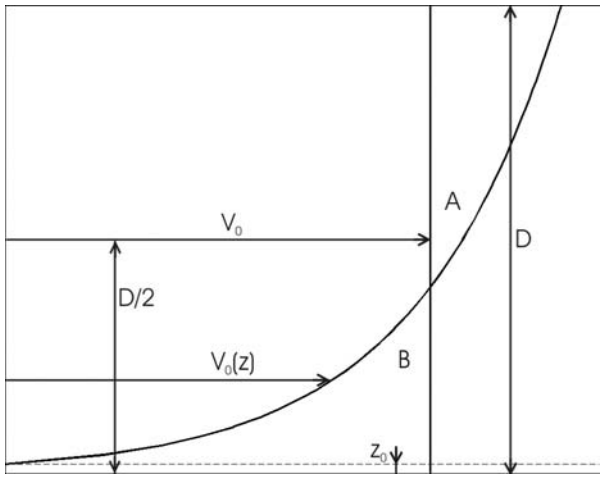

Figure 2.7 Estimation of the logarithmic wind speed profile in the first computational cell near a wall.

The condition to find parameter *a* is:

$$\int_{z=z_0}^{z=D} a \ln\left(\frac{z}{z_0}\right) dz = V_0\left(D - z_0\right). \tag{2.64}$$

Or this means that the area *A* and *B* must be the same. The fitting parameter can be calculated as follows:

$$a = \frac{V_0\left(D - z_0\right)}{z_0 + D\left[\ln\left(\frac{D}{z_0}\right) - 1\right]} \tag{2.65}$$

For heights lower than z_0, flow velocity stays zero and as a consequence, there are no contributions to the gradient. The derivative normal to the border of the

parallel velocity component is calculated piece-wise over the first computational cell and gives:

$$\frac{\partial v_0(z)}{\partial z} = \frac{1}{(D-z_0)} \int_{z=z_0}^{z=D} \frac{\partial v_0(z)}{\partial z} dz = \frac{a}{(D-z_0)} \ln\left(\frac{D}{z_0}\right) \tag{2.66}$$

The approach to better represent the gradients in the background flow near a wall is investigated in a numerical experiment. Sound propagation over flat ground in the presence of a logarithmic wind speed profile is considered. Simulations are performed for a perfectly reflecting as well as a highly absorbing ground. A point source emitted pure tones. Sound frequencies between 50 Hz en 500 Hz were considered. The spatial discretisation step was $1/10^{th}$ of the wavelength of sound under investigation. The Courant number was 1. Simulations with and without the use of such special cells in the first row of air cells near the interface with the soil were compared. A logarithmic wind speed profile with a roughness length of 1 mm, and parameter *a*, equal to 1, was used. Differences were found at the locations were destructive interference occurs. Effects were well below 0.5 dB. It can be concluded that in this typical outdoor sound situation, low frequencies are rather insensitive to sharp gradients. For the highest frequencies considered in this example, the spatial discretisation step was small enough to resolve the wind speed gradient.

Larger effects can however be expected for the case of sound propagation in flows at high velocities, e.g. near the walls in a duct. Since this is not a case of interest in this work, no further investigation on this subject is performed.

2.2.9 Grid refinement

A grid refinement is implemented to solve the particular problem of reflection and transmission of sound waves between two mediums with a large difference in acoustic impedance. The acoustic waves are usually transmitted only to a limited degree. This means that a large, exponential decrease in amplitude is observed at such an interface, which cannot be resolved in a coarse grid. A fine grid on the interface is needed therefore in order to perform accurate calculations. For the particular problem of sound reflection from finite-impedance boundaries and from ground cells (see Chapter 2.3.1.b), a (one-dimensional) grid refinement in the direction normal to the interface is developed.

The approach as described in Ref. [28] will be used here. In the latter, the walls of the Voronoi cells, where the acoustical velocities are defined, are placed in the

middle in between two pressures. Such a scheme is stable when the temporal discretisation step is calculated based on the dimensions of the smallest cell [28].

Suppose a refined *layer 12* in between *grid 1* and *grid 2*, as shown in Figure 2.8. Assume that

$$dx_{12} = \frac{dx_1 + dx_2}{2}, \tag{2.67}$$

where dx_{12} is the spatial discretisation step of the refined layer in between two uniform grids with (different) spatial discretisation steps dx_1 and dx_2. By obeying this condition, the acoustic velocities throughout the full simulation space are situated in the middle in between two pressures. The (virtual) places (indicated with the open circle in Figure 2.8) of the pressures involved in taking the pressure gradients at the velocities are the same for adjoining cells.

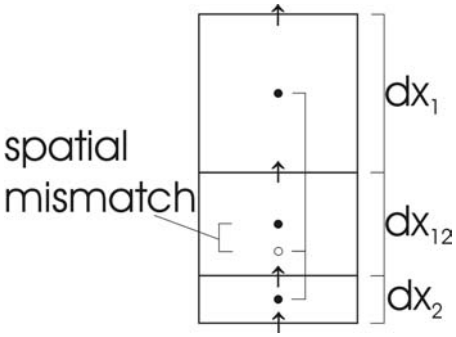

Figure 2.8 Representation of a transition layer and spatial mismatch in solving the velocity equation at an interface.

The pressure equation in the transition layer will still be calculated on its original location in the staggered grid (namely in the middle of the cells, indicated with the filled circles in Figure 2.8). Although this results in a spatial mismatch in the transition layer, only one layer of cells deviates from the other Cartesian cells in this grid refinement approach. Besides, this approach results in an easier implementation.

The spatial mismatch, which equals $0.25(dx_1-dx_2)$, will result in numerical reflection on the refined layer. This can however be minimised by decreasing the difference in the spatial discretisation step of neighbouring cells. This means that multiple layers of cells are needed to obtain gradual transition when going from a coarse to a fine grid. The object-oriented implementation makes this possible.

Transition layers are considered as single-layered, staggered-grid objects. The use of multiple grids is possible in a single simulation space. Every velocity and pressure belongs to (only) one of these grids, where the spatial discretisation step is constant. The velocities at the interface between different grids are linked to the relevant pressures and velocities in neighbouring grids. After initialisation, the geometry of the grid is reduced to a linked list of objects and could therefore be cleared from memory. The described approach to refine grids is easily applied to multiple transitions. Single-layered grids replace adjoining grids of transition layers. In this way, a gradual transition between the coarse and fine grid is achieved.

The use of a single, temporal discretisation step in the full simulation domain also leads to numerical reflection on the interface between a fine and coarse grid. The phase error will be different in both grids. This means that sound waves, travelling between the fine and coarse grid, face a difference in numerical impedance, which causes reflection. A gradual transition is needed to minimise this kind of numerical reflection.

Another possible approach is using a higher-order scheme to calculate spatial derivatives. Although numerical reflection could be minimised in an easier way, a difficult treatment is expected near the interface of different propagation media. Since the grid refinement is especially needed very close to the ground, this approach is not considered in this work.

When there is a background flow, no additional problems arise due to the use of the quantities ξ and χ. However, accuracy will be somewhat lower compared to the equations in absence of flow since the spatial mismatch is involved in different terms of the time-stepping equations.

Numerical reflection on the grid refinement is quantified with a numerical simulation. A pulse propagating from a coarse to a fine grid, normal incident on the interface, is simulated. The grid is refined by a factor 4. An increasing number of transition layers are used to move from the coarse to the fine grid. The spatial discretisation steps of the transition layers decrease linearly. Condition (2.67) is satisfied in this grid. The numerical reflection is defined as the total reflected sound energy relative to the energy of the incident pulse on the interface between the coarse and fine grid. The use of a single transition step reduces the numerical reflection already with 20 dB, compared to an abrupt transition at the interface between the coarse and the fine grid With increasing number of transition layers, the (artificial) numerical reflection becomes smaller, as shown in Figure 2.9.

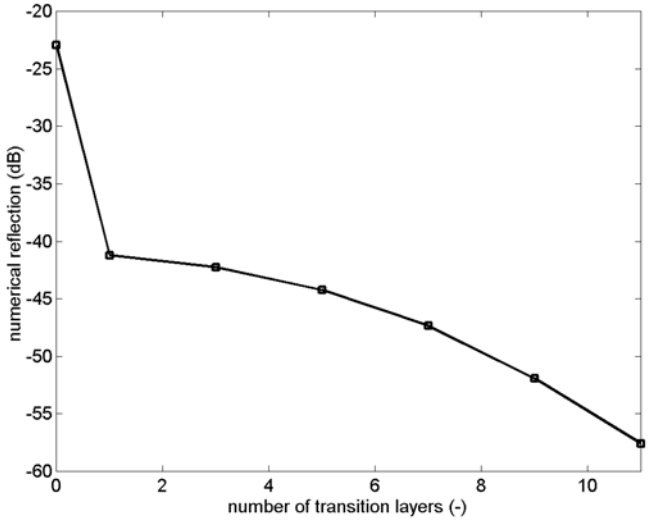

Figure 2.9 Numerical reflection on the interface between a coarse and a fine grid, with increasing number of transition layers.

To obtain stability, the Courant number, based on the smallest spatial discretisation step in the simulation space, is set to 1. As a result, propagation in the coarse grid is not optimal when considering phase errors. For this reason, the refinement ratio should be kept small.

2.3 Boundary conditions

2.3.1 Physical boundaries

2.3.1.a Perfectly reflecting boundary

As stated earlier, an acoustic hard material can be easily implemented in a staggered grid. At the simulation borders of an orthogonal grid, only acoustic velocities, normal to that border, are possible. These velocities have to be zero to simulate perfect reflection.

2.3.1.b Finite-impedance boundary – Ground model

The interaction of acoustic waves and the soil is important in many outdoor sound propagation applications. In this chapter, it is investigated how the reflection from natural grounds (or more general: reflection from frequency-dependent finite-impedance boundaries) could be modelled in the finite-difference time-domain model.

The characteristic, acoustic impedance of a medium is defined as the ratio of the acoustic pressure and the acoustic velocity. Since there is a (large) difference in the characteristic impedance of (free) air and a (natural) soil, part of the energy of an incident sound wave will be reflected. The other part is transmitted into the ground. In outdoor sound propagation, it is mainly the reflected part that is of interest. The acoustic impedance of a ground surface, which is the ratio of the acoustic pressure and normal acoustic velocity near the ground, is continuous. This makes it possible to simulate reflection from grounds by means of a finite-impedance boundary, which is a widely applied approach.

Only for normal incidence, a sound wave travelling into the soil will be orthogonal to the ground surface. In this case, the acoustic impedance of the ground surface equals the characteristic impedance inside the (homogeneous) ground. When sound is incident under a certain angle, the transmitted wave will travel inside the ground under an angle, not normal anymore to the ground surface. However, it is still a good approximation to consider the sound wave travelling in a direction normal to the surface [31]. As a result, the acoustic impedance of the ground can be set equal to the acoustic impedance of the ground surface. This is called the local reaction approximation. The alternative, the extended reacting ground approach, assumes that the acoustic impedance of a ground surface depends on the angle of incidence. For natural soils in practice, little difference is observed between locally and extended reacting ground surfaces [31].

A wide variety of ground impedance models can be found in acoustic literature, ranging from very simple, semi-empirical to detailed, theoretically based models. An impedance model gives the relation between the acoustic surface impedance and the physical parameters that describe the structure of the ground. In general, the magnitude of the impedance decreases with increasing frequency. An example of a simple and easy-to-apply impedance model is the 1-parameter model of Delany and Bazley [32]. Although this model was developed for (highly) porous, fibrous materials, it is widely used to simulate reflection from grassland. The (effective) flow resistivity is the only parameter that determines the impedance of the soil in this model. The lower the flow resistivity (or the higher the air permeability), the lower is the acoustical surface impedance [33].

The D&B model is often used for other soil types based on acoustically deduced effective flow resistivity values [34]. Attenborough et al. have shown that more detailed models are needed to acoustically characterize non-grassland grounds [e.g. 35]. An example of such a model is the 4-parameter model [36]. The ground is acoustically described by its flow resistivity, porosity of the air-filled pores, the pore shape factor and the turtuosity. Typical values for various types of soils can be found. Some approximations of this model, like e.g. the 3-parameter model and the 2-parameter model, are proposed.

As illustrated, a lot of information is available for the calculation of the reflection from natural ground surfaces in frequency-domain. Besides impedance models, techniques to deduce ground impedance from measurements are numerous [e.g. 37].

Different approaches for the simulation of reflection from natural grounds in a time-domain method are possible. A first possibility is the transformation of a complex frequency-dependence to a time-domain function. However, to account for a fully general frequency-dependent impedance, the calculation of a convolution in time-domain for each time-step and for each point on the boundary is needed. This is of course very computational costly, since also a long integration time is needed to ensure accuracy.

In Ref [38] an approximation is developed for the simulation of typical absorbing boundary conditions at low frequencies encountered in room acoustics. This approach uses a single integration in time. The complex impedance of the form

$$Z(\omega) = Z_0 + Z_1 j\omega + \frac{Z_{-1}}{j\omega}, \tag{2.68}$$

where j equals $\sqrt{-1}$, can be fitted in the *FDTD* calculation scheme. The second term in equation (2.68) corresponds to a time-derivative, while the third term can be approximated by integration in time. Both can easily be discretised. A complex impedance for a single frequency can be simulated. The imaginary part of the impedance is frequency-dependent, while the real part is independent of frequency. The acoustic impedance of most natural grounds has an imaginary part as well as a real part that is inversely proportional to the frequency. So this model should be extended. This will make it necessary to solve multiple integrals in time-domain. Since this approach is expected to be numerical inefficient, it is not further investigated. Using digital filter theory could approximate the calculation of these integrals in time-domain. A reduced computational effort will be obtained, however with loss of accuracy.

A third approach to simulate reflection from a soil in a time-domain model is including the ground medium in the calculation domain [18, 39, 40]. This means that sound propagation in the ground itself needs to be described. Such a ground model can be categorized as non-locally reacting.

A possible approach is considering ground as a poro-elastic medium. This is done e.g. in references [39] and [41]. In more simple models, only the air in between the ground particles vibrates, while the particles form a rigid frame. Zwikker and Kosten propose such a poro-rigid model. In the latter, the ground is described by three parameters: flow resistivity (R), porosity (φ) and the structure factor (k_s). The linear equations for sound propagation in a porous medium, assuming a rigid frame, are:

$$\nabla \cdot p + \rho' \frac{\partial \boldsymbol{v}}{\partial t} + R\boldsymbol{v} = 0\,, \tag{2.69}$$

$$\frac{\partial p}{\partial t} + \rho' c'^2 \nabla \cdot \boldsymbol{v} = 0\,, \tag{2.70}$$

$$\rho' = \frac{\rho_0 k_s}{\varphi}\,, \tag{2.71}$$

$$c' = \frac{c}{\sqrt{k_s}}\,. \tag{2.72}$$

In these equations, a damping term is introduced, based on the flow resistivity. The mass density of the soil (ρ') and the speed of sound in the ground (c') are adapted using the porosity and structure factor of the ground. The structure factor is a parameter that can be adapted to account for the specific structure of the pores in the ground. Experimental values range from 3 to 7 [42]. The previous equations reduce to free sound propagation in air when $k_s = 1$, $\varphi = 1$ and $R = 0$.

It can be derived that the normalized, acoustic impedance of a medium obeying equations (2.69), (2.70), (2.71) and (2.72) equals:

$$\frac{Z}{Z_0} = \sqrt{\frac{R}{\rho\omega\varphi} j + \frac{k_s}{\varphi^2}}\,. \tag{2.73}$$

The (complex) wave number inside the ground on the other hand is:

$$k = \frac{\omega}{c}\sqrt{\frac{R\varphi}{\rho\omega}j + k_s}\ . \tag{2.74}$$

The impedance of the Zwikker and Kosten model (2.73) is similar to the frequency-impedance relation of many natural ground surfaces. In Ref. [18] sound propagation over flat ground is simulated using the above described ground model in a similar finite-difference time-domain implementation. It was concluded that results are in good agreement with solutions of the Helmholtz equation in frequency-domain.

These linear equations are easy to discretise in the finite-difference time-domain scheme. Linear interpolation in time is used for the discretisation of the damping term in the velocity equation. The discrete velocity and pressure equation for sound propagation inside the ground are:

$$v^{l+0.5}_{\alpha(\alpha+0.5)} = \frac{(1-G)}{(1+G)}v^{l-0.5}_{\alpha(\alpha+0.5)} - \frac{\varphi}{(1+G)k_s}\frac{dt}{\rho_0}\left[\frac{p^l_{(\alpha+1)} - p^l}{d\alpha}\right], \tag{2.75}$$

with

$$G = 0.5\frac{Rdt\varphi}{\rho_0 k_s}, \tag{2.76}$$

$$p^{l+1} = p^l - \frac{c^2\rho_0}{\varphi}dt\sum_{\beta}\left(\frac{v^{l+0.5}_{\beta(\beta+0.5)} - v^{l+0.5}_{\beta(\beta-0.5)}}{d\beta}\right). \tag{2.77}$$

As stated before, each cell can have its own propagation equation and acoustic properties in the object-orientated implementation. Effects like compacting of soils can be easily modelled by increasing e.g. porosity with depth within the ground.

It is assumed that the physical, acoustic boundaries are impermeable for the background flow, which is a good approximation for most applications. Therefore, the background flow is parallel to these boundaries. It is further assumed that the flow has no influence on the acoustic impedance.

The accuracy of reflection from the ground is now investigated in a simple test. A plane wave, normal incident on a few ground cells is simulated. Based on the incident and ground-reflected pulse, the complex acoustic impedance of the soil is calculated. In Figure 2.10, a comparison between the acoustic impedance as

obtained by the *FDTD* simulation and the analytical impedance is made, with decreasing spatial discretisation step. The real part, the imaginary part and the magnitude of the normalized, complex impedance are considered separately. It is important to finely discretise the computational grid, normal to the interface between the soil and the air, to have a good correspondence in the full frequency range considered. In each simulation, the Courant number equals 1. With increasing magnitude of the impedance, a finer grid will be needed.

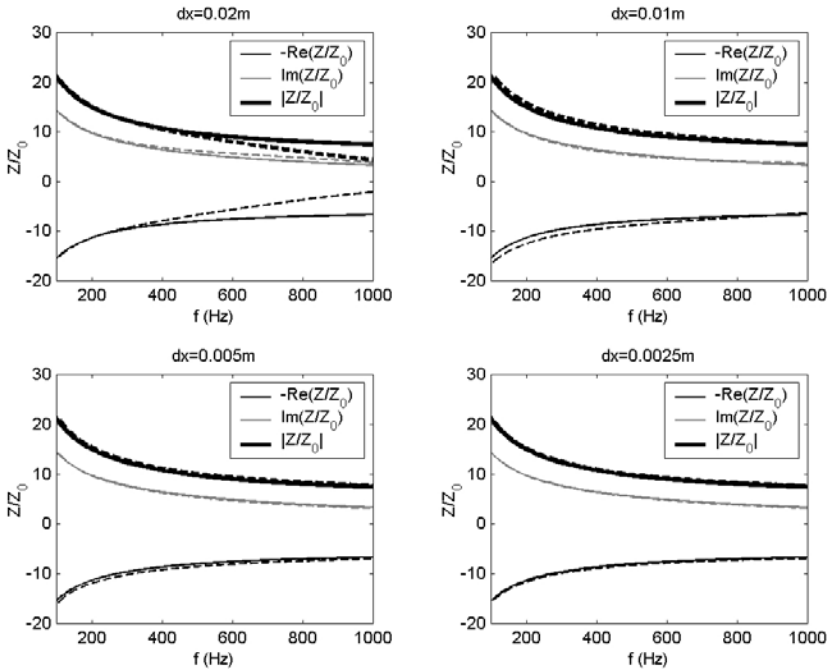

Figure 2.10 Comparison between the numerically obtained (dashed lines) and analytical (full lines) complex impedance. The real part (Re), imaginary part (Im) and the magnitude (| |) are compared. Following set of ground parameters is used: k_s =3, φ = 0.3 and R= 100 kPa s/m^2.

In practical applications, the discretisation needed at the interface between soil and air is too fine and therefore too computational costly to be used in the rest of the computational grid. For efficient calculations, a non-uniform grid is needed. Only in the direction, orthogonal to the ground surface, refinement is applied. More information on the refinement strategy is found in Chapter 2.2.9. Refining the coordinate direction parallel to the interface is far less important as to ground

reflection. In Figure 2.11, a typical grid near the interface air-ground is shown. To prevent numerical reflection when sound propagates through multiple refined layers, a gradual transition between the largest and the smallest cells is applied. However, since the time discretisation step is kept constant in the grid, the ratio between the spatial discretisation steps in both grids should be small. The fine grid determines the time step for stability reasons. As a result, the Courant number in the coarse grid will be smaller than unity and the phase error increases.

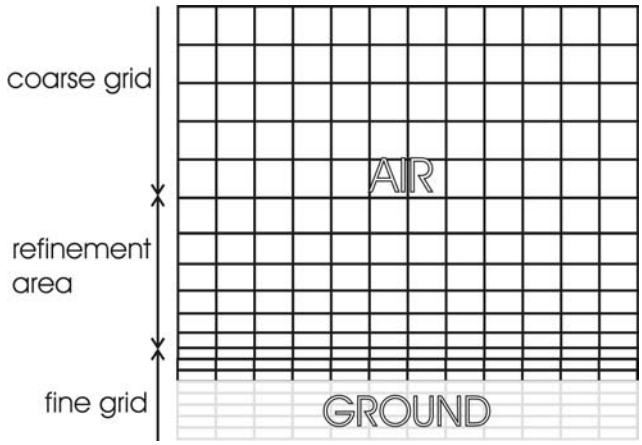

Figure 2.11 Grid refinement near the interface air-ground, along one coordinate axis.

2.3.2 Perfectly Absorbing Boundaries (*PAB*)

The calculation domain is often not physically bounded, e.g. in outdoor sound propagation simulations. The unlimited propagation region has to be truncated to limit the simulation domain. This truncation may not influence the acoustic calculations: reflections are not allowed. So-called "perfectly absorbing boundary" conditions must be applied at the border of the simulation grid.

For some special cases, the need for *PABs* can be circumvented by working with a short, broadband pulse. The reflections from the non-physical boundaries need to be removed from the time-domain signal. An important condition is that the non-physical boundaries and points of interest are sufficiently apart from each other so there is no overlap between signal of interest and unwanted reflections. Sound propagation over flat ground without screens [18] and the use of a single noise barrier are examples for which this method can be used. A case of interest, namely a sound source in between two noise barriers, as often encountered in

traffic noise situations, needs the application of *PABs*. Multiple reflections between the barriers will otherwise interfere with reflections from boundaries, resulting in inaccurate calculations. For simulations in which impulse responses are long, it is almost impossible (with respect to computational resources) to keep extending the simulation domain to prevent that reflections arrive at the receiver before the relevant signal has completely damped out.

2.3.2.a First-order approximation

A first-order approximation for the *PAB* in a background flow is introduced. For the acoustic field quantities we assume

$$p = Z_0 v_n \,, \tag{2.78}$$

$$Z_0 = \rho c \,, \tag{2.79}$$

where v_n is the orthogonal component of the particle velocity on the *PAB* (pointing outward), and Z_0 is the characteristic impedance of air. Since there is no difference in acoustic impedance between the propagating medium and the border, reflection is absent (in theory) for a normal incidence plane wave.

It is assumed that the background flow is orthogonal to the *PAB*, but not necessarily uniform. Both assumptions correspond well to practical situations like inflow and outflow in ducts, or linear or logarithmic wind speed profiles outdoors.

No gradients in the background flow normal to the *PAB* are assumed. Let the boundary be orthogonal to direction α and situated at position $\alpha+0.5$. So equation (2.58), applicable to parallel flow, can be used as a starting point. To discretise pressure gradients on the border, some adaptations have to be made since pressure is not known outside the simulation region. For a right boundary, assuming the α-axis is running from left to right, following approximation is used:

$$\frac{p^l_{(\alpha+1)} - p^l}{d\alpha} \approx \frac{p^l_{(\alpha+0.5)} - p^l}{0.5 d\alpha} \,. \tag{2.80}$$

However $p^l_{(\alpha+0.5)}$ does not fit the calculation grid. To express it as a function of the known velocity in this point, a condition for perfect absorption is introduced.

To discretise the velocity in equation (2.78), not only the known velocity at time *(l-0.5) dt* is used, but also the unknown velocity at time *(l+0.5) dt*:

$$p^{l}_{(\alpha+0.5)} = Z_0\left(\frac{v^{l+0.5}_{\alpha(\alpha+0.5)} + v^{l-0.5}_{\alpha(\alpha+0.5)}}{2}\right). \tag{2.81}$$

This linear interpolation in time improves stability and accuracy. The third term of equation (2.58) is approximated by:

$$\frac{\partial \chi^{l}_{\alpha(\alpha+0.5)}}{\partial \alpha} = \frac{\chi^{l}_{\alpha(\alpha+0.5)} - \chi^{l}_{\alpha(\alpha-0.5)}}{d\alpha}, \tag{2.82}$$

since χ is not know outside the simulation region.

Using equations (2.80), (2.81) and (2.82) in equation (2.58) results, after some calculations, in the discrete *PAB* equation for a right border:

$$v^{l+0.5}_{\alpha(\alpha+0.5)}\left(1+\frac{dtZ_0}{d\alpha\rho_0}\right) = v^{l-0.5}_{\alpha(\alpha+0.5)}\left(1-\frac{dtZ_0}{d\alpha\rho_0}\right)$$

$$-dt\sum_{\beta\neq\alpha}\left[\frac{\left(\chi^{l}_{\beta(\beta+0.5)} + \chi^{l}_{\beta(\beta-0.5)}\right)}{2}\,\frac{\left(v_{0\alpha(\alpha+0.5,\beta+1)} - v_{0\alpha(\alpha+0.5,\beta-1)}\right)}{2d\beta}\right] \tag{2.83}$$

$$-dtv_{0\alpha(\alpha+0.5)}\left(\frac{\chi^{l}_{\alpha(\alpha+0.5)} - \chi^{l}_{\alpha(\alpha-0.5)}}{d\alpha}\right) + \left[\frac{2dt}{d\alpha\rho_0}\right]p^{l}.$$

For the left border, a similar equation may be obtained. The calculation of χ on the border itself is described is Chapter 2.3.3.

The first-order approximation is computational efficient, since the simulation domain does not need to be extended. However, simulations will show that the accuracy of this first-order approximation is limited. More accurate *PAB* conditions like perfectly matched layers, part of the family of damping layers, will be often necessary.

2.3.2.b Perfectly Matched Layer (*PML*)

Very good *PABs* namely the "Perfectly Matched Layers" were developed by Berenger [43] for electromagnetic *FDTD* simulations. *PMLs* have shown to be very useful for the acoustic finite-difference time-domain method too (e.g. [44, 45]). In References [46] and [47], the *PML* theory is applied to absorb acoustic, vorticity and entropy waves, supported by the linearised Euler (*LE*) equations in

uniform mean flow. These equations were developed for large Mach number-flow simulations that use the *LE* equations in its original form.

It is known that the theoretical reflection coefficients at the interface between the (physical) computational domain (=interior domain) and the *PMLs* are zero, independent of the angle of incidence and frequency of the waves. When applying a *PML* (or Berenger boundary condition), the simulation domain has to be extended with a limited number of cells, in which a non-physical propagation occurs. These extra cells describe sound propagation in a strongly, (artificially) damping medium. For the calculation of sound propagation inside the Berenger layer, damping coefficients κ are introduced in the acoustic equations. The derivation of the *PML* equations in this work assumes a uniform background flow, normal (= direction α) to the interface between the *PML* and propagating medium:

$$\frac{\partial p_{\perp}}{\partial t} + c^2 \rho_0 \frac{\partial v_{\alpha}}{\partial \alpha} + V_{0\alpha} \frac{\partial p_{\perp}}{\partial \alpha} + \kappa_{1,\perp} p_{\perp} = 0 , \tag{2.84}$$

$$\frac{\partial p_{//}}{\partial t} + c^2 \rho_0 \sum_{\gamma \neq \alpha} \frac{\partial v_{\gamma}}{\partial \gamma} + V_{0\alpha} \frac{\partial p_{//}}{\partial \alpha} + \kappa_{1,//} p_{//} = 0 , \tag{2.85}$$

$$p_{\perp} + p_{//} = p , \tag{2.86}$$

$$\rho_0 \left[\frac{\partial v_{\alpha}}{\partial t} + V_{0\alpha} \frac{\partial v_{\alpha}}{\partial \alpha} \right] + \frac{\partial p}{\partial \alpha} + \kappa_{2,\perp} v_{\alpha} = 0 , \tag{2.87}$$

$$\rho_0 \left[\frac{\partial v_{\beta}}{\partial t} + V_{0\alpha} \frac{\partial v_{\beta}}{\partial \alpha} \right] + \frac{\partial p}{\partial \beta} + \kappa_{2,//} v_{\beta} = 0 , \beta \neq \alpha . \tag{2.88}$$

In the previous equations, the acoustic pressure is split in two artificial components: one normal to the Berenger-interface ($p_{\perp}$), and the other component parallel to the interface ($p_{//}$). This is called the split-field approach and results in an additional degree of freedom. The latter is necessary since perfect matching is otherwise only obtained for normal incidence [43]. In contrast to the derivation in Ref. [46], and following the original theory presented by Berenger [43] applied to the acoustic field, the components of the velocity are not split. This extra splitting, besides the splitting of the pressure, should result in improved accuracy. However, it will be shown that the *PMLs* derived in this chapter are already sufficiently non-reflecting. It was shown however that this splitting of the physical quantities could result in instability, especially for high Mach number flows [48]. In Ref. [47], a *PML* is developed

only in un-split variables, resulting however in complicated equations to be solved.

In the pressure equations, damping coefficients $\kappa_{1,\perp}$ and $\kappa_{1,//}$ are introduced, respectively for the component orthogonal and parallel to the Berenger interface. In the equation for the velocity component normal to the interface and in the direction of the flow, $\kappa_{2,\perp}$ is used. In the velocity equations parallel to the Berenger boundary, a damping coefficient $\kappa_{2,//}$ is added.

In opposition to the derivation of the equations for sound propagation in background flow, the Berenger medium needs to be anisotropic: damping depends on the angle of incidence. This condition is necessary to find proper conditions for the damping coefficients in the Perfectly Matched Layer. This means that the assumption concerning the rotor of the acoustic velocity (2.18) is not used during the derivation. As a result, the equation for the acoustic velocity in direction β ($\neq\alpha$), orthogonal to the direction of the flow, changes slightly: the derivative of v_α to β is changed by the derivative of v_β to α in the term that contains $V_{0\alpha}$ in equation (2.88). Equations (2.87) and (2.88) could be derived from equation (2.57), taking into account that only uniform background flow is considered here.

In the next pages, the conditions for the damping coefficients to obtain perfect matching are investigated. For more clarity, two-dimensional sound propagation is considered. It will be shown however that there are only conditions for the coordinate directions normal to the interface between the interior domain and the *PMLs*.

Conditions for perfect matching

A first condition that needs to be satisfied is continuity on the interface between the interior cells and the *PML* cells. A plane wave in a uniform background flow V_0, incident under an angle θ relative to the normal on the interface (direction α) for a co-moving observer, can be written as:

$$v_\alpha = v_{0,\alpha} e^{-jk\cos\theta(\alpha - V_{0\alpha}t) - jk\sin\theta\beta} e^{-j\omega t}, \tag{2.89}$$

$$p = p_0 e^{-jk\cos\theta(\alpha - V_{0\alpha}t) - jk\sin\theta\beta} e^{-j\omega t}. \tag{2.90}$$

The relation between the amplitude of the acoustic velocity and acoustic pressure outside the Berenger layer follows directly from equation (2.61):

$$v_{0,\alpha} = -\frac{k\cos\theta}{\rho_0\omega} p_0 \,. \tag{2.91}$$

An analogous plane wave in the Berenger layer is defined as:

$$v_{\alpha,PML} = Tv_{0,\alpha} e^{-jk\cos\theta(\alpha - V_{0\alpha}t) - jk\sin\theta\beta - \gamma_\alpha(\alpha - V_{0\alpha}t) - \gamma_\beta\beta} e^{-j\omega t}, \tag{2.92}$$

$$p_{PML} = Tp_0 e^{-jk\cos\theta(\alpha - V_{0\alpha}t) - jk\sin\theta\beta - \gamma_\alpha(\alpha - V_{0\alpha}t) - \gamma_\beta\beta} e^{-j\omega t}, \tag{2.93}$$

where T is the transmission coefficient. For full transmission, T equals one. The parameters γ_α and γ_β are the damping coefficients along the two coordinate axes.

The relation between the amplitude of the acoustic velocity and pressure inside the Berenger layer is calculated by inserting equations (2.92) and (2.93) in equation (2.87). Following relation is found:

$$v_{0,\alpha} = \frac{\left(jk\cos\theta + \gamma_\alpha\right)}{\left(-j\omega\rho_0 + \kappa_{2,\perp}\right)} p_0 \,. \tag{2.94}$$

Analogous, the amplitude of the acoustic velocity in the directions parallel to the interface is:

$$v_{0,\beta} = \frac{\left(jk\sin\theta + \gamma_\beta\right)}{\left(-j\omega\rho_0 + \kappa_{2,//}\right)} p_0 \,. \tag{2.95}$$

The amplitude of the (normal) acoustic velocity on the interface between the interior cells and Berenger cells is the same. Using equations (2.91) and (2.94) gives following relation:

$$-\frac{k\cos\theta}{\rho_0\omega} = \frac{\left(jk\cos\theta + \gamma_\alpha\right)}{\left(-j\omega\rho_0 + \kappa_{2,\perp}\right)}, \tag{2.96}$$

which will be used further in the search for conditions of the damping terms.

In a second part of this derivation, the relation between the (artificial) components of the acoustic pressure in the *PML* and the other parameters involved are analysed. The components of the pressure waves inside the absorbing medium in background flow, incident under an angle θ for a co-moving observer can be written as:

$$p_{\perp,PLM} = p_{0,\perp} e^{-jk\cos\theta(\alpha - V_{0\alpha}t) - jk\sin\theta\beta - \gamma_\alpha(\alpha - V_{0\alpha}t) - \gamma_\beta\beta} e^{-j\omega t}, \tag{2.97}$$

$$p_{//,PLM} = p_{0,//} e^{-jk\cos\theta(\alpha - V_{0\alpha}t) - jk\sin\theta\beta - \gamma_\alpha(\alpha - V_{0\alpha}t) - \gamma_\beta\beta} e^{-j\omega t}. \tag{2.98}$$

Introduction of (2.97) and (2.92) in the orthogonal pressure equation (2.84) gives following relation in frequency-domain. The amplitude of the acoustic velocity normal to the interface is replaced according to equation (2.94):

$$\left(-j\omega + \kappa_{1,\perp}\right) p_{0,\perp} - c^2\rho_0 \frac{\left(jk\cos\theta + \gamma_\alpha\right)^2}{\left(-j\omega\rho_0 + \kappa_{2,\perp}\right)} \left(p_{0,\perp} + p_{0,//}\right) = 0. \tag{2.99}$$

A second condition is found based on equation (2.85). The parallel pressure wave equation (2.98) is used, in combination with equation (2.95). This results in:

$$\left(-j\omega - \gamma_\alpha V_{0\alpha} + \kappa_{1,//}\right) p_{0,//} - c^2\rho_0 \frac{\left(jk\sin\theta + \gamma_\beta\right)^2}{\left(-j\omega\rho_0 - \gamma_\alpha\rho_0 V_{0\alpha} + \kappa_{2,//}\right)} \left(p_{0,\perp} + p_{0,//}\right) = 0. \tag{2.100}$$

Equations (2.99) and (2.100) form a homogenous set of equations:

$$\begin{bmatrix} \left(-j\omega + \kappa_{1,\perp}\right) - c^2\rho_0 \dfrac{\left(jk\cos\theta + \gamma_\alpha\right)^2}{\left(-j\omega\rho_0 + \kappa_{2,\perp}\right)} & -c^2\rho_0 \dfrac{\left(jk\cos\theta + \gamma_\alpha\right)^2}{\left(-j\omega\rho_0 + \kappa_{2,\perp}\right)} \\ -c^2\rho_0 \dfrac{\left(jk\sin\theta + \gamma_\beta\right)^2}{\left(-j\omega\rho_0 + \kappa_{2,//}\right)} & \left(-j\omega + \kappa_{1,//}\right) - c^2\rho_0 \dfrac{\left(jk\sin\theta + \gamma_\beta\right)^2}{\left(-j\omega\rho_0 + \kappa_{2,//}\right)} \end{bmatrix} \begin{bmatrix} p_{0,\perp} \\ p_{0,//} \end{bmatrix} = 0 \tag{2.101}$$

To have a solution different from the zero-solution (p_0=0), the determinant of the coefficient-matrix must equal zero. When developing this determinant, one gets the following equation:

$$\left(-j\omega + \kappa_{1,\perp}\right)\left(-j\omega + \kappa_{1,//}\right) - \frac{c^2\rho_0\left(-j\omega + \kappa_{1,//}\right)}{\left(-j\omega\rho_0 + \kappa_{2,\perp}\right)}\left(-k^2\cos^2\theta + 2\gamma_\alpha jk\cos\theta + {\gamma_\alpha}^2\right)$$

$$- \frac{\left(-j\omega + \kappa_{1,\perp}\right)c^2\rho_0}{\left(-j\omega\rho_0 + \kappa_{2,//}\right)}\left(-k^2\sin^2\theta + 2\gamma_\beta jk\sin\theta + {\gamma_\beta}^2\right) = 0. \tag{2.102}$$

In this equation, γ_α and γ_β must tend to zero to obtain perfect absorption, since every change in the impedance of the medium in which sound propagates results

in reflection. This means that the k^2-term is dominant to the other terms in the second and third term on the left hand side. So equation (2.102) simplifies to equation (2.103), taking into account the continuity condition on the interface (2.96):

$$\left(-j\omega+\kappa_{1,\perp}\right)\left(-j\omega+\kappa_{1,//}\right)+\left(-j\omega+\kappa_{1,\perp}\right)\left[c^2\rho_0\frac{k^2\sin^2\theta}{\left(-j\omega\rho_0+\kappa_{2,//}\right)}\right]$$

$$\left[-c^2k^2\frac{\cos^2\theta}{\omega^2\rho_0}\right]\left(-j\omega+\kappa_{1,//}\right)\left(-j\omega\rho_0+\kappa_{2,\perp}\right)=0 \quad (2.103)$$

Possible conditions for the damping coefficients in a perfectly matched layer must be independent of the angle of incidence θ. So this variable may not determine the solution of equation (2.103). This can be achieved when using the following goniometric identity: $\sin^2\theta+\cos^2\theta=1$.

In order to be able to eliminate the angle of incidence in equation (2.103), the coefficients of the terms that contain $sin^2\theta$ and $cos^2\theta$ must be equal:

$$\left(-j\omega+\kappa_{1,\perp}\right)\left[\frac{c^2\rho_0k^2}{\left(-j\omega\rho_0+\kappa_{2,//}\right)}\right]=\left[\frac{-c^2k^2}{\omega^2\rho_0}\right]\left(-j\omega+\kappa_{1,//}\right)\left(-j\omega\rho_0+\kappa_{2,\perp}\right). \quad (2.104)$$

Working this out and grouping the relevant variables, the following conditions have to be satisfied:

$$\begin{cases}\kappa_{2,\perp}+\kappa_{2,//}+\kappa_{1,//}\rho_0-\rho_0\kappa_{1,\perp}=0 & \rightarrow\omega^2\\ \kappa_{1,//}\left(\kappa_{2,\perp}+\kappa_{2,//}\right)+\dfrac{\kappa_{2,//}\kappa_{2,\perp}}{\rho_0}=0 & \rightarrow j\omega\\ \kappa_{1,//}\kappa_{2,//}\kappa_{2,\perp}=0 & \rightarrow cst\end{cases} \quad (2.105)$$

A solution of this set of equations is:

$$\kappa_{2,//}=\kappa_{1,//}=0, \quad (2.106)$$

$$\kappa_{1,\perp}=\frac{\kappa_{2,\perp}}{\rho_0}. \quad (2.107)$$

The damping terms in the parallel pressure equation and parallel velocity equation must equal zero. The relation between the damping terms in the

orthogonal velocity equation and orthogonal pressure equation is the mass density of the interior domain. A (theoretical) perfectly matched layer is obtained when taking into account conditions (2.106) and (2.107). This condition is independent of the angle of incidence and frequency of the incident wave. For simplicity, following notations will be used further in this work: $\kappa_1 = \kappa_{1,\perp}$ and $\kappa_2 = \kappa_{2,\perp}$.

The conditions to obtain perfect matching do not depend on the uniform background flow in our approach. When the direction of the uniform background flow and the normal on the interface between the interior cells and the *PML* cells is not the same, straightforward changes to the velocity equations (2.87) and (2.88) must be made. The damping term is simply added to the equation for the velocity component normal to the interface.

Only the situations where there is an interface between the interior domain and the *PMLs* are considered. Near the corners of a grid, there will also be a *PML-PML* interface. It is found that when using a sufficient number of cells to form the *PML*, it is not necessary to consider corners as a different case in our applications. The *PML* of one of the directions is used towards the borders of the grid.

Discrete expression to calculate the quantities χ and ξ when perfectly matched layers are involved, are given in Appendix A.

PML in discrete FDTD grid

When obeying the conditions for perfect matching, there will be no reflection in theory. In a discrete *FDTD* grid however, some numerical reflection is observed because of the abrupt change in damping between field cells and *PML* cells, and by the truncation of the grid. To minimize the discontinuity at the interface, Berenger [49] proposed to gradually change the material parameters along the normal axis on the interface, according to

$$\kappa_1(x) = \kappa_{1,MAX}\left(\frac{x}{d_{PML}}\right)^m, \tag{2.108}$$

where x is the depth inside the layer normal to the interface and d_{PML} is the total thickness of the *PML*. It was found by Berenger that the parameter m is preferably chosen between 3 and 4 [49]. In Reference [44], a value of 4 resulted in the best performance. Liu et al. [45] found that for *PMLs* consisting of about

10 cells, a quadratic profile for the damping coefficients gives a better absorption than a linear one.

Performance of PML

In this part, the performance of the *PML* is examined and the parameters involved are analysed. Simulations are performed both in absence and presence of background flow. For most simulations, a normal incident plane wave is used in a two-dimensional grid (see Figure 2.12). When reflection from the *PML* with increasing angle of incidence is analysed, a large two-dimensional grid is used in which a point source is situated (see Figure 2.12). The *PML* is bordered by a perfectly reflecting plane at the end.

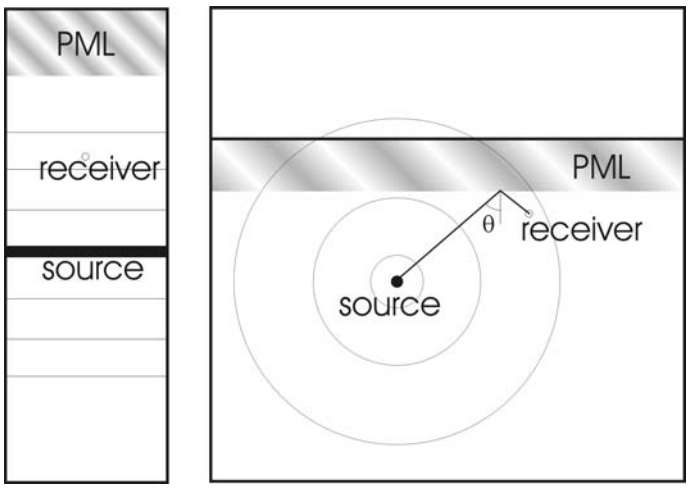

Figure 2.12 Overview of the grid for sound propagation respectively normal incident and incident under an angle θ on the *PML*.

In all cases, except when the influence of the frequency is investigated, the source emits a Gaussian wavelet, with a centre frequency f_c of 500 Hz and a bandwidth BW of 150 Hz:

$$p = A\sin\left(2\pi f_c t\right)e^{-\frac{(t_0-t)^2}{\sigma}}, \tag{2.109}$$

$$BW = \frac{1}{2\sqrt{\sigma}}, \tag{2.110}$$

where A is the amplitude of the emitted signal, t_0 is a time delay, and σ is a parameter linked to the length of the signal. The Courant number equals 1 in all the simulations.

The performance of the *PML* is quantified by the reflection coefficient R_{PAB}:

$$R_{PAB} = 10 \log_{10} \left[\frac{\sum_{pulse} p_{refl}^2}{\sum_{pulse} p_{ref}^2} \right], \tag{2.111}$$

where p_{refl} is the amplitude of the acoustic pressure of the pulse reflected from the *PAB*, and p_{ref} is the incident pulse on the *PAB* (or reference pulse). The total energy of the incident and reflected pulse is considered for the calculation of the reflection coefficient. For the plane wave configuration, geometrical divergence is zero. The incident and reflected pulse can be measured at the same location and the reflection coefficient can be calculated after separating the pulses in the time signal. When using a point source in a two-dimensional grid, there will be some geometrical divergence. The difference in the decrease of amplitude of the reference pulse and the *PML*-reflected pulse is kept as low as possible by limiting the difference in travel distance. For that purpose, the receptor points are placed very close to the *PML*. Two simulations are necessary. A first simulation is performed in the presence of the *PML*. To obtain the reference signal, a large grid is used with the simulation borders far away from the receiver. Both time responses have to be distracted from each other to find the *PML*-reflected pulse.

2.3.2.b..1 κ_1 *and* m

In a first set of simulations, an optimal set of the damping parameter κ_1 and scaling parameter m is sought in absence of background flow. A plane wave, normal incident on the interface between the Berenger layer and the interior domain is considered. The *PML* consists of 20 computational cells. In Figure 2.13, the reflection coefficient is shown for 3 values of the scaling parameter, with increasing values for κ_1. Optimal performance for this *PML* is found for m close to 4. With decreasing values of m, the minimum in reflection is more pronounced. For values of κ_1 smaller than the optimal value, a steep slope is observed. Once passed this minimum, performance stays approximately constant, especially for large values of m.

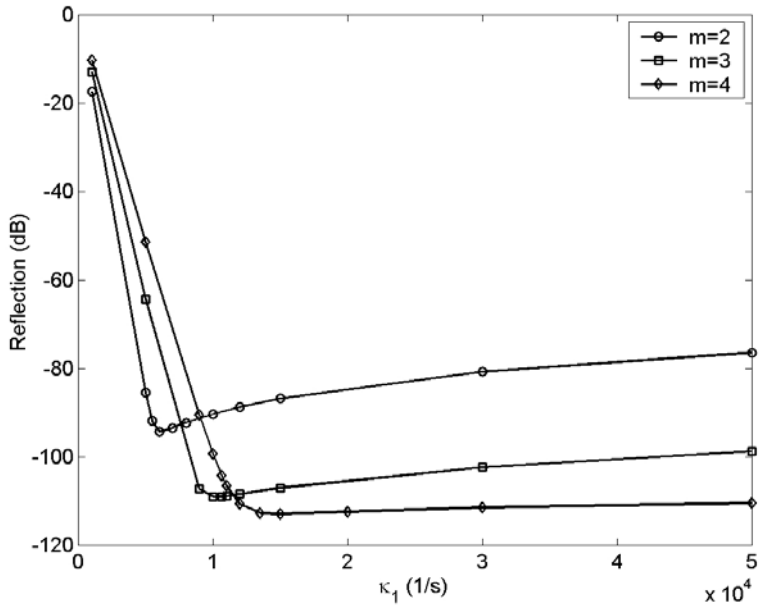

Figure 2.13 Reflection from the *PML* with increasing value of the damping coefficient κ_1, for different scaling parameters *m*.

At other frequencies, this same behaviour is found. From Figure 2.14, it can be concluded that the efficiency of the *PML* is independent of the frequency of the incident (plane) wave. An optimal value for κ_1 was found at each frequency. The graphs in Figure 2.14 are indicated with the central frequencies of the different Gaussian pulses that were used. The bandwidth of each signal was 10 % of the central frequency. The *PML* consists in all cases of 20 computational cells. The scaling parameter *m* is kept constant at 3. Simulations are performed for a Courant number equal to 1, and 10 cells per wavelength were used. It can also be observed that optimal values for the damping coefficient are almost proportional to the frequency under investigation.

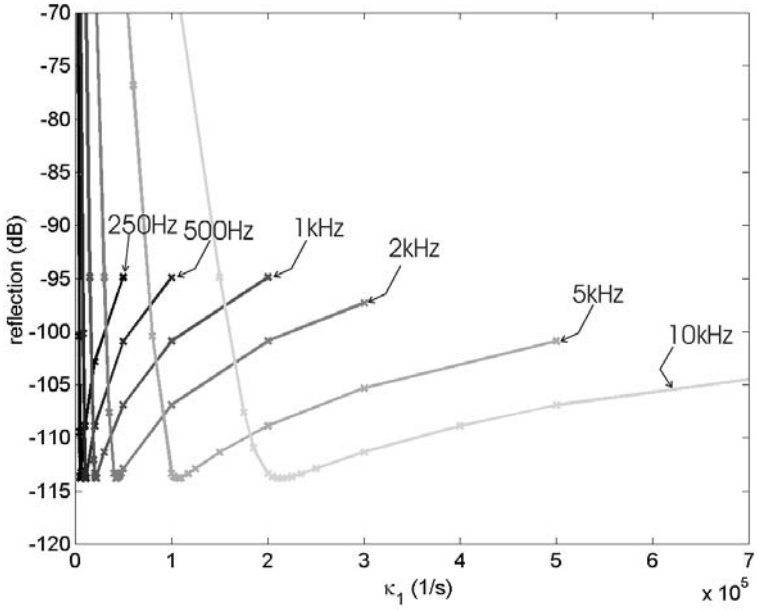

Figure 2.14 Reflection from the *PML* with increasing value of the damping coefficient κ_1, for frequencies ranging from 250 Hz to 10 kHz. The scaling parameter *m* equals 3.

2.3.2.b..2 Angle of incidence and number of cells in PML

It is investigated how the *PML* behaves when the thickness of the layer is increased, in combination with various angles of incidence θ. In outdoor sound propagation simulations, oblique incident sound waves on *PABs* are often present. Receivers are close to the ground, while sound propagation needs to be calculated over long distances. As a result, the height of the computational grid must be as low as possible considering computational resources. In the presence of flow however, one needs to make the simulation domain sufficiently high in order to take effects from a refracting atmosphere into account. This means that on the top layer *PAB*, the angles of incidence will be large. In theory, the conditions for the damping coefficients are made independent of the angle of incidence. In this chapter, the relation between the angle of incidence and thickness of the *PML* layer in discrete *FDTD* is explicitly investigated.

An overview of the grid set-up is shown in Figure 2.12. *PMLs* with a thickness ranging from 5 grid cells to 40 grid cells are considered. Reflection of sound waves on the first-order approximation *PAB* is also analysed for increasing angles of incidence. Results are shown in Figure 2.15. For each thickness of the

PMLs, an optimal combination of parameters κ_1 and m is sought in order to have a minimal, average reflection for angles between 20 degrees and 80 degrees.

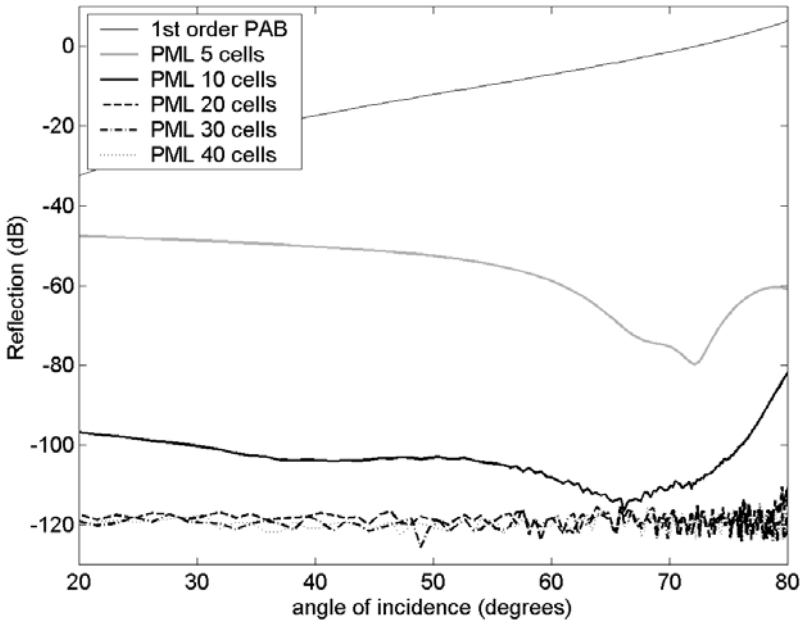

Figure 2.15 Reflection (in dB) from the *PAB* with increasing angle of incidence. The first-order approximation (see Chapter 2.3.2.a) as well as *PMLs* with a thickness of 5, 10, 20, 30 and 40 grid cells are used.

In Figure 2.15, the first-order approximation *PAB* is shown to be of limited practical use. The main reason that this kind of absorbing boundary is considered is that the simulation domain does not need to be extended and fine-tuned. As a result, this is a computational cheap method and easy to apply. For normal incidence, a decrease in reflection of about 40 dB is obtained. With increasing angle of incidence, the reflection from this boundary increases. In this approach (see Chapter 2.3.2.a), only the normal component to the boundary is absorbed. It was found experimentally that an optimised *PML* consisting of only 2 cells has yet a better overall performance in the range of angles of incidence considered.

Using the Berenger theory, the performance of the *PAB* is increased by some orders of magnitude, starting from a thickness of about 10 cells. With an increasing number of cells, the performance of the *PML* increases. Starting from

20 cells, only very small improvements are possible by further increasing the number of cells. For a thickness larger than 30 computational cells, a reduction in reflection of 120 dB is achieved for all the angles of incidence considered. For reflection coefficients lower than –100 dB, signals become noisy. The amplitudes in these cases are very low, and even the smallest numerical inaccuracy results in irregular curves. For the layers consisting of 5 and 10 cells, there is an important variation in the reflection coefficient with increasing angle of incidence. This is caused by the fact that the transmitted wave in the *PML* is not sufficiently damped when it reaches the perfectly reflecting plane behind the *PML*. As a result, this wave reflects on the hard material and re-enters the interior field. There will be interference with the wave that is reflected at the interface between the *PML* and the field cells.

2.3.2.b..3 PML in uniform background flow

The performance of the Berenger boundary condition in increasing uniform background flow, normal to the Berenger interface, is examined. Optimal values for both the damping coefficients and scaling parameter are used for a *PML* consisting of 20 computational cells, in absence of flow. In Figure 2.16, the increase in reflection coefficient by the uniform flow ΔR_u is shown. The latter is defined as the reflection coefficient in a uniform background flow minus the reflection coefficient in absence of flow.

Introducing a uniform background flow does not result in a large decrease of the *PML* performance. For wind speeds encountered outdoors, effects are well below 2 dB. The reason for this decrease in performance should not be attributed in first place to the behaviour of the Berenger layer itself. This effect is caused by the use of a prediction step (in absence of flow) in between two time steps in the discretised equations. Detailed information on this topic can be found in Chapter 2.5, dealing with the numerical accuracy of the *FDTD* scheme in background flow.

The question rises whether the *PML* could be further optimised depending on the background flow velocity. The theoretical conditions to obtain a perfect match are shown to be independent of the background flow. Numerical tests indicated that such an optimisation does not result in a significant decrease of the reflection coefficient. Effects are usually lower than 1 dB.

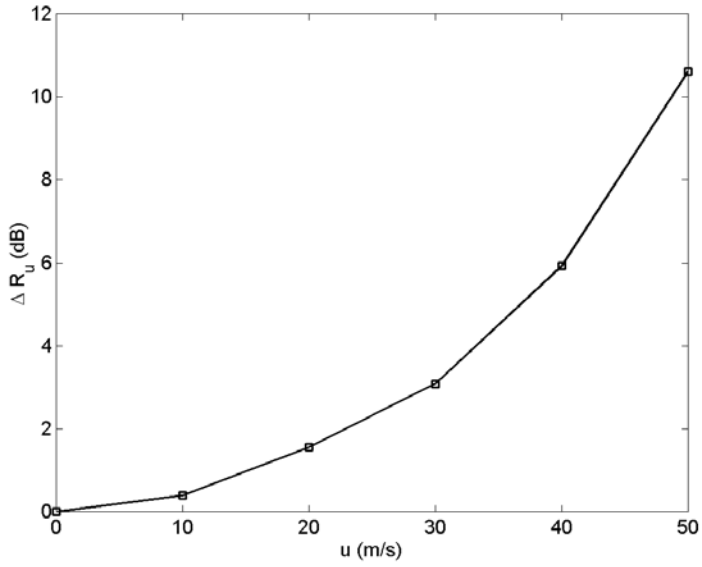

Figure 2.16 Increase in reflection coefficient (dB) by the presence of a uniform background flow.

2.3.2.b..4 PML in non-uniform background flow

Instead of a uniform background flow, a non-uniform background flow, normal to the *PML* interface is investigated. A linear gradient is introduced in the flow. Although the *PML* conditions are derived for a uniform background flow, it is now examined how the uniform flow *PML* behaves when gradients in the background flow are present. A practical case of interest, namely a logarithmic velocity profile, creates large gradients in the background flow, (very) close to the ground surface. $\Delta R_{n\text{-}u}$ is now defined as the reflection coefficient in non-uniform flow (with a certain linear gradient) minus the reflection coefficient in uniform background flow.

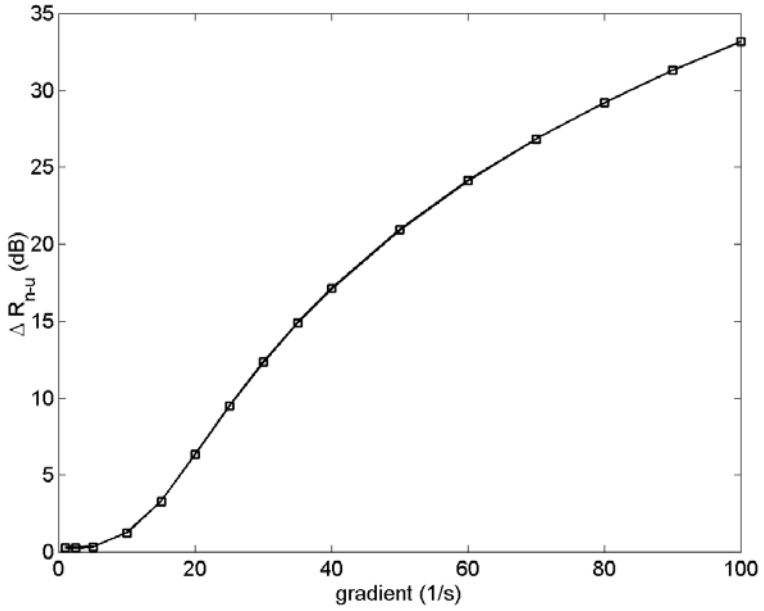

Figure 2.17 Decrease in reflection coefficient (dB) with increasing magnitude of the linear gradient in the background flow, relative to uniform background flow.

It is shown in Figure 2.17 that the decrease in performance of the *PML* is significant in strong gradients. An increase in the reflection coefficient of 35 dB, relative to uniform background flow, is obtained for a strong gradient of 100/s. Such a gradient is typically observed at the first computational cells near the ground surface when there is a logarithmical wind speed profile. When taking e.g. a *PML* of 40 cells, the decrease in reflection will still be larger than 80-90 dB. Already at very limited heights, gradients in a logarithmic profile will become small. It can be concluded that the performance of a *PML*, derived for uniform background flow, decreases with a few orders of magnitude in strongly non-uniform flow. When choosing optimal parameters for the Berenger layers, performance will still be acceptable. In practical situations, very strong gradients in the flow occur at a few places only. As a result, the uniform flow *PMLs* can be used without problems in non-uniform flow.

2.3.3 χ on a border

The calculation of χ on the borders of a simulation region needs to be modified, depending on the type of boundary condition. As an example, the equations for χ at a first-order perfectly absorbing boundary is given below. The pressure gradient in equation (2.54) is discretised in the same way as during the derivation of the *PAB* and gives:

$$\chi^{l}_{\alpha(\alpha+0.5)} = v^{l-0.5}_{\alpha(\alpha+0.5)} - \frac{0.5dt}{\rho_0}\frac{Z_0\chi^{l}_{\alpha(\alpha+0.5)} - p^{l}}{0.5d\alpha}, \tag{2.112}$$

and leads further to

$$\chi^{l}_{\alpha(\alpha+0.5)} = \frac{v^{l-0.5}_{\alpha(\alpha+0.5)}}{\left(1+\frac{Z_0dt}{d\alpha\rho_0}\right)} + \frac{dt}{\left(d\alpha\rho_0 + Z_0dt\right)}p^{l}. \tag{2.113}$$

In Appendix A, an overview of the discrete equations to calculate χ at physical and non-physical borders is given. One has to keep in mind that time-stepping is performed over half a time discretisation step, neglecting all terms in the equations introduced by the background flow.

2.4 Stability considerations

Explicit *FDTD* is not unconditionally stable. It is well known that the Courant number (*CN*, see equation (2.36)) must be smaller than one to guarantee stability in absence of background flow. In the presence of background flow, a general stability condition has not been obtained analytically. Therefore, stability is investigated experimentally. In a one-dimensional simulation space, a Gaussian pulse with centre frequency of 500 Hz and a bandwidth of 250 Hz propagates between a source and a recorder in a uniform background flow. To terminate the simulation space, Berenger layers are optimised in terms of total energy reflection. Since a reduction in reflection of more than 120 dB is achieved, the boundary conditions will influence stability only to a small degree.

When a simulation is unstable, a spurious signal is observed in the time signal, after the pulse of interest has reached the receiver and is damped out. The rate of growth of this instability depends on the Courant number and magnitude of the background flow. In order to quantify this, "Time To Instability" (*TTI*) is defined. This is the simulation time between the moment where the signal of interest reaches its maximum and the moment where the instability signal reaches this same pressure level. In Figure 2.18, *TTI* is plotted as a function of

the Courant number for a few Mach numbers. The *CN* in a uniform background flow v_0 in one dimension is defined as

$$CN = \frac{(c + v_0)dt}{dx}. \tag{2.114}$$

The effect of the Mach number on stability is significant. Using background flows with Mach numbers lower than 0.2 results in completely stable simulations for *CNs* smaller than 1.2. In many practical cases and for outdoor sound propagation, stability therefore is not of primary concern, since the introduction of a small background flow does not result in a significantly more severe stability condition. For higher Mach numbers, the *TTI* strongly depends on the *CN*. For the Mach numbers shown in Figure 2.18, a *CN* may be found where the slope becomes very steep, and this point may be considered as a rough stability criterion As long as the *CN* is smaller than that value, or when the simulation time is considerably shorter than the *TTI*, no stability problems arise.

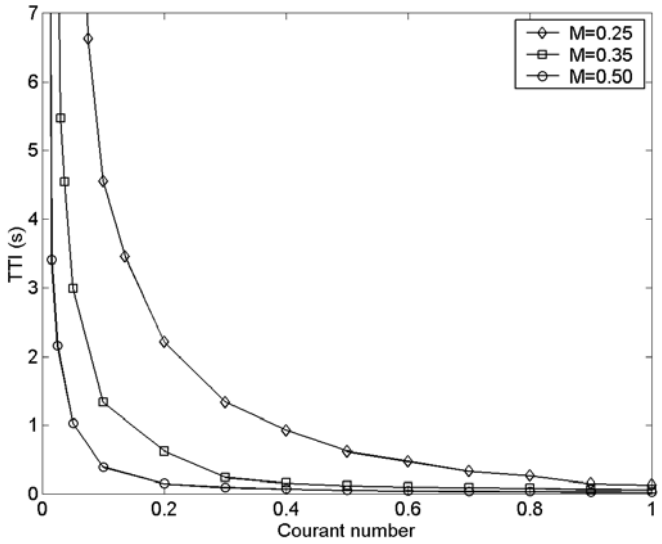

Figure 2.18 Time to instability (*TTI*) for a uniform background flow of Mach numbers *0.25*, *0.35* and *0.50*, as a function of the Courant number in a one-dimensional simulation space.

2.5 Numerical accuracy

To check the accuracy of the model, a *FDTD* simulation of sound propagating in a one-dimensional duct in a uniform background flow is compared to its known solution. Theoretically, the amplitude at each frequency stays constant throughout the duct, while a linear phase shift is expected.

The simulation domain is shown in Figure 2.19. Two locations are defined, downstream from the source. The distance between point *1* and *2* (= ΔL) is equal to 40 spatial discretisation steps. A Gaussian pulse, containing a wide range of sound frequencies, propagates from point *1* to point *2*.

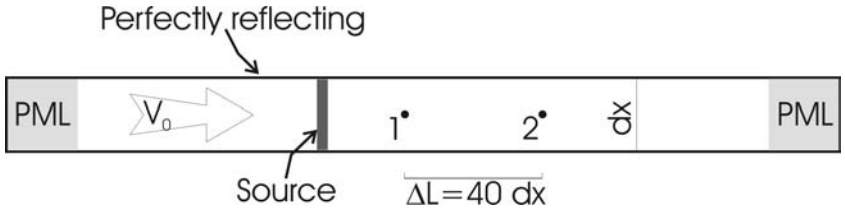

Figure 2.19 Simulation domain for one-dimensional accuracy tests.

The modulus of the Fourier transforms at both places are compared to obtain the (relative) amplitude error ε_F:

$$\frac{|F_1|}{|F_2|} = 1 \pm \varepsilon_F \,. \tag{2.115}$$

The theoretical, linear phase shift depends on the frequency and can be expressed by

$$\Delta\zeta = \omega \Delta t_{12} = \frac{2\pi f \Delta L}{c + v_0}, \tag{2.116}$$

where Δt_{12} is the time delay between point *1* and *2*, f is frequency of the propagating wave, ω its angular frequency, c is the speed of sound and v_0 is the uniform background flow velocity. To quantify the (relative) phase error ε_ζ, the theoretical phase shift is compared to the phase shift as obtained by the *FDTD* simulation:

$$\frac{\Delta\zeta_{theory}}{\Delta\zeta_{FDTD}} = \frac{\omega \Delta t_{12}}{\zeta_1(\omega) - \zeta_2(\omega)} = 1 \pm \varepsilon_\zeta \,, \tag{2.117}$$

where ζ_i is the phase at point i.

It can be shown analytically that the *FDTD* equations conserve amplitude in the absence of flow. The phase shift nevertheless is not always error free. This also results in amplitude errors when interference between acoustic waves becomes important, e.g. in confined spaces and for the calculation of e.g. the depth of the ground dip outdoors.

A formulation for the phase error in a three-dimensional, infinite simulation domain is derived in Reference [15]:

$$\frac{\zeta_{FDTD}}{\zeta_{theory}} = \frac{2\arcsin\left(c\,dt\sqrt{\sum_{\alpha=x,y,z}\left[\frac{\sin^2\left(0.5k_\alpha\,d\alpha\right)}{d\alpha^2}\right]}\right)}{c\,dt\sqrt{\sum_{\alpha=x,y,z}k_\alpha^2}}, \tag{2.118}$$

where k_α is the wave number in direction α. From this, it can be deduced that there are no phase errors in absence of flow in a one-dimensional simulation space, as long as the following condition is fulfilled (for propagation in the x-direction):

$$c\,dt = dx\,. \tag{2.119}$$

This means that the one-dimensional Courant number must equal one. With decreasing Courant number, the phase error increases.

In a two-dimensional or three-dimensional grid, it is not possible to choose spatial steps and time steps in such a way that the phase error is zero for all directions of propagation. Only when the direction of propagation is along the diagonal of the grid cells, and for a two-dimensional or three-dimensional Courant number equal to one, this error is zero [15].

In Figure 2.20 and Figure 2.21, the ratio of the phase difference between both locations as obtained from the *FDTD* simulation and the theoretical phase shift is shown. In abscissa, the number of cells per wavelength is shown. In Figure 2.20, a uniform background flow of 50 m/s is used for different Courant numbers. In Figure 2.21, the effect of the magnitude of the background flow is investigated, while the Courant number is kept constant at 1. With decreasing Courant number and increasing Mach number, the error on the phase increases. For small Courant numbers, the curves in Figure 2.20 are indistinguishable. For large ratios of the wavelength and the spatial discretisation step, the effect of both the background flow and the Courant number on the phase error becomes small.

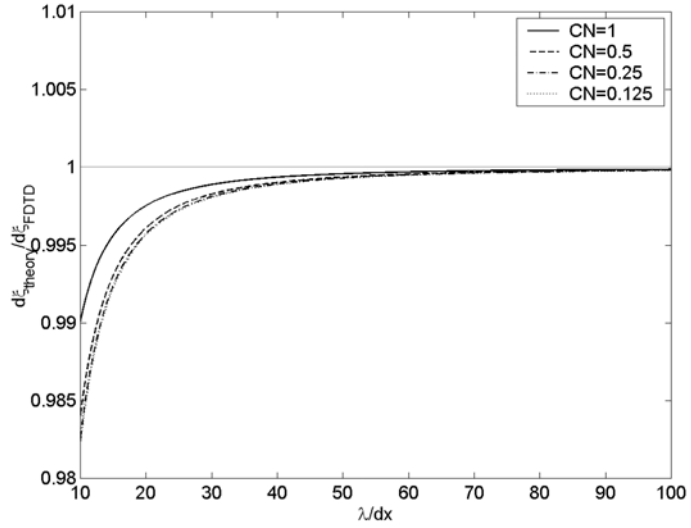

Figure 2.20 Accuracy of the phase in a uniform background flow of 50 m/s for different Courant numbers, as a function of number of cells per wavelength, in a one-dimensional simulation space.

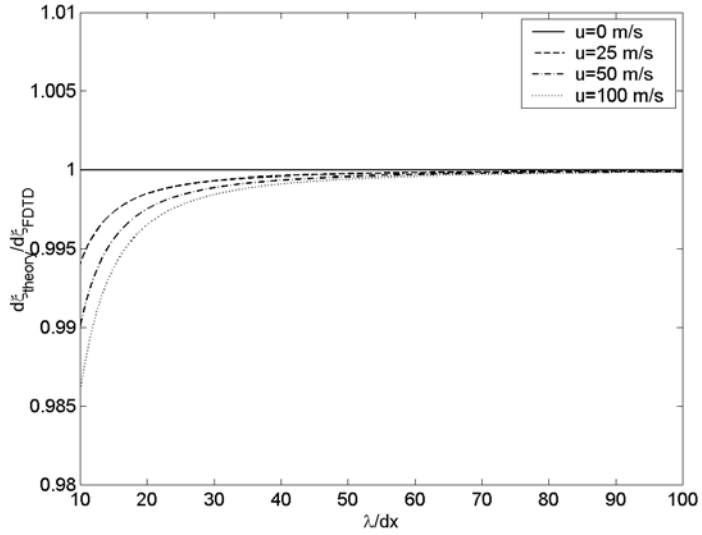

Figure 2.21 Accuracy of the phase with increasing number of cells per wavelength, in a one-dimensional simulation space. Different uniform background flow velocities are used. The Courant numbers equals 1.

In Figure 2.22 and Figure 2.23, the amplitude error is investigated. The ratio of the modulus at locations *1* and *2* is given with increasing number of cells per wavelength. In Figure 2.22, the background flow is 50 m/s. The effect of the Courant number is shown. In Figure 2.23, the Courant number equals 1 while the background flow ranges from 0 m/s to 100 m/s. It can be concluded that the amplitude error increases when the Courant number increases. Using a higher number of simulation cells per wavelength largely reduces the amplitude error, however at an increased computational cost. With increasing background flow velocity, the amplitude error increases significantly, in contrast to the phase error. In absence of flow, deviations from 1 cannot be observed in Figure 2.23.

The amplitude error reflects clearly the low Mach number approximation used in this work. The prediction step, neglecting background flow, in between two time-steps of both the velocity and pressure equation will be more accurate for smaller time discretisation steps. With increasing background flow, the approximation will be less accurate (for a fixed time step).

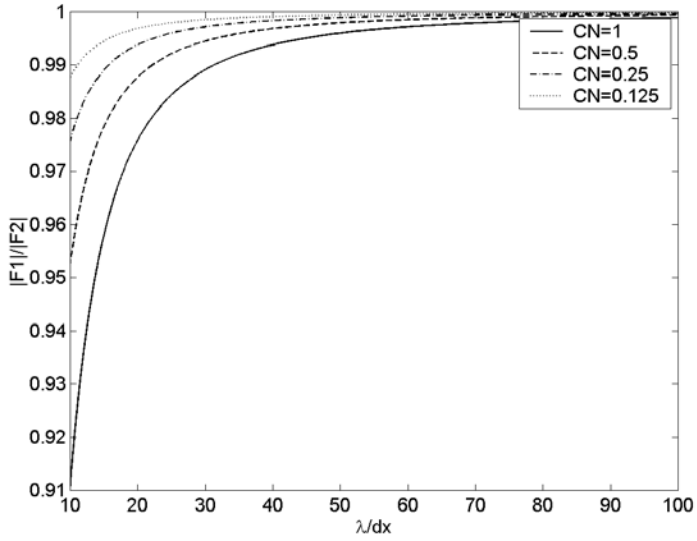

Figure 2.22 Accuracy of the amplitude in a uniform background flow of 50 m/s for different Courant numbers with increasing number of cells per wavelength, in a one-dimensional simulation space.

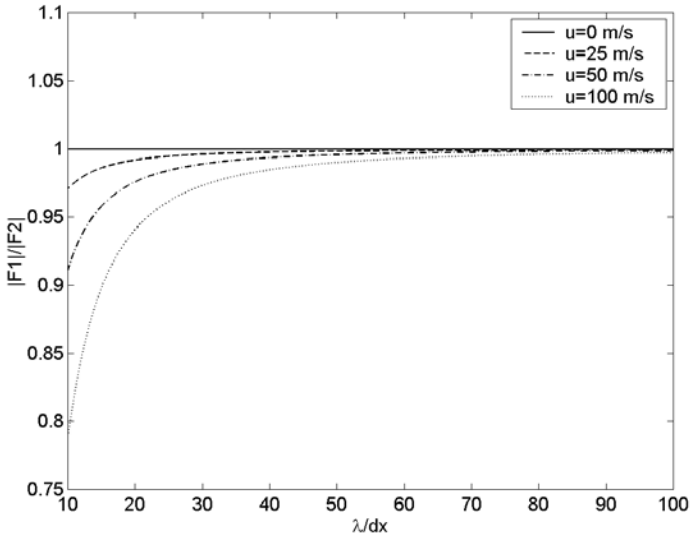

Figure 2.23 Accuracy of the amplitude with increasing number of cells per wavelength, in a one-dimensional simulation space. Different uniform background flow velocities are used. The Courant numbers equals 1.

It is clear that demands to minimise the phase and amplitude error for the simulation of acoustic waves in background flow are conflicting. For high Mach numbers, the Courant number needs to be small to conserve amplitude. On the other hand, small Courant numbers result in larger phase errors. Using a sufficient number of simulation cells relative to the wave numbers considered provides a solution for these conflicting demands, of course taking into account the available computational resources. In case of small flow velocities, accuracy is not significantly affected compared to the non-flow equations.

To have an idea of the numerical accuracy in a two- or three-dimensional simulation space, one has to divide the one-dimensional Courant number as used in the figures in this chapter by the square root of 2 or 3 (when the spatial discretisation step in each direction is the same). However, the situation becomes a lot more complex, e.g. when the flow is not parallel with the propagation direction of the sound waves.

2.6 Turbulent flow and acoustic scattering

2.6.1 Atmospheric turbulence

Most airflows encountered outdoors are (strongly) turbulent: the momentary velocity field is highly fluctuating in time. Atmospheric turbulence is caused by wind shear and by buoyancy forcing. The surface-layer wind produces turbulent energy by friction with the ground surface (or with obstacles). The length scales of these vortices (that are also called “eddies”) are typically in the order of the height above the surface (or in the order of the height of the obstacles). Solar heating of the ground, and as a result, conduction of heat to the layers of air just above the ground, is another way to produce turbulent motion. The presence of both warm air volumes, rising from the surface, and the colder surrounding air results in large recirculating flows in the atmosphere.

Because of the velocity gradients that are present in the eddies, there will be some friction by the viscous properties of air. A limited amount of the energy present in the vortex will be dissipated, and a number of smaller eddies is formed at a lower energy level. These smaller eddies will create on their turn even smaller eddies. As a consequence, the atmosphere consists of a collection of eddies with a wide range of length scales, from typically millimetres to kilometres [50].

Different models are available to describe the relation between the turbulent energy at the different length scales e.g. the Gaussian, the Kolmogorov and the von Kármán spectrum of turbulence. These spectra describe a homogeneous and isotropic turbulent field.

The spectrum of turbulent motions can usually be partitioned into three sub-ranges. With decreasing length scale or with increasing (turbulent) spatial wave number κ, the energy-containing sub-range (or source region), the inertial sub-range and the dissipation sub-range are usually identified. The inertial sub-range is bordered by the outer scale length (L_0) and the inner scale length (l_0). In the source region, eddies are not universal and largely depend on local flow conditions. In the inertial and dissipation sub-ranges, more universal behaviour is observed. Values for the outer length scale are in the order of a few 10 metres to 100 metre [51]. This value varies however very much with e.g. atmospheric conditions, height above the ground and terrain topography [50]. The value l_0 is typically in the order of a few millimetres at ground level.

In the inertial region, energy is efficiently passed between successive scales: the dissipation of energy at each transition is small compared to the energy received. As a result, a constant slope in this region of the energy spectrum is observed. Kolmogorov found that for high Reynolds number flows (like the flows

encountered in the atmosphere), the energy is proportional to the spatial wave number to the –5/3 power [52] in this region. In the dissipation sub-range (for Reynolds numbers of about 1), an important part of the turbulent kinetic energy is converted into heat, which results in a rapid decrease of energy with increasing spatial wave number.

For the sound frequencies of interest outdoors, it is mainly the inertial sub-range and source region that are of importance. The dissipation sub-range can generally be ignored [51]. The source region is responsible for phase fluctuations, while the inertial sub-range drives amplitude fluctuations [53]. Acoustic scattering is observed at places where sound pressure levels are low like in shadow zones, and becomes important when the wavelength is in the same order of the eddy size [31]. Therefore, a good modelling of the inertial sub-range is of primary concern.

The Kolmogorov spectrum agrees well with experimental data in the inertial sub-range. The von Kármán spectrum yields the same spectrum in the inertial range as the Kolmogorov spectrum, and has a maximum in the transition region between the energy-containing and the inertial region. The Kolmogorov spectrum on the other hand uses in the source region the same slope as in the inertial-range, and over-predicts the energy content for these large eddies. As a result, the von Kármán spectrum is supposed to be the most realistic spectrum when considering a wide range of turbulent scales [54]. The Gaussian spectrum was designed to approximate only the source region, and decays too rapidly in the inertial region [50]. However, the Gaussian spectrum is often used with "fitted" parameters in order to agree with the von Kármán spectrum in a certain wave number range [50].

2.6.2 *CFD* simulation of turbulent flow

Even today, numerical simulation of flows at high Reynolds numbers is still a challenge. There are a lot of *CFD* techniques available, ranging from very simple models to simulation techniques that need super-computers. Direct numerical simulations (*DNS*) and Large-Eddy Simulations (*LES*) are the main techniques for numerically simulating turbulent flows in time-domain. The *DNS*-technique solves the Navier-Stokes equations directly. In principle, no assumptions are made concerning turbulence. All scales of turbulence are resolved, depending on the spatial and temporal discretisation. The necessary discretisations are however so fine that this type of simulation is not of practical use on PC's. *DNS* is rather a test case for "turbulence models".

Large-Eddy Simulations are based on the fact that mainly the large-scale movements are important for the transport of energy and mass. The large scales are resolved for explicitly, while small scales are replaced by a parameter model (subgrid-scale models (SGS)). The large eddies are strongly dependent on the flow and environment, while the smaller scales are more universal and isotropic, and therefore more easy to parameterise. In a *LES*, the high-frequent components of the flow field are in essence averaged out locally. The "low-passed filtered" form of the Navier-Stokes equations is solved. Even *LES* are extremely demanding as to computational resources. Moreover, simulations are nowadays only possible for flows at low Reynolds numbers.

For "statistically-stable" turbulent flows, the Reynolds-Averaged Navier-Stokes (*RANS*) equations may be solved. Such a simulation will not provide information on the time history of a turbulent flow. The quantities involved for solving the flow problem are assumed to have an average value and momentary fluctuations around that average. The average values of the fluctuating parts equal zero. However, models are needed to calculate the averages when products of such fluctuating parts are involved. A widely applied model for engineering purposes in the *RANS* approach is the k-ε model. Turbulent effects are introduced by means of two extra equations to quantify the turbulent kinetic energy (k) and its dissipation rate (ε).

Only the large recirculating flows are modelled with the k-ε model. Vortices with length scales in the same order as the acoustic wavelengths do not appear in the simulated flow field. As already stated, these scales of turbulence drive acoustic scattering.

2.6.3 Generation of scattering, turbulent flow field

With respect to scattering of sound, wind velocity fluctuations are usually dominant to temperature fluctuations in the atmosphere [55]. The energy in the inertial range of the temperature turbulence spectrum decreases as $k^{-8/3}$ when the spatial wave number increases, instead of $k^{-5/3}$ for the kinetic energy turbulence spectrum [55]. As a result, the velocity fluctuations are much more energetic for the range of scales that most influences acoustic scattering [30, 55]. Also when buoyancy forcing is the dominant mechanism for turbulence production, the effect of velocity fluctuations is usually more important than that of temperature fluctuations [56]. Temperature fluctuations will generally be more important for propagation through a stably stratified flow, such as occurs near the ground on windless nights [56]. Therefore, only turbulent wind velocity fluctuations will be considered.

In order to introduce scattering on wind velocity fluctuations, the turbule theory [57] will be applied. The turbulent flow field is constructed by adding randomly located and randomly orientated eddies (or "turbules") of many different size to the flow field, calculated using e.g. a *RANS-CFD* model.

Although other models exist, e.g. based on a mode decomposition of the turbulent field [55], the turbule model is chosen since it is very suited to be used in combination with the finite-difference time-domain model in flow. Local variations of the (turbulent) flow field are easily accounted for.

Relations between the parameters at different scales were derived in order to obtain a Kolmogorov spectrum [57, 58] and a von Kármán spectrum [54]. We are mainly interested in the inertial sub-range, where both spectra are identical. For simplicity, the relations based on the Kolmogorov spectrum are discussed in this chapter.

A single velocity turbule is characterized by the location of its midpoint $\boldsymbol{b}$, length scale a_α at scale α, and an envelope function describing the decrease of the velocity with distance from the midpoint. A single velocity turbule using a Gaussian envelope function is calculated from [58]:

$$\boldsymbol{v} = \boldsymbol{\Omega}_\alpha \times \left(\boldsymbol{r} - \boldsymbol{b}\right) e^{-\frac{|\boldsymbol{r}-\boldsymbol{b}|^2}{a_\alpha^2}}, \tag{2.120}$$

where r indicates a position and $\boldsymbol{\Omega_\alpha}$ is the angular velocity vector at scale α. The orientation of the angular velocity vector is random, while its amplitude Ω_α depends of the scale of turbulence. A spherical and symmetrical, solenoidal flow is obtained. In case of a homogeneous distribution of the midpoints of the turbules, the Kolmogorov turbulence spectrum in the inertial range will be obtained [58]. In Ref. [57], the general turbule parameters, the magnitude of the angular velocity Ω_1 and the length scale of the first scale a_1 are linked to the structure velocity parameter C_v^2 of a Kolmogorov spectrum:

$$\Omega_1 = \sqrt{\frac{C_v^2}{0.34\frac{\phi}{\mu} a_1^{4/3} \Gamma(17/6)}}, \tag{2.121}$$

where Γ is the gamma function, ϕ is the packing fraction, and μ is a parameter that describes the relation between successive length scales.

The packing fraction is calculated from

$$\phi = n_\alpha a_\alpha^3, \tag{2.122}$$

where n_a is the number density of the turbules with size a_α. Successively smaller turbule sizes are related to each other by

$$\frac{a_{\alpha+1}}{a_\alpha} = e^{-\mu}. \tag{2.123}$$

The structure velocity parameter C_v is a general characterization of the strength of turbulence. For the Kolmogorov spectrum of turbulence, this parameter is related to the outer length scale L_0 and the variance of velocity fluctuations in one direction (since turbulence is assumed to be isotropic) [56]:

$$C_v^2 = \frac{2L_0^{\frac{2}{3}}}{3\sigma_v^2}. \tag{2.124}$$

The relation between the angular velocity at different scales is given by the following expression:

$$\Omega_\alpha = \Omega_1 \left(\frac{a_1}{a_\alpha} \right)^{\frac{2}{3}}. \tag{2.125}$$

To obtain a homogenous turbulent field, the part of the atmosphere under consideration is divided at each scale in a number of cubic cells of dimension d_α. In each cell, one turbule is placed at a random location. The size of the cubic cells are related to the length scale:

$$d_\alpha = n_\alpha^{-\frac{1}{3}} \tag{2.126}$$

or

$$d_\alpha = a_\alpha \phi^{-\frac{1}{3}}. \tag{2.127}$$

In practical applications, the dimensions of the computational domain limit the largest scale of turbulence that can be taken into account. The smallest scale of turbulence must be greater than the spatial discretisation step in order to produce a non-divergent, rotating turbule. So the acoustic *FDTD* grid limits the range of scales that can be modelled. However, it are mainly the eddies with sizes in the order of the wavelength of the sound that are important when quantifying

scattering. When taking 10 cells per wavelength in an *FDTD* grid, it is expected that the relevant scales of turbulence are present.

The turbule model assumes the "frozen turbulence" approach. This is justified by the fact that the time variation of the turbulent medium is usually much slower than the acoustic travel time between source and receiver in practical applications [55, 59]. This makes it however necessary to produce a certain number of random realisations (or snapshots) of the turbulent flow field, and to simulate sound propagation through each of these mediums. Sound pressure levels are then averaged out (energetically) to imitate a temporal mean. A sufficient number of simulations are needed to produce statistical correct simulation results. By taking the mean of different realisations, also the loss of coherence by a turbulent flow field is modelled.

However, if information is needed on the time-dependency of amplitude and frequency (i.e. spectral broadening of signals), the advection of eddies must be accounted for as the distances and scattering angles change when the eddies move, and as a result the scattered energy at fixed receivers [58].

In the above approach, homogeneous and isotropic turbulence is assumed. It is known that both conditions are usually not met in the atmosphere. Measurements indicated that wind speed fluctuations in the along wind direction are significantly larger than in the (horizontal) crosswind direction and vertical direction [60]. The variance of wind speed fluctuations is proportional to the square of the friction velocity. As a consequence, the degree of turbulence will increase as wind speed increases. It is further known that the outer scale of turbulence is proportional to the height above the ground surface [56]. So it can be concluded that in a refracting atmosphere, a homogenous and isotropic turbulent flow field will only be an approximation.

A possible way to link the turbule model to the simulated flow field is scaling the angular velocity of a turbule with the square root of the local value of the turbulent kinetic energy k_{local} according to

$$\Omega'_{\alpha} = \Omega_{\alpha} \sqrt{\frac{k_{local}}{k_{ref}}} \,. \tag{2.128}$$

The turbulent kinetic energy field k_{local} could be obtained from a flow simulation with the k-ε turbulence model. The parameter k_{ref} is used so that the total turbulent kinetic energy as a result from applying the turbule model fits the turbulent energy present in the *CFD* flow field. A trial-and-error procedure is necessary.

This approach may serve as a first estimation of scattering from an inhomogeneous turbulent atmosphere. The increase in the strength of turbulence when wind speed increases, as well as the larger turbulent energy near obstacles, is accounted for.

Chapter 3

Applications

3.1 Sound propagation in a refracting atmosphere with the normal mode solution (theoretical validation)

An analytical expression to calculate sound propagation above a complex impedance plane in a layered atmosphere can be found for following type of (effective) sound speed profile [61]:

$$c_z = \frac{c_0}{\sqrt{1 \pm \frac{2z}{R}}}, \tag{3.1}$$

where c_z is the speed of sound at height z and c_0 is the speed of sound at ground level. Using the plus sign in the above equation results in an upwardly refracting profile, a minus sign represents a downwardly refracting atmosphere. When z is small relative to R, equation (3.1) approximates a linear, effective sound velocity profile:

$$c_z = c_0\left(1 \mp \frac{z}{R}\right). \tag{3.2}$$

The gradient of this linear sound speed profile can be calculated as follows:

$$\frac{dc}{dz} = \frac{c_0}{R}. \tag{3.3}$$

R can now be seen as the curvature of the ground surface that results approximately in the same bending of sound rays as if there was a linear sound speed profile above a flat ground [62]. We first consider the case of a downward refracting atmosphere. The normal mode solution resolves the wave solution into a sum of individual modes. The sound pressure resulting from a line source at height h_s for a receiver at distance r and height z is given by:

$$p(r,z) \approx \frac{2\pi i}{l} \sum_n \frac{e^{ik_n r} Ai\left(\tau_n + \frac{h_s}{l}\right) Ai\left(\tau_n + \frac{z}{l}\right)}{k_n \left(\tau_n \left[Ai(\tau_n)\right]^2 - \left[Ai'(\tau_n)\right]^2\right)}. \tag{3.4}$$

In this equation, *Ai* is the Airy function and *Ai'* its derivative. The n^{th} (horizontal) wave number k_n is defined by:

$$k_n = \sqrt{k_0^2 + \frac{\tau_n}{l^2}}. \tag{3.5}$$

The horizontal wave number at ground level is:

$$k_0 = \frac{2\pi f}{c_0}. \tag{3.6}$$

In the equations above, τ_n represents the n^{th} zero of following equation:

$$Ai'(\tau_n) + q\, Ai(\tau_n) = 0. \tag{3.7}$$

Parameter q determines the pole location in the normal mode solution and depends on the impedance of the ground and parameter l (which is called the wave layer thickness in Ref. [61]):

$$q = \frac{ik_0 l \rho c_0}{Z}, \tag{3.8}$$

$$l = \left(\frac{R}{2k_0^2}\right)^{\frac{1}{3}}. \tag{3.9}$$

The number of zeros is infinite. It was shown however in Ref. [61] that this summation can be truncated in practice after taking n_{max} modes:

$$n_{\max} = \frac{2}{3} \frac{f}{\left|\frac{dc}{dz}\right|}. \tag{3.10}$$

The number of necessary terms in the normal mode sum is directly proportional to the frequency and inversely proportional to the sound velocity gradient. The modes of higher order undergo rapid exponential decay since k_n will have a large imaginary part.

In the case of an upwardly refracting atmosphere, the following equations need to be used [62] to calculate the sound pressure resulting from a line source:

$$p(r,z) \approx \frac{2\pi e^{\frac{i\pi}{6}}}{l} \sum_n \frac{e^{ik_n r} Ai\left(\tau_n + \frac{h_s}{l} e^{\frac{2i\pi}{3}}\right) Ai\left(\tau_n + \frac{z}{l} e^{\frac{2i\pi}{3}}\right)}{k_n \left(\left[Ai'(\tau_n)\right]^2 - \tau_n \left[Ai(\tau_n)\right]^2\right)}, \tag{3.11}$$

$$k_n = \sqrt{k_0^2 + \frac{\tau_n}{l^2 e^{\frac{2i\pi}{3}}}}, \tag{3.12}$$

$$Ai'(\tau_n) + q\, e^{\frac{2i\pi}{3}} Ai(\tau_n) = 0. \tag{3.13}$$

The other quantities are the same as for the normal mode solution. This set of equations is called the residue series solution. In contrast to the normal mode solution, this solution converges quickly.

More information on the theoretical background can be found in the cited references. It is important to stress that in this approach only the ground-reflected waves are accounted for. As a result, this solution will be correct at distances where the direct wave is small in comparison to the latter.

Sound propagation over a flat, perfectly reflecting ground is investigated. Finite-difference time-domian simulations accounting for background flow are compared to analytical solutions. Equations (3.4) and (3.11) are evaluated to simulate a downwardly and upwardly refracting atmosphere. For the simulation in an atmosphere at rest, the sound pressure as a result from the interaction between the direct and ground-reflected wave can be calculated with the following formula:

$$p = i\pi H_0^1(kr_1) + R_p i\pi H_0^1(kr_2), \tag{3.14}$$

where H_0^1 is the Hankel function of the first kind and zero-order, R_p is the plane wave reflection coefficient, r_1 and r_2 are the direct and ground-reflected ray path lengths. The use of a plane wave reflection coefficient (instead of the cylindrical-wave reflection coefficient) to simulate reflection for cylindrical wave fronts resulted in only minor errors in our test set-up. Since the analytical solutions for a refracting atmosphere may only be used at sufficient distances from the source, this solution is analysed for distances starting from 50 m. Moreover, significant differences between the non-moving, the downwardly refracting and the upwardly refracting atmosphere are only observed at distances larger than 50 m

for the sound frequency considered, except near the ground dip (see Chapter 3.2). In Figure 3.1, sound pressure levels with increasing distance from the source are shown. The reference pressure is taken at 50 m for the 3 states of the atmosphere. Results from the *FDTD* simulations, as well as the analytical solution in absence of flow, are also evaluated at smaller distances. The height of the source is 6.375 m, receivers are at 1.125 m above the ground surface. The gradients of the linear sound speed profiles are +0.1/s and –0.1/s. The sound frequency is 100 Hz.

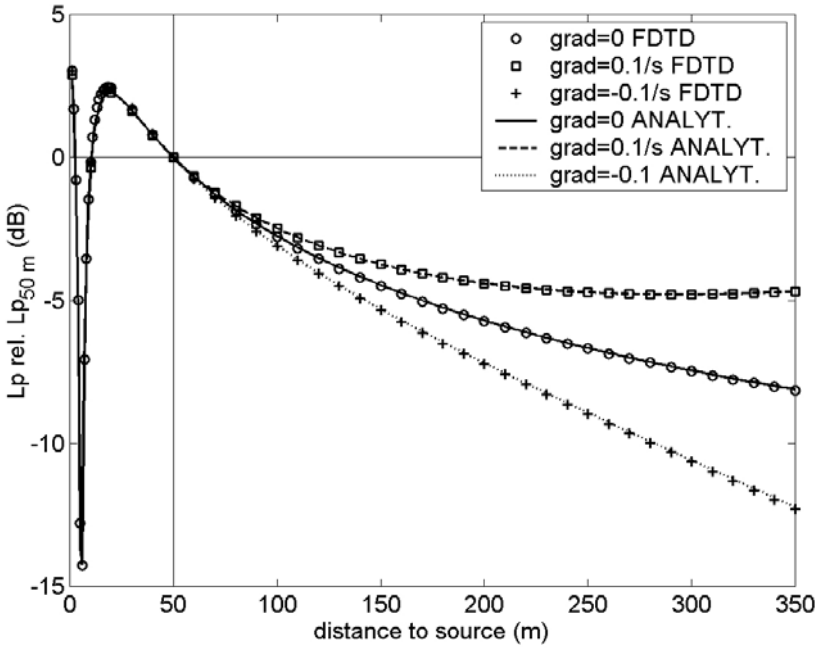

Figure 3.1 Sound pressure levels (for 100 Hz), relative to the sound pressure level at 50 m, with increasing distance to the source. Analytical solutions are compared to *FDTD* simulations, for an atmosphere at rest, a downwardly and upwardly refracting atmosphere.

The *FDTD* simulations correspond very well to the analytical solutions. This (simple) example may serve as a first validation of the numerical scheme, developed in this work.

3.2 Effect of refracting atmosphere on ground dip (simulation)

The influence of a refracting atmosphere on the ground dip is shown in Ref. [18]. A point source is situated at a height of 0.5 m above the ground, the receiver is at a height of 1.5 m. The distance between source and receiver is 5 m. Frequencies between 100 Hz and 1000 Hz are considered. This same configuration is used in this work, which can be considered as a test case for a typical sound propagation situation encountered outdoors.

A line source is simulated in a two-dimensional grid. Three types of grounds are simulated. First, a perfectly reflection plane is considered. Next, the ground model of Zwikker and Kosten (see Chapter 2.3.1.b) is used, for a soil with a flow resistivity of 10 kPas/m² and 100 kPas/m². For both, the other ground parameters are kept constant: k_s =3 and φ = 0.3. A linear wind speed profile with a gradient of ± 3/s is used. Wind (in absence of turbulence) is blowing from the source to the receiver: sound will be refracted downwardly in case of a plus sign, upwardly in case of a minus sign. Simulation results are shown in Figure 3.2, relative to free sound propagation. A pulse with the energy concentrated in the frequency interval of interest is emitted. The Fourier spectrum is calculated, after performing zero padding to increase resolution on the frequency axis.

A ground dip is observed when there is destructive interference between the direct wave from source to receiver and the ground-reflected wave. When the soil becomes softer, this minimum in the spectrum becomes less pronounced since an increasing part of the ground-reflected wave is absorbed by the ground medium. As a result, interference becomes smaller.

The presence of a downwardly refracting atmosphere results in a shift of the ground dip towards lower frequencies. The direct wave travels at higher effective sound speed than the ground-reflected wave, since both sound waves propagate in a different part of the medium. As a result, the frequency for which the phase difference becomes 180 degrees decreases [18]. For natural grounds, the minimum becomes more pronounced because of the increased interaction between the sound waves and the soil. When the (effective) sound speed decreases with height, the opposite effects are observed: the ground dip shifts to higher frequencies, while the minimum is somewhat less deep. The simulations shown in Figure 3.2 (more precisely for the atmosphere at rest and for the downwardly refracting atmosphere) correspond well to the *LE* simulations and the *PE* calculations in Reference [18].

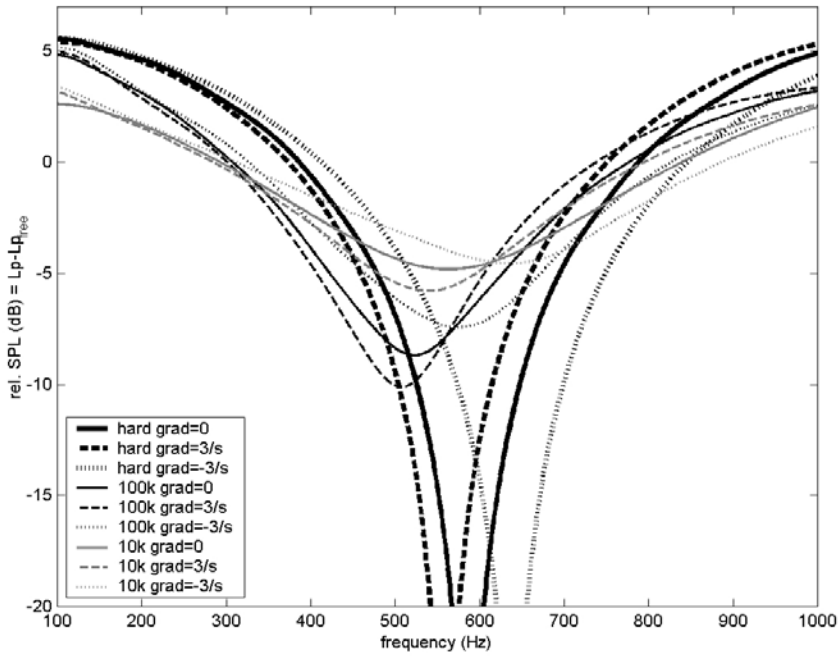

Figure 3.2 Effect of the presence of a downwardly (grad=3/s) and upwardly (grad=-3/s) refracting atmosphere on the ground dip, for a hard soil, and for a soil with a flow resistivity of 10kPa s/m² and 100 kPa s/m². For comparison, the simulations are also performed in a medium at rest (grad=0).

It has to be noted that in a realistic situations, interference minima are strongly influenced by atmospheric turbulence, especially near hard grounds [e.g. 63]. Due to fluctuations in phase and amplitude, the ground dip becomes less pronounced.

3.3 Effect of wind on single noise barrier efficiency (experimental validation)

Sound propagation over a single noise barrier in wind was studied by Salomons in a wind tunnel experiment at scale [64]. Screen-induced refraction of sound with increasing wind speed was investigated. The wind direction was normal to the noise barrier and downwind sound propagation was studied. The wind tunnel

floor in the test section was perfectly reflecting. Upwind from the source, the floor was covered with a rough layer in order to create a realistic atmospheric wind speed profile. The noise barrier was assumed to be perfectly reflecting and infinitely thin. A scaling ratio of 1:30 was used. The experimental results obtained by Salomons will be compared to numerical simulations with the finite-difference time-domain model accounting for background flow. Our simulations are also compared to numerical computations by the *PE* model in a refracting atmosphere by Salomons [64], as well as to simulations with the *LE* model by Blumrich and Heimann [17].

An overview of the test set-up is given in Figure 3.3. At full scale, the noise screen height was 5.55 m. The source was positioned at a height of 1.89 m, 30 m before the screen. At one distance behind the noise barrier (60 m) and at two heights above the ground surface (6 m and 12 m), sound pressure levels were measured.

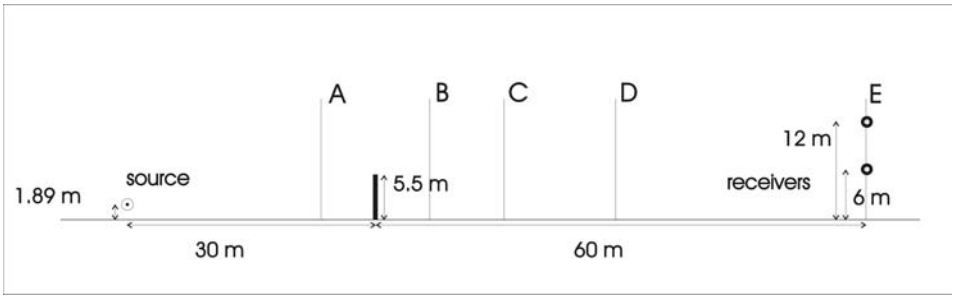

Figure 3.3 Overview of the experimental test set-up, with indication of the places A, B, C, D and E where measured and simulated wind profiles are compared.

The comparison is made for the 250 Hz octave band (185 Hz to 375 Hz) and the 500 Hz octave band (370 to 750 Hz). The sound pressure levels of these octave bands are calculated based on 20 equidistant frequencies. Wind speeds ranged from 2 m/s to 14 m/s, measured at a height of 9 m (= z_{ref}). At the entrance of the test section, the wind speed profile is logarithmic [64]:

$$v(z) = \frac{v_{z_{ref}}}{\ln\left(1+\frac{z_{ref}}{z_0}\right)} \ln\left(1+\frac{z}{z_0}\right), \tag{3.15}$$

where z is the height above the surface, v_z is the velocity at height z and z_0 is the roughness length. The average roughness length of both the rough and smooth

section was found to be 1 mm [64]. More details on this experiment are described in the above-mentioned paper.

In Figure 3.4, our results (*FDTD*) are compared to the experimental data, to the *PE* calculations [64], and to the *LE* calculations [17]. The effect of wind on noise barrier performance is shown with increasing (incident) wind speed, measured at a height of 9 m. The effect of wind is quantified by the difference between the sound pressure level in the presence and absence of wind, at the same location.

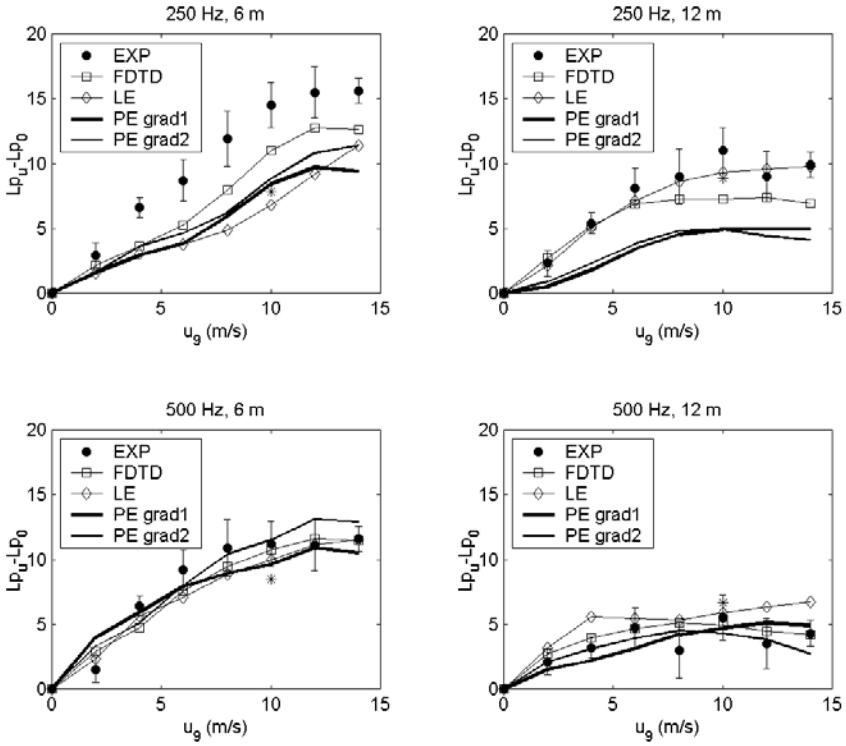

Figure 3.4 Comparison between the *FDTD* model, *LE* model by Blumrich and Heimann and the experimental results by Salomons. In abscissa, the (incident) wind speed at a height of 9 m is shown, in ordinate the relative sound pressure level for the frequency band under consideration. The *PE* calculations by Salomons are indicated with *PE* grad1 and *PE* grad2, indicating the use of different simulated (effective) sound speed gradients [64]. Measurements at a height of 6 m and 12 m are shown, for the octave bands at 250 Hz and 500 Hz. The * in the figures are the simulation results for *FDTD*, based on the same wind speed profiles as used during the *LE* calculations.

For the (low) frequency band of 250 Hz at a height of 6 m, the *FDTD* model results in some better agreement with measurements in comparison to the other models. At the receiver height of 12 m, both the *FDTD* and *LE* model approximate the experimental data better than the *PE* calculations. All models simulate the experimental data well for the frequency band of 500 Hz.

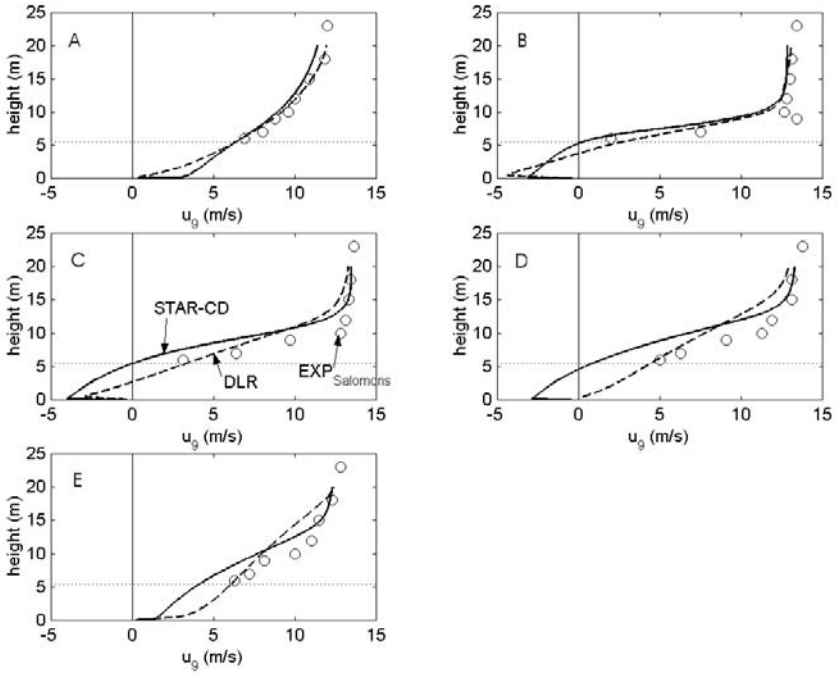

Figure 3.5 Comparison of measured and simulated wind speed profiles at 5 places in the wind tunnel (see Figure 3.3). De *STAR-CD* calculations are shown with the full lines, the flow calculations of Blumrich and Heimann (*DLR*) with the dashed lines. The experimental data is presented by the open circles.

In general, the *FDTD* simulations agree well with the *LE* model. Since *FDTD* and *LE* are similar models, differences probably arise from the calculation of the flow profiles. The flow simulations with *STAR-CD* and those performed by Blumrich and Heimann (*DLR*) are compared to wind speed measurements in the tunnel (see Figure 3.5). At 5 places, as defined in Figure 3.3, and for a wind speed of 10 m/s (at a height of 9 m), this comparison is made. Wind speed data is available only at heights above the noise barrier, since recirculating flow could

not be measured [64]. Near the noise barrier, calculations agree reasonably with the measurements. Near the location of the receivers, there is some deviation. This is probably due to the finite dimensions of the wind tunnel, which is not accounted for during the *CFD* simulations. When the same background flow field is used, the *FDTD* and *LE* model agree better (shown by the * in Figure 3.4, for a wind speed of 10 m/s), except for 500 Hz at 6 m.

For single noise barriers and the observation points considered, the approach of sound propagation in time-domain, taking into account time-invariant calculations of the flow, is capable to simulate the complex effect of wind on noise barrier performance. The screen-induced refraction of sound is well described by the proposed model.

3.4 Using rows of trees to improve noise barrier performance in wind (case-study)

3.4.1 Introduction

Meteorological effects on noise barrier performance

A reduction of the efficiency of noise barriers in wind has been analysed in many publications [63, 64, 65, 66, 67, 68, 69]. This negative effect is attributed to the screen-induced refraction of sound. The presence of non-streamlined obstacles, like thin, rectangular noise barriers, will severely disturb the ambient, logarithmical wind speed profile that is usually observed above flat ground. Streamlines become compressed above the noise barrier, resulting in large wind speeds. Since the wind speed on top of the barrier is zero, large (positive) gradients in wind speed are present. As a consequence sound waves are bent downwards into the acoustic shadow zone of the barrier. The noise barrier efficiency decreases strongly.

At distances starting from $20H$ behind the noise barrier, where H is the noise barrier height, wind profiles become identical to the incident profile [68]. So for receivers far from the acoustic shadow zone, screen-induced refraction of sound is not important [64]. Since shielding by a noise barrier is limited by diffraction at large distances, screen-induced refraction of sound plays an important role in the (whole) shielded zone behind a noise barrier.

The presence of gradients in wind speed is considered to be the main actor when looking at meteorological influences on noise barrier performance, at short distance behind the barrier. Temperature profiles are supposed to remain unaltered by the presence of noise barriers. Salomons stated that in most practical situations the wind effect dominates [64].

Turbulence also affects noise barrier performance. Sound pressure levels downwind from a noise barrier are increased by screen-induced turbulence and by the turbulent fluctuations advected by the flow. Scattering on advected turbulence, which is also observed in absence of a barrier, becomes now more important since sound pressure levels are decreased by the action of the screen. Effects are mainly observed for sound propagation over long distances and for high frequencies [108, 70]. Another effect at large distances is that the superposition of scattered waves on diffracted waves will result in fluctuations of phase and amplitude, smoothing out interference patterns. At limited distances, scattering on screen-induced turbulence is observed. Turbulent effects are considered to be small in comparison to the screen-induced refraction [69]. The simulations in Ref. [71] confirm this statement. For a sound frequency of 500 Hz, the time-averaged effect of screen-induced turbulence was only 0.2 dB, while the screen-induced refraction amounted to about 4 dB. Temporal fluctuations of the noise levels are more important: a standard deviation of about 1 dB is observed in the latter.

Taking this information into account, and since we are interested in broadband noise, turbulent scattering will not be considered in this chapter.

Possible solutions

Adequate solutions to cope with the problem of screen-induced refraction of sound by wind are not presented yet. Salomons e.g. proposed a different shape of a noise barrier namely a vented screen. With such a configuration, the large wind-speed gradients should be present at heights well below the screen height. Smooth and more streamlined barriers like earth berms may also be beneficial in this respect [64].

Heimann and Blumrich [72] performed calculations of various screen geometries in wind. Noise barriers with sloping parts and (small) openings were considered. Sound propagation over single screens above a perfectly reflecting ground surface was simulated, taking into account detailed wind profiles around the barriers. An average improvement of a few dB's in a wind situation was possible for some configurations. Distances up to 20H were considered. Care is however needed since a worse situation in absence of wind was often encountered, relative to an equivalent, classical, thin and rectangular noise barrier. This rather small improvement should also be balanced against the increase in construction cost of such complicated screens, relative to the classical screen.

In this work, another solution, not focusing on the barrier itself, is proposed. The effect of a vegetation screen (a row of trees), acting as a windbreak just behind

the barrier, is investigated. Trees as windbreaks to border arable land have been used for hundreds of years as a method of improving crop productivity. Significant yield increases have been attributed to shelter effects (e.g. improved soil moisture, higher pollination, higher $C0_2$ levels and less mechanical damage to the plants).

Important advantages of placing trees behind noise barriers are the possibility to treat existing noise barrier configurations and the fact that this is a relatively inexpensive measure. A reduction in wind speed will also result in general in a decrease of turbulence strength. Besides the main purpose i.e. wind reduction, some additional beneficial effects might be expected.

It is shown in Ref. [73] that naturally constructed barriers may lead to a decreased annoyance since their acceptance is usually higher. A barrier made of wood with a (technical) worse performance may subjectively perform as good as a more efficient concrete noise barrier. In this view, it could be expected that placing trees and small bushes, covering e.g. a concrete barrier, may result in a better annoyance rating. Placing trees behind a barrier on the receiver side will also result in a better integration of a noise barrier in the landscape and improves its visual impact. Traffic noise is also influenced by visual stimuli: with a decreasing degree of urbanisation, the perception becomes less unpleasant [74]. So trees may be useful for wind speed reduction purposes and from a psycho-acoustical point of view.

However, when placing trees behind a noise barrier, one needs to account for the full effect of vegetation on sound propagating through it. Effects may originate from an increased scattering on the trees tops and from wind-induced vegetation noise. This is investigated during a field research (see further).

Experiments

The investigation of the use of rows of trees behind noise barriers consists in 3 parts. First, a traffic noise situation at scale is modelled in a wind tunnel experiment. An important frequency interval of the traffic noise spectrum is studied (frequencies ranging from 500 Hz to 1 kHz). In a second part, a field experiment along a highway is conducted. In a last step, numerical simulations are performed. Based on the data of the wind tunnel study, the finite-difference time-domain method is validated for the case of sound propagation over noise barriers in the presence of rows of trees. Finally, the parameters involved in placing windbreaks behind noise barriers are investigated and optimised.

The wind tunnel study and the field experiment are complementary, and will reduce uncertainties inherent in both types of experiments. In the wind tunnel,

different configurations of single noise barriers and barriers on either side of a line source were tested, in combination with windscreens. Measurements were performed at distances up to 10 times the barrier height behind the noise barrier in downwind direction, for a perpendicular incident wind. The wind velocities in the experiment were 6.4 m/s (*wind 1*) and 11 m/s (*wind 2*), measured above the boundary layer in the wind tunnel. The acoustic source is well characterized. Uncertainties mainly come from the fact that this is a scale-model. It is known e.g. that turbulence is a quantity that does not scale. In this experiment, synthetic windscreens are used as a model for the wind reduction capacity of natural trees. The acoustic effect of the trees is not modelled. Remarks on this topic are made further is this chapter.

A field experiment was performed at a site along a highway, where at some places behind a noise barrier a row of trees is present. A continuous measuring campaign was set up. Acoustical data and meteo data were collected simultaneously. The wind speeds used in the wind tunnel experiment were relatively high due to practical limitations of the wind tunnel. In the full-scale experiment, all naturally occurring wind speeds will be present in the data set. The effect of wind directions, other than normal incident in downwind direction, can be investigated. Real trees are involved in the field experiment. This means that the full influence of trees on sound propagation (not only the modification of wind profiles) will be observed.

However, the in-situ experiment also has some disadvantages. Only one configuration i.e. the present one is tested. The monitoring is performed at one fixed place behind the noise barrier. Since only two microphones are used (a first one behind the barrier without trees and a second one behind the noise barrier with trees), only the net effect of the trees can be investigated. In the full-scale experiment, disturbance by sources other than traffic may occur. However, since the traffic noise source is dominant, these disturbances will have a negligible influence on the average measured sound levels. The height of the top of the atmospheric boundary layer in the field experiment is not known, and will be quite variable throughout the measurement campaign. In the wind tunnel study on the other hand, every wind situation is reproducible and controllable. The height of the top of the boundary layer can be measured and somewhat adapted. This also means that natural variations in the wind are not accounted for in the wind tunnel study.

The remarks in previous paragraphs make the wind tunnel experiment more suitable for the validation of numerical schemes. In the wind tunnel study, the incident wind profile is known in detail. In the field study, at only one place, namely behind the noise barrier, wind speed is measured. *CFD* simulations

would therefore be hard to validate due to this limited amount of experimental wind data. Another difficulty that should be addressed is the characterization of the acoustic source as a result of traffic flow on 6 lanes.

3.4.2 Wind tunnel study

3.4.2.a Experimental set-up and instrumentation

The experiments were performed in the wind tunnel of the International Centre for Eremology, Ghent University, Belgium [75]. This is a closed-circuit tunnel (see Figure 3.6): after leaving the test section, the air re-enters the system. A minimum wind speed of 6.4 m/s can be obtained. The width of the wind tunnel is 1.2 m, while the height in the test section in our set-up was 1.6 m.

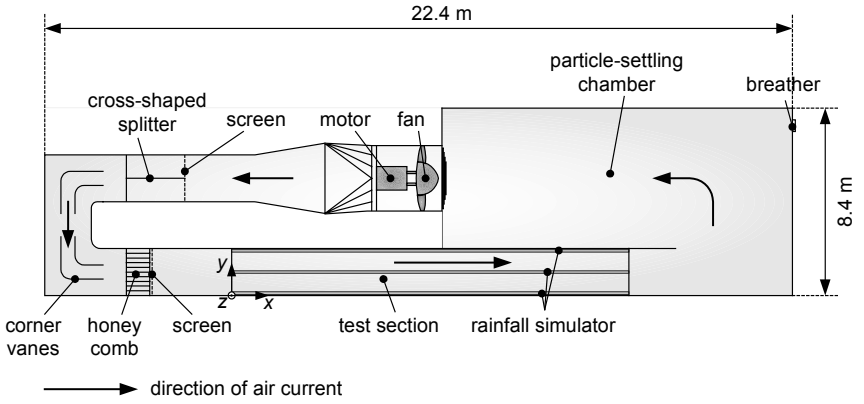

Figure 3.6 Overview of the I.C.E. wind tunnel.

In wind tunnel experiments, it is important to create a realistic boundary layer. This is however hard to accomplish. Only a large scaling factor (e.g. 100) could solve this problem. But experiments at such a scale would be difficult to perform accurately. Very small microphones are needed, together with a high-precision positioning system, a very smooth wall and floor, etc. Since the acoustic frequencies in a scale model with a large scaling factor are very high, air absorption must be reduced e.g. by working in a different propagation medium. To increase the thickness of the boundary layer in our experiments, roughness elements and spires are placed before the test section in the tunnel, as shown in Figure 3.7.

Figure 3.7 Roughness elements, placed before the test section in the wind tunnel, to increase the thickness of the boundary layer.

This results in a boundary layer of approximately 60 cm. At this height, 99% of the free-stream wind speed is reached. A scaling factor of 20 is used. This means that the height of the top of the corresponding full-scale boundary layer is much smaller than the typical heights observed in the atmosphere. It is however expected that the part of the atmosphere that will affect sound propagation (close to the surface, where the large gradients in wind speed occur) is modelled adequately. When noise barriers are present, it is also important that the height of the top of the boundary layer is well above the height of the noise barrier (in our case a few screen heights) for a good modelling of the influence of this obstacle on the wind profile.

Length is scaled with a factor 20. When looking at noise barrier performance, the ratio between the wavelength of sound and barrier height is important. So the frequencies in the scale model need to be a factor 20 larger in order to draw conclusions for traffic noise frequencies at full scale. The experimental sound frequencies ranged from 10 kHz to 20 kHz. This means that the frequencies in full scale will range from 500 Hz to 1000 Hz.

The properties of air do not scale. As a result, air absorption will be enhanced in the scale model, since it increases with increasing frequency. This effect will however be small, since the propagation distances are limited.

Both the speed of sound and the wind speed do not scale. This means that their ratio is the same at full scale and in the scale model. As a consequence, refraction of sound in the scale model will be similar to refraction at full scale. The Reynolds number gets scaled: wind speed and the viscosity of air do not scale, while length does scale. This means that the degree of turbulence in the scale model is 20 times smaller. As already mentioned, the experiment is performed only close to the barrier (up to a distance of 10 times the barrier height), and therefore it can be assumed that refraction of sound will be more important than turbulent effects. An overview of the parameters involved, with the indication whether they scale or not, is given in Table 3.1.

Table 3.1 Distinction between the scalable and non-scalable parameters and ratios involved in the wind tunnel experiment.

parameters that scale	**parameters that do not scale**
length	speed of sound
frequency of sound	wind velocity
Reynolds number	refraction of sound
	ratio length-wavelength of sound
	viscosity
	air absorption

In this study, downwind sound propagation over noise barriers is studied, for normal incidence. The barriers are made of very hard fibre plates, and have a height of 18 cm and a thickness of 1 cm.

Sound propagation in the wind tunnel is considered to be two-dimensional. The sidewalls in the tunnel are acoustical hard and act as mirrors. A narrow opening (8 mm) is cut out in the false floor (see Figure 3.8) of the test section in such a way that a coherent line source at ground level, over the complete width of the tunnel, is constructed. Underneath the gap, a loudspeaker box (acoustic hard) is placed, filled with tweeters, emitting a signal between 10 kHz and 20 kHz, consisting of pure tones with frequencies separated by 50 Hz. In this way, the emitted frequencies can be easily distinguished from wind tunnel noise. The line source had a sufficiently flat frequency spectrum. The tweeters have a diameter of 25 mm, and emit a constant sound pressure level in the frequency range of interest. The radiation pattern of the tweeters is of minor importance since the dimensions of the box determine the source directivity. Measurements in an anechoic chamber have indicated that this source has a uniform power emission over the full width of the box to within 1 dB. Reflection from the ceiling of the wind tunnel is prevented by using rock wool (with a thickness of 5 cm), which is very efficient in absorbing the experimental frequencies.

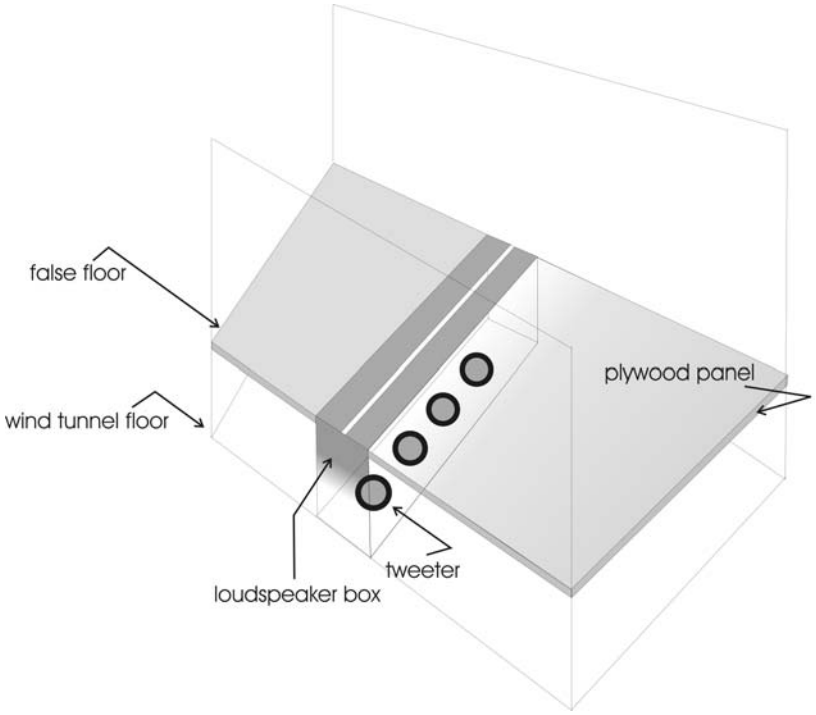

Figure 3.8 Sketch indicating how the line source at ground level was constructed in the wind tunnel.

The pressure field is measured with a ½-inch Bruel and Kjaer microphone (type 4190), with a flat response (±1 dB) up to 20 kHz, for normal incidence. The microphone can be placed with high precision at selected locations behind the downwind barrier. Distances ranged from 3 times the barrier height up to 10 times the barrier height. The microphone is placed $0.47H$ (where H is the height of the noise barrier) above the surface (8.5 cm at scale). This corresponds to the average height of the human ear at full scale (with a scaling factor of 20). To average out short-term fluctuations in the propagation parameters, 20 independent samples were used, measured during a period of about half a minute.

The spectrum of the background noise levels in the wind tunnel is shown in Figure 3.9 for a free-stream wind speed of 11 m/s, measured above the boundary layer. The background noise level amounts to 85 dB at a frequency of 1 kHz, 50 dB at 10 kHz and 20 dB at 20 kHz. Therefore it is quite easy to generate experimental sound levels well above this background level at frequencies between 10 and 20 kHz.

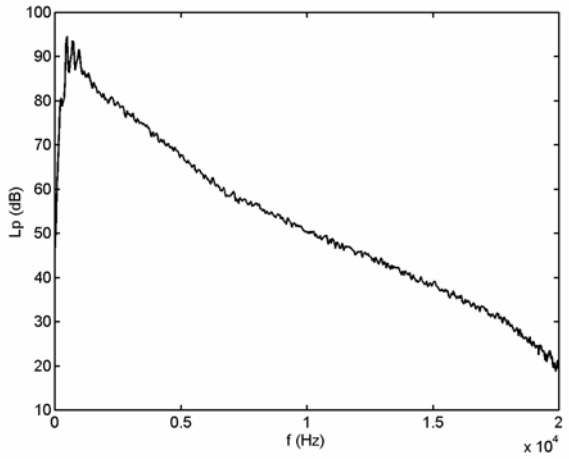

Figure 3.9 Background noise level in the wind tunnel, operating at 11 m/s.

Wind velocities are measured with 16 mm vane probes, with a precision of ± 0.1 m/s (see Figure 3.7). Only the positive, horizontal component of the wind speed can be measured with the available vanes. Data is obtained at a frequency of 1 Hz, and is averaged over a sample period of one minute. These values are then used to calibrate the *CFD* software *STAR-CD* [26] to obtain more detailed information on the air movement in the tunnel.

3.4.2.b Acoustical characterization of wind tunnel floor and noise barrier

The false floor in the wind tunnel consisted of plywood panels. To quantify reflection from this finite-impedance boundary, cross-spectrum measurements have been performed in an anechoic chamber. For frequencies between 10 kHz and 20 kHz, reflection coefficients for normal incidence between 0.4 and 0.5 were measured. Since confidence intervals on the measurements were quite large (± 0.1), these values are used as a first approximation. The parameters of the ground model described in Chapter 2.3.1.b are optimised, based on measured sound pressure levels at different distances from the source, in absence of noise barriers and in absence of wind. A trial-and-error procedure was set up to find a set of soil parameters that fitted the data well. In Figure 3.10 (a), total sound pressure levels in the (flat) frequency interval 10 kHz – 20 kHz at different locations in the wind tunnel are shown, relative to the first measure point.

Following ground parameters were used: k_s =1, φ = 0.5 and R= 100 kPa s/m^2. This means that a reflection coefficient (for normal incidence) of 0.40 at 10 kHz, and 0.36 at 20 kHz is obtained. The values obtained by the simulations lie within the range of the measured reflection coefficients.

Since flow resistivity may be scaled linearly [68, 76], a soil with a flow resistivity of 5 kPa s/m^2 at full scale is modelled. It has to be mentioned that the used panels were roughened and this results in a much softer surface than expected for plywood.

The simulated insertion loss (*IL*) for both a single noise barrier and a noise barrier on either side of the line source in absence of wind is compared to experimental data in Figure 3.10 (b) and (c). Simulations with a perfectly reflecting noise barrier were compared to simulations where a slightly absorbing noise barrier was used. Applying a small absorption coefficient (α = 0.06) at the surface of the barrier resulted in better agreement with experimental data.

The differences between measurements and simulations, especially when noise barriers are present, are probably due to the experimental set-up. As was indicated by the measurements of the absorption coefficient, the ground panels were not very homogeneous, resulting in local differences in acoustic impedance. As a result, agreement between measurements and simulations is worse at some distances. However, it was possible to find ground parameters that resulted in reasonable good agreement with measurements, as shown in Figure 3.10. Sound propagation over unscreened ground in case of a source at ground level is less sensitive to local changes in ground impedance, so for this situation agreement is better.

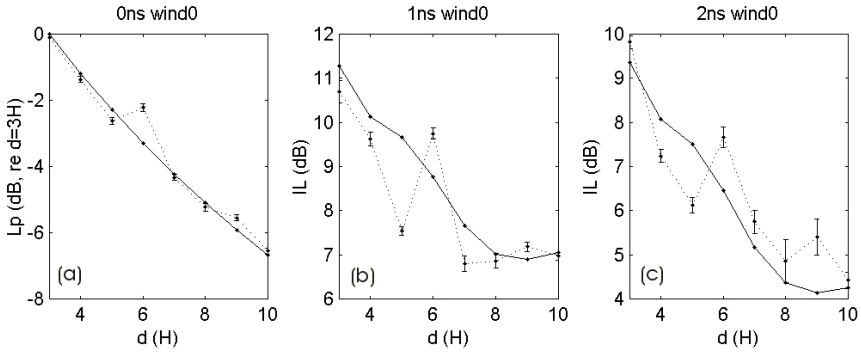

Figure 3.10 Results of fitting of both ground parameters and surface impedance of the noise barrier(s). In abscissa, the distance relative to the location of the (downwind) noise barrier is shown, expressed in screen heights. In (a), total sound pressure levels for the (flat) frequency interval 500-1000 Hz, relative to the first measurement point, for flat ground without screens, are shown. In (b) and (c) the insertion loss is presented with increasing distance behind the (downwind) noise barrier, for respectively a single noise barrier and a noise barrier on either side of the source (an overview of relevant distances and dimensions is given in Figure 3.12). Parameter fitting was done in absence of wind. Experimental results are indicated by the dashed lines, *FDTD* simulations by the full lines. The errorbars on the experimental data are an indication of the standard deviation based on 20 independent measurements.

3.4.2.c Windscreens

As a scale model for the wind reduction capacity of the canopy of trees, synthetic windscreens are used. Windbreaks are defined as structures that reduce wind speed, not only at the structure itself, but also at a certain windward and leeward distance (e.g. rows of trees or synthetic windscreens). When simulating or measuring the effect of windbreaks on wind profiles, porosity is the major property [77]. In this view, the synthetic windscreens can be used as a model for a row of trees with similar porosity.

A picture of the woven, polyester windscreen used in the experiments is given in Figure 3.11. It has a weight of 230-240 g/m^2 and a tensile strength of 1900 N/cm on wrap and weft. Its elasticity at breakage is about 20%. The screen has uniformly distributed square openings of 1 mm^2. The porosity of this windscreen is 32%.

To quantify the overall efficiency of a windscreen in terms of wind speed reduction, the normalized total reduction coefficient (TRc_n) is often used, and is defined as

$$TRc_n = \frac{1}{NM}\sum_{i}^{N}\sum_{j}^{M}\left[1-\frac{u_{ij}}{u_{0ij}}\right], \tag{3.16}$$

where i is an index representing a longitudinal distance behind the windscreen, j is an index representing a height above the ground surface, N is the number of observations along the longitudinal axis, M is the number of observations along the vertical axis, u_{ij} is the measured wind speed in presence of the screen at the place with index ij and u_{0ij} is the measured wind speed in absence of the screen at place ij.

The windscreens are firmly attached over the width of the wind tunnel, so the inevitable bending of the screen (in the middle) due to the wind is restricted to the natural movement of trees in wind (taking the scale factor of 20 into account).

Experiments revealed that a single windscreen with a porosity of about 32%, placed on the ground, results in a maximum total normalized reduction coefficient. This coefficient was calculated over the main area in which windscreens influence the wind profile i.e. heights ranging from 0.125 to 1.25 windscreen heights, and distances ranging from 2 times the screen height upwind from the windscreen to 32 times the screen height downwind from the windscreen [78]. In literature on windbreaks, values of optimal porosity for overall wind speed reduction range from 25% to 45%.

Although the porosity of (a single row of) trees for most species ranges from 50% to 70%, lower porosity can be achieved with a single row of selected (dense) species (e.g. hedges or some spruce species), or by simply planting an extra row of trees close behind the other one [77]. It is expected that planting a variety of trees in a single row might decrease porosity as well.

Figure 3.11 Picture of the windscreens used in the experiment.

3.4.2.d Tested configurations

Single noise barriers and noise barriers on either side of the acoustic source are tested, in combination with different configurations of windscreens. Large (2*H*, where *H* is the height of the noise barrier) and small (1*H*) windscreens are used, behind or in between the noise barriers. Some configurations with (large) gaps in the windscreens are also considered. An overview can be found in Figure 3.12. The noise barriers are placed at a distance of two times the barrier height, downwind and upwind from the line source, which is situated at ground level. Sources at ground level are important with respect to traffic noise. Tyre noise, which is excited very close to the street surface, is known to be the main noise source for traffic at high speeds [79]. Downwind sound propagation is considered, for a normal incident wind direction.

3.4.2.e Experimental results

The insertion loss *IL* of a noise barrier is defined as the sound pressure level in the frequency interval under investigation in absence of barriers minus the sound pressure level in the presence of noise barriers, at the same place.

The effect of the windscreens can be quantified by their net insertion loss *net IL*. The *net IL* is defined as the sound pressure level in the frequency interval under investigation for a certain noise barrier configuration *without* windscreens minus the sound pressure level of the same noise barrier configuration *with* windscreens, at the same place and for the same (incident) wind speed, measured above the boundary layer.

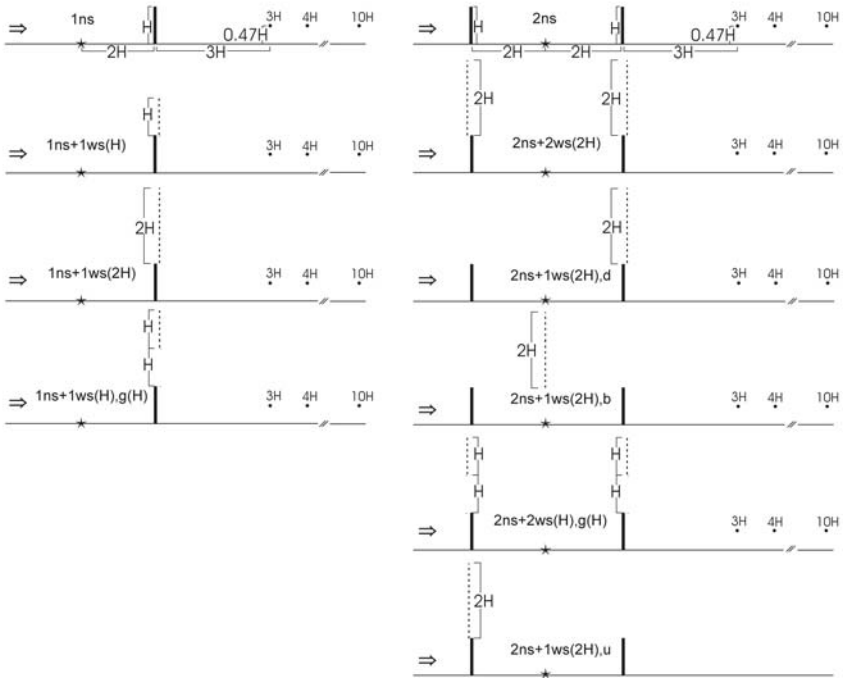

Figure 3.12 Overview of the tested configurations and their dimensions, relative to the noise barrier height. The configurations have the following codes: *1ns* = **1** **n**oise **s**creen; *1ns+1ws(H)* = **1** **n**oise **s**creen and **1** **w**ind**s**creen (height of windscreen = barrier height); *1ns+1ws(2H)* = **1** **n**oise **s**creen and **1** **w**ind**s**creen (height of windscreen = 2 times the barrier height); *1ns+1ws(H),g(H)* = **1** **n**oise **s**creen and **1** **w**ind**s**creen with a gap of length *H* in the windscreen, *2ns* = **2** **n**oise **s**creens; *2ns+2ws(2H)* = **2** **n**oise **s**creens and **2** **w**ind**s**creens; *2ns+1ws(2H),d* = **2** **n**oise **s**creens and **1** **w**ind**s**creen, placed behind the **d**ownwind noise barrier; *2ns+1ws(2H),b* = **2** **n**oise **s**creens and **1** **w**ind**s**creen, placed **b**etween the noise barriers; *2ns+2ws(H),g(H)* = **2** **n**oise **s**creens and 2 **w**ind**s**creen, with a **g**ap of length *H* in both windscreens; *2ns+1ws(2H),u* = **2** **n**oise **s**creens and 1 **w**ind**s**creen, placed before the **u**pwind noise barrier (*only in simulations*).

The effect of wind on noise barrier performance is significant (see Table 3.2, Table 3.3 and Table 3.4, and also Figure 3.14 and Figure 3.15). Close to the barrier (from 3*H* to 6*H*), only small differences in *IL* arise. The wind tunnel experiments of DeJong and Stusnick confirm these results [65]. At larger distances, the wind effect becomes important. Quantitative agreement with other experiments is found [64]. With increasing wind speed, the performance of the

noise barriers becomes worse. At a distance of 10*H*, more than 10 dB in barrier performance for a normal incident wind of 11 m/s is observed. As a consequence, the single noise barrier in our test becomes useless at that distance. For noise barriers on either side of the line source, almost the same trends are noticed. The overall performance for this configuration in absence of wind is worse, due to reflection on the screen located upwind from the source. For the highest wind speed in the experiment, at distances larger than 8*H* behind the downwind screen, the presence of the noise barrier results in a significantly worse situation. Propagation over unscreened ground would result in a better attenuation at these distances.

Results for the *net IL* are given in Table 3.5 and Table 3.6. Based on the data in absence of wind, it can be concluded that the windscreens are about acoustical neutral. The average *net IL* values are close to zero.

Without considering the configurations with gaps in the windscreens (*1ns+1ws(H),g(H)* and *2ns+2ws(H),g(H)*), following observations can be made. At limited distances from the downwind noise barrier, the net effect of the windscreens is small, and sometimes slightly negative. This effect can be attributed to scattering on the windscreen. At larger distances, the net effect of the windscreens is always positive.

When comparing a single noise barrier with a low (*1H*, *1ns+1ws(H)*) and a high (*2H*, *1ns+1ws(2H)*) vegetation screen, there is not much difference between them. It seems that only the zone just above the barrier needs to be shielded to improve the insertion loss for the receivers considered.

If noise barriers are present at either side of the line source, a larger improvement by placing windscreens can be obtained. The performance of a single noise barrier can be improved with 3dB at a distance of 10*H* behind the downwind noise barrier, while an increase of 6dB is possible for a noise barrier on either side of the source and for a good placement of the windscreen(s). The best configuration among the tested ones seems to be the one with a large windscreen behind the downwind noise barrier (*2ns+1ws(2H)*).

The configurations with gaps in the windscreens result in an important, negative effect close to the barriers, which makes them less suitable. The positive *net IL* up to 4dB for the large wind speed and configuration (*1ns+1ws(H),g(H)*) is probably due to experimental errors. This statement is confirmed by the observation that at low wind speeds these (relatively) large positive effects are not measured. Moreover, this is the only case where the trends observed at *wind1* are not found at *wind2* for the same configuration. Simulations (see further) will confirm this statement.

Table 3.2 Measured *IL* (in dB) at the test distances (expressed in screen heights) in absence of wind, together with the averages over the first part (av. *3H-6H*) and second part (av. *7H-10H*) of the test section, and a global average (av. *3H-10H*).

u = 0 m/s	*1ns*	*1ns+1ws(H)*	*1ns+1ws(2H)*	*1ns+1ws(1H),g(H)*	*2ns*	*2ns+2ws(2H)*	*2ns+1ws(2H),d*	*2ns+1ws(2H),b*	*2ns+2ws(H),g(H)*
3H	10.7	10.8	10.9	10.2	9.8	9.5	9.5	9.4	9.5
4H	9.6	9.9	9.4	8.7	7.2	8.2	8.4	7.5	7.7
5H	7.5	7.5	7.6	7.6	6.1	6.2	6.4	5.5	6.3
6H	9.7	9.6	10.1	8.7	7.7	7.4	7.7	7.7	7.5
7H	6.8	7.2	7.9	6.5	5.7	4.9	5.5	5.4	5.5
8H	6.9	7.3	6.8	6.2	4.9	4.8	5.1	5.3	4.9
9H	7.2	7.4	7.4	6.2	5.4	5.9	4.9	5.3	4.8
10H	7.0	6.2	7.1	5.7	4.4	4.4	4.9	4.5	4.0
av. 3H-6H	9.3	9.4	9.3	8.8	7.7	8.0	8.1	7.5	7.8
av. 7H-10H	7.0	7.0	7.3	6.1	5.1	5.0	5.1	5.1	4.8
av. 3H-10H	8.2	8.2	8.4	7.5	6.4	6.4	6.6	6.3	6.3

Table 3.3 Measured *IL* (in dB) at the test distances (expressed in screen heights) for a wind speed of 6.4 m/s (measured above the boundary layer).

u= 6.4 m/s	*1ns*	*1ns+1ws(H)*	*1ns+1ws(2H)*	*1ns+1ws(1H),g(H)*	*2ns*	*2ns+2ws(2H)*	*2ns+1ws(2H),d*	*2ns+1ws(2H),b*	*2ns+2ws(H),g(H)*
3H	10.6	10.7	10.2	9.9	9.2	9.4	8.9	9.3	8.9
4H	9.8	9.6	9.3	8.4	7.6	8.2	8.4	8.0	7.2
5H	7.7	7.9	8.1	5.8	5.6	6.5	6.6	6.3	5.2
6H	9.6	9.9	9.9	7.0	6.4	7.3	7.8	7.3	6.5
7H	7.3	7.9	7.9	5.0	5.0	5.4	6.6	5.3	4.8
8H	5.4	5.8	5.9	3.2	2.1	4.0	4.6	3.4	2.8
9H	4.3	5.4	5.3	1.9	1.6	3.0	5.2	3.2	2.2
10H	2.8	3.7	3.8	1.1	0.3	2.2	3.7	2.4	1.3
av. 3H-6H	9.4	9.5	9.4	7.8	7.2	7.8	7.9	7.7	7.0
av. 7H-10H	5.0	5.7	5.7	2.8	2.3	3.7	5.0	3.6	2.8
av. 3H-10H	7.2	7.6	7.5	5.3	4.7	5.8	6.5	5.6	4.9

Table 3.4 Measured *IL* (in dB) at the test distances (expressed in screen heights) for a wind speed of 11 m/s (measured above the boundary layer).

u= 11 m/s	*1ns*	*1ns+1ws(H)*	*1ns+1ws(2H)*	*1ns+1ws(1H),g(H)*	*2ns*	*2ns+2ws(2H)*	*2ns+1ws(2H),d*	*2ns+1ws(2H),b*	*2ns+2ws(H),g(H)*
3H	10.0	10.1	9.6	8.8	8.9	9.4	8.4	9.5	7.5
4H	8.3	8.9	8.6	5.8	6.9	7.7	7.5	8.0	6.4
5H	7.0	7.7	7.3	4.1	5.0	7.2	7.1	6.1	4.5
6H	6.9	8.2	7.8	3.9	4.6	6.3	7.9	6.8	4.3
7H	3.2	4.9	5.4	4.9	1.5	3.5	5.6	4.1	1.5
8H	2.1	4.2	4.5	4.6	-0.8	2.7	4.6	3.1	0.6
9H	0.0	2.8	3.2	3.7	-2.7	1.3	3.5	1.5	-1.1
10H	-0.8	2.1	2.5	3.2	-3.3	0.9	2.2	0.9	-0.6
av. 3H-6H	8.0	8.7	8.3	5.6	6.4	7.7	7.7	7.6	5.7
av. 7H-10H	1.1	3.5	3.9	4.1	-1.3	2.1	4.0	2.4	0.1
av. 3H-10H	4.6	6.1	6.1	4.9	2.5	4.9	5.9	5.0	2.9

Table 3.5 *Net IL* (in dB) by the windscreens at the test distances (expressed in screen heights), together with the averages over the first part (av. *3H-6H*) and second part (av. *7H-10H*) of the test section, and a global average (av. *3H-10H*). The configurations with one noise barrier are considered. Three wind speeds, measured above the boundary layer, are shown: u=0 m/s, u=6.4 m/s and u=11 m/s.

	1ns+1ws(H)			*1ns+1ws(2H)*			*1ns+1ws(1H),g(H)*		
	u = 0 m/s	u= 6.4 m/s	u= 11 m/s	u = 0 m/s	u= 6.4 m/s	u= 11 m/s	u = 0 m/s	u= 6.4 m/s	u= 11 m/s
3H	0.1	0.1	0.1	0.2	-0.4	-0.4	-0.5	-0.7	-1.2
4H	0.2	-0.2	0.6	-0.2	-0.5	0.3	-0.9	-1.4	-2.5
5H	0.0	0.2	0.7	0.1	0.4	0.3	0.1	-1.8	-2.9
6H	-0.1	0.2	1.4	0.3	0.3	0.9	-1.0	-2.6	-3.0
7H	0.4	0.5	1.7	1.1	0.6	2.2	-0.3	-2.3	1.7
8H	0.4	0.3	2.1	-0.1	0.4	2.4	-0.7	-2.3	2.5
9H	0.2	1.1	2.9	0.2	0.9	3.2	-1.0	-2.4	3.8
10H	-0.8	0.9	2.9	0.1	1.0	3.3	-1.2	-1.7	4.0
av. 3H-6H	0.0	0.1	0.7	0.1	-0.1	0.3	-0.6	-1.6	-2.4
av. 7H-10H	0.1	0.7	2.4	0.3	0.7	2.8	-0.8	-2.2	3.0
av. 3H-10H	0.1	0.4	1.5	0.2	0.3	1.5	-0.7	-1.9	0.3

Table 3.6 *Net IL* (in dB) by the windscreens at the test distances (expressed in screen heights), together with the averages over the first part (av. *3H-6H*) and second part (av. *7H-10H*) of the test section, and a global average (av. *3H-10H*). The configurations with a noise barrier on either side of the source are considered. Three wind speeds, measured above the boundary layer, are shown: u=0 m/s, u=6.4 m/s and u=11 m/s.

	2ns+2ws(2H)			*2ns+1ws(2H),d*			*2ns+1ws(2H),b*			*2ns+2ws(H),g(H)*		
	u = 0 m/s	u= 6.4 m/s	u= 11 m/s	u = 0 m/s	u= 6.4 m/s	u= 11 m/s	u = 0 m/s	u= 6.4 m/s	u= 11 m/s	u = 0 m/s	u= 6.4 m/s	u= 11 m/s
3H	-0.3	0.1	0.5	-0.3	-0.4	-0.5	-0.4	0.1	0.6	-0.3	-0.3	-1.4
4H	1.0	0.6	0.8	1.2	0.8	0.6	0.3	0.3	1.1	0.5	-0.4	-0.5
5H	0.0	1.0	2.2	0.3	1.0	2.1	-0.6	0.8	1.0	0.2	-0.3	-0.5
6H	-0.2	0.8	1.7	0.0	1.3	3.3	0.0	0.8	2.2	-0.2	0.1	-0.3
7H	-0.8	0.4	2.0	-0.2	1.6	4.1	-0.4	0.2	2.6	-0.2	-0.2	0.1
8H	0.0	2.0	3.4	0.2	2.6	5.4	0.4	1.3	3.8	0.0	0.7	1.4
9H	0.5	1.3	4.0	-0.5	3.5	6.1	-0.1	1.6	4.1	-0.6	0.6	1.5
10H	0.0	1.9	4.2	0.5	3.5	5.5	0.1	2.1	4.1	-0.4	1.0	2.6
av. 3H-6H	0.1	0.6	1.3	0.3	0.7	1.4	-0.2	0.5	1.2	0.0	-0.2	-0.7
av. 7H-10H	-0.1	1.4	3.4	0.0	2.8	5.3	0.0	1.3	3.7	-0.3	0.5	1.4
av. 3H-10H	0.0	1.0	2.4	0.2	1.7	3.3	-0.1	0.9	2.4	-0.1	0.2	0.4

3.4.2.f Simulation of noise barrier performance in wind in the presence of windscreens

CFD calculations

The *CFD* software *STAR-CD* is used to calculate the wind flow in detail in the neighbourhood of the noise barriers. Calibration of the simulated flow field is performed as follows.

Wind velocities, in absence of noise barriers are measured in the wind tunnel at a height of 3 cm, 8.5 cm, 18 cm, 28.5 cm and 42.5 cm above the surface, for a wind speed of 6.4 m/s and 11 m/s (measured above the boundary layer). This information is used to find the appropriate parameters of a typical, logarithmic wind speed profile:

$$v_z = \frac{u_*}{\kappa} \ln \frac{z}{z_0}, \tag{3.17}$$

where z is the height above the surface, v_z is the velocity at height z, κ is the von Kármán constant (= 0.4), u_* is the friction velocity and z_0 is the roughness length. A curve-fit on the experimental results yielded respectively u_* = 0.3 m/s and z_0 = 0.2 mm for 6.4 m/s, and u_* = 0.77 m/s and z_0 = 1 mm for 11 m/s. This information is used as an inflow boundary condition for the *CFD* calculations.

Measurements of flow velocities at different locations throughout the wind tunnel in the presence of two noise barriers without windscreens (*2ns*) are used in a second step to find an appropriate turbulence model and its parameters. A wind speed of 11 m/s above the boundary layer is used for that purpose.

This calibration is based only on the positive horizontal components of the flow velocity since the vertical and negative horizontal component could not be measured with the available anemometers. Every measurement lasted 1 minute, with a sample frequency of 1 Hz. This is necessary since the flow in the wind tunnel is turbulent. For further comparison, the time-averaged values are used. The standard deviation on the velocity measurements has an average value of about 0.3 m/s.

Good correspondence between wind velocity calculations and experimental data is obtained using a steady state, k-ε turbulence flow model, as shown in Figure 3.13. At most places, the differences between simulated and measured horizontal flow velocities are below 1 m/s. Taking into account the time dependence of the flow, this is a good approximation. In between the noise barriers and in the recirculation zone behind the barriers, measurements and simulations are not compared below the noise barrier height, since backflow could not be measured.

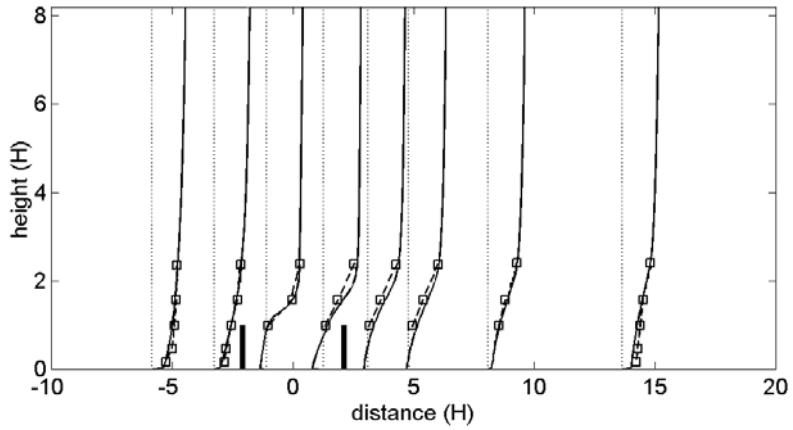

Figure 3.13 Wind profiles at some place in the wind tunnel. *CFD* calculations are indicated with the full lines, the measurements are shown with the squares.

To model the wind reduction by the windscreens, the pressure drop as a function of the orthogonal component of the flow velocity through the windscreen is inserted. Measurements in the velocity range of interest have indicated that the pressure drop over the windscreens in our test set-up can be described with high correlation (R^2 = 99.6%) by the following quadratic equation:

$$\Delta p_0 = a v_0^2 + b v_0 , \tag{3.18}$$

with a = 5.040 Pa s^2/m^2 and b = 0.092 Pa s/m, for a windscreen of 32% [80].

FDTD calculations

Since the windscreens have shown to be more or less acoustical neutral, only the influence of the windscreens on the background flow is modelled.

In Figure 3.14 and Figure 3.15, a comparison between measured and numerically simulated *net IL* (for the frequency interval 500-1000 Hz) is made for respectively the single noise barrier configurations and the configurations were at either side of the source a noise barrier is present. Results are shown with increasing distance, for both the low wind speed (*wind1*) and the high wind speed (*wind2*) tested in the wind tunnel.

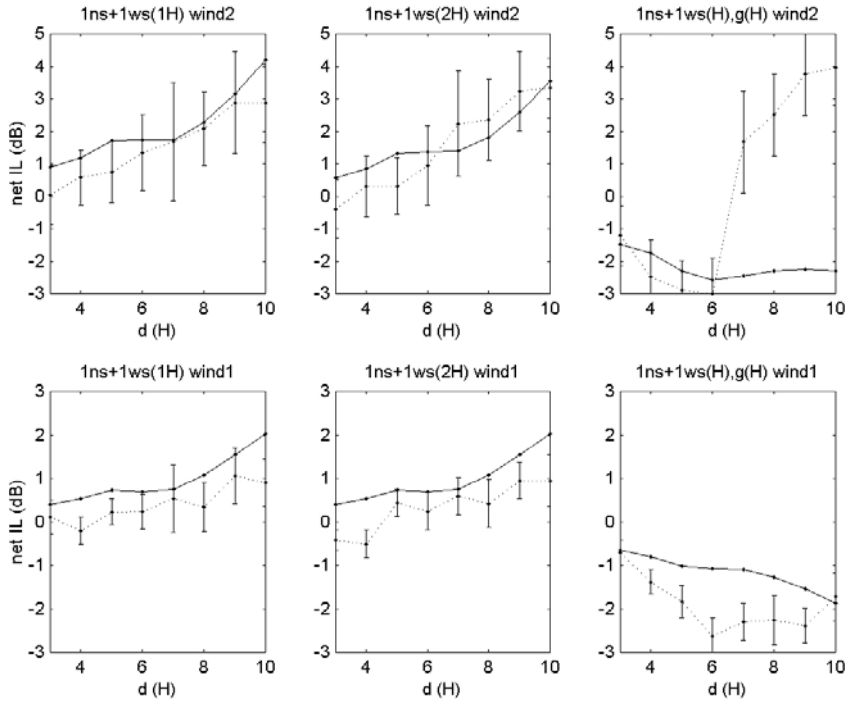

Figure 3.14 Comparison between *FDTD* simulations (full lines) and experimental results (dashed lines) for single noise barrier configurations. In the upper plots, the incident wind speed, measured above the boundary layer was 11 m/s (wind2), in the lower figures 6.4 m/s (wind1).

In general, the agreement between measurements and simulations is good. Besides the capability of the model to simulate screen-induced refraction of sound (as shown in Chapter 3.3), the effect of wind reduction by windscreens or trees is well described. The comparison between measurements and simulations is performed at only one height above the surface. E.g. differences in the position of the measurement points in the experiment and in the simulations may be responsible for a local, worse correspondence, since the wavelengths of the experimental sound frequencies are small.

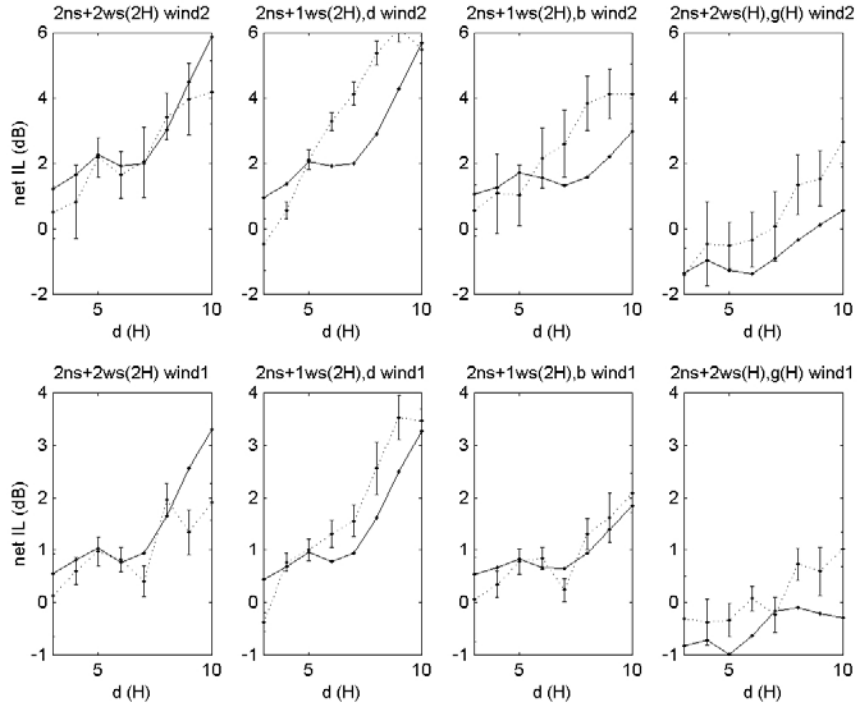

Figure 3.15 Comparison between *FDTD* simulations (full lines) and experimental results (dashed lines) for noise barriers on either side of the source. In the upper plots, the incident wind speed, measured above the boundary layer was 11 m/s, in the lower figures 6.4 m/s.

Significant differences between measured and simulated data are observed for some double noise barrier configurations in combination with a large wind speed (*wind2*) (e.g. *2ns+1ws(2H),d* and *2ns+1ws(2H),b*). In contrast to e.g. situation *2ns+2ws(2H)* where shielding by the windscreens is larger, a more complex and turbulent wind flow is observed, which makes these configurations more difficult

to simulate accurately. In Figure 3.16 and Figure 3.17, the turbulent kinetic energy (k) field for some configurations at *wind2* is shown. The presence of windscreens decreases turbulent intensity in the acoustic shadow zone, except for the situations with gaps in the windscreens. Large values of k indicate places where the instantaneous (background) flow velocity is highly fluctuating.

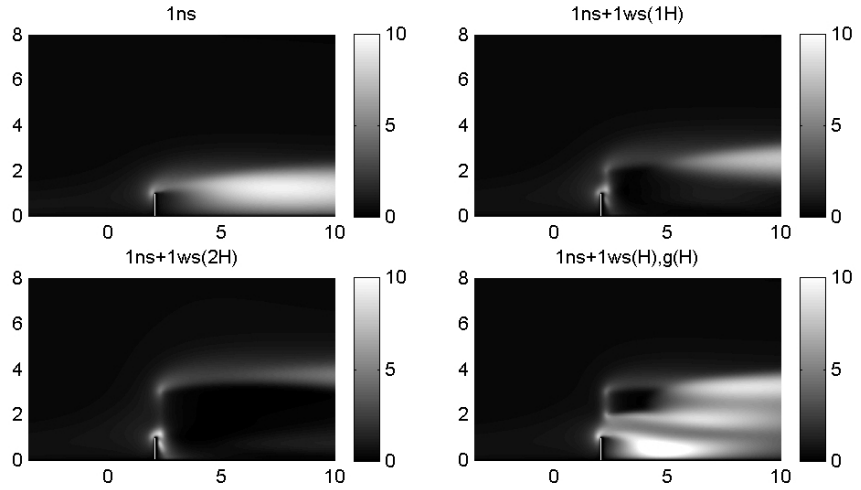

Figure 3.16 Field plots of turbulent kinetic energy k (expressed in m²/s²) for the single noise barrier configurations. Distances, relative to the location where the acoustic source is present, and heights above the ground are expressed in noise barrier heights.

For configurations *1ns+1ws(H),g(H)* and *2ns+2ws(H),g(H)* a highly turbulent flow field is observed, already for *wind1*. This makes accurate prediction of *net IL* for the situations with large gaps in the windscreens more difficult. Nevertheless, trends and the negative *net IL* are predicted. The large discrepancy between measured and simulated net insertion loss for situation *1ws(H),g(H)* at large distances in the presence of *wind2* is supposed to be due to experimental errors (see section 3.4.2.e). This statement is confirmed by the acoustical simulations: negative values of *net IL* remain at all simulated distances.

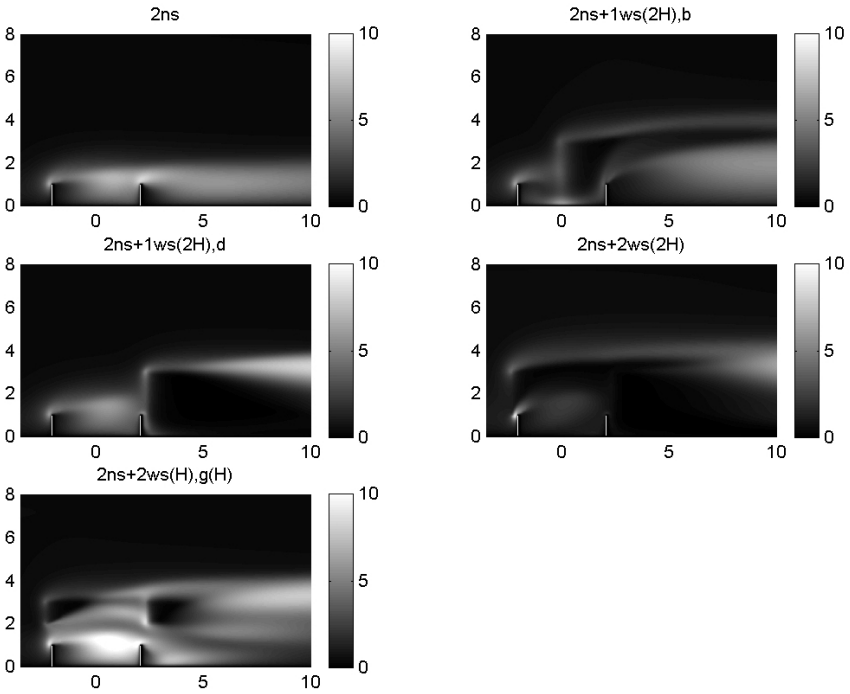

Figure 3.17 Field plots of turbulent kinetic energy *k* (expressed in m²/s²) for some configurations with noise barriers on both sides of the source. Distances, relative to the location where the acoustic source is present, and heights above the ground are expressed in noise barrier heights.

Large-scale velocity turbulence is taken into account during the *CFD* simulation by using the steady-state, k-ε turbulence model. Small eddies that are responsible for acoustic scattering in the shadow zone of the barrier, and their increased angular strength by the screen-induced turbulence, is not modelled. Nevertheless, most configurations seem adequately modelled. Moreover, in the configurations of windscreens with practical applications (without gaps), a reduction in the strength of turbulence is observed. Since we are also interested in the total effect of frequency intervals, it is expected that effects due to the variable nature of the flow will be small.

3.4.2.g Interaction between acoustic waves and perforated screens

The used screens are in the path of the sound passing just over the barrier. In absence of wind, there will be some reflection caused by the porous windscreens, which is expected to be small. This is proven by the data in Table 3.5 and Table 3.6: in absence of wind, the average values for *net IL* approximate zero (see further). In flow, theory on perforated screens predicts a larger interaction between sound waves and the screens. Besides reflection, there will be some absorption of acoustic energy. It is investigated theoretically to what extent the interaction between sound and screen is important in the total effect of the windscreens.

The use of a perforated screen provides absorption of acoustic energy by vorticity production of the acoustic motions near aperture edges. This effect becomes important in flow, since this generated vorticity is convected away. In this way, a certain amount of energy of the sound wave is permanently lost [81]. This effect can be quantified as proposed in Ref. [81]. The area-averaged (acoustic) velocity $v_{aperture}$ in a circular aperture is related to the pressure drop over the aperture by the following formula [81]:

$$\rho_0 \frac{A_{aperture}}{K_R} \frac{dv_{aperture}}{dt} = -\Delta p \,, \tag{3.19}$$

where $A_{aperture}$ is the area of one circular aperture and K_R is de Raleigh conductivity of the aperture. The latter has the dimension of length, and is analogous to resistance in Ohm's law. The apertures are assumed to be homogeneously distributed over the screen. The screen itself is supposed to be infinitely thin. The acoustic velocity over a screen with porosity α equals:

$$v = \alpha v_{aperture} \,. \tag{3.20}$$

Porosity can be written by the following identity:

$$\alpha = NA_{aperture} \,, \tag{3.21}$$

where N is the number of apertures per unit area of the screen. The Raleigh conductivity of a circular aperture in convective flow with velocity U_c can be calculated with the following expression:

$$K_R = 2R_{aperture}\left(1+\frac{\frac{\pi}{2}I_1(S_n)e^{-S_n}-iK_1(S_n)\sinh(S_n)}{Sn\left[\frac{\pi}{2}I_1(S_n)e^{-S_n}+iK_1(S_n)\cosh(S_n)\right]}\right), \quad (3.22)$$

where I_1 and K_1 are the modified Bessel functions of the first order, and respectively first and second kind, where $R_{aperture}$ is the radius of the (equivalent) circular aperture and S_n is the Strouhal number, defined as:

$$S_n = \frac{\omega R}{U_c}. \quad (3.23)$$

When the Strouhal number is large, equation (3.22) simplifies to:

$$K_R \approx 2R_{aperture}\left(1-\frac{i}{S_n}\right) \text{ for } \quad S_n \to \infty. \quad (3.24)$$

The (energetic) reflection coefficient R and transmission coefficient T can be calculated using the following formulas:

$$R = \left|\frac{k_0\cos\theta}{k_0\cos\theta + i2NK_R}\right|^2, \quad (3.25)$$

$$T = \left|\frac{i2NK_R}{k_0\cos\theta + i2NK_R}\right|^2, \quad (3.26)$$

where θ is the angle of incidence. The absorption coefficient A is calculated from equation (3.27):

$$A = 1 - R - T. \quad (3.27)$$

In absence of flow, there will (only) be reflection on the windscreens. It is calculated that for an (average) incident angle of 45° and a frequency of 15 kHz, the reflection coefficient is about 7%. This means that 0.34 dB of the effect of the windscreens can be attributed to the interaction between the perforated screens and the acoustic waves. The average horizontal wind velocity component in the aperture will not be larger than 3 m/s in all of the tested configurations. Using previous equations, the absorption of acoustic energy by the perforated screen should be smaller than 3%. Since the reflection by the windscreen is not affected by the flow, this means that for the net effect of the windscreens in flow, maximum 0.47 dB can be assigned to reflection and absorption. Therefore it is

concluded that the positive effect of the windscreens, caused by the interaction between the perforated screen and the acoustic waves, is small in comparison with the decreased screen-induced refraction.

3.4.2.h Conclusions

The wind tunnel study has indicated that screen-induced refraction of sound is important when considering noise barrier performance in wind. A traffic noise situation at scale was set up. A line source emitted a flat frequency interval between 500 Hz and 1000 Hz at full scale. For both a single noise barrier and a noise barrier on either side of a line source, the barrier efficiency becomes zero or even negative for a large wind speed, at distances larger than 8H. In the presence of windscreens, improvements up to 3 dB are possible for the single noise barrier configuration, and up to 6 dB for the double noise barriers in the experiment. The influence of the altered wind profile on sound propagation over noise barriers can be simulated with success for most configurations of windscreens, based on (average) flow calculations with the k-ε model. Worse correspondence between measurements and simulations at some place may be due to the inhomogeneous acoustical impedance of the wind tunnel floor, and by turbulent scattering into the acoustic shadow zone, which is not accounted for. However, the configurations of windscreens with practical applications (without gaps) lead to a decrease in the strength of turbulence near the barriers.

3.4.3 Field experiment

3.4.3.a Interactions between trees and sound

The interactions between trees and sound waves have been analysed by many authors. In this chapter, an overview is given of some studies on important phenomena like scattering and attenuation of sound by trees behind a barrier, wind-induced vegetation noise, and sound propagation through multiple rows of trees.

Schuller et al. measured the effect of a row of trees (in absence of wind) behind a small barn, and noticed a reduced attenuation at high frequencies (>1-2 kHz) due to scattering, while the mid-frequencies were more attenuated [82, 83]. When the trees lost their leafs, the positive effect in the mid-frequency range remained unchanged.

Trees in wind will also generate noise. Schuller et al. stated that deciduous trees with a dense canopy produce high-frequent sound. Noise levels from deciduous trees in wind are proportional to the number of leaves [82]. As for deciduous

species, the rustling of leaves finds its origin in vibrations induced by the unsteady contacts between leaves and neighbouring leaves or branches. Indeed, a leaf alone in a flow generates almost no sound, in contrast to two leaves between which contacts are allowed. Noise from coniferous species is generated aero-acoustically: the von Kármán vortex shedding behind the needles will force the needles to vibrate. The spectrum of such an "aeolian tone" has a peak at the Strouhal frequency, which is proportional to the flow velocity and inversely proportional to the dimension of the needle cross-section [84]. Both in-situ experiments at the edge of different forests and experiments in an anechoic chamber are performed by Fegeant [84, 85]. The shape of the emission spectra does not change with increasing wind speed for deciduous trees. Emission peaks can be found around 4-5 kHz. Branches are responsible for the low frequency emission, while the rustling of leaves generates a high-frequent sound. It is also stated that some species generate more noise than others do, and the difference may be in the order of 10 dB. The aspen is an example of a "noisy species", while birches and oaks generate less noise when there is wind [85]. Boersma characterized the natural ambient sound environment inside a deciduous forest with increasing wind speed [86]. Schuller et al. [82], Fegeant [85] and Boersma [86] indicate that wind-induced vegetation noise (sound pressure levels, in decibels) increases linearly with the logarithm of wind speed. In Ref. [82] a factor of 50 is cited for A-weighted sound pressure levels. Below a wind speed of 7-8 m/s, wind-induced vegetation noise did not follow this proportionality, and increases more slowly when wind speed increases. For non-weighted, peak levels at the edge of a deciduous forest, a factor of 30 is measured by Fegeant [85], starting from a wind speed of 2 m/s. In the experiments of Boersma [86], a factor of 50-55 is found for the A-weighted, 95^{th} percentile values, based on measurements during periods of 30 minutes. The monitoring took place inside a deciduous forest. Below 3 m/s (measured above the canopies), wind speed did not affect the sound pressure levels by the trees.

Many descriptions of experiments can be found in literature on sound propagation through multiple rows of trees (forests). For frequencies lower than 1 kHz, ground attenuation is considered to be the prominent factor in absorption of sound due to the formation of a highly porous humus layer [87]. In Reference [88], the separate effect of tree trunks is investigated by means of detailed numerical simulations. The ground surface was modelled as perfectly reflecting. It was shown that for frequencies below 1kHz, the multiple reflections between tree trunks also results in an important attenuation, depending on the number density and the cross-section radius of the tree trunks.

For higher frequencies (above 1 kHz) the attenuation is caused by vegetation. While trunks and branches will mainly reduce sound by scattering, leafs will

scatter and also absorb sound, due to viscous dissipation and energy losses caused by heat conduction through the boundary layer of leaves [87]. Martens et al. investigated the absorption of sound energy by single leaves and stated that a very small amount of energy is effectively absorbed. Since the number of leafs in the canopy of trees is very large, this is an important factor [89]. With increasing frequencies the absorption will become the most important factor [90].

Several rough approximations for high frequency attenuation of sound propagating through trees can be found in literature. A square-root law for frequency dependence of sound attenuation by vegetation is proposed i.e. 3 dB increase in attenuation per doubling of frequency. Other models predict 6 dB attenuation per doubling of frequency. Of course these estimations are strongly dependent on vegetation type, vegetation density, distribution of trunk diameters, etc. [87, 91, 92]. Martens also performed an experiment with a model forest in an anechoic chamber. In the mid-frequency range, dependent of the type of vegetation, there is often a small amplification of sound at the canopy height, relative to the situation without trees. Higher frequencies will be largely reduced when propagating through the vegetation. Foliage can be considered in this way as a low-pass filter [93]. Total sound pressure levels resulting from traffic noise will not be changed when propagation through rows of trees: the frequencies of the dominant peaks are too low to be amplified or weakened [93]. Roadside trees do not significantly influence traffic noise at ground level [94].

In the wind tunnel experiment, the acoustical interactions between trees and sound are not modelled. Only the wind reduction capacity of a row of trees is accounted for. Therefore, a field experiment is performed to confirm that placing a row of trees is a valuable solution to improve noise barrier performance in wind in traffic noise situations.

3.4.3.b Site description

The in-situ experiment is performed along a major highway (E40), near the city of Aalst, in Belgium. A sketch of the geometrical configuration of the field experiment is given in Figure 3.18, together with the relevant distances relative to the noise barrier height. An ortho-photo of the part of the highway under investigation is shown in Figure 3.19, while in Figure 3.20 some photographs are shown on either side of the barrier at points *A* and *B*. On both sides of the highway, a long concrete noise barrier is situated with an average height of 4 m. The highway consisted of 3 traffic lanes and an emergency lane in both directions. A somewhat raised verge is situated in the middle of the highway. The distance between the noise barriers on either side of the road is about 32 m.

Measuring station *A* is placed behind a part of the noise barrier where no trees are present. A single row of trees (and bushes) of about two times the barrier height is situated at measuring point *B*.

The distance between point *A* en *B* is about 100 m. Simultaneous measurements are performed, together with meteo-observations near point *A*. The noise barrier height at place *A* (3.75 m) is somewhat lower than at place *B* (4.25 m). The measurements will be performed at the same distances and heights relative to the noise barrier height at both places. The ground near point *A* is a sandy (grass)land. Measuring point *B* is situated in a pasture with a uniform grass-covered soil.

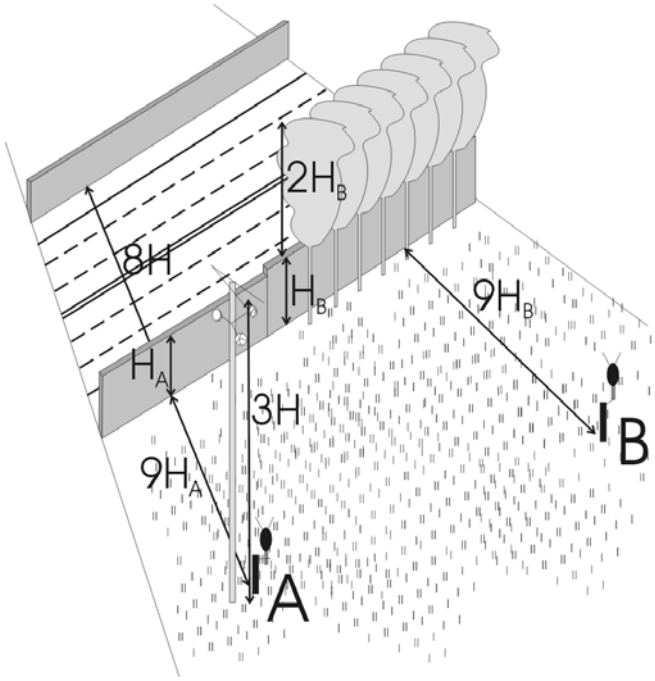

Figure 3.18 Sketch of the geometrical configuration of the in-situ experiment. The relevant distances and heights are shown, relative to the noise barrier height(s). H_A and H_B are the noise barrier heights near microphone positions *A* and *B* respectively, *H* is the average height of the noise barriers of part of the highway under investigation.

Figure 3.19 Ortho-photo indicating the positions of the two microphones.

Figure 3.20 Photographs near point *B* (on the left) and *A* (on the right), taken from the highway towards the noise barrier (above), and from the microphone positions towards the noise barrier (below).

Hourly countings of the number of vehicles (averaged over all the days of the week) near the noise barrier under investigation, measured by the Flemish government in 2000, are given in Figure 3.21. The traffic density on the part of the highway under investigation is sufficiently high to make traffic noise a continuous and dominant contribution to the noise climate.

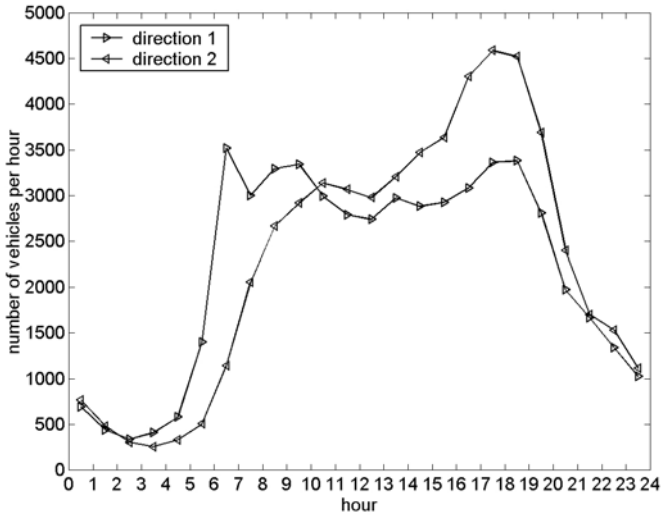

Figure 3.21 Number of vehicles per hour, averaged over all days of all week in the year 2000. The microphones are placed behind the noise barrier closest to the traffic lanes in direction 1.

A wide variety of trees are present behind the barrier at site *B*. The monitoring is performed continuously and lasted from the middle of the summer (end of July 2001) to the beginning of fall (end of October 2001). So the trees were in (full) leaf during the experiment. A quick determination revealed that the population consisted in first place of ashes (*Fraxini*) and rowan trees (*Sorbus aucuparia L.*). Also some oaks (*Querci*) were present, together with small bushes.

The (visual) porosity of the canopy of trees at measuring point B can only be estimated roughly. A possible way to do this is using a digital photograph. With standard image processing software, a multicoloured detailed picture of the trees is reduced to a 1-bit per pixel image. The (white) air stays white, the green (leafs) and brown (branches and twigs) colours become black. The number of pixels in each category can be counted and in this way the porosity can be

calculated. Using this procedure, the visual porosity of the canopy is estimated in the range from 13% to 15%. The porosity during windy conditions can however be higher due to the movement of branches and twigs and results in a larger unobstructed area. A second estimate of the porosity has been made at the end of October 2001, and yielded 24%.

3.4.3.c Experimental set-up and instrumentation

At point *A* en *B* ½ inch microphones (SIP95, 01dB) are used, together with the B&K outdoor set UA1404 (windscreen, shelter from rain and birdspikes). Calibration has been done with a pistonphone 4220 B&K. The microphones at both measuring stations are placed at 80% of the top of the barrier and at 9 times the barrier height behind it. Detailed spectra are measured with a frequency analyser (2144 B&K, microphone 4188 B&K) at a few occasions during the experiment.

Since measurements of sound pressure levels will be performed in (high) wind speeds, special attention is paid to the estimation of noise levels generated by wind in the microphones. In an anechoic chamber, the noise in a microphone equipped with the outdoor set, generated by a steady, non-turbulent wind is measured. The microphone is placed on a rotating arm instead of creating a moving air stream. A similar experiment is described in Ref. [95]. In this way the additional creation of sound by e.g. a fan is avoided. With increasing angular velocity or wind speed, the noise (in dB(A)) increases approximately linearly with the logarithm of the wind speed (in m/s) (see equation (3.34)). The noise caused by turbulence in the incident wind itself may also contribute to increased sound pressure levels in the microphones [96]. No further attention is paid to this kind of wind-induced noise, since it can be considered being part of the natural ambient sound environment [97].

A-weighted total equivalent sound pressure levels over periods of 1 minute are recorded. A period of 1 minute is assumed to be large enough to have the same emission at places *A* and *B*. Smaller time periods could result in a different source strength near both receiver at a given time. Wind effects will be averaged out too much when considering longer integration periods.

At a height of 12 m, an anemometer and a windvane are placed. Statistical parameters concerning wind speed and wind direction are recorded over (same) sample periods of 1 minute. The acquisition rate is 0.2 Hz. A pluviometer indicates the rainfall intensity. With decreasing wind speed, the wind direction becomes in general more variable. To exclude sample periods with a variable wind direction, some limits are set. The wind direction is measured with a

resolution of 1 degree. To retain enough data, some deviation δ from the average wind directions in a sample period $\langle\theta\rangle$ relative to the wind direction under investigation θ_0 is tolerated, and defined as:

$$\left|\langle\theta\rangle - \theta_0\right| < \delta \,. \tag{3.28}$$

To exclude samples periods in which the wind direction is too variable, the sector in which 68% of the acquisitions fall (= *S*) is also limited. This sector *S* is usually taken as two times the value of δ. If not stated differently, δ = 30° and *S* = 60°.

One has to take into account differences in soil coverage between points *A* and *B* when calculating the effect of the trees on the barrier performance with increasing wind speed. This can be done by comparing the differences in equivalent sound pressure levels between *A* and *B* in wind ($L_{Aeq,1\min}(\mathrm{i}\,|\,\mathrm{A,u})$ and $L_{Aeq,1\min}(\mathrm{i}\,|\,\mathrm{B,u})$) to the average difference in equivalent sound pressure level between both places in absence of wind ($L_{Aeq,1\min}(\mathrm{A,0})$ and $L_{Aeq,1\min}(\mathrm{B,0})$). So the net effect on noise barrier performance by the trees (= $dLp(i\,|\,u)$) in wind for wind speed *u* at datapoint *i* is calculated as follows:

$$\begin{aligned} dLp(i\,|\,u) = &\left[L_{Aeq,1\min}(\mathrm{i|A,u}) - L_{Aeq,1\min}(\mathrm{i|B,u})\right] \\ &-\left\langle L_{Aeq,1\min}(\mathrm{A,0}) - L_{Aeq,1\min}(\mathrm{B,0})\right\rangle, \end{aligned} \tag{3.29}$$

where the operator $\langle\ \rangle$ denotes the average over the full period.

At the height were the meteo data is measured, there will be some wind most of the time. As a consequence, a windless period is considered to be a period where the average wind speed is lower than 1 m/s. So *u* = 0 m/s must be read as *u* < 1 m/s.

Some statistical parameters will be used for the discussion of the experimental data. The sample estimate of the population standard deviation of *dLp* for wind speed (class) *u* is defined as:

$$\sigma_{dLp}(u) = \sqrt{\sum_{i}^{n} \frac{\left[dLp(i\,|\,u) - \langle dLp(u)\rangle\right]^2}{n-1}}\,, \tag{3.30}$$

where *n* is the number of samples and $\langle dLp(u)\rangle$ is an estimate of the mean improvement by the trees based on the sample, for the wind speed (class)

considered. The standard error of the mean takes into account both population variance and sample size:

$$\sigma_{\overline{dLp}}(u) = \sqrt{\frac{\sigma^2_{dLp(u)}}{n}} \,. \tag{3.31}$$

Depending on the type of analysis, both quantities are used.

3.4.3.d A row of trees behind a noise barrier in wind

Results and discussion
About 112000 useful 1-minute datapoints (combined acoustical data and meteo data) were collected during this measurement campaign. From this dataset, about 87000 datapoints were retained after removing rainy periods and disturbance by noise from other sources than traffic. The latter is based on the assumption that a large discrepancy in sound pressure levels (> 7 dB(A)) between both measurement sites indicates the presence of a disturbing noise source. This threshold is (intuitively) set, taking into account that the improvement of the barrier performance in presence of the trees is well below that value.

In Figure 3.22, the $L_{A,eq,1min}$ is shown for one week during the measuring campaign, indicating a typical, daily behaviour. During the day, two local maxima are observed that can be attributed to rush hour in the morning and evening. A local minimum around noon is usually seen, except in the weekends. During daytime, the A-weighted total equivalent sound pressure levels are quite constant and exceed 60 dB(A) most of the time. The minimum measured $L_{A,eq,1min}$ at night was about 50 dB(A) and falls in the period between 2 and 4 o'clock. The measured sound levels follow the same trends as the averaged, hourly countings shown in Figure 3.21.

Wind speed data is grouped in classes with a width of 1 m/s, for which the centre value of the classes is given for identification in the next plots.

The effect of the presence of trees behind a noise barrier for wind directions orthogonal to the noise screen ($\delta = 30$, $S = 60$) is first analysed, for both upwind and downwind sound propagation. The average net effect per wind speed class is shown in Figure 3.23.

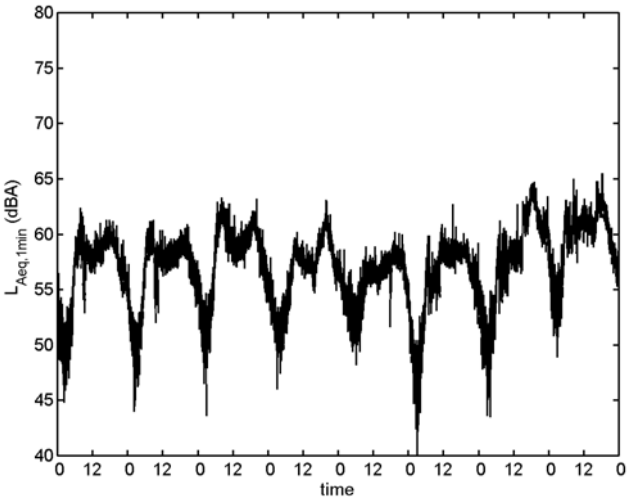

Figure 3.22 Measured $L_{A,eq,1min}$ values for the period from 10 (Wednesday) to 17 (Wednesday) October 2001. In abscissa, midnight (0 hours) and noon (12 hours) are shown for each day.

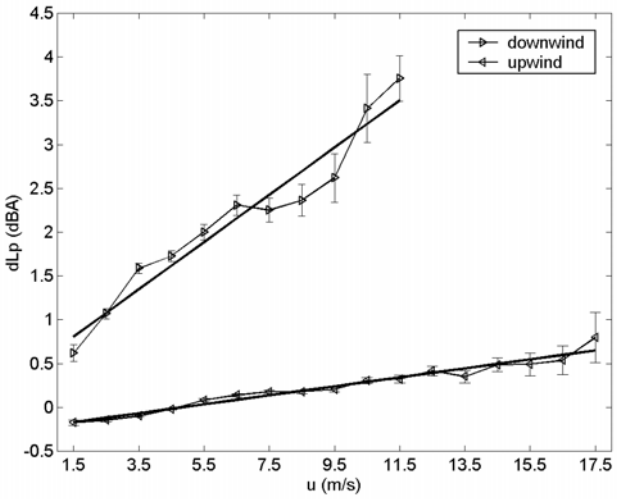

Figure 3.23 Average net efficiency of the presence of a row of trees behind a noise barrier, with increasing wind speed. The effect of wind directions orthogonal to the noise barrier is shown, for both downwind and upwind sound propagation. The best-fitted linear curves on these data are given. Errorbars (standard error of mean) for each wind speed class are drawn.

Even for low wind speeds, trees cause a net positive effect for downwind sound propagation. An almost linear relationship between wind speed and improvement of the barrier behaviour by trees is observed. The best-fitted linear curve based on the average improvement by a single row of trees (in leaf) with increasing wind speed can be described by the following equation (with $R^2 = 0.94$):

$$dLp = 0.40 + 0.27u \,, \tag{3.32}$$

with dLp in dB(A) and u in m/s, measured at a height of 12 m. For wind speeds higher than 10 m/s, an improvement of more than 3 dB(A) is obtained.

In the wind tunnel study the net effect of the windscreens was in the same order of magnitude, and was larger for the high wind speed (11 m/s) than for the low wind speed (6.4 m/s). A direct comparison is however not possible due to differences in geometrical test set-up.

Upwind sound propagation is only slightly affected by the trees. For low wind speeds (< 4 m/s), there is a net negative effect since the upward refraction of sound by the wind is counteracted by the wind speed reduction by the trees. Higher wind speeds will not be reduced sufficiently to prevent upward refraction of sound. The best-fitted curve based on the average improvement by trees with increasing wind speed can be described by (with $R^2 = 0.96$):

$$dLp = -0.25 + 0.05u \,, \tag{3.33}$$

with dLp in dB(A) and u in m/s, measured at a height of 12 m.

The errorbars for upwind sound propagation are smaller, since this wind direction occurred more often during the measurement campaign. It should be emphasised that for high wind speeds the results need to be interpreted with care due to the relatively small amount of data. A statistical analysis is performed to check whether the net improvement with increasing wind speed is significant in the next chapter.

To be of practical use, the above-mentioned effects should not be too sensitive on wind direction. Therefore it is investigated to what extent the wind direction may deviate from exact orthogonal direction to still observe the above mentioned effects. With increasing values for δ and S in case of orthogonal, downwind sound propagation, the net effect of the trees decreases slightly (see Figure 3.24). For values of δ up to 45°, this decrease is only 0.5 dB(A). For upwind sound propagation and for a wind direction orthogonal to the noise barrier, the negative net effect by trees is slightly more pronounced when δ is small (see Figure 3.25). For higher wind speeds, no significant differences can be observed, taking into account the limited amount of data when values of δ are small. It can be

concluded that the net effect of trees behind noise barriers is not sensitive to deviations in wind direction.

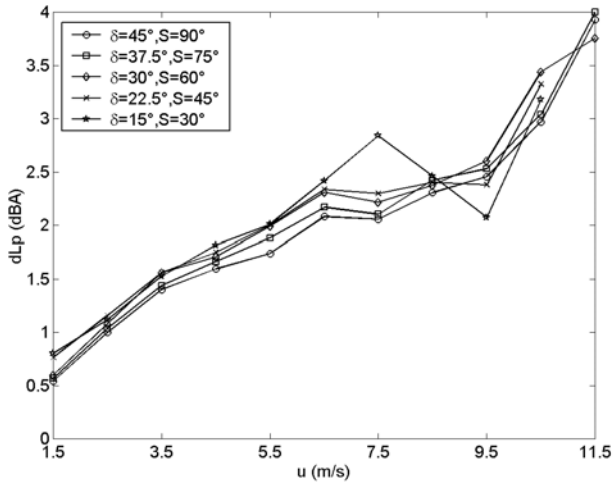

Figure 3.24 Average net efficiency of placing a row of trees behind a noise barrier with increasing wind speed, for a normal incident wind direction and downwind sound propagation. Deviations to the normal direction range from 15° to 45°.

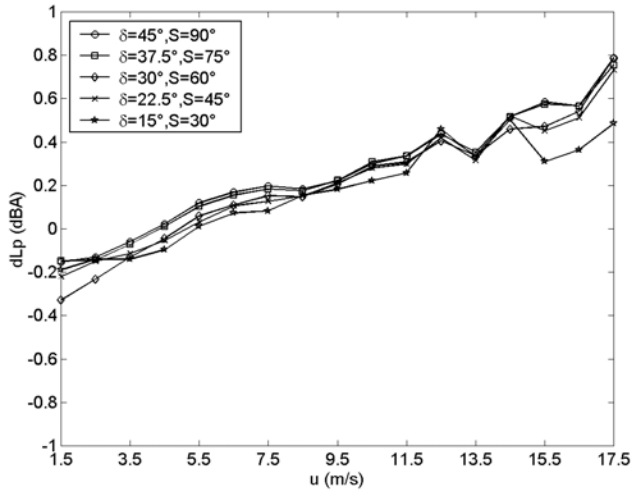

Figure 3.25 Average net efficiency of placing a row of trees behind a noise barrier with increasing wind speed, for a normal incident wind direction and upwind sound propagation. Deviations to the normal direction range from 15° to 45°.

With increasing wind speed, the standard error of the mean increases due to a decreasing amount of data, as shown in Figure 3.26 for downwind sound propagation and in Figure 3.27 for upwind sound propagation. This trend is not observed for very low wind speeds since wind direction in these classes is often too variable. As a result, many datapoints are excluded from the dataset for low wind speeds. When values of δ and S decrease, the standard error of the mean becomes larger. However, standard errors are still small, and give confidence in the results obtained.

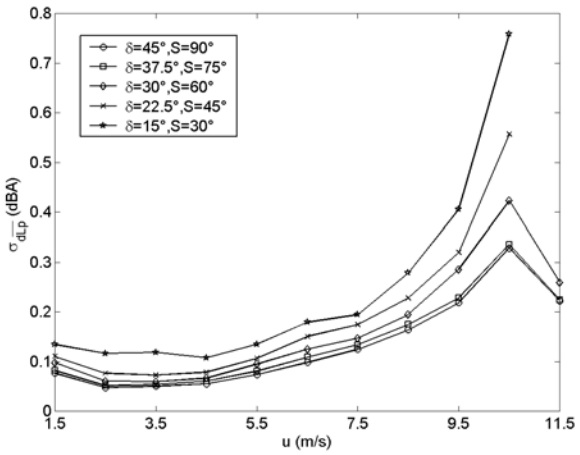

Figure 3.26 Standard error of mean on the efficiency of placing a row of trees behind a noise barrier with increasing wind speed, for a normal incident wind direction and downwind sound propagation. Deviations to the normal direction range from 15° to 45°.

Possible disturbing factors affecting the measurements in the presence of wind are noise generation in microphones and wind-induced vegetation noise. The remainder of this section is devoted to excluding these effects.

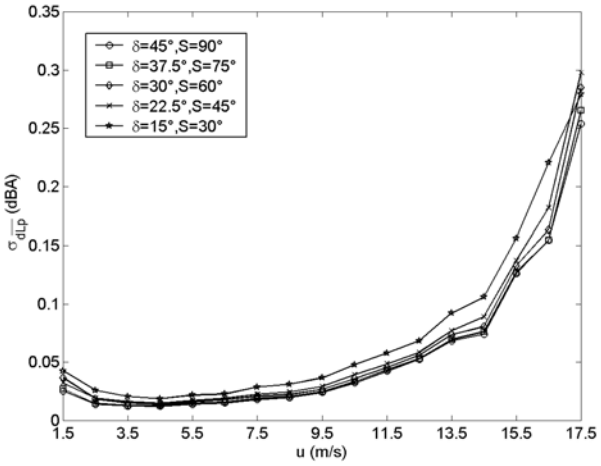

Figure 3.27 Standard error of mean on the efficiency of placing a row of trees behind a noise barrier with increasing wind speed, for a normal incident wind direction and upwind sound propagation. Deviations to the normal direction range from 15° to 45°.

An estimation of the wind-induced microphone noise is obtained from the experiment with the rotating arm as described in Chapter 3.4.3.c. The relationship between sound pressure levels generated by wind and wind velocity was investigated for the combination of microphone and outdoor equipment used in the monitoring campaign. The best-fitted linear regression line in the logarithm of the wind speed yields

$$L_{wind} = 56.2\log(u) - 10.6\,, \tag{3.34}$$

with L_{wind} in dB(A) and u in m/s.

Wind speeds in the field experiment are measured at a height of 12 m. The heights where the microphones are positioned are at most 3.4 m. So wind speeds will be well below 10 m/s at the microphone positions. Since the measured $L_{Aeq,1min}$ values behind the screens are in all cases higher than 50 dB(A), wind-induced noise in the microphone will not influence the measurements.

The effect of wind-induced vegetation noise is also estimated to be small. In an experiment by Fegeant [85], emission peak levels very close to the edge of deciduous forests (oaks, aspens and birches) are measured. During the cited experiment it was found that sound pressure levels (in dB) are proportional to 30 times the logarithm of the wind speed (in m/s), for the wind speed interval between 2 and 10 m/s. This relationship will be used here to estimate the wind-

induced vegetation noise as a function of wind speed. This relationship will however also be used outside the measurement interval of Ref. [85] making it only a rough estimation. The relationships between wind speed and wind-induced vegetation noise by Schuller [82] and Boersma [86] are less suited for this comparison. In Ref. [86], measurements are performed inside a deciduous forest. In Ref. [82], an estimation of the wind-induced vegetation noise is only possible for large wind speeds, since the proportionality between wind-induced vegetation noise and the logarithm of the wind speed was not found below 7-8 m/s.

The 95th percentile value of our measurements is chosen to evaluate vegetation noise since it samples the periods where instantaneous traffic density is low and therefore noise from the trees is more likely to be observed, especially for high wind speeds. In Figure 3.28, the measured 95th percentile (total) sound pressure levels (measured at place *B*) with increasing wind speed are shown. For high wind speeds, the wind-induced vegetation noise is expected to be completely responsible for the background noise. So the 95th percentile values will be the upper limit for the wind-induced vegetation noise. The trend line of Fegeant allows to estimate sound pressure levels generated by trees in wind at lower wind speeds. These 95th percentile values in our experiment are expressed in dB(A). Since wind-induced vegetation noise resulting from deciduous species has an emission peak near 4-5 kHz [85], one has to take into account differences up to 1 dB when comparing A-weighted with unweighted sound pressure levels as obtained in Ref. [85].

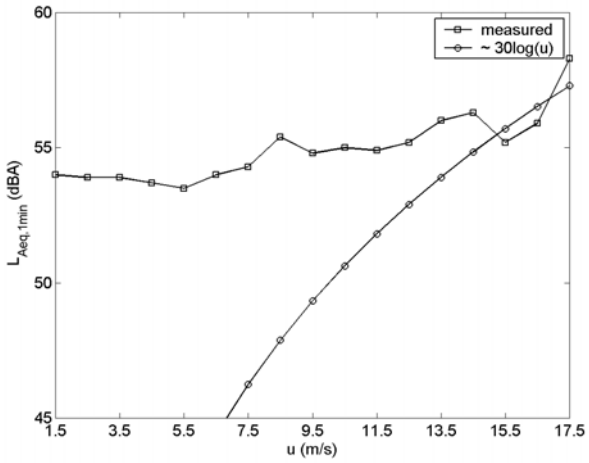

Figure 3.28 Estimation of wind-induced vegetation noise (dB) and measured "background noise" (dB(A)) with increasing wind speed.

Based on Figure 3.28, it can concluded that for wind speeds below 10 m/s, wind-induced vegetation noise will not influence the sound pressure levels from traffic.

Statistical significance of observations

A statistical analysis is necessary since the improvement of the barrier performance by the trees (*dLp*) relative to the variation on these data is low. A second reason to perform a statistical analysis is the large difference in the amount of data per wind speed class.

An overview of the standard deviation on the net effect of trees per wind speed class is given in Figure 3.29. With increasing wind speed, the sound pressure levels become more variable. This may be caused by the increased degree of turbulence when wind speed increases. This trend is not clearly observed since the number of observations in some classes is low. For downwind sound propagation the standard deviation is higher than for upwind sound propagation.

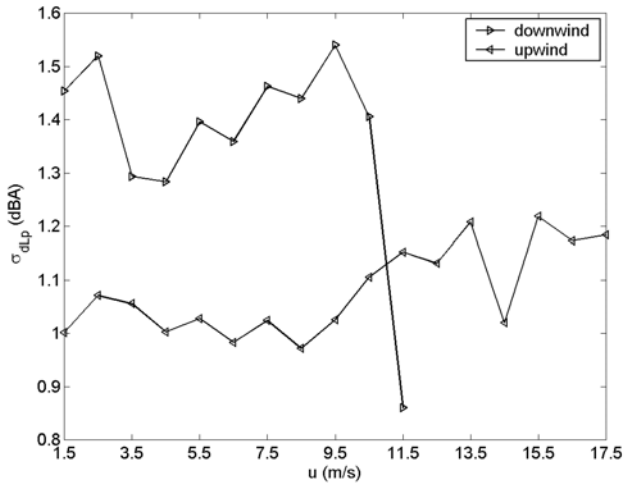

Figure 3.29 The standard deviation on the effect of trees per wind speed class, for an orthogonal incident wind direction, for downwind and upwind sound propagation.

A variance analysis has been performed to see if the improvement of the performance of the noise barrier in wind by the trees is significant when comparing different wind speed classes. The data of most wind classes have equal variance. The condition requiring a normal distribution of the data is also fulfilled, and if not, the large amount of data in most wind speed classes will

compensate. The least-significant-difference test has been used to check whether the averages of two data sets are equal. The null hypothesis states that the average improvement by the trees for two wind speed classes is equal. When this hypothesis can be rejected with a certainty of 95%, the data will be considered different. The probability that 2 wind speed classes have an equal mean is given in Table 3.7 (a) for downwind sound propagation, in Table 3.7 (b) for upwind sound propagation and in Table 3.7 (c) for a wind direction parallel to the noise barrier. Combinations that can be considered equal (with an error of 5%) are placed in the grey-filled boxes.

For wind flowing parallel to the noise barrier, there's a high probability that the results for *dLp* from different wind speed classes are equal. Only a small number of wind speed classes can be considered different. These results indicate that using relative measurements is justified in the experiment. For downwind and upwind sound propagation, the effects of the low wind speed classes are significantly different from each other, except for some neighbouring classes. For wind speeds higher than 10 m/s and for upwind sound propagation, no distinction (with a certainty of 95%) between different wind speed classes can be made.

Table 3.7 Probability that the net effect by trees for each combination of wind speed classes is equal, for a normal incident wind direction and downwind sound propagation (a), for a normal incident wind direction and upwind sound propagation (b), and for a wind direction parallel to the noise barrier (c). In the headers of the columns and rows, the centre values (in m/s) of the wind speed classes (with a width of 1 m/s) are shown. An example: for downwind sound propagation, the chance that the average net effect of the trees for wind speeds between 3 m/s and 4 m/s is equal to the net effect of wind speeds between 4 and 5 m/s is 12%.

(a)

	1.5	2.5	3.5	4.5	5.5	6.5	7.5	8.5	9.5	11	12
1.5		0.00	0.00	0.00	0.00	0.00	0.00	0.00	0.00	0.00	0.00
2.5			0.00	0.00	0.00	0.00	0.00	0.00	0.00	0.00	0.00
3.5				0.12	0.00	0.00	0.00	0.00	0.00	0.00	0.00
4.5					0.01	0.00	0.00	0.00	0.00	0.00	0.00
5.5						0.04	0.11	0.07	0.02	0.00	0.00
6.5							0.74	0.80	0.26	0.01	0.00
7.5								0.61	0.19	0.00	0.00
8.5									0.41	0.01	0.00
9.5										0.09	0.02
11											0.55
12											

(b)

	1.5	2.5	3.5	4.5	5.5	6.5	7.5	8.5	9.5	11	12	13	14	15	16	17	18
1.5		0.43	0.02	0.00	0.00	0.00	0.00	0.00	0.00	0.00	0.00	0.00	0.00	0.00	0.00	0.00	0.00
2.5			0.02	0.00	0.00	0.00	0.00	0.00	0.00	0.00	0.00	0.00	0.00	0.00	0.00	0.00	0.00
3.5				0.00	0.00	0.00	0.00	0.00	0.00	0.00	0.00	0.00	0.00	0.00	0.00	0.00	0.00
4.5					0.00	0.00	0.00	0.00	0.00	0.00	0.00	0.00	0.00	0.00	0.00	0.00	0.00
5.5						0.01	0.00	0.00	0.00	0.00	0.00	0.00	0.00	0.00	0.00	0.00	0.00
6.5							0.18	0.24	0.05	0.00	0.00	0.00	0.00	0.00	0.00	0.01	0.01
7.5								0.96	0.43	0.00	0.00	0.00	0.01	0.00	0.01	0.01	0.01
8.5									0.42	0.00	0.00	0.00	0.01	0.00	0.01	0.01	0.01
9.5										0.02	0.02	0.00	0.03	0.00	0.01	0.02	0.02
11											0.79	0.06	0.51	0.04	0.11	0.11	0.05
12												0.13	0.66	0.06	0.14	0.14	0.06
13													0.42	0.47	0.53	0.42	0.14
14														0.19	0.27	0.23	0.09
15															0.95	0.74	0.24
16																0.80	0.27
17																	0.37
18																	

(c)

	1.5	2.5	3.5	4.5	5.5	6.5	7.5	8.5	9.5	11	12
1.5		0.08	0.00	0.00	0.00	0.00	0.03	0.04	0.52	0.76	0.56
2.5			0.09	0.00	0.04	0.02	0.39	0.39	0.54	0.20	0.97
3.5				0.04	0.59	0.35	0.69	0.89	0.15	0.06	0.77
4.5					0.18	0.46	0.06	0.18	0.02	0.01	0.48
5.5						0.67	0.44	0.65	0.10	0.04	0.68
6.5							0.28	0.46	0.06	0.03	0.61
7.5								0.88	0.28	0.11	0.85
8.5									0.27	0.11	0.81
9.5										0.47	0.78
11											0.48
12											

3.4.3.e A row of trees behind a noise barrier in absence of wind

Spectra at both sites are measured. The sound pressure levels in 1/3-octave bands, averaged out over a period of 1 minute, in a windless period, are shown in Figure 3.30.

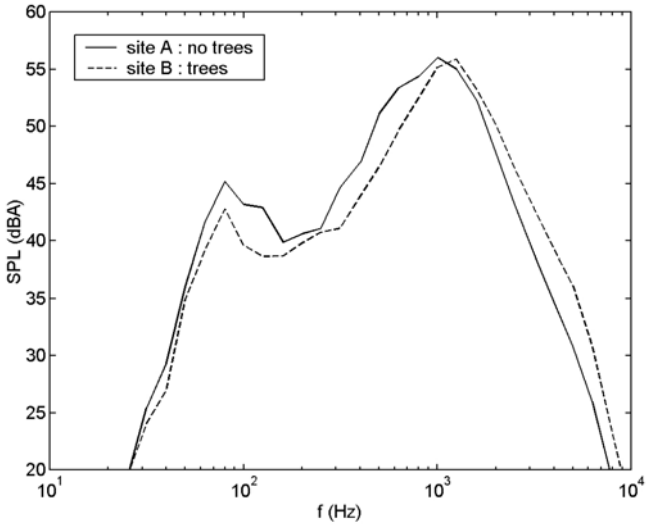

Figure 3.30 Spectra measured at *A* and *B* in a windless period.

The acoustic source at location *A* and *B* is the same, since the microphones are only 100 m apart along the direction of the highway. The section of the highway under investigation has the same road surface. Differences in spectra between both places may result from differences in ground coverage and differences in geometry, and from the presence of trees.

To separate out the effect of the trees (combined with the effect of the noise barrier) from differences in ground effect and geometry, some calculations are performed. As a simple model for the diffraction of traffic noise over the noise barrier, a line source is placed on top of the barrier. The sound pressure as a result from the interaction between the direct and reflected waves can be calculated using equation (3.14).

No specific measurements were done to quantify the ground impedance at the site under investigation. Both the Delany and Bazley model [32] and the 2-parameter model of Attenborough [98] were used to estimate ground impedance. Appropriate values for the non-acoustic parameters of the soils were found in

literature [35, 99]. An effective flow resistivity of 400 kPa s/m^2 is used for the sandy soil at site *A*. For the pasture at site *B*, a value of 200 kPa s/m^2 is chosen. The 2-parameter model also needs an estimation of the effective layer thickness (0.02 m at site A, 0.025 m a site B). The relative differences in sound pressure levels between place *A* and *B* as a function of frequency is given in Figure 3.31.

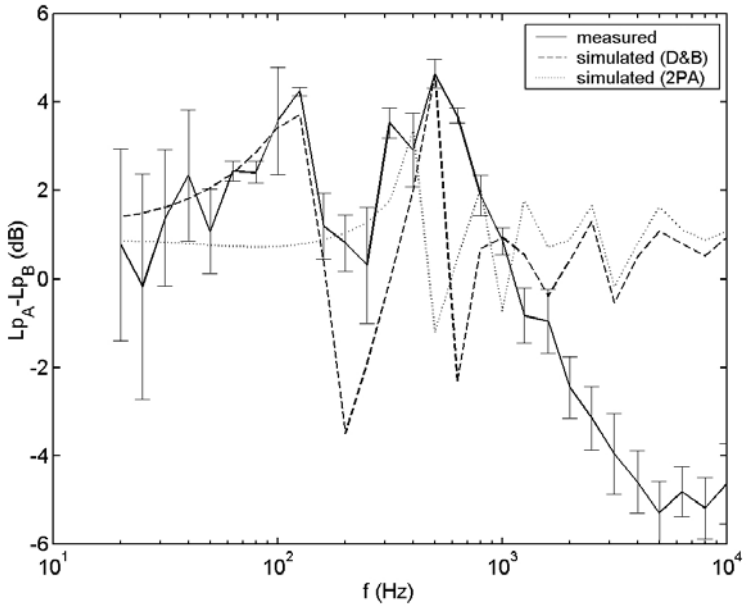

Figure 3.31 Measured differences in sound pressure levels between *A* and *B* in a windless situation, together with the simulated differences between both places accounting for different ground effects and differences in geometry. The ground impedance model of Delany and Bazley (D&B) and the 2-parameter model of Attenborough (2PA) are used. The errorbars indicate the standard errors of mean on the differences between measured sound pressure levels at both places.

By comparing the simulated ground effect with the measurements, the effect of the trees (combined with the noise barrier) can be estimated. For frequencies higher than 1-2 kHz, differences cannot be explained anymore by the ground effect, and find their origin in scattering on the canopy of the trees. This is consistent with other experiments found in literature [82]. For frequencies near 10 kHz, an increased sound pressure level of about 6 dB is observed behind the noise barriers with trees [83, 87]. Both impedance models agree well for frequencies higher than 1 kHz. As to the Delany and Bazley model, trees have

little influence for frequencies lower than 100 Hz. The 2-parameter model on the other hand already indicates some attenuation for these very low frequencies. Between 100 Hz and 1 kHz, the presence of trees results in a small but statistical significant attenuation of sound independently of the impedance model used to eliminate differences in ground type. This typical increased attenuation in the mid-frequency range and a decreased attenuation at higher frequencies, resulting from the placement of a row of trees behind a barrier, are consistent with the measurements of Schuller et al. [82].

It is clear that a row of trees can have a (small) positive or negative effect depending on the spectrum of the source (in absence of wind). However, the contribution from the increased scattering of sound in the high-frequency range to the total A-weighted sound pressure levels will be small for traffic noise. Therefore placing a row of trees behind noise barriers along highways will not result in a significantly lower attenuation in a windless situation.

3.4.3.f Conclusion

A field experiment set up to study the feasibility of increasing noise barrier performance in downwind conditions by modifying wind profiles with trees used as windbreaks was described in the previous chapters. Already for low wind speeds, a statistical significant (but small) decrease of the reduction of barrier insertion loss for downwind sound propagation is observed. With increasing wind velocity, this effect increases. For wind speeds between 6 m/s and 7 m/s, measured with an anemometer at a height of 12 m, an increase in insertion loss of more than 2 dB(A) is obtained. For wind speeds between 11 m/s and 12 m/s, the use of trees behind a barrier results in an improvement of almost 4 dB(A). For wind directions up to 45° away from the downwind direction, the effect is only 0.5 dB(A) lower. So the net effect of trees behind barriers is not very sensitive to deviations in wind direction. For upwind sound propagation, the positive effect of the wind (upward refraction) is neutralised for low wind speeds. This results in a slightly worse situation (maximum -0.5 dB(A)). For higher wind speeds the use of trees has a small positive effect (< 1 dB(A)). An analysis of variance revealed that for downwind and upwind sound propagation for an orthogonal incident wind direction, only for high wind speeds and for some neighbouring wind speed classes, differences in net improvement were not significant with a certainty of 95%.

The presence of a row of trees behind a noise barrier results in increased sound pressure levels at high frequencies due to scattering on the canopy of the trees. Typical traffic noise however produces only a small amount of acoustic energy

in the high-frequency range relative to low frequency bands. So the contribution of this scattered sound to the total A-weighted sound pressure levels is small. For highways with dense traffic, wind-induced vegetation noise is also proven to be of minor importance.

The results obtained in this field trial follow the same trends as in the wind tunnel experiment. This increases confidence in critical approximations made in the wind tunnel experiment such as the representation of trees by woven, polyester windbreaks. This field experiment confirms the positive effect of windbreaks (trees) on the performance of noise barriers in downwind situations and allows concluding that a combination of noise barriers with trees and bushes should be considered in future applications.

3.4.4 Optimisations

In Chapters 3.4.4.a, 3.4.4.b, 3.4.4.c and 3.4.4.d, some parameters involved in the design of an optimal configuration of windscreens are analysed. The results are presented for one configuration, a single noise barrier with a large windscreen behind it (*1ns+1ws(2H)*) and for a source emitting main energy in the frequency interval ranging from 250 to 500 Hz, with a bandwidth of 250 Hz. The ground surface upwind from the noise barrier is perfectly reflecting, while downwind a very soft ground is used in order to prevent that reflections from the soil make the effects caused by the changed wind flow less clear in the figures. The same set of ground parameters as in the wind tunnel is used (k_s =1, φ = 0.5, R= 5 kPa s/m^2), except in Chapter 3.4.4.d, where the effect of the ground parameters (more specific flow resistivity) is investigated explicitly.

In Chapter 3.4.4.e, the global effect of the different windscreen configurations as shown in Figure 3.12 is investigated for a typical traffic noise spectrum. Single noise barrier configurations and noise barriers on either side of the source are considered. In between the noise barriers, a (perfect) hard street surface is chosen, while downwind a realistic, natural soil is simulated (a typical grassland with k_s = 3, φ = 0.3 and R=300 kPa s/m²).

Unless otherwise stated, following parameters are used during the simulations. The configurations of noise barriers and windscreens, as shown in Figure 3.32, are used. Two-dimensional sound propagation is studied: both the noise barrier(s) and line source are infinitely long. The distance between the line source and the noise barrier(s) is in all cases *2H* (with *H* the height of the noise barrier, which equals 3.6 m), except in Chapter 3.4.4.c, where the distance between source and noise barrier is investigated explicitly. The noise barriers are perfectly reflecting. The logarithmic wind speed profile described by equation

(3.17) is used at the inflow, with a roughness length of 1 mm and a friction velocity of 0.5 m/s. This results in a wind speed of 11 m/s at a height of 10 m above the ground surface.

The "region of interest" is defined as the rectangular area behind the (downwind) noise barrier, up to a distance of 20*H* and up to a height of 1*H* (see Figure 3.32). The (spatial) distribution of the relevant quantities (e.g. *net IL*) are computed in this zone on a two-dimensional grid with observation points that are apart from each other at distances that equal $1/10^{th}$ of the shortest wavelength under consideration. In this way, global effects of the parameters analysed and the different windscreen configurations will be presented in a condensed way, however providing sufficient information.

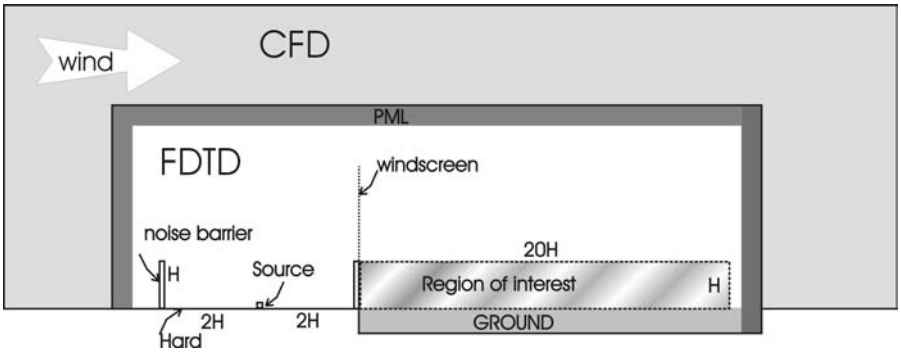

Figure 3.32 Overview of the simulation region, indicating the *CFD* grid and the *FDTD* grid, the region of interest and relevant dimensions (not true to scale).

3.4.4.a Effect of porosity of windscreens

It is important to analyse the sensitivity of the effect of the windbreaks on porosity to quantify the effect of e.g. deciduous trees throughout the year. The pressure drop of various windscreens as a function of flow velocity, for porosities ranging from 6% to 90%, was measured in detail [80]. These materials could be described accurately in the velocity range of interest by equation (3.18). The values for the parameters *a* and *b*, as used during the flow calculations, are presented in Table 3.8.

Table 3.8 Values for parameters *a* and *b*, to be used in equation (3.18) [80].

porosity (-)	a (Pa s²/m²)	b (Pa s/m)
0.16	54.313	-24.214
0.32	5.04	0.092
0.47	1.538	-0.533
0.59	0.842	0.553
0.76	0.491	-0.248

During the experiment, a porosity of 32% has shown to be approximately acoustical neutral, or at least, effects arising from the interaction between the windscreens and acoustic waves are significant smaller than effects from the changed wind profile. Lower porosities may result in important acoustical shielding and scattering. So for porosities down to about 32%, the screens are considered to be acoustical neutral. Simulations, neglecting these acoustic effects for very low porosity-screens (< 32%), indicated that with decreasing porosity the (theoretical) *net IL* will increase and eventually reaches an asymptotic value (see Figure 3.33).

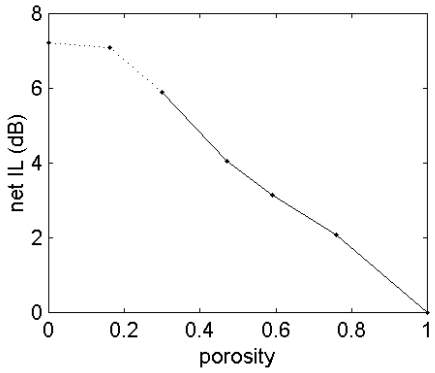

Figure 3.33 *Net IL* with decreasing porosity for the frequency interval 250-500Hz at a height of *0.5H*, and at a distance of *7H* downwind from the noise barrier. Configuration *1ns+1ws(2H)* is simulated. The wind speed was 11 m/s at a height of 10 m. For porosities lower than 0.32 a pointed line is used: these simulations do not represent a physical situation since acoustic shielding is not accounted for.

The spatial distribution of observations in the region of interest (as defined in the beginning of this chapter) over 1-dB *net IL* intervals for different porosities is shown in Figure 3.34. The magnitude of the total wind effect (*WE*, this is the difference in sound pressure level behind a noise barrier in absence of windscreens, with and without wind) is also presented. With increasing porosity,

the maximum in the distribution is more pronounced, and the region where placing trees causes negative effects is larger. The high *net IL* classes become more populated with decreasing porosity. The average *net IL* with increasing porosity was 2.8 dB, 1.6 dB, 1.0 dB and 0.6 dB (for a porosity of respectively 32%, 47%, 59% and 76%). The average wind effect in the region of interest was 4.5 dB. In general, a low porosity of the canopy of trees results in a better performance in wind.

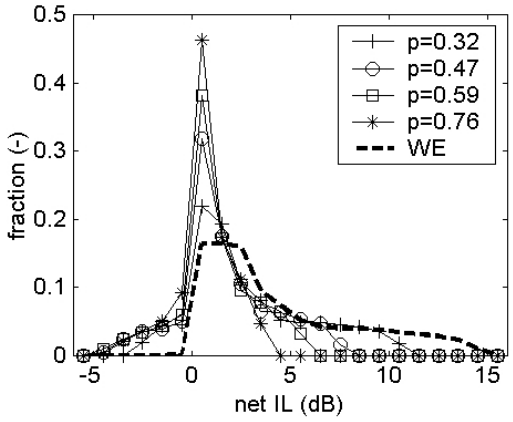

Figure 3.34 Spatial distribution of *net IL* and *WE* for the frequency interval 250-500Hz, in the region of interest, for various porosities, ranging from 0.32 to 0.76. Configuration *1ns+1ws(2H)* is simulated. The wind speed was 11 m/s at a height of 10 m.

3.4.4.b Effect of wind speed

To analyse the effect of wind speed on *net IL* numerically, calculations for wind speeds ranging from 3 m/s to 15 m/s are performed, at a reference height of 10 m, following equation (3.15). The roughness length was 1 mm. A windscreen with a porosity of 0.32 is used. *Net IL* with increasing wind speed, at different distances behind the noise barrier, for receiver positions at a height of 0.5*H* is shown in Figure 3.35. For distances closer than 10*H*, the linear relationship between wind speed and *net IL* as observed during the field experiment is recovered. At larger distances, this trend is not preserved and a maximum is observed: high wind speeds do not result anymore in the highest values for *net IL*. The overall effect of wind speed in the region of interest is illustrated with the histograms in Figure 3.36. More compact information is shown in Figure 3.37 by means of the numerical average over the region of interest of the *WE* and

net IL with increasing wind. As wind speed increases, the high *net IL* classes get larger fractions in the distribution. For low wind speeds, the fractions present in the negative *net IL* classes are somewhat smaller.

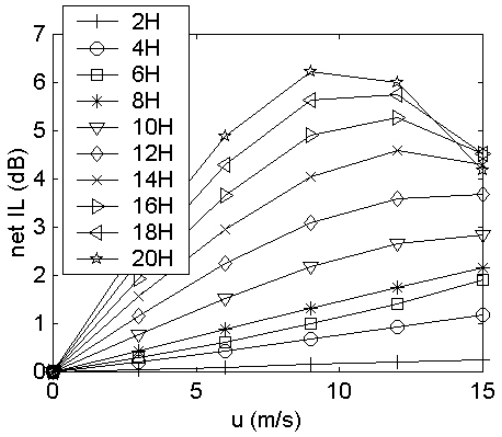

Figure 3.35 *Net IL* with increasing wind speed, at various distances behind the noise barrier, at a fixed height (= 0.5*H*). Results for the frequency interval 250-500Hz are shown. Configuration *1ns+1ws(2H)* is simulated (with a porosity of 32%).

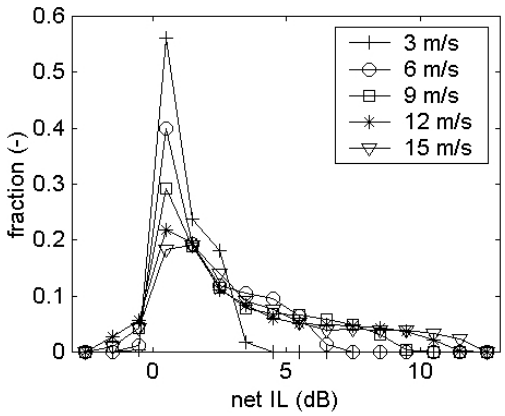

Figure 3.36 Spatial distribution of *net IL* in the region of interest, for the frequency interval 250-500Hz, for various incident wind speeds. Configuration *1ns+1ws(2H)* is simulated (with a porosity of 32%).

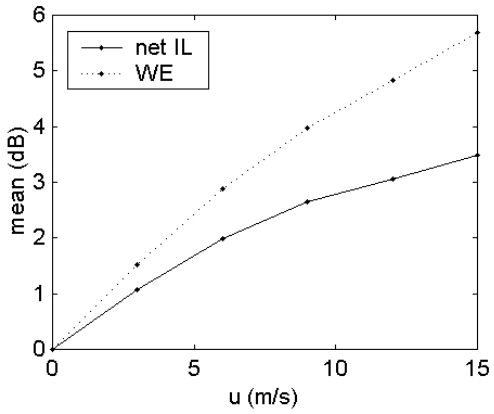

Figure 3.37 Average values of *WE* and *net IL*, for the frequency interval 250-500Hz, in the region of interest, with increasing incident wind speed. The same *net IL* data as in Figure 3.36 is used.

3.4.4.c Effect of distance between source and noise barrier(s)

It is investigated how the magnitude of the *WE* and *net IL* behave with increasing distance between the noise source and the noise barrier. Simulations are performed for a windscreen with a porosity of 32% and for an incident wind speed of 11 m/s (at a height of 10 m). In Figure 3.38, the average *WE* and *net IL* in the region of interest are shown with increasing distance between the line source and the barrier(s), for both a single noise barrier configuration (a) and noise barriers on either side of the source (b). In case of a double noise barrier, the distances between the source and both noise barriers are increased (or stated otherwise: the distance indicated in Figure 3.38 (b) is half the distance between the noise barriers). A large windscreen ($2H$) is placed behind the (downwind) noise barrier in both cases.

In general, the positive effect of the windscreen is larger in the double noise barrier situation. When the source is moved away from the barrier, the reduction of barrier performance by wind increases. For the single noise barrier configuration, *net IL* follows this trend, and the ratio between *WE* and *net IL* stays almost the same for the distances under consideration. When a noise barrier is present on both sides of the source, the *WE* initially grows faster with distance. The efficiency of the windscreen for small distances between source and barrier is higher but decreases for larger distances. At very limited distances between the

source and noise barrier (e.g. 1*H*), wind effects are completely neutralised, in contrast to the single noise barrier configuration. It is expected that for large distances between the source and the noise barriers, effects from the upwind noise barrier will become negligible, and as a result, the same behaviour will be observed as for a single noise barrier.

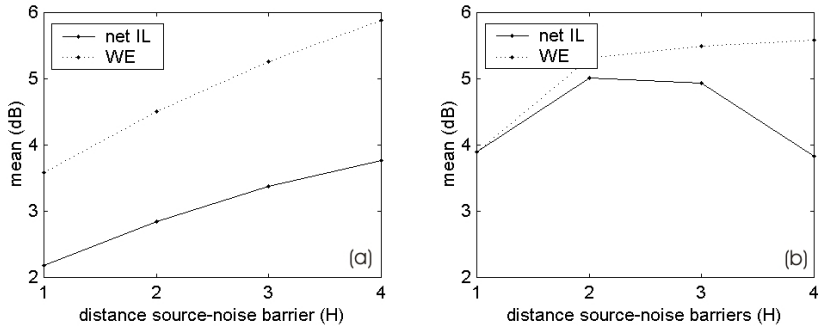

Figure 3.38 Average values of *net IL* (for configurations *1ns+1ws(2H)* (a) and *2ns+1ws(2H),d* (b)) and *WE* (for a single noise barrier *1ns* (a) and a noise barrier on either side of the source *2ns* (b)) for the frequency interval 250-500Hz, in the region of interest, with increasing distance between source and noise barrier. A wind speed of 11 m/s (at a height of 10 m) and a porosity of 0.32 are used.

3.4.4.d Effect of ground impedance on the effect of windscreens

The effect of the soil parameters in the area downwind from the noise barrier is investigated. Simulations have been performed for a soil with a flow resistivity of 10 kPa s/m², 100 kPa s/m² and 300 kPa s/m², and also for a perfectly reflecting ground surface. Porosity of the soil φ is 32%, the structure factor k_s equals 3 (except for the perfectly reflecting soil). Results for the average *IL*, *WE* and *net IL* in the region of interest are shown in Figure 3.39. The *IL* of the barrier increases with the hardness of the soil, or with increasing flow resistivity. The average *net IL* and *WE* on the other hand are hardly dependent on the soil parameters. The distribution of *net IL* for the different soils considered here reveals some more information (see Figure 3.40). With increasing surface impedance, the very high as well as negative *net IL* values occur more often due to the presence of interference patterns caused by increased reflections on the soil.

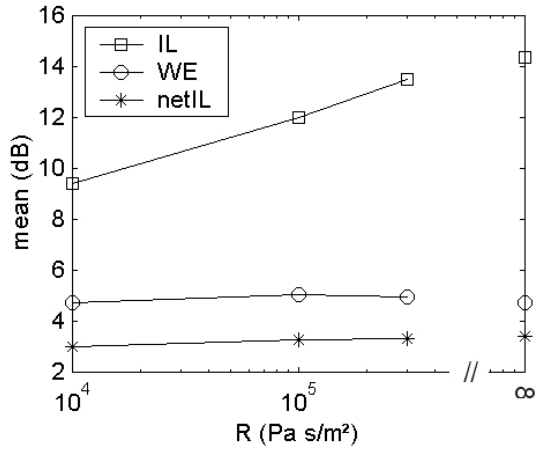

Figure 3.39 Mean insertion loss (*IL*), magnitude of the wind effect (*WE*) and *net IL* (in dB) by the presence of a large windscreen (2*H*) with increasing flow resistivity of the soil, in the region of interest.

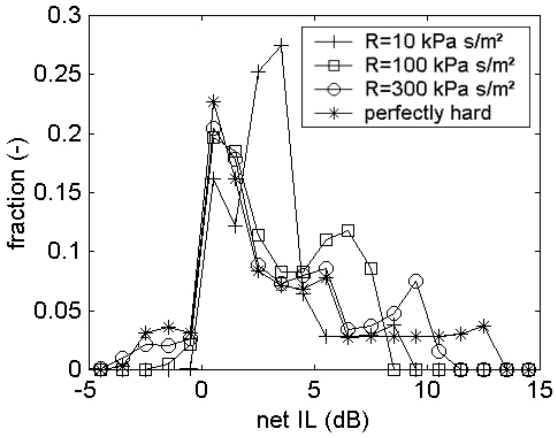

Figure 3.40 Spatial distribution of *net IL* (in dB) in the region of interest for different values of flow resistivity of the soil, downwind from the noise barrier.

3.4.4.e Global effect of the different windscreen configurations for traffic noise

Finally we analyse the effect of windscreens for the configurations shown in Figure 3.12, in the region of interest (as defined in the beginning of the chapter), for a typical traffic noise spectrum [93] and a natural soil (k_s = 3, φ = 0.3 and

R=300 kPa s/m²). The wind speed at a height of 10 m above the surface was 11 m/s. In Figure 3.41 and Figure 3.42, the distribution of the observations in the region of interest as regards *net IL* values is shown. Different configurations of windscreens (with a porosity of 0.32), for respectively single noise barriers and noise barriers on either side of the line source, are considered. The magnitude of the wind effect (*WE*) is also presented in these figures.

In Figure 3.43, the vertical (positive) gradients of the horizontal component of the background flow near the barriers are shown.

Placing a large windscreen (2*H*) behind a single noise barrier instead of a smaller one (1*H*) does not result in a significant improvement in the area considered. The average values of *net IL* (2.1 dB for the small windscreen, 2.3 dB for the large windscreen) as well as the distributions are very similar. This behaviour was also observed during the wind tunnel experiment.

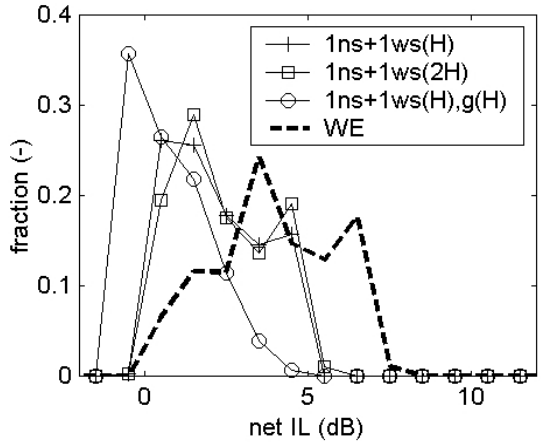

Figure 3.41 Spatial distribution of the *net IL* regarding total sound pressure levels resulting from typical traffic noise, for different configurations of windscreens, applied to single noise barriers in the region of interest (as defined in the beginning of this chapter). A wind speed of 11 m/s (at a height of 10 m) and a porosity of 0.32 are used. The magnitude of the wind effect (*WE*) is also shown.

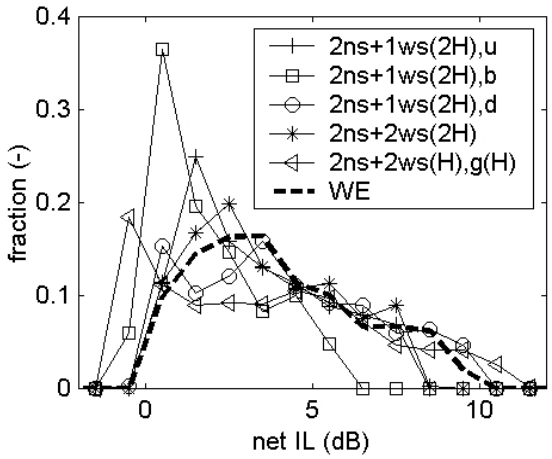

Figure 3.42 Spatial distribution of the *net IL* regarding total sound pressure levels resulting from typical traffic noise, for different configurations of windscreens, applied to noise barriers on either side of the source, in the region of interest (as defined in the beginning of this chapter). A wind speed of 11 m/s (at a height of 10 m) and a porosity of 0.32 are used. The magnitude of the wind effect (*WE*) is also shown.

The configurations with noise barriers on either side of the road and windscreens linked up to the barriers (*2ns+1ws(2H),u*; *2ns+2ws(2H)* and *2ns+1ws(2H),d*) result in positive effects in the complete region of interest. Average values of the improvement by placing windscreens are respectively 3.3 dB, 3.6 dB and 4.1 dB, while the average *WE* equals 4.0 dB. These findings are consistent when looking at the magnitude of the areas in which no positive gradients in the horizontal background flow occur, as shown in Figure 3.43. Placing a windscreen behind the downwind noise barrier seems to be the best choice. This same conclusion was drawn from the wind tunnel experiment, for part of the traffic noise spectrum and up to distances of 10*H*. Based on the comparison between experimental data and simulations (see Chapter 3.4.2.f - *FDTD* calculations) however, this difference between the two configurations was not observed. As already stated, this was a comparison at only one specific height above the ground surface, and for part of a traffic noise spectrum.

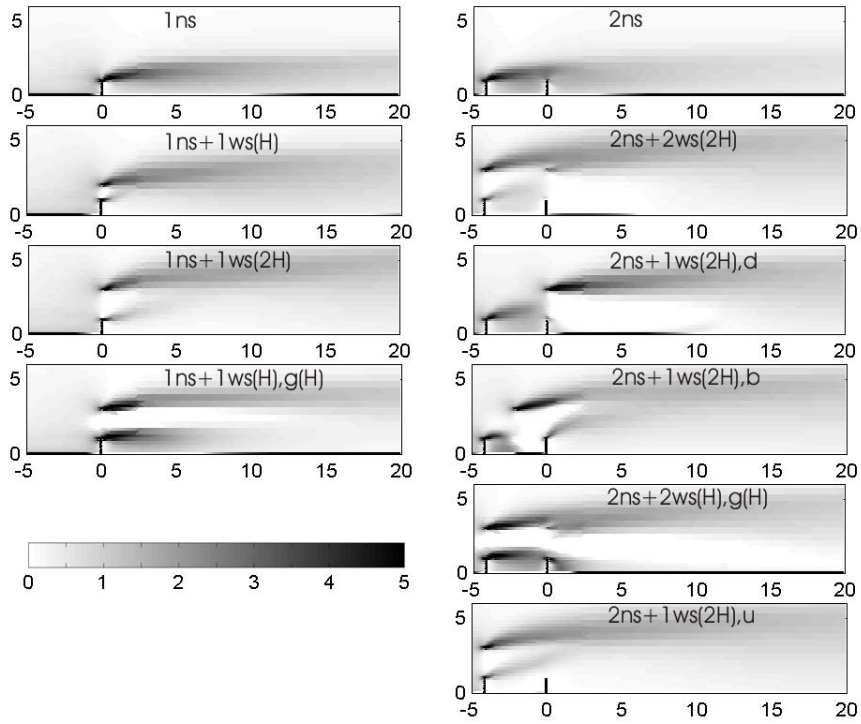

Figure 3.43 Vertical (positive) gradients in the horizontal background flow component (in 1/s) near the barriers for the configurations under investigation. The gradients in the range 0/s to 5/s are shown.

At first sight, one could expect that the more wind speed is reduced (by placing additional windscreens), the higher the improvement in noise barrier performance. However, the area in which positive gradients in the horizontal component of the wind speed are absent is larger for the situation *2ns+1ws(2H),d*. On the other hand, the maximum values of the gradients are observed near the top of the windscreen in the latter, which lies closer to the acoustic shadow zone. The wind speed profiles near both barrier configurations are shown in Figure 3.44 and indicate that downwardly as well as upwardly refracting flows are present near the acoustic shadow zone of the barriers. In situation *2ns+1ws(2H),d* upward refraction will be larger at the leeside of the downwind noise barrier. Another difference between these two configurations may come from a larger turbulence strength in the region in between the two noise barriers for the case *2ns+1ws(2H),d* (see Figure 3.17). This comparison

illustrates that noise barrier performance in wind, in combination with windscreens, is the result of the complex interactions caused by the multiple reflections between the barriers, the multiple diffraction paths, upwardly and downwardly refracting flows and turbulence effects (probably to a smaller degree). Designing wind profiles for optimal noise barrier performance is not a trivial task, and detailed analysis is necessary to evaluate each configuration.

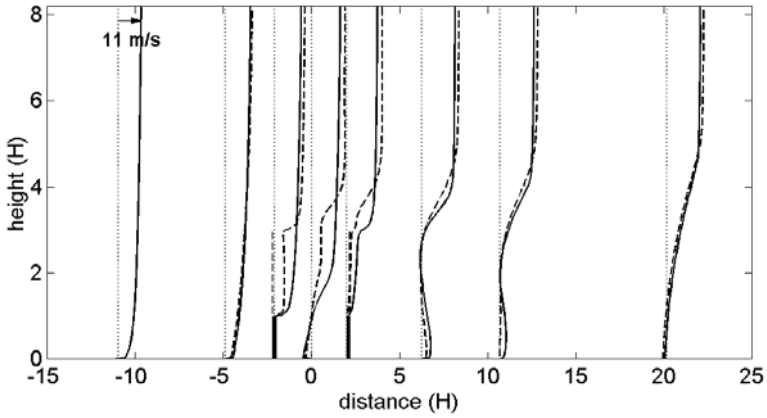

Figure 3.44 Wind speeds profiles along the wind tunnel at selected locations. The incident wind velocity above the boundary layer is 11 m/s. Distances (relative to the position of the source) and heights are expressed in screen heights. The velocity profiles for configuration *2ns+2ws(2H)* are represented by the dashed lines, for configuration *2ns+1ws(2H),d* the full lines are used. For each profile, the line of zero wind speed is indicated with the dotted lines.

In contrast to the single noise barrier configurations, it is possible to almost completely cancel the effect of wind in the region of interest for noise barriers on either side of the road. The distribution of the magnitude of the wind effect (*WE*) and the distribution of some windscreen-configurations are indeed very close to each other, for total sound pressure levels from traffic noise. In case of single noise barriers, a significant region near the acoustic shadow zone without (positive) gradients in the background flow is not found. The wind flow near the barriers in case of e.g. configuration *2ns+1ws(2H),d* results in a large area without gradients, ranging from ground level to the top of the windscreen (3*H*) and up to a distance of 10*H*.

Using a windscreen in between the noise barriers (*2ns+1ws(2H),b*) results in a more limited improvement: the average *net IL* is 1.8 dB. In contrast to the configurations where the windscreens are linked up to the noise barriers, a sharper maximum is observed and a small fraction of the observations lies within the negative *net IL* classes.

In the wind tunnel experiment, it was observed that the configurations with a gap between noise barrier and windscreen result in negative *net IL* at the distances investigated (ranging from 3*H* to 10*H*). It is shown in Figure 3.41 that for the single noise barrier configuration, the maximum in the distribution of *net IL* values is negative, and only a small average effect of 0.8 dB can be obtained. For the double noise barrier configuration with gaps in the windscreens, a local maximum is observed at negative values for *net IL*. The negative effects occur only at limited distances (< 6*H*). It can be observed that the gradients on top of the downwind noise barrier are hardly affected by placing a windscreen (with a gap). Moreover, extra downwardly refracting flows are now present near the bottom of the windscreen, resulting in the negative effects, as observed during the experiment and with numerical simulations.

However, the average value of *net IL* in the region of interest for configuration *2ns+2ws(H),g(H)* equals 3.5 dB. At larger distances, this configuration performs even better than the other ones. The largest values of *net IL* (see Figure 3.42) are observed for this configuration. Figure 3.43 shows that this is the only situation where a large area without positive gradients is present above the barrier height, starting from about 10*H*. In general however, one could conclude that large gaps in the windscreens are less suitable because of the negative wind effects close behind the downwind noise barrier.

In Figure 3.45 and Figure 3.46, more detailed information is shown by means of contour plots for the double noise barrier configuration. In Figure 3.45, sound pressure levels are shown in absence of wind (a), in presence of wind (without windscreens) (b) and in presence of both wind and a large windscreen behind the downwind noise barrier (*2ns+1ws(2H),d*) (c). In Figure 3.46 the insertion loss in absence of wind (a) is shown together with some quantities derived from Figure 3.45: namely the magnitude of the *WE* (b) and the *net IL* or the improvement by placing a windbreaks behind the downwind noise barrier (c). In both figures, an area up to a distance of 20*H* behind the downwind noise barrier and up to a height of 6*H* is shown. The effect of wind is significant: a decrease in barrier efficiency of more than 8 dB is noticed at distances starting from 15*H* (see Figure 3.46 (b)). A zone is observed above the noise barrier height where values of *WE* are negative. This means that positive effects from the action of wind on the sound pressure levels are expected in this area. Placing a windscreen expands

this zone towards lower heights, but it still lies far away from the region where receivers are expected.

The region in which improvement is observed by placing a row of trees behind the noise barrier is bordered by the dashed, tick black line in Figure 3.46 (c). The main zone of interest for noise reduction by barriers is covered. At most places, the *net IL* approximates the *WE* for this configuration of windscreens, indicating that wind effects are neutralised.

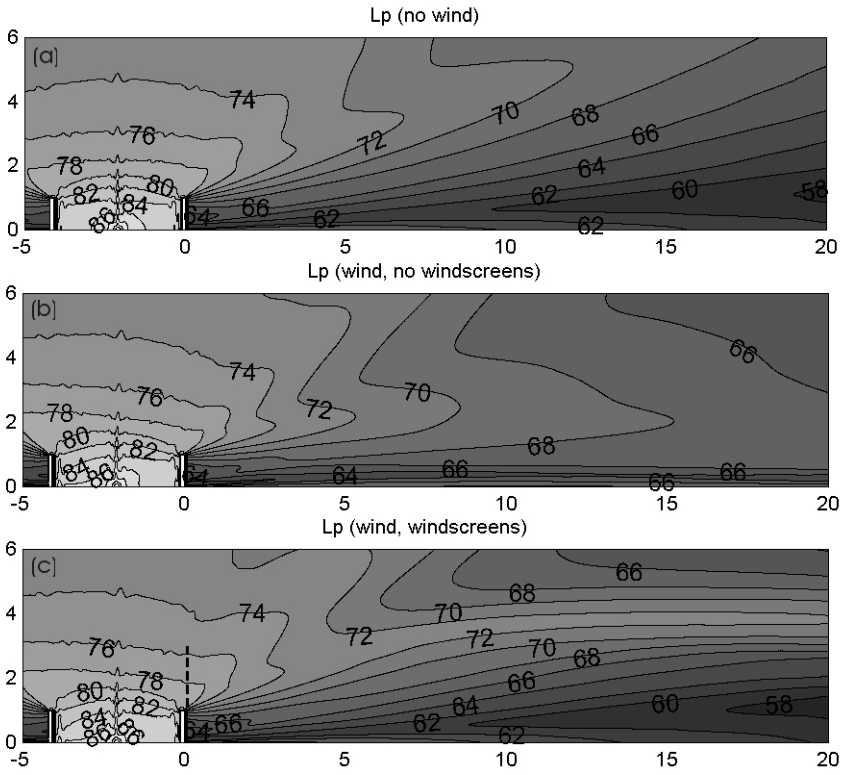

Figure 3.45 Numerically simulated sound pressure levels in absence of wind (a), in presence of wind (without windscreens) (b) and in presence of both wind and a large windscreen (2*H*, porosity of 32%) behind the downwind noise barrier (c), for sound pressure levels resulting from typical traffic noise. Distances and heights are expressed in noise barrier heights. The values in the field plots are in dB.

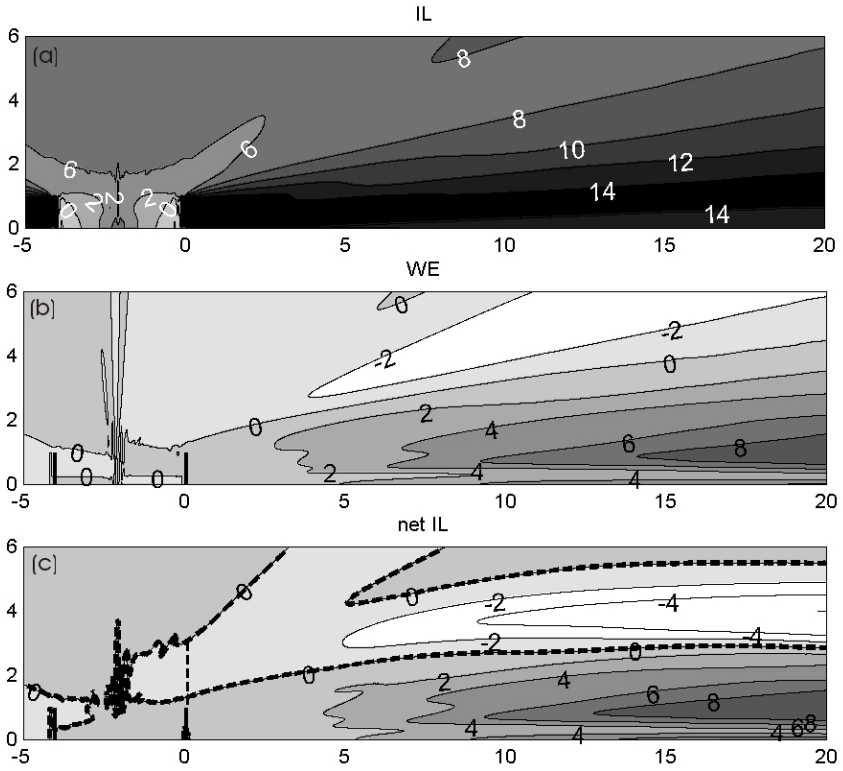

Figure 3.46 Numerically simulated *IL* in absence of wind (a), the magnitude of the wind effect (*WE*) (b) and the *net IL*, as a result of placing a windscreen (2*H*, porosity of 32%) behind the downwind noise barrier (c), for total sound pressure levels resulting from typical traffic noise. Distances and heights are expressed in noise barrier heights. The values in the field plots are in dB.

3.4.4.f Conclusions

The finite-difference time-domain method, taking into account background flow, has shown to be a powerful tool for the investigation of the parameters involved in placing windscreens or rows of trees behind noise barriers. In this part of the study, a full region behind the noise barriers is considered. With increasing porosity, the effect of placing a row of trees behind a noise barrier becomes less effective. The maximum effects in the area considered are lower, and the number of places where negative effects are observed increase.

In high wind speeds, it is possible to obtain a larger improvement as a result from placing windscreens. At distances smaller than 10*H* downwind from a single noise barrier, the linear relationship between *net IL* (expressed in dB) and wind speed (expressed in m/s) is observed just like in the field experiment.

Increasing the distance between source and noise barrier results in a decrease in noise barrier performance in wind (or an increase in *WE*). For a single noise barrier configuration with the use of a large windscreen behind it, *net IL* and the wind effect follow the same trend. Different behaviour is observed when noise barriers are present on either side of the source. When the source is very close to the noise barriers, the action of wind is completely neutralised. With increasing distance, the net efficiency of the windscreens decreases, while the wind effect keeps increasing, however to a small degree. For the situation that was investigated, the average effect in the region of interest is only slightly affected by the soil impedance downwind from the noise barrier.

In a typical traffic noise situation, it is possible to complete cancel out wind effects up to a distance of 20*H*, and up to a height of 1*H*, when placing a large windscreens behind the downwind noise barrier. The best overall results are obtained when the windscreens are linked up to the noise barriers. Gaps between the top of the noise barrier and the bottom of the windscreens results in negative effects at limited distances, and should therefore not be considered. At large distances however, they could perform as well as the other configurations of windscreens.

It was shown that designing wind profiles for optimal noise barrier performance is not a trivial task. The effect of windscreens or rows of trees is the result of the complex interactions caused by the multiple reflections between the barriers, the multiple diffraction paths, upwardly and downwardly refracting flows and turbulence. Detailed analysis is necessary to evaluate each configuration.

3.5 Sound propagation over rows of houses in the presence of wind (case-study)

3.5.1 Introduction - Quiet side

Access to a quiet place is important for inhabitants of a city. Such a quiet place could be e.g. a backyard behind a large (shielding) building or a room that does not face the street. Easy access to such places has shown to reduce the percentage highly annoyed residents in a noisy area [100]. Another study reported that people living in rows of houses with an orientation parallel to a

motorway were in general less annoyed than people living in houses with an orientation perpendicular to a motorway. This difference in annoyance is attributed to having a shielded and therefore quiet back-façade [101]. Based on these results, it was e.g. stated in the Swedish action plan against noise that a noisy situation could be compensated with simultaneous access to a quiet environment. A general environmental noise guideline is therefore less suited [102] in order to improve the city noise climate.

Traffic is the main noise source in a city. Since the construction of quieter vehicles is a very slow process, little benefit is expected from further improving cars with respect to noise emission in the coming years [102]. As a result, current studies to solve the city noise problem focus on the protection of quietness in cities, justified by the compensation strategy as discussed above. An important measure to obtain this is good city planning e.g. by managing traffic flows or by optimising building orientation. Another possibility is highly insulating the façades on the noisy sides.

The sound pressure levels in a typical backyard near a street canyon are usually low, due to the shielding of tall buildings. As a consequence, secondary sources may become important when calculating sound levels at quiet places. E.g. noise coming from distant traffic may contribute. Also atmospheric effects may become important in this view. There will be refraction of sound into a backyard for downwind receivers, due to the large positive gradients in the wind speed. At rooftop level, wind velocity is zero and rapidly increases with height. Due to the complex flow observed near specific configurations of buildings and roof types, refraction of sound becomes complicated. The wind flow encountered above a city is usually highly turbulent. There is a lot of advected turbulence in the flow due to the large number of interaction of the wind flow with obstacles upstream. In this chapter, it is investigated how wind affects the quietness of backyards and back-façades.

A “street canyon” is present when a street is in between two closed rows of tall buildings. This is a common configuration in large cities. Such a street canyon can be seen as a reverberant room with an open roof, since the façades of buildings are usually acoustical quite hard. Multiple diffraction paths are present to nearby backyards. Sound pressure levels are usually high in a street canyon with dense traffic. At sufficient distance from the source, the sound pressure level distribution along the height and width of the canyon is generally even [103].

The façades of real buildings are usually not smooth: there will be irregularities and these cause diffuse reflection. The consideration of pure specular reflection is unreasonable in many cases [104]. It is stated in Ref. [105] that in the

viewpoint of urban noise reduction, it is better to design the building façades as diffusely reflective rather than acoustically smooth. With increasing degree of roughness of the façades facing the street, the reverberation time in the street canyon becomes lower and sound pressure levels decrease more rapidly along the length of the street [105]. It has been proven experimentally that with a given sound pressure level, noise annoyance is greater when the reverberation time is longer [106].

Taking care of diffusely reflecting boundaries in an urban environment has shown to be important, as illustrated in previous paragraphs. Therefore it is also investigated in Chapter 3.5.2.e how the roughness of the façades influences sound pressure levels in the backyard.

3.5.2 Sound propagation from street canyon to backyard

3.5.2.a Configuration

The wind flow as observed near a specific street canyon depends on the whole configuration of buildings upstream. Since it is not possible to simulate in detail the flow above a complete city, some approximations need to be made. We will simulate an idealized configuration of a street canyon where an acoustic source and a nearby backyard, enclosed by two buildings, are present. An overview of the tested configuration is shown in Figure 3.47.

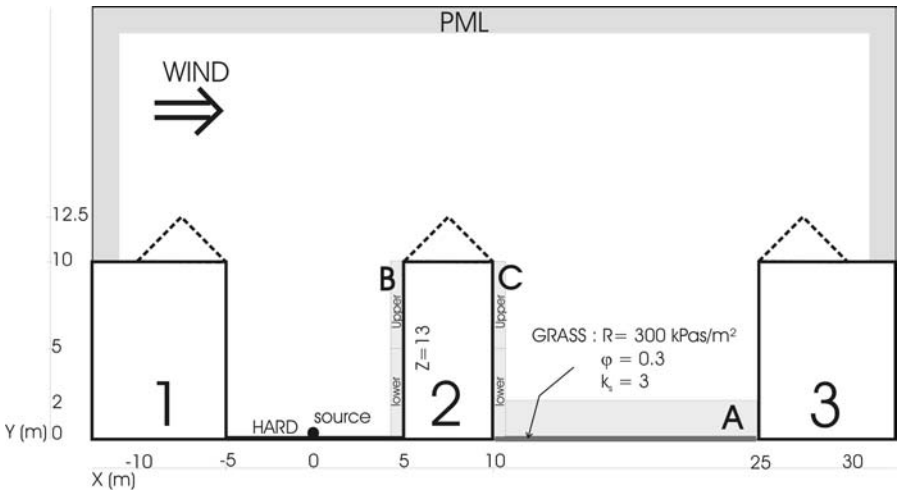

Figure 3.47 Overview and dimensions of the tested configuration, with indication of the regions A, B and C, used to present simulation results.

A two-dimensional simulation is performed. Sound propagation from the street canyon to the nearby backyard is considered. All buildings have a height of 10 m. The width of the street canyon is 10 m as well. The backyard is enclosed by buildings that are at a distance of 15 m from each other. The middle building (number 2) has a width of 5 m. An infinite line source is situated in the middle of the street canyon at ground level. The simulated row of houses is infinitely long as well. This means that only sound propagation over the rooftops may contribute to the sound pressure levels in the backyard.

The street surface coverage is perfectly reflecting. For the façades, a normalized acoustic (real) impedance of 13 is used, which simulates reflection from bricks. In the backyard, a piece of grassland is simulated with the Zwikker and Kosten model and following parameters: R = 300 kPas/m², $\varphi = 0.3$ and $k_s = 3$.

Above the upwind building, a logarithmic wind speed profile is used as an inflow boundary condition, starting from roof top level. Distant sources are not considered.

3.5.2.b Sound propagation paths

Sound energy is transferred to the backyard mainly by diffraction. Due to the multiple reflections between the buildings 1 and 2 in the street canyon, refraction of sound may contribute to the sound pressure level obtained in the backyard. Only after a large number of reflections, sound rays leaving the street canyon propagate nearly parallel to the rooftop. Only these rays will be sufficiently bent downwards before the façade of building 3 is reached. Then, by multiple reflections in the backyard, receivers near the ground may be reached. Rays that leave the street canyon without reflections or only after a few reflections do not contribute to the sound pressure level in the nearby backyard by means of refraction. The typical distances between the buildings that enclose backyards are too small when comparing the strength of (even large) refraction with the speed of sound. However, these rays may still influence the sound climate at more distant locations downwind. Increased sound pressure levels in the presence of wind may also come from a combination of diffraction of sound near the top of façade B, followed by refraction into the backyard.

Turbulent scattering is important when the length scales of the eddies have the same dimension as the wavelength of the propagating sound. According to (classical) scattering theory, the incident sound energy is spread over a range of propagation angles after the acoustic wave and the vortex have interacted. Most energy is however scattered in forward direction and this scattered energy decreases with deviations from that direction. This means that the multiple reflections between the buildings, as discussed in previous paragraph, also become important concerning scattering of sound into the backyard. For the simulation of sound pressure levels in a nearby-located backyard, it is not important to simulate turbulence at large heights above the buildings. It is estimated that only a small amount of acoustic energy would reach receivers due to the increased scattering angle, the increased propagation path length, and also due to the larger number of interactions between the wave and turbules.

3.5.2.c Effect of refraction

As an inflow boundary condition, a logarithmic wind speed profile is used, starting from rooftop level. The wind speed at a height of 15 m (or 5 m above the buildings) was chosen to be 10 m/s, while a roughness length of 0.01 m was used. The k-ε turbulence model is used (turbulent intensity, i.e. the root mean square of the velocity fluctuations divided by the mean velocity, at the inflow was 5%, the length scale 1 m). It is not possible to generalize wind speed profiles above buildings in urban areas since they largely depend on the local and upwind conditions. The flow field near the street canyon and backyard is shown in Figure 3.48, for the flat roof and the saddle-backed roof configuration. The (interpolated) magnitude of the flow velocity in the acoustic grid is shown. During the *CFD* simulation, borders were sufficiently away from the structures that influence the flow, especially in case of a saddle-backed roof.

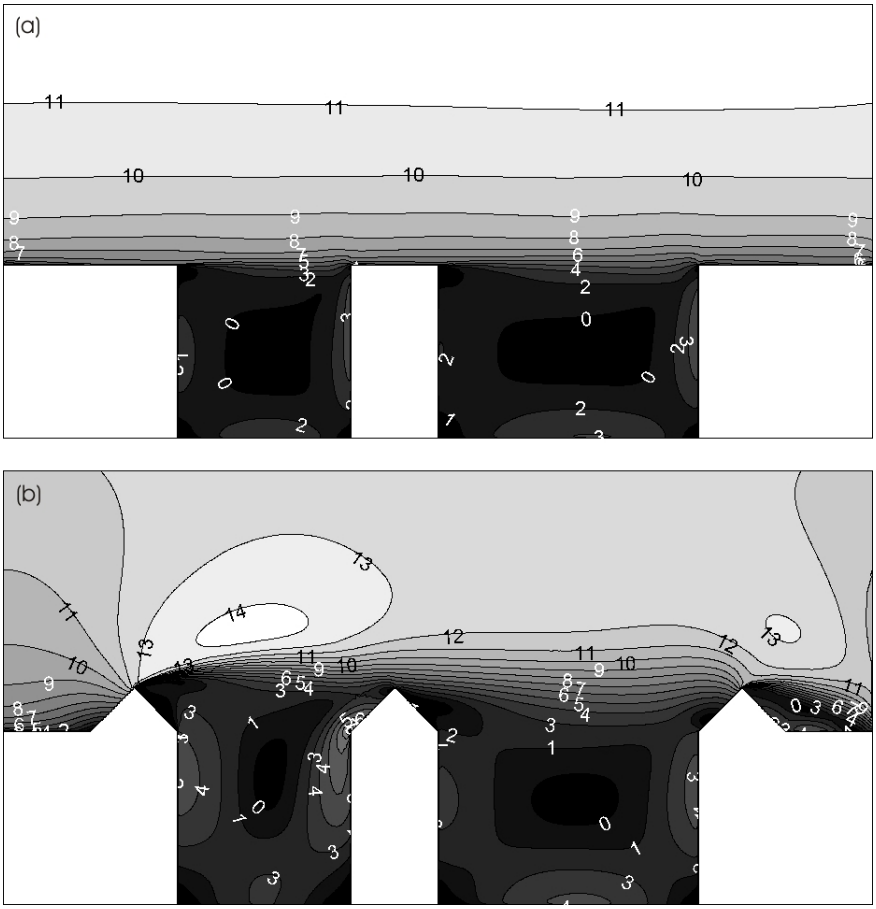

Figure 3.48 Contours of the magnitude of the flow velocity (expressed in m/s) near the street canyon and backyard, for the flat roof (a) and saddle-backed roof (b) configuration.

The introduction of the saddle-backed roofs, or more in general flow-disturbing objects, makes the flow field more complex. A wake is formed on the leeside of the saddle-backed roofs. The overall vertical (positive) gradients of the horizontal component of the background flow near the canyons are somewhat increased. However, at the height of the flat rooftop, gradients are larger for the flat roof configuration. This is illustrated with the field plots in Figure 3.49.

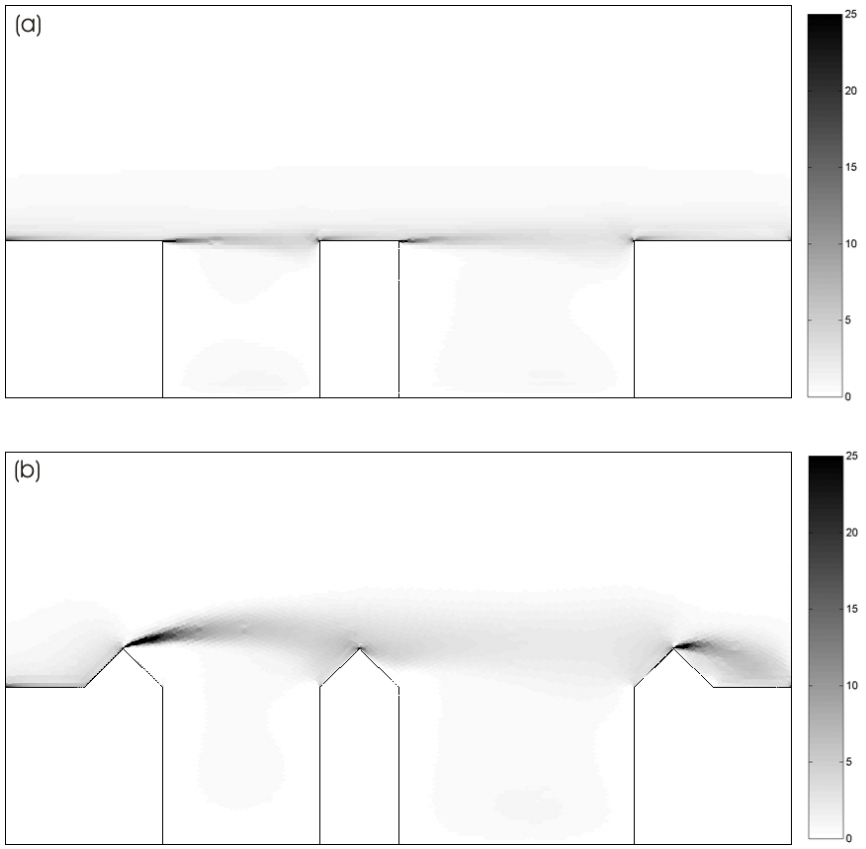

Figure 3.49 Field plots of the vertical gradient of the horizontal component of the background flow, expressed in 1/s, for the flat roof (a) and saddle-backed roof (b) configuration.

Possible receivers in the backyard are expected in region *A*, ranging from ground level to a height of 2 m over the full width of the backyard (see Figure 3.47). In this area, the (spatial) distribution of values of the Wind Effect (*WE*) is calculated, on a two-dimensional grid with observation points that are apart from each other at distances that equal $1/10^{th}$ of the shortest wavelength under consideration. The wind effect is defined as the sound pressure level in presence of wind minus the sound pressure level in absence of wind, at a fixed place. Frequency interva1s, with main energy in the range from 125 to 250 Hz, 250 to 500 Hz and 500 to 1000 Hz are considered. The bandwidths (see equation (2.110)) are respectively 125, 250 and 500 Hz.

In Figure 3.50 and Figure 3.51, the spatial distribution of values of the wind effect in region *A* for the flat and saddle-backed roof configuration are shown. For the flat roof configuration, average effects in region *A* of respectively 1.8 dB, 3.7 dB and 6.5 dB are observed: with increasing frequency, the effect of the wind becomes larger. The corresponding values in case of a saddle-backed roof are respectively 1.5 dB, 1.6 dB and 1.8 dB. The sound pressure levels in the backyard in the latter are less influenced by the action of wind.

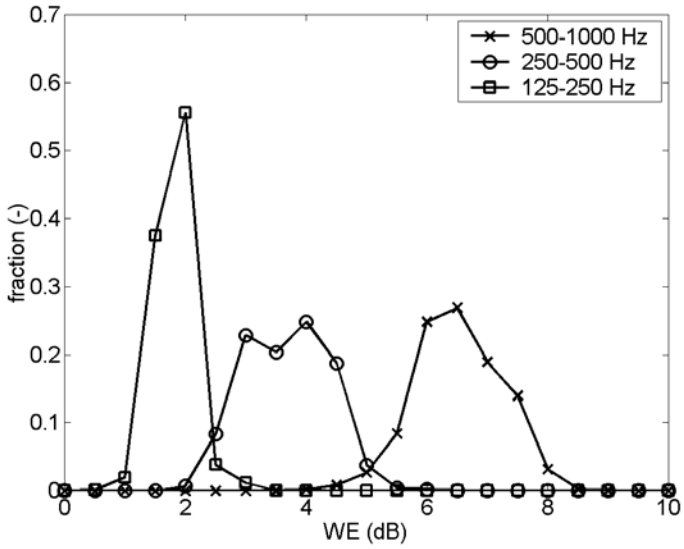

Figure 3.50 Spatial distribution of the values of the wind effect (*WE*) for the flat roof configuration, expressed in dB, in region *A* (see Figure 3.47).

The sound pressure levels observed in the backyard are the result of complex interference patterns caused by the multiple reflections between the buildings, the frequency-dependent reflection from the soil and the action of the wind. The differences in the width and shape of the spatial distributions as observed in Figure 3.50 and Figure 3.51 are an illustration of this.

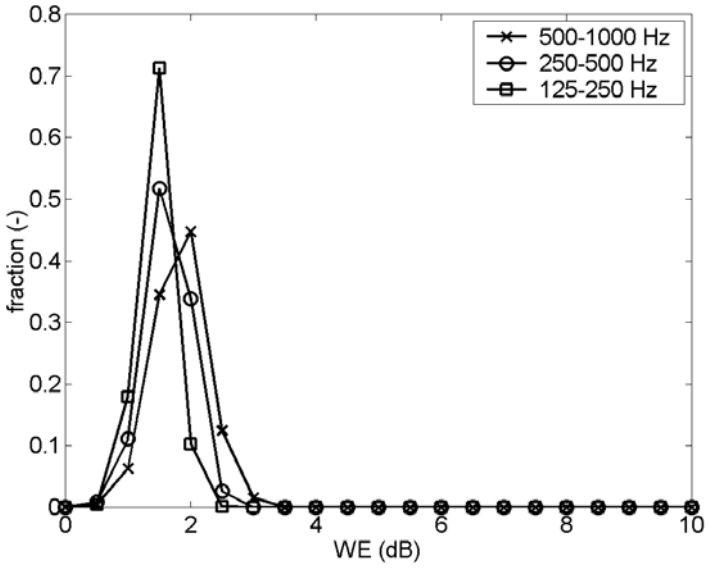

Figure 3.51 Spatial distribution of the values of the wind effect (*WE*) for the saddle-backed roof configuration, expressed in dB, in region *A* (see Figure 3.47).

3.5.2.d Effect of turbulent scattering

Parameters of the turbulent flow field

The velocity structure parameter is needed for the estimation of the angular velocity of the largest scale of turbulence considered. Above a flat ground, it is possible to quantify the (velocity) turbulence strength, based on the friction velocity, which second power is proportional to the variance of the velocity components [56], and based on an estimation of the outer scale of turbulence. Using equation (2.124), the structure velocity parameter can be estimated for an isotropic and homogeneous, turbulent field. However, it is expected that these relations are not valid above a city.

In Ref. [107], measurements of the velocity structure parameter were performed in calm winds (< 4 m/s) and in stronger winds (4-7 m/s), in the neighbourhood of a 2.44-m wide and 2.55-m high barrier. Values of C_v^2 were in the range 0.4 – 2 $m^{4/3}/s^2$ for the calm wind situation, and from 8 to 17 $m^{4/3}/s^2$ in the stronger wind situation.

Based on the above findings, simulations have been performed for C_v^2 of 10 $m^{4/3}/s^2$ and 20 $m^{4/3}/s^2$.

The turbule theory, as described in Chapter 2.6.3, will be used to construct a scattering, turbulent field. Turbulent scattering in practical situations outdoors becomes important from about 500 Hz, when considering long propagation distances [108]. With increasing frequency, scattering on turbulent inhomogeneities increases.

The turbule model is a three-dimensional model. It is however not possible to simulate sound propagation through a full three-dimensional turbulent atmosphere for the frequencies of sound where effects are expected. Even in a two-dimensional simulation domain, large frequencies (higher than 1000 Hz) cannot be easily modelled due to the limited computational resources. Moreover, it is necessary to simulate sound propagation through a sufficient number of realisations of the turbulent field.

Taking into account computation times, but also considering sound frequencies high enough to observe scattering on turbulence, the simulations are performed for a sound frequency of 1000 Hz. It is however expected that the received sound spectrum in a backyard does not contain much energy at higher frequencies when considering traffic noise.

In a simplified numerical experiment, scattering by a full three-dimensional, turbulent field is simulated. This data is compared to the analogous situation in two dimensions, where the vortices are replaced by circles, with (at random) clockwise or counter-clockwise orientation. It was found that the three-dimensional structure velocity parameter C_v must be scaled with a factor of approximately 1/3 when scattering from a two-dimensional turbulent flow is to be simulated. As a result, a C_v^2 of 10 $m^{4/3}/s^2$ and 20 $m^{4/3}/s^2$ corresponds to a value of respectively 10/9 $m^{4/3}/s^2$ and 20/9 $m^{4/3}/s^2$ in the two-dimensional simulations performed here.

Application of the turbule model

Scattering is mainly observed when the length scale of turbulence and the wavelength have the same order of magnitude. The (velocity) turbulent flow field is constructed by introducing eddies with length scales that are larger and smaller than the wavelength considered. The largest scale was 1.5 m (scale number 1), while the smallest scale, limited by the computational grid, was 0.047 m (scale number 6). The length scale at scale number $n+1$ is chosen to be half the length scale at scale number n, which results in a parameter μ of 0.69. With decreasing length scale, the angular velocity increases according to equation (2.125) (see Figure 3.52).

A homogenous turbulent field above the (flat) buildings is constructed using the approach as described in Chapter 2.6.3. The relation between the side of the

squares cell (defined in order to obtain a homogeneous turbulent atmosphere as described in Chapter 2.6.3) and the length scale (d_α/a_α) is chosen to be 8. The latter determines the packing fraction (see equation (2.122)) and yields 0.002.

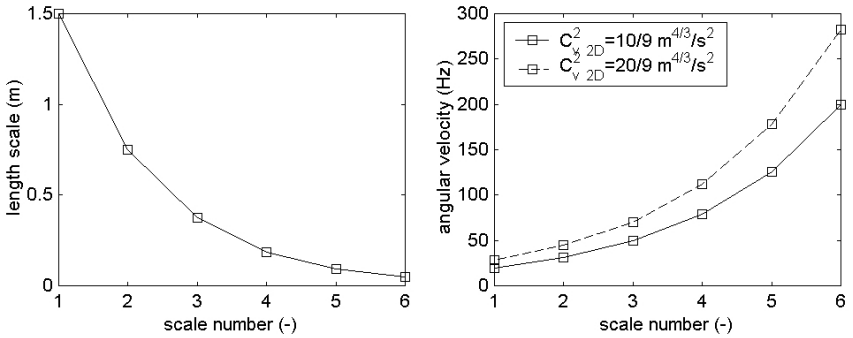

Figure 3.52 Length scales and angular velocities with increasing scale number, as used for the construction of the turbulent flow field.

In Figure 3.53, the turbulent kinetic energy field of one realization of a homogeneous turbulent field is shown. The vortices at each scale of turbulence can be identified. This field is superimposed on the flow field as obtained by the *RANS-CFD* simulation with the k-ε model.

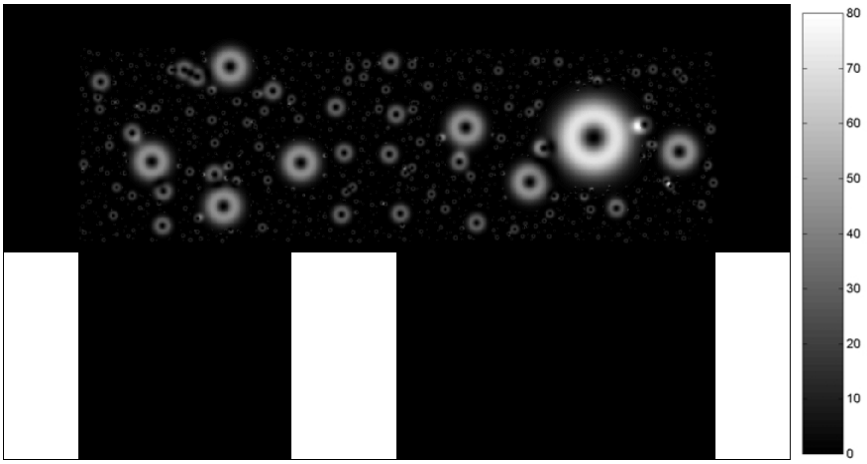

Figure 3.53 Turbulent kinetic energy field $0.5\left|\boldsymbol{v}_i\right|^2$ (in m²/s²) for a single realization of the homogeneous, two-dimensional turbulent flow field. The C_v^2 in two dimensions is 10/9 $m^{4/3}/s^2$.

The energy spectrum resulting from the turbulent field in Figure 3.53 is shown in Figure 3.54. The typical slope of -5/3 when plotting turbulent kinetic energy (arbitrary scale) with increasing (one-dimensional) spatial wave number is found in a log-log plot, for the range of length scales considered.

The effect of turbulent scattering into the backyard is shown in Figure 3.55, for a frequency of 1000 Hz. The spatial distribution of the effect of wind on sound propagation in region *A* in absence of turbulent scattering and in the presence of homogeneous turbulence is shown. Simulations, accounting for an increase in turbulence strength near the (flat) rooftops are also performed. In the latter, the angular velocities of the turbules are scaled according to equation (2.128). The average effects as a result of 10 realisations (for each case where turbulence is involved) are shown. Making small-scale eddies explicit in the flow field by means of the turbule model results in an increase in the average effect of wind with 1.7 dB and 2.6 dB upon refraction, for respectively homogeneous and building-induced turbulence, in case of a three-dimensional C_v^2 of 10 $m^{4/3}/s^2$. In case of a stronger degree of turbulence (C_v^2 = 20 $m^{4/3}/s^2$), these values are respectively 2.1 dB and 2.7 dB. Scattering in the backyard is increased when taking into account building-induced turbulence. Considering 10 realisations of the turbulent field results in values that are statistical different (with a certainty of more than 99 %) relative to the simulation where only refraction is present. The difference between mean sound pressure levels in a homogenous, turbulent atmosphere and the simulation where building-induced scattering is accounted for, is less statistical significant. In case of a C_v^2 of 10 $m^{4/3}/s^2$, the simulation results are different at a probability of 93 %, while in case of a value of C_v^2 of 20 $m^{4/3}/s^2$, the simulation results can not be considered different anymore.

The main increase in sound pressure level in the backyard in the presence of wind can be attributed to the building-induced refraction of sound (about 10 dB in this situation). Turbulence is responsible for a further increase of a few extra decibels. However, the use of the turbule model to include turbulent scattering in this specific (and complicated) situation is not validated with experiments. These results should therefore be used with care.

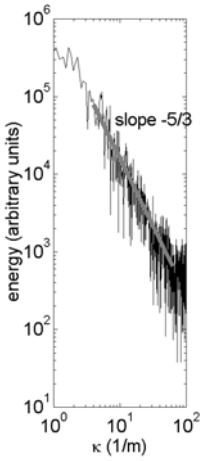

Figure 3.54 Turbulent energy spectrum of the realization of the turbulent field shown in Figure 3.53. In abscissa, the spatial wave number is shown, in ordinate the energy in arbitrary units.

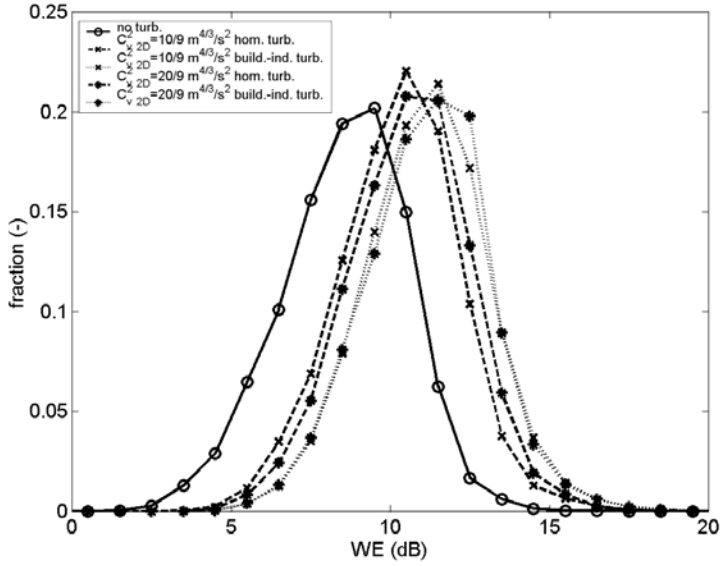

Figure 3.55 Spatial distribution of the wind effect in the region of interest *A*, for 1000 Hz. The effect of refraction without (small-scale) scattering, the effect of a homogeneous turbulent field, and a turbulent field accounting for building-induced turbulence are shown. Values of $C_{v^2\,2D}$ of 10/9 $m^{4/3}/s^2$ and 20/9 $m^{4/3}/s^2$ are used in these simulations.

3.5.2.e Effect of roughness of façades

Diffuse reflection is included in the simulation by making the façades of the buildings somewhat irregular. Each computational cell directly near the façades, along the full height of the buildings, is replaced with a chance of 50% by a building element. In Figure 3.56, the distribution of (total) sound pressure levels in the street and backyard is shown, relative to the maximum level in the street canyon. The line source in the street canyon emitted a frequency interval with main energy in the range from 250 Hz to 500 Hz (with a bandwidth of 250 Hz). All façades, in both the street canyon and backyard, are made rough.

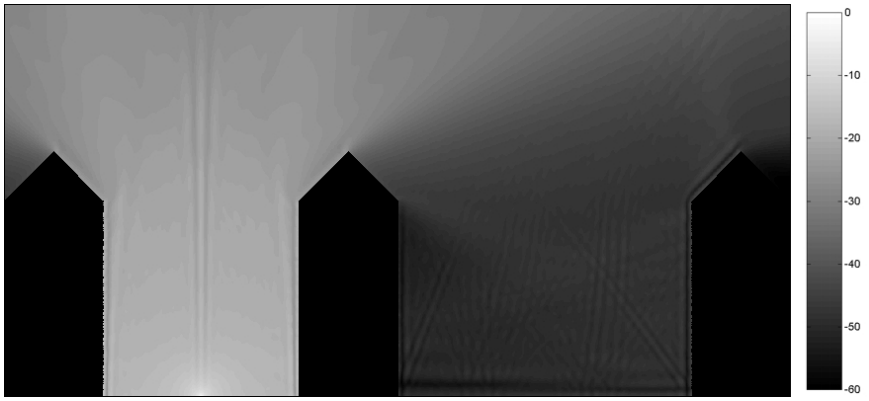

Figure 3.56 Distribution of sound pressure levels (in dB), relative to the maximum level, in the street canyon and backyard. All façades are rough. The frequency interval 250-500 Hz is considered.

The effect of placing (small) roughness elements near the façades is now investigated in more detail. At a height of 1 m, in the middle of the street canyon, the reverberation of fully specular and diffusely reflecting façades are compared, for a normalized acoustic impedance of 13. A perfect hard, fully specular reflecting façade is also simulated. The decrease in sound pressure level relative to the direct sound in the street canyon is shown in Figure 3.57 with increasing time. The line source emitted a pulse with main energy in the frequency interval ranging from 500 Hz to 1000 Hz (with a bandwidth of 500 Hz). With respect to reverberation, two measures are often used namely the Early Decay Time (*EDT*) and Reverberation Time (*RT30*). *EDT* is calculated from the initial 10 dB decrease. *RT30* is determined by using the rate of decay given by the linear regression of the simulated decay curve from a level 5 dB below the initial value to 35 dB below.

With increasing absorption of the walls, sound pressure levels decay more rapidly in the street canyon, resulting in important differences in *RT30* (1.56 s for hard wall, 0.49 s for absorbing wall) and also in *EDT* (0.11 for hard wall, 0.06 for absorbing wall). When also diffuse reflection is taken into account, the reverberation time becomes smaller: there is a significant difference in *RT30*, which reduces to 0.34 s, while the *EDT* reduces to 0.05 s and stays close to the value of a specular reflecting wall. These findings are consistent with the measurements and simulations e.g. in reference [105].

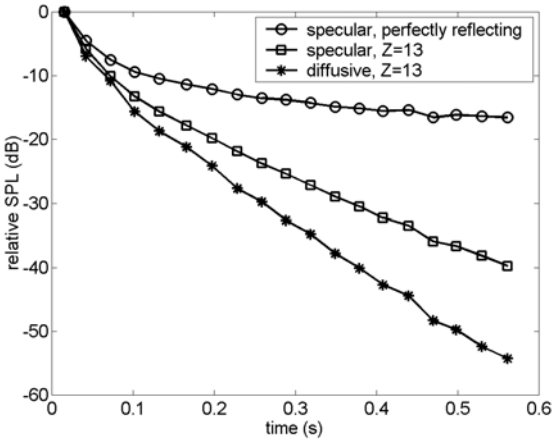

Figure 3.57 Decrease in sound pressure level in the street canyon, relative to the direct sound, with increasing time, for the frequency interval 500-1000 Hz. Fully specular reflection is simulated (for a perfectly reflecting and absorbing façade), as well as diffusive reflection (for an absorbing façade).

The effect of diffusely reflecting façades on sound pressure levels in the backyard is shown in Figure 3.58 and Figure 3.59, for the flat and saddle-backed roof configuration, in absence of wind. The spatial distribution of the observations of the difference between a fully specular and diffusely reflecting façade is calculated. With increasing frequency, reflections from the façades become more diffuse and sound pressure levels in the backyard are decreased. The main reason for this positive effect is that in case of diffusely reflecting boundaries, the average sound path length is longer. As a result, the total energy loss compared to specular reflection for sound propagating between two locations is larger [105], and less acoustic energy is leaving the street canyon. Average effects are respectively 3.3 dB, 4.4 dB and 8.3 dB for the frequency intervals with main energy in the range from 125 Hz to 250 Hz, 250 Hz to 500

Hz and 500 Hz to 1000 Hz (with bandwidths of respectively 125 Hz, 250 Hz and 500 Hz) in the flat roof configuration. For the saddle-backed roofs, these values are 2.8 dB, 3.0 dB and 5.4 dB. Also when the wavelength of sound considered is large compared to the dimensions of the roughness elements, positive effects are observed. In the saddle-backed roof configuration, the effect of a rough façade on sound levels in the shielded area is somewhat smaller, especially for the high frequencies.

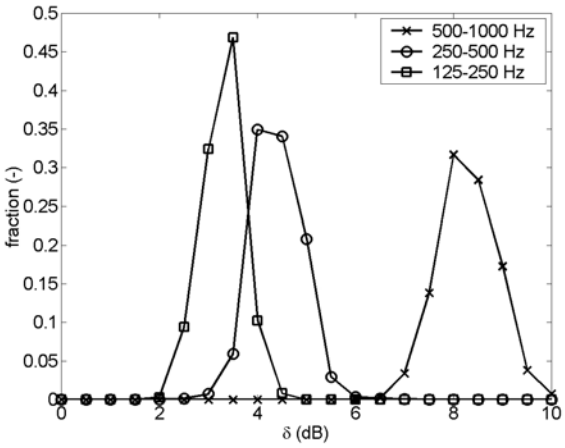

Figure 3.58 Spatial distribution of the difference in sound pressure level between a flat and a rough façade in region *A*, for a flat roof configuration.

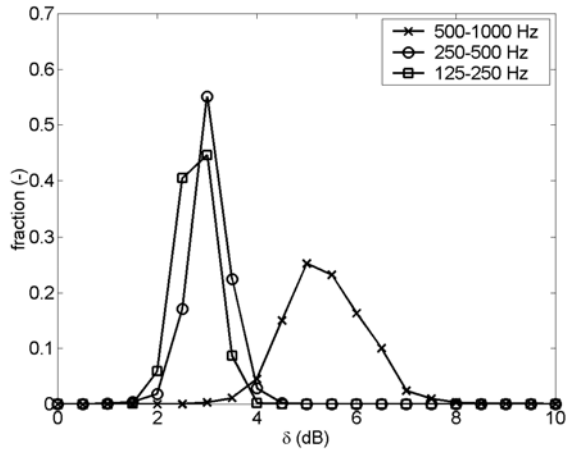

Figure 3.59 Spatial distribution of the difference in sound pressure level between a flat and a rough façade in region *A*, for a saddle-backed roof configuration.

3.5.2.f Façade exposure

In this chapter, the shielding by the middle building is considered. The sound pressure levels in region *B* and *C*, averaged over the lower part (from 0 m tot 5 m) and over the upper part (from 5 m to 10 m) of the façade, are compared. In Table 3.9 and Table 3.10, an overview is given of the difference in façade exposure between the street side and the side that faces the backyard. Calculations have been done for 3 frequency intervals, for the configuration with a flat and a saddle-backed roof and in the presence and absence of wind.

The shielding by the buildings for both roof types, and in the presence and absence of wind, increases with frequency. Only in the upper part of the flat-roof building in presence of wind, the shielding for the 500-1000Hz frequency interval is somewhat smaller than for the 250-500Hz frequency interval.

Table 3.9 Average shielding by the middle building in the lower part (from ground level to 5 m).

	no wind		wind	
frequency interval	flat roof	saddle-backed roof	flat roof	saddle-backed roof
125-250 Hz	26.1	26.1	24.1	24.6
250-500 Hz	29.9	29.3	26.4	28.7
500-1000 Hz	34.5	34.1	28.1	32.0

Table 3.10 Average shielding by the middle building in the upper part (from 5 m to 10 m).

	no wind		wind	
frequency interval	flat roof	saddle-backed roof	flat roof	saddle-backed roof
125-250 Hz	24.7	26.1	23.3	24.9
250-500 Hz	28.3	30.0	25.7	28.6
500-1000 Hz	30.9	33.8	25.6	32.2

In Figure 3.60 and Figure 3.61, the effect of roof type and the wind effect (*WE*) on the shielding of the building are investigated in more detail. For the flat roof configuration, the wind effect increases with increasing frequency. The (negative) effect by the wind on the shielding of the building is somewhat larger for the lower part. In case of a saddle-backed roof, the effect of wind on the shielding by the buildings stays more or less the same with increasing frequency. General effects are smaller than in case of a flat roof.

The effect of roof type on the lower part of the building in absence of wind is small and no general trend with frequency is seen. The upper part is more affected by roof type: with increasing frequency, the saddle-backed rooftop provides a better shielding of sound. This is logical since the actual height of the building when there is a saddle-backed roof is larger. The difference between both roof types is enhanced by the action of wind: more than 6 dB difference is seen instead of 3 dB in absence of wind for the frequency interval 500-1000 Hz

and the upper part of the building façade. The lower part of the façade follows this trend as well, but effects are somewhat lower than for the upper part.

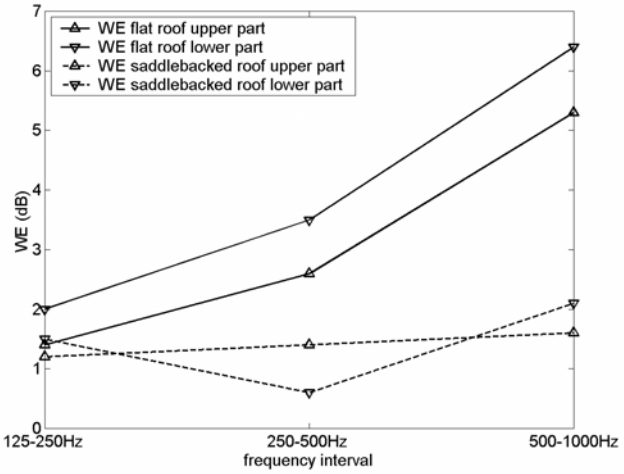

Figure 3.60 Effect of wind on the difference in exposure between the front and back façade, for the lower part and upper part of the building, with increasing frequency interval.

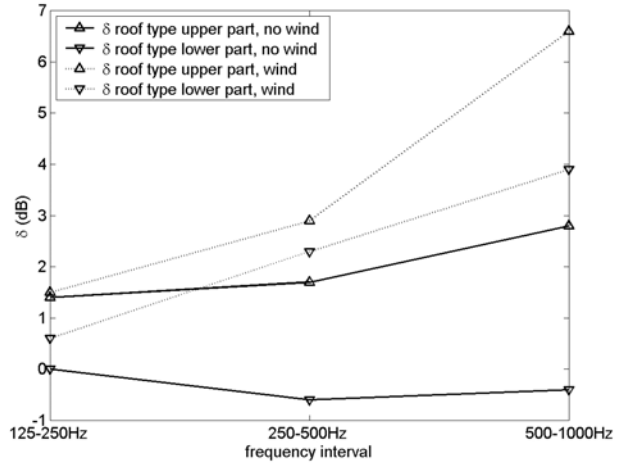

Figure 3.61 Effect of roof type on the difference in exposure between the front and back façade, for the lower part and upper part of the building, with increasing frequency interval.

3.5.3 Conclusions

Sound propagation from a street canyon to a nearby backyard, which is a typical situation in an urban area, is studied. The access to quiet rooms on the back-façade or to a silent backyard is important since it may compensate a noisy street side. The *FDTD* method is capable of simulating the multiple specular and diffuse reflections in the street canyon and backyard, diffraction over non-flat roof types, and reflection from natural grounds. It is also possible to take into account atmospheric effects. The effect of wind, namely refraction of sound and turbulent scattering on the observed sound pressure levels in the backyard, is investigated in detail. It was shown that the interaction of the wind flow and roof type is important when looking at refraction of sound over a building. In case of a flat roof and receivers near the ground in the backyard, the effect of wind increases with frequency and amounts to a mean value of 6.5 dB for the frequency interval 500-1000 Hz, for a wind speed of 10 m/s at a height of 15 m (or 5 m above the buildings). Maximum effects are even larger. When there are saddle-backed roofs, wind effects are significantly smaller in the simulated configuration, and amount only to a maximum of 2.1 dB for the frequency intervals considered.

When also considering small-scale turbulent scattering above the buildings, the effect of the wind is increased with a few dB's for a sound frequency of 1000 Hz. This effect of turbulence is assumed to increase drastically for higher frequencies. However, it is expected that the received sound spectrum in a backyard does not contain much energy at higher frequencies when considering traffic noise.

Diffuse reflection on the façades is important. When only specular reflection is accounted for, sound pressure levels in the backyard are overestimated.

It can be concluded that atmospheric effects and other complex phenomena like diffuse reflection from façades are important when calculating sound pressure levels in a highly shielded area in a city. The finite-difference time-domain method, accounting for background flow, provides important information on this subject. Calculations like the ones presented in this chapter could be a starting point for engineering methods with respect to accurate urban noise mapping. In realistic situations, sound pressure levels in the backyard will be increased some more due to the presence of distant sources. The simulations in this chapter have not been validated with experimental data. Especially the simulation results where acoustic scattering on turbulence is considered should be used with care.

Chapter 4

Conclusions – Further research

In this work, it is shown how the finite-difference time-domain simulation technique can be used to simulate sound propagation in a moving medium. The engineering approach of sound propagation in a "background flow" is applied. The interactions between the sound waves and the flow are limited. The acoustic waves do not influence the flow field, and generation of sound is not considered. The main actions of wind on sound propagation outdoors namely convection, refraction and scattering of sound are accounted for.

The acoustic quantities are considered as a perturbation of the (linearised) Euler equations. Special care was necessary to obtain a stable time-stepping equation for the acoustic velocity in a wide range of applications. The use of a (kinetic) energy conservation form of the momentum equation, as well as the fact that the rotational part of the acoustic velocity could be neglected in low Mach number flows, have shown to be important steps during the derivation of the acoustic velocity equation.

The equations are discretised in a staggered grid, in space and time. To obtain an efficient (and still explicit) calculation scheme, some terms in the equations were replaced by a first approximation in absence of flow. In between two successive time steps of both the pressure and velocity equations, a prediction step was introduced to calculate the acoustic pressure and velocity in a motionless medium at this intermediate time, at each calculation point in the grid. It is shown that this approach also results in a more easy treatment near simulation borders and prevents doing the same calculations when updating nearby acoustic pressures and velocities.

This approach does not result in a significant increase in the amplitude and phase error when simulating sound propagation in the presence of typical wind speeds outdoors. Therefore, using 10 cells per wavelength is still a good compromise between accuracy and the necessary computational resources. For large flow velocities, accurate simulations are also possible, provided that the number of cells per wavelength is largely increased. A numerical example indicated that the stability criterion in absence of flow can be used, when adding the flow velocity to the speed of sound. This holds for the small flow velocities encountered outdoors. For larger Mach numbers, this condition becomes more severe.

In outdoor sound propagation, ground models and perfectly absorbing boundaries to truncate the unlimited propagation domain, are important themes.

Reflection from natural soils in time-domain is simulated with the Zwikker and Kosten model. The acoustic equations are adapted to describe sound propagation inside (a few layers of) the ground, based on three parameters: flow resistivity, porosity and the structure factor.

For situations where impulse responses are very long e.g. due to the multiple reflections between noise barriers on either side of the road, as encountered in traffic noise situations, perfectly absorbing boundaries are necessary. The Perfectly Matched Layer technique is applied to sound propagation in a uniform background flow, and has shown to be a very efficient absorbing boundary condition. Perfectly Matched Layers with a thickness of only a few cells perform already better than the first-order approximation of a perfectly absorbing boundary. Reflection stays well below –120 dB for a wide range of angles of incidence, when using optimised damping parameters and a sufficient number of cells (> 20). When these equations are used in the presence of a non-uniform flow, their efficiency is reduced with a few 10 dB's, making it still a sufficiently damping boundary condition.

The model was used with success to quantify the effect of wind on sound propagation in some situations of practical interest outdoors.

The model was illustrated with two examples of sound propagation over flat ground. A refracting atmosphere above a finite-impedance ground results in a frequency shift of the ground dip, and affects the magnitude of the interference minimum. Finite-difference time-domain simulations of sound propagation over a perfectly reflecting ground at some longer distances correspond well to calculations with the semi-analytical, normal mode solution.

Sound propagation over noise barriers in the presence of wind was investigated in detail in this work. Screen-induced refraction of sound by wind strongly decreases downwind noise barrier performance. The use of a row of trees behind the noise barrier(s), acting as a windbreak, has shown to be an interesting and practical solution to this problem. This was proven by means of a wind tunnel experiment, a field experiment along a highway and by numerical simulations.

In the wind tunnel experiment, different configurations of single noise barriers and noise barriers on either side of the line source, in combination with synthetic windscreens were tested. Depending on the location of the windscreens, an important reduction of the screen-induced refraction of sound was achieved.

The finite-difference time-domain simulation technique, accounting for background flow, is able to adequately simulate sound propagation over noise

barriers in the presence of wind. Good agreement with a wind tunnel experiment, described in literature, was found. For most configurations of noise barriers in combination with windscreens, the net effect of the windscreens, as measured during our wind tunnel experiment, could be simulated with success as well.

The field experiment confirmed that the positive effects by the synthetic windscreens in the wind tunnel were also observed for real rows of trees. A direct comparison was made between part of a noise barrier along a highway with and without a row of trees, at limited distance from each other. A linear relationship between the improvement of downwind noise barrier efficiency by placing a row of trees and the wind speed was found. Measurements in absence of wind have shown that the presence of trees will not significantly decrease noise barrier performance when looking at total, A-weighted sound pressure levels from traffic noise, due to its low-frequent spectrum.

The model developed in this work has shown to be a powerful tool to investigate the parameters involved when sound propagation in the presence of noise barriers in wind, in combination with windbreaks, is considered. Simulations in a region downwind from the noise barrier(s) showed that the porosity of the windbreaks, wind speed, and the distance between the acoustic source and noise barrier(s) are important parameters to quantify the efficiency of the windbreaks. The impedance of the soil downwind has only a small influence on the efficiency of the windbreaks. For a typical traffic noise situation, it is possible to completely cancel out wind effects up to a distance of $20H$ behind the downwind noise barrier, and up to a height of $1H$, when placing a large windscreen behind the downwind noise barrier. Detailed analysis is necessary to evaluate each configuration, since the effect of windbreaks on noise barrier performance is the result of the complex interactions between the multiple reflections between the barriers, the multiple diffraction paths, upwardly and downwardly refracting flows and also turbulence, however to a smaller degree.

Sound propagation from a street canyon to a nearby backyard, which is a typical situation in an urban area, was studied. The access to quiet rooms on the back-façade or to a silent backyard is important since it may compensate a noisy street side. Atmospheric effects have shown to be responsible for an important increase in sound pressure levels at these highly-shielded places. The simulation technique developed in this work can take into account the complex interactions between:

- the multiple reflections, specular as well as diffusive, in the street canyon and in the backyard,
- the refracting, complex flow field above the buildings in the presence of flow-disturbing structures like saddle-backed roofs,
- the frequency-dependent (complex) reflection from a piece of grass-land,
- and the effects of a scattering, turbulent atmosphere, by means of the turbule model.

However, the (large) effects of refraction by wind and scattering on turbulence into the backyard need experimental validation. It is however expected that this would be a rather difficult task and would take a long measurement campaign, since one has to wait for appropriate meteorological conditions. Moreover, measuring tools to capture the quick variations in wind speed are needed.

The main disadvantage of the finite-difference time-domain simulation technique is the large need for computer memory and the long computation times. This makes finite-difference time-domain simulations a low-frequency or mid-frequency technique on actual PC's. Moreover, when the effects of non-uniform and rotational flows need to be accounted for, the necessary computational resources are largely increased. The memory demand increases roughly with a factor 3 relative to simulating sound propagation in a motionless medium. With the equations derived for simplified background flows, it is possible to make some gain in computation time. Memory use on the other hand has shown to decrease only to a small degree.

As a consequence, the distances over which sound can be simulated are limited, and decreases strongly when higher sound frequencies are considered. Although the developed model is fully three-dimensional, the simulation of e.g. a point source in practical situations is usually not possible. It is therefore considered that the main challenge lies in making the finite-difference time-domain technique more efficient with respect to the use of computational resources. Although the power of PC's grows fast, some approaches will be necessary to be able to simulate sound propagation at larger distances and at higher frequencies in the near future.

The question rises e.g. whether it is still necessary to solve the full-wave equations at a certain distance from e.g. a noise barrier on either side of a source. Only horizontal flow is observed at these locations, and simulating one-way sound propagation will be sufficient. Therefore, the coupling of finite-difference time-domain simulations with more appropriate techniques like e.g. the Parabolic Equation method might be an interesting research direction.

The use of higher order schemes, that are very common in up-to-date aero-acoustical simulation techniques, might lead to a decrease in the necessary number of grid cells per wavelength, without loss of accuracy. This will lead to a decrease in memory use. The main disadvantage of such schemes are the difficult implementation near complex obstacles and in parts of the simulation domain where different propagation equations are used close to each other e.g. at the air-ground interface. In an object-oriented environment, it is possible to combine different simulation techniques. Parts of a grid not near any border of the simulation domain, or at sufficient distance from obstacles, might benefit from using higher-order schemes.

In a uniform Cartesian grid, small structures, but also sloping and curved surfaces can not be represented in an efficient way. A case of practical interest is e.g. sound propagation over tilted noise barriers or noise barriers with a curved top. A possible way to overcome this problem is applying a (multi-dimensional) grid refinement, for a local, accurate representation of such structures. However, attention should be paid to prevent reflection and instability at the interface of coarse and refined parts of the grid. Besides, phase and amplitude errors in each part of the grid should be kept as low as possible. The use of Voronoi cells, and finite volume cells could also be considered in this respect.

Appendix A

Expressions for χ and ξ

In this appendix, an overview is given of some discrete expressions to calculate χ and ξ. These quantities are associated with the prediction steps (in absence of flow), in between updating two successive velocity and pressure fields, during the time-stepping algorithm.

The expressions (2.46) and (2.54), to be used in the general pressure and velocity equation, not near and border, were derived in Chapter 2.2.3.

The first-order approximation of a perfectly absorbing boundary (equation (2.113)) was calculated in Chapter 2.3.3.

On a perfectly reflecting border, one needs to set χ to zero, as was done for the acoustical velocity:

$$\chi^{l}_{\alpha(\alpha+0.5)} = 0 . \tag{A.1}$$

Near the interface between the ground and the air, following equations should be applied. To update a pressure point in air, near the interface with the ground, the value of ξ of the first layer of cells inside the ground is needed, and is calculated with:

$$\xi^{l+0.5} = p^{l} - 0.5dt\frac{c^2\rho_0}{\varphi}\sum_{\alpha}\left(\frac{v^{l+0.5}_{\alpha(\alpha+0.5)} - v^{l+0.5}_{\alpha(\alpha-0.5)}}{d\alpha}\right). \tag{A.2}$$

The value of χ on the interface between ground and air is calculated with the following formula:

$$\chi^{l}_{\alpha(\alpha+0.5)} = \frac{1}{\left[1+0.25\frac{Rdt\varphi}{\rho_0 k_s}\right]}\left(v^{l-0.5}_{\alpha(\alpha+0.5)}\left[1-0.25\frac{Rdt\varphi}{\rho_0 k_s}\right] - \frac{0.5dt\varphi}{\rho_0 k_s}\frac{\left(p^{l}_{(\alpha+1)} - p^{l}\right)}{d\alpha}\right). \tag{A.3}$$

Expressions for χ and ξ to be used in the *PML* equations depend on the orientation of the pressure and velocity component, relative to the interface between the interior domain and the *PML* domain.

To perform time-stepping for the orthogonal pressure component inside the *PML*, the latter must receive the result of the evaluation of next expression at nearby (orthogonal) pressure points:

$$\xi_{\perp}^{l+0.5} = \left(1+0.25dt\kappa_1\right)^{-1}\left[\left(1-0.25dt\kappa_1\right)p_{\perp}^{l} - 0.5dtc^2\rho_0\left(\frac{v_{\perp(\alpha+0.5)}^{l+0.5} - v_{\perp(\alpha-0.5)}^{l+0.5}}{d\alpha}\right)\right], \tag{A.4}$$

Where $v_{\perp}$ is the component of the acoustical velocity, normal to the interface between the interior cells and *PML* cells.

To perform time-stepping for the parallel pressure component inside the *PML*, the latter must receive the result of the evaluation of next expression at nearby pressure points:

$$\xi_{//}^{l+0.5} = p_{//}^{l} - 0.5dtc^2\rho_0\sum_{//}\left(\frac{v_{//(\alpha+0.5)}^{l+0.5} - v_{//(\alpha-0.5)}^{l+0.5}}{d\alpha}\right). \tag{A.5}$$

The summation in previous equation is performed over the velocity components, parallel to the *PML* interface.

To perform time-stepping for a velocity component in the *PML*, orthogonal to the interface, the cells that are involved must return the result of the evaluation of following expression:

$$\chi_{\perp(\alpha+0.5)}^{l} = \left(1+\frac{0.25dt}{\rho_0}\kappa_2\right)^{-1}\left[\left(1-\frac{0.25dt}{\rho_0}\kappa_2\right)v_{\perp(\alpha+0.5)}^{l-0.5} - 0.5\frac{dt}{\rho_0}\frac{\left(p_{(\alpha+1)}^{l} - p^{l}\right)}{d\alpha}\right], \tag{A.6}$$

The *PML* velocity (exactly) on the interface between the interior cells and the *PML* cells is always orthogonal to that interface, and the same expression is evaluated in that point.

To perform time-stepping at the parallel components of the velocity inside the *PML*, the same formula to calculate χ as in the interior domain (equation (2.54)) should be used.

Appendix B

Simulation parameters

In the table below, an overview is given of the most important simulation parameters, as used for the applications in this work.

SECTION	simulation	ground	obstacles	wind	turbulence	dx (m)	refined dx (m)	dt (μs)	frequency (range)
3.1	downward + upward refraction above perfectly reflecting ground	perfectly reflecting	none	no wind + linear gradient	none	0.25	none	500	100 Hz
3.2	downward + upward refraction above finite-impedance ground	ground model	none	no wind + linear gradient	none	0.02	0.005	12.5	100-1000Hz
3.3	screen-induced refraction	perfectly reflecting	single noise barrier	no wind + detailed flow field	none	0.05	none	100	185Hz-750Hz
3.4.2.b	extracting ground parameters	ground model	none	no wind	none	0.002	none	4	10kHz-20kHz
3.4.2.b	extracting noise barrier parameters	ground model	single noise barrier + noise barriers on either side of the source	no wind	none	0.002	none	4	10kHz-20kHz
3.4.2.f	screen-induced refraction	ground model	single noise barrier + noise barriers on either side of the source	detailed flow field (windscreens)	none	0.002	none	4	10kHz-20kHz
3.4.4.a	porosity of windscreens	perfectly reflecting upwind, ground model downwind	single noise barrier	no wind + detailed flow field (windscreens)	none	0.08	none	160	250-500Hz
3.4.4.b	effect of wind speed	perfectly reflecting upwind, ground model downwind	single noise barrier	no wind + detailed flow field (windscreens)	none	0.08	none	160	250-500Hz
3.4.4.c	distance source-noise barriers	perfectly reflecting upwind or in between noise barriers, ground model downwind	single noise barrier + noise barriers on either side of the source	no wind + detailed flow field (windscreens)	none	0.08	none	160	250-500Hz
3.4.4.d	effect ground impedance downwind	perfectly reflecting upwind, ground model downwind	single noise barriers	no wind + detailed flow field (windscreens)	none	0.08	0.02	50	250-500Hz
3.4.4.e	traffic noise situation	perfectly reflecting upwind or in between noise barriers, ground model downwind	single noise barrier + noise barriers on either side of the source	no wind + detailed flow field (windscreens)	none	0.04	0.02	50	125-1000Hz
3.5.2.c, 3.5.2.f	refraction over roof tops	perfectly reflecting in street canyon, ground model in backyard	houses, flat roof + saddle-backed roof top	no wind + detailed flow field	none	0.04	0.02	50	125-1000Hz
3.5.2.d	refraction over roof tops +turbulent scattering into shadow zone	perfectly reflecting in street canyon, ground model in backyard	houses, flat roof top	no wind + detailed flow field + turbule model	yes	0.04	0.02	50	1000 Hz
3.5.2.e	specular and diffuse reflection on façades	perfectly reflecting in street canyon, ground model in backyard	houses, flat roof top + saddle-backed roof top, rough + flat façades	no wind	none	0.04	0.02	50	125-1000Hz

References

[1] D. Botteldooren, L. Dekoninck, J. Thoen, J. Caerels, E. van Walsum : "Lawaai", MIRA-T 2001 (Milieu- en natuurrapport Vlaanderen: thema's), Vlaamse Milieumaatschappij, Garant Uitgevers nv (2001) 235-249.

[2] ISO 9613-2 : “Acoustics – Attenuation of sound during propagation outdoors”.

[3] M. West, R. A. Sack, F. Walkden : The fast field program. A second tutorial: application to long range sound propagation in the atmosphere. Applied Acoustics **33** (1991) 199-228.

[4] R. Raspet, W. Wu : Calculation of average turbulence effects on sound propagation based on the fast field program formulation. J. Acoust. Soc. Am. **97** (1995) 147-153.

[5] K. E. Gilbert, M. J. White : Application of the parabolic equation to sound propagation in a refracting atmosphere. J. Acoust. Soc. Am. **85** (1989) 630-637.

[6] E. M. Salomons : Diffraction by a screen in downwind sound propagation: a parabolic-equation approach. J. Acoust. Soc. Am. **95** (1994) 3109-3117.

[7] X. Di, K. E. Gilbert : The effect of turbulence and irregular terrain on outdoor sound propagation. Proceedings of the 6th Symposium on long-range sound propagation (1994), Ottawa, Canada, 315-333.

[8] R. A. Sack, M. West : A parabolic equation for sound propagation in two dimensions over any smooth terrain profile: the generalised terrain parabolic equation (GT-PE). Applied Acoustics **45** (1995) 113-129.

[9] K. E. Gilbert, R. Raspet, X. Di : Calculation of turbulence effects in an upward-refracting atmosphere. J. Acoust. Soc. Am. **87** (1990) 2428-2437.

[10] E. Premat, Y. Gabillet : A new boundary-element method for predicting outdoor sound propagation and application to the case of a sound barrier in the presence of downward refraction. J. Acoust. Soc. Am. **108** (2000) 2775-2783.

[11] R. Raspet, G. Baird, W. Wu : Normal mode solution for low-frequency sound propagation in a downward refracting atmosphere above a complex impedance plane. J. Acoust. Soc. Am. **91** (1992) 1341-1352.

[12] E. M. Salomons, A. C. Geerlings, D. Duhamel : Comparison of a ray model and a Fourier-boundary element method for traffic noise situations with multiple diffractions and reflections. Acustica – Acta Acustica **83** (1997) 35-47.

[13] D. H. Crombie, D. C. Hothersall, S. N. Chandler-Wilde : Multiple-edge noise barriers. Applied Acoustics **44** (1995) 353-367.

[14] T. Okubo, K. Fujiware : Efficiency of a noise barrier with an acoustically soft cylindrical edge for practical use. J. Acoust. Soc. Am. **105** (1999) 3326-3335.

[15] D. Botteldooren : Finite-difference time-domain simulation of low-frequency room acoustic problems. J. Acoust. Soc. Am. **98** (1995) 3302-3308.

[16] D. Botteldooren : Time-domain simulation of the influence of close barriers on sound propagation to the environment. J. Acoust. Soc. Am. **101** (1997) 1278-1285.

[17] R. Blumrich, D. Heimann : A linearized Eulerian sound propagation model for studies of complex meteorological effects. J. Acoust. Soc. Am. **112** (2002) 446-455.

[18] E. M. Salomons, R. Blumrich, D. Heimann : Eulerian time-domain model for sound propagation over a finite-impedance ground surface. Comparison with frequency-domain models. Acustica– Acta acustica **88** (2002) 483-492.

[19] S. Wang : Finite-difference time-domain approach to underwater acoustic scattering problems. J. Acoust. Soc. Am. **99** (1996) 1924-1931.

[20] N. Endoh, Y. Tanaka and T. Tsuchiya : Analysis of sound filed of ultrasonic transducer in air with temperature variation by FDTD. Proceedings of 17th International Congress on Acoustics ICA (2001), Rome, Italy.

[21] J. Virieux : P-SV wave propagation in heterogeneous media: Velocity-stress finite difference method. Geophysics **51** (1986) 889-901.

[22] Z. El Hachemi, M. Tournour, R. Hallez, C. McCulloch, F. Mendonca : An implementation of acoustic analogy methods for aero-acoustics: linking CFD and computational acoustics. Proceedings of 10th International Congress on Sound and Vibration ICSV (2003), Stockholm, Sweden.

[23] M. Snellen, L. van Lier, J. Golliard, E. Védy : Prediction of the flow-induced noise for practical applications using the SNGR method. Proc. of 10th International Congress on Sound and Vibration ICSV (2003), Stockholm, Sweden.

[24] A. D. Pierce : Acoustics : an introduction to its physical principles and applications. McGraw-Hill, New York, 1981.

[25] J. H. Ferziger, M. Peric : Computational methods for fluid dynamics. New York, Springer, 1997.

[26] Computational dynamics LTD : STAR-CD (version 3.100A), 2000.

[27] Fluent Inc. : FLUENT (version 6.0), 2001.

[28] D. Botteldooren : Acoustical finite-difference time-domain simulations in a quasi-Cartesian grid. J. Acoust. Soc. Am. **95** (1994) 2313-2319.

[29] A. V. Oppenheim and R. W. Schafer : Digital signal processing. Prentice-Hall, New Jersey, 1975.

[30] V. E. Ostashev : Acoustics in moving inhomogeneous media. E & FN Spon, London, 1997.

[31] E. M. Salomons : Computational atmospheric acoustics. Kluwer, Dordrecht, 2001.

[32] M. Delaney, E. Bazley: Acoustical properties of fibrous absorbent materials. Applied Acoustics **3** (1970), 105-116.

[33] K. Attenborough, T. Waters-Fuller, K. M. Li, J. A. Lines : Acoustical properties of Farmland. J. agric. Eng. Res. **76** (2000) 183-195.

[34] T. F. W. Embleton, J. E. Piercy, G. A. Daigle : Effective flow resistivity of ground surfaces determined by acoustical measurements. J. Acoust. Soc. Am. **78** (1985) 970-980.

[35] N. M. Hess, K. Attenborough, N. W. Heap : Ground characterization by short-range propagation measurements. J. Acoust. Soc. Am. **87** (1990) 1975-1986.

[36] K. Attenborough : Ground parameter information for propagation modeling. J. Acoust. Soc. Am. **92** (1992) 418-427.

[37] S. Taherzadeh, K. Attenborough : Deduction of ground impedance from measurements of excess attenuation spectra. J. Acoust. Soc. Am. **105** (1999) 2039-2042.

[38] D. Botteldooren: Finite-difference time-domain simulation of low-frequency room acoustic problems. J. Acoust. Soc. Am. **98** (1995) 3302-3308.

[39] H. Dong, A. M. Kaynia, C. Madshus, J. M. Hovem : Sound propagation over layered poro-elastic ground using a finite-difference model. J. Acoust. Soc. Am. **108** (2000) 494-502.

[40] O. Kr. O. Pettersen, V. Henriksen, M. Bjorhus, U. Kristiansen, G. Taraldsen : Numerical calculations of sound propagation over ground surfaces. Proceedings of 17th International Congress on Acoustics ICA (2001), Rome, Italy.

[41] M. A. Biot : Theory of propagation of elastic waves in a fluid-saturated porous solid. I. Low frequency range. J. Acoust. Soc. Am. **28** (1956) 168-178.

[42] C. Zwikker, C. W. Kosten : Sound absorbing materials (Elsevier, New York, 1949).

[43] J. P. Berenger : A Perfectly matched layer for the absorption of electromagnetic waves. J. Comp. Physics **114** (1994) 185-200.

[44] F. D. Hastings, J. B. Schneider, S. L. Broschat : Application of the perfectly matched layer (PML) absorbing boundary condition to elastic wave propagation. J. Acoust. Soc. Am. **100** (1995) 3061-3069.

[45] Q. H. Liu, J. Tao : The perfectly matched layer for acoustic waves in absorptive media. J. Acoust. Soc. Am. **102** (1997) 2072-2082.

[46] F. Q. Hu : On Absorbing Boundary Conditions for Linearized Euler Equations by a Perfectly Matched Layer. J. Comp. Phys. **129** (1996) 201-219.

[47] S. Abarbanel, D. Gottlieb, J. S. Hesthaven : Well-posed perfectly matched layers for advective acoustics. J. Comp. Phys. **154** (1999) 266-283.

[48] F. Q. Hu : A stable, perfectly matched layer for linearized Euler equations in unsplit physical variables. J. Comp. Physics **173** (2001) 455-480.

[49] J. P. Berenger : Perfectly matched layer for the FDTD solution of wavestructure interaction problems. IEEE Antennas Propagation Symposium **44** (1996) 110-117.

[50] D. K. Wilson, J. G. Brasseur, K. E. Gilbert : Acoustic scattering and the spectrum of atmospheric turbulence. J. Acoust. Soc. Am. **105** (1999) 30-34.

[51] D. K. Wilson, V. E. Ostashev : A Reexamination of acoustic scattering in the atmosphere using an improved model for the turbulence spectrum. Proceedings of Battlespace Atmospherics and Cloud Impacts on Military Operations Conference (2000), Fort Collins, USA.

[52] A. N. Kolmogorov : The local structure of turbulence in incompressible viscous fluid for very large Reynolds numbers. C. R. Acad. Sci. IRSS **30** (1941) 301-305.

[53] D. K. Wilson, D. W. Thomson : Acoustic propagation through anisotropic, surface-layer turbulence. J. Acoust. Soc. Am. **96** (1994) 1080-1095.

[54] G. H. Goedecke, V. E. Ostashev, D. K. Wilson, H. J. Auvermann : von Kármán spectra of temperature and velocity fluctuations. Proceedings of 9th International Congress on Sound and Vibration ICSV (2002), Orlando, USA.

[55] P. Blanc-Benon, L. Dallois, D. Juvé : Long range sound propagation in a turbulent atmosphere within the parabolic equation approximation. Acustica – Acta Acustica **87** (2001) 659-669.

[56] D. K. Wilson : A turbulence spectral model for sound propagation in the atmosphere that incorporates shear and buoyancy forcings. J. Acoust. Soc. Am. **108** (2000) 2021-2038.

[57] G. H. Goedecke, H. J. Auvermann : Acoustic scattering by atmospheric turbules. J. Acoust. Soc. Am. **102** (1997) 759-771.

[58] G. H. Goedecke, R. C. Wood, H. J. Auvermann, V. E. Ostashev, D. I. Havelock, C. Ting : Spectral broadening of sound scattered by advecting atmospheric turbulence. J. Acoust. Soc. Am. **109** (2001) 1923-1934.

[59] W. E. McBride, H. E. Bass, R. Raspet, K. E. Gilbert : Scattering of sound by atmospheric turbulence: a numerical simulation above a complex impedance boundary. J. Acoust. Soc. Am. **90** (1991) 3314-3325.

[60] J. C. Kaimal, J. C. Wyngaard, Y. Izumi, O. R. Coté : Spectral characteristics of surface layer turbulence. Q. J. R. Meteorol. Soc. **98** (1972) 563-589.

[61] R. Raspet, G. Baird, W. Wu : Normal mode solution for low-frequency sound propagation in a downward refracting atmosphere above a complex impedance plane. J. Acoust. Soc. Am. **91** (1992) 1341-1352.

[62] A. Berry; G. A. Daigle : Controlled experiments on the diffraction of sound by a curved surface. J. Acoust. Soc. Am. **83** (1988) 2047-2058.

[63] G. A. Daigle, J. E. Piercy, T. F. W. Embleton : Effects of atmospheric turbulence on the interference of sound waves near a hard boundary. J. Acoust. Soc. Am **64** (1978) 622-630.

[64] E. M. Salomons : Reduction of the performance of a noise screen due to screen-induced wind-speed gradients. Numerical computations and wind tunnel experiments. J. Acoust. Soc. Am **105** (1999) 2287-2293.

[65] R. DeJong, E. Stusnick : Scale model studies of the effect of wind on acoustic barrier performance. Noise control engineering **6** (1976) 101-109.

[66] K. B. Rasmussen : Sound propagation over screened ground under upwind conditions. J. Acoust. Soc. Am. **100** (1996) 3581-3586.

[67] K. B. Rasmussen, M. G. Arranz : The insertion loss of screens under the influence of wind. J. Acoust. Soc. Am. **104** (1998) 2692-2698.

[68] N. Barriere, Y. Gabillet : Sound propagation over a barrier with realistic wind gradients. Comparison of wind tunnel experiments with GFPE computations. Acustica– Acta acustica **85** (1999) 325-334.

[69] E. M. Salomons, K. B. Rasmussen : Numerical computations of sound propagation over a noise screen based on an analytic approximation of the wind speed field. Appl. Acoustics **60** (2000) 327-341.

[70] G. A. Daigle : Diffraction of sound by a noise barrier in the presence of atmospheric turbulence. J. Acoust. Soc. Am. **71** (1982) 847-854.

[71] D. Heimann, R. Blumrich : Time-domain simulations of sound propagation through screen-induced turbulence (submitted to Applied Acoustics).

[72] D. Heimann, R. Blumrich : Modeling the wind effect on the acoustical performance of various screen geometries. 9th International Congress on Sound and Vibration ICSV (2001), Orlando, USA.

[73] T. Meloni, F. Fischer: Factors moderating the effect of noise barriers. Proceedings of NOISE-CON (2000), Newport Beach, USA.

[74] S. Viollon, C. Lavandier, C. Drake : A sound judgment depending on the urban visual setting ? Proceedings of the joint meeting "Berlin 99" : ASA / EAA / DAGA (1999), Berlin, Germany.

[75] D. Gabriels, W. Cornelis, I. Pollet, T. Van Coillie, M. Ouessar : The I.C.E. wind tunnel for wind and water erosion studies. Soil Technology **10** (1997) 1-8.

[76] Y. Gabillet, G. A. Daigle, A. L'Espérance : Sound propagation in a wind tunnel: Comparison of experiments with FFP and residue solution. Applied Acoustics **43** (1994) 321-331.

[77] L. J. Hagen, E. L. Skidmore : Windbreak drag as influenced by porosity. Transactions of the American Society of Agricultural Engineers **14** (1971) 464-465.

[78] W. M. Cornelis, D. Gabriels, R. Hartmann, T. Lauwaerts : Simulation of windbreaks for wind-erosion control in a wind tunnel. Proceedings of International Symposium : 50th Anniversary USDA-ARS Wind Erosion Research at Kansas University (1997), Manhattan, USA.

[79] U. Sandberg, J. A. Ejsmont : Tyre/road noise reference book. Informex, Kisa, Sweden, 2002.

[80] W. Dierickx : Flow reduction of synthetic screens obtained with both a water and airflow apparatus. J. Agric. Eng. Res. **71** (1998) 67-73.

[81] M. S. Howe : Acoustics of fluid-structure interactions (Chapter 5.3 "interactions with perforated screens"). Cambridge University press, Cambridge, 1998.

[82] W. M. Schuller, J. H. de Zeeuw : Barrieres met bomen. Nederlands Akoestisch Genootschap, publikatienummer **56** (1980) 70-96.

[83] W. M. Schuller, J. H. de Zeeuw : Acoustic effect of trees on barriers. Proceedings of Internoise 1981, 253-256.

[84] O. Fegeant : Wind-induced vegetation noise. Part I : A prediction model. Acustica – Acta acustica **85** (1999) 228-240.

[85] O. Fegeant : Wind-induced vegetation noise. Part II : Field measurements. Acustica – Acta acustica **85** (1999) 241-249.

[86] H. F. Boersma, R. S. Etienne : Characterization of the natural ambient sound environment. Proceedings of Internoise 1996, 2465-2468.

[87] D. Aylor : Noise reduction by vegetation and ground. J. Acoust. Soc. Am. **51** (1972) 197-205.

[88] D. Heimann : Numerical simulation of wind and sound propagation through an idealised stand of trees. Acustica– Acta acustica **89** (2003) 779-788.

[89] M. J. M. Martens, A. Michelsen : Absorption of acoustic energy by plant leaves. J. Acoust. Soc. Am. **69** (1981) 303-306.

[90] F. Fricke : Sound propagation through vegetation. J. Sound Vib. **91** (1984) 149-158.

[91] D. Aylor : Sound transmission through vegetation in relation to leaf area density, leaf width, and breadth canopy. J. Acoust. Soc. Am. **51** (1972) 411-414.

[92] M. A. Price, K. Attenborough, N. W. Heap : Sound attenuation through trees : Measurements and models. J. Acoust. Soc. Am. **84** (1988) 1836-1844.

[93] M. J. M. Martens : Foliage as a low-pass filter : Experiments with model forests in an anechoic chamber. J. Acoust. Soc. Am. **67** (1980) 66-72.

[94] S. H. Tang, P. P. Ong : A Monte Carlo technique to determine the effectiveness of roadside trees for containing traffic noise. Applied Acoustics **23** (1988) 263-271.

[95] R. N. Hosier, P. R. Donavan : Microphone windscreen performance. National Bureau of Standards Reports NBSIR79-1599 (Jan. 1979).

[96] S. Morgan, R. Raspet : Investigation of the mechanisms of low-frequency wind noise generation outdoors. J. Acoust. Soc. Am. **92** (1992) 1180-1183.

[97] H. F. Boersma : Characterization of the natural ambient sound environment: measurements in open agricultural grassland. J. Acoust. Soc. Am. **101** (1997) 2104-2110.

[98] K. Attenborough : Acoustical impedance models for outdoor ground surfaces. J. Sound Vib. **99** (1985) 521-544.

[99] M. J. M. Martens, L. A. M. van der Heijden, H. H. J. Walthaus, W. J. J. M. Van Rens : Classification of soils based on acoustic impedance, air flow resistivity, and other physical soil parameters. J. Acoust. Soc. Am. **78** (1985) 970-980.

[100] E. Öhrström : Psycho-social effects of traffic noise exposure. J. Sound and Vibr. **151** (1991) 513-517.

[101] M. Bacelon : La gêne due au bruit de la circulation automobile. Cahier des CSTB **88** (1967).

[102] T. Kihlman : Quiet side and high façade insulation – means to solve the city noise problem. Proceedings of Internoise 2001, The Hague, The Netherlands.

[103] J. Kang : Numerical modelling of the sound fields in the urban streets with diffusely reflecting boundaries. J. Sound Vibr. **258** (2002) 793-813.

[104] R. H. Lyon : Role of multiple reflections and reverberation in urban noise propagation. J. Acoust. Soc. Am. **55** (1974) 493-503.

[105] J. Kang : Sound propagation in street canyons: Comparison between diffusely and geometrically reflecting boundaries. J. Acoust. Soc. Am. **107** (2000) 1394-1404.

[106] J. Kang : Experiments on the subjective assessment of noise reduction by absorption treatments. Chinese Noise and Vibration Control **5** (1988) 20-28.

[107] J. Forssén, M. Ögren : Thick barrier noise-reduction in the presence of atmospheric turbulence: measurements and numerical modelling. Applied Acoustics **63** (2002) 173-187.

[108] J. Forssen : Calculation of sound reduction by a screen in a turbulent atmosphere using the parabolic equation method. Acustica – Acta acustica **84** (1998) 599-606.